STABILITY OF CONSTRAINED CAPILLARY INTERFACES

A Dissertation

Presented to the Faculty of the Graduate School

of Cornell University

in Partial Fulfillment of the Requirements for the Degree of

Doctor of Philosophy

by

Joshua Blake Bostwick

May 2011

STABILITY OF CONSTRAINED CAPILLARY INTERFACES

Joshua Blake Bostwick, Ph.D.

Cornell University 2011

Surface tension acting at an interface holds an underlying liquid in motionless equilibrium. If the interface is partially supported, the extent and type of wetting-contact can significantly influence the stability of the equilibrium configuration. This dissertation addresses a number of questions related to the stability and dynamics of constrained interfaces subject to capillarity. The problems considered here fall into two distinct classes.

The first class of problem is concerned with the extent-of-constraint and restricts to interface disturbances with immobile or 'pinned' contact lines. Here the base-state volume is taken to be 'filling', or the static interface shape intersects the surface-of-support tangentially, such as a spherical-belt or cylindrical-cup solid support. With regards to the drop under spherical-belt support, the base-state is stable, oscillations persist and the effect of the constraint is to modify the spectrum and modal structure of the unconstrained problem, as well as introduce a low-frequency mode. In contrast, a cylindrical interface is subject to capillary instability and more particularly Plateau-Rayleigh break-up, which can be partially stabilized by either a cylindrical-cup or end-plane support. Here introducing a weak-secondary curvature to the cylindrical cup-like support can either stabilize or destabilize this new family of nearly-cylindrical toroids. This is referred to as the torus-lift of the cylinder and is used in conjunction with a symmetrization procedure to prove a large-amplitude stability result for cylindrical lens-like menisci.

The second class of problem is focused on the dynamics of the three-phase contact-line and also the effect of base-state volume. In considering the contact-line dynamics of the sessile drop, an instability related to translational or 'walking'

motion is catalogued and two types of modal crossings are observed. The first is related to contact-line mobility and relevant to experimentally-observed contact-line instabilities, while the second is associated with symmetry-breaking of the hemispherical base-state. A similar 'walking' instability is observed for the static rivulet, which is shown to be related to the phenomenon of rivulet meandering. Lastly, a 'bounding' method is developed and applied to the family of catenoids to reproduce well-known stability results and generate new ones without explicitly calculating the second variation.

BIOGRAPHICAL SKETCH

Joshua Blake Bostwick was born on January 9th, 1981 in Wauwatosa, Wisconsin, where he also graduated from high school in May 1999. As a youth, he played a number of sports such as tennis, basketball and soccer. He enjoyed the most success with soccer, traveling throughout the country with his club team to compete in high-level tournaments and winning the Wisconsin State Championship in 1998 with his high school team.

In the fall of 1999, he enrolled at the University of Wisconsin-Milwaukee (UWM) to pursue degrees in both Civil Engineering & Mechanics and Physics. While at UWM, Josh had the privilege to work with Dr. Michael Weinert as an REU student on first principles electronic structure calculations with application to MgO(111) crystal defects. Around this time he was also introduced to Dr. Chris Papadopoulos, who was the instructor in his Strength of Materials course. Dr. Papadopoulos noticed Josh's potential immediately and asked him to begin grading papers for his mechanics classes. While working together, Dr. Papadopoulos introduced him to the more subtle points of mechanics. This sparked Josh's interest in the subject and ultimately led to the selection of his senior project on Kane's equations. On the basis of this work and also academic performance, he was granted the 2005 Outstanding Student Award. Josh graduated from UWM with a B.S.E. in Civil Engineering & Mechanics and a B.A. in Physics with a minor in Mathematics in 2005.

During the fall of 2005, Josh began working on his Ph.D. in Theoretical & Applied Mechanics (TAM) at Cornell University. He worked as a teaching assistant while completing his graduate coursework. In honor of his teaching accomplishments at Cornell, he was given the 2010 H.D. Block Award for teaching excellence in engineering mathematics, which was awarded on the basis of both student and

faculty feedback.

It was during his second year that he began working with Dr. Paul Steen on the dynamics of constrained capillary interfaces with application to liquid drops, bridges and toroids. During the fall semester of 2007, he had the opportunity to work, under a NSF IREE grant, on computational level set methods applied to capillary interfaces with Dr. Peter Ehrhard at Dortmund Universitat in Dortmund, Germany. The work completed under the direction of Dr. Steen, which has been partially supported by a NASA grant, is disseminated in this dissertation and also appears in select journal articles.

I would like to dedicate this dissertation to Emily, for her patience and support.

ACKNOWLEDGEMENTS

A number of individuals have helped make this dissertation possible and I would like to acknowledge a few of them here.

Foremost, I would like to express my deepest appreciation to my advisor, Paul Steen, for his guidance and encouragement. It has been an honor and a privilege to work with Paul. I would also like to recognize the other distinguished members of my committee, Eberhard Bodenschatz (Physics) and Sidney Leibovich (MAE), and thank them for providing valuable suggestions in preparing this thesis and also taking the time to serve. In addition, I am grateful to the Department of Theoretical & Applied Mechanics (TAM) for the learning environment they have created and also their support during my tenure there. Finally, I would like to thank Chris Papadopoulos for introducing me to the field of Mechanics and TAM.

I am indebted to all the members of the Steen research group for many stimulating discussions and also their invaluable suggestions in preparing the content of this dissertation. It has been a pleasure to work with so many talented people, who share similar research interests.

It would not have been possible to complete this thesis work without the infinite support of a loving family. I thank my mother Mary for her encouragement, understanding and strength during hard times; my sister Audra for teaching me about perseverance and redemption; my niece Cora for bringing a little levity to my day and reminding me not to take life/myself so seriously; and finally my late father Ed, who has always driven me to succeed and continues to inspire me daily.

Lastly, in numerical order only, I would like to express my gratitude to Emily Jung, whose sacrifices have more than paralleled my own throughout this journey. It has truly been a blessing to have her in my life.

TABLE OF CONTENTS

LIST OF FIGURES

CHAPTER 1

INTRODUCTION

Capillary interfaces are ubiquitous in nature and have been studied extensively since the time of Young (1805) and Laplace (1806), who introduced the notion of surface tension. Early work on the subject was primarily focused on isolated surfaces, while more recently there has been an interest in partially-supported interfaces with an emphasis on the dynamics of the three-phase contact-line. Interest in wetting conditions can be attributed to a large number of capillary-based technological innovations, such as liquid lens focusing, spin-casting processes and micro-fluidics, to name a few. In all such applications, detailed knowledge regarding the stability of the constrained capillary interface is essential. As could be expected, the extent and type of wetting-contact can significantly influence both the stability and dynamics.

1.1 Motivation

One typically encounters capillary interfaces in courses on hydrodynamic stability when being introduced to classic results, such as the Rayleigh oscillations of a spherical drop (Rayleigh, 1879) or Plateau-Rayleigh break-up of a liquid cylinder (Plateau, 1863; Rayleigh, 1879). These classic examples will be referred to as 'unconstrained' problems, because the respective interface does not contact a solid-support or the fluid domain is isolated. In contrast, a 'constrained' interface partially contacts a solid-support and also has a three-phase contact-line, defined as the geometric curve formed at the intersection of the solid, liquid and gas phases. With regards to terrestrial applications, most technologies that employ capillary interfaces are constrained and the classical results (unconstrained) can be of lim-

ited utility, but may certainly be used as a guide to understanding the physics. In general, the constrained problem is more difficult to analyze than the unconstrained problem, because one must establish the appropriate governing equations at the contact-line. Two such models are used in this thesis. The first assumes the contact-line is immobile or 'pinned', while the second has a dynamic contact-line, whose motion is governed by a prescribed constitutive law.

The problems considered in this thesis are motivated by a number of scientific phenomenon and technological innovations, which can be related to the classic (unconstrained) problems mentioned above. Some applications which utilize drops include; adaptive liquid lens focusing for optical devices (Lopez & Hirsa, 2008), droplet ejection for ink-jet printing (James *et al.*, 2003*b*) and drop atomization for spray-cooling and fuel injection (Vukasinovic *et al.*, 2007). Similarly, both the crown-splash problem (Deegan *et al.*, 2008) and the upstream meniscus in the planar-flow melt-spinning device (Steen & Karcher, 1997) can be viewed as a constrained cylindrical-like interface. The aforementioned applications, which all have immobile or pinned contact lines, require a thorough understanding of the dynamics of the constrained capillary interface to ensure maximal control over the respective process. For example, the adaptive liquid lens consists of a system of coupled spherical-cap droplets, whose focal length can be quickly and continuously varied by acoustic (pressure) pulses (Lopez *et al.*, 2005). To efficiently process images from this device, the frequency spectrum and corresponding interface deformations are required. This information, which is unavailable from the classic (unconstrained) problem (Rayleigh, 1879), is computed here.

In addition to numerous industrial applications, the moving contact-line is also of great scientific interest, because of the limited understanding of the physics there.

One of the most commonly accepted constitutive laws relates the contact-angle to the contact-line speed. In this thesis, application of this particular constitutive law is shown to produce a number of distinct results, which may be used to validate or invalidate said law. With regards to applications, the dynamics of the moving contact-line are important for droplet manipulation in microfluidics and coating processes. For example, a ratchet-like translational motion (instability) is observed for sessile drops on chemically-treated gradient surfaces (Daniel *et al.*, 2004). Similarly, Noblin *et al.* (2009) have shown that this translational motion can be directionally controlled by both horizontal and vertical forcing, while Brunet *et al.* (2009) demonstrated that under external forcing a sessile drop can overcome the influence of gravity and be driven up a sloped incline against gravity. The translational droplet motion mentioned above may be related to a 'walking' instability for sessile drops that is catalogued in this thesis and has not been previously reported. Finally, rivulets of liquids on solid surfaces, whose stability is important to heat transfer applications, can be viewed as constrained cylinder-like interfaces with dynamic contact-lines (Davis, 1980; Weiland & Davis, 1981).

Lastly, the dynamic stability calculations for constrained capillary interfaces under both contact-line models can become quite involved and are generally handled using computational-based approaches, such as finite element methods. The solution methods developed in this thesis are straightforward and essentially analytic, which make the computations tractable. For example, by formulating the constrained problem in the unifying framework of functional analysis one may smoothly interchange between contact-line models without significantly changing the solution method. Finally, a bounding technique is developed to generate a sufficient condition for the static stability of the catenoid without explicitly calculating the second variation.

1.2 Mathematical background

When referring to the stability of an equilibrium configuration one needs to distinguish between static or dynamic stability. While the two types of stability may be interpreted differently there certainly exists situations where the linear stability results are coincident, as is the case for an interface of uniform surface tension σ holding an underlying fluid.

To establish this parallel, consider static stability first. As postulated by Young and Laplace, a capillary surface $\boldsymbol{x} = \boldsymbol{r}(u, v)$ defined with surface coordinates u, v behaves like an elastic membrane with an energy U proportional to its surface area

$$\frac{1}{\sigma} U = \int_{\Gamma} |\boldsymbol{r}_u \times \boldsymbol{r}_v|. \tag{1.1}$$

The system is in equilibrium if the first variation of surface energy

$$\frac{1}{\sigma} \delta U = \int_{\Gamma} (\kappa_1 + \kappa_2 - \mu)\ y + \int_{\gamma} (\boldsymbol{n} \cdot \boldsymbol{n_1} - \cos\alpha) \frac{y}{\sin\alpha}, \tag{1.2}$$

vanishes for all allowable disturbances y. Here the constant μ is a Lagrange multiplier, necessary to ensure volume conservation and related to the pressure on the interface Γ by the Young-Laplace equation

$$p/\sigma = \kappa_1 + \kappa_2 \equiv 2H, \tag{1.3}$$

which relates the pressure to the sum of the principal curvatures κ_1, κ_2 of the interface. Equivalently, surfaces of constant mean curvature H are necessarily in static equilibrium. Similarly, a balance of forces on the contact line γ yields the Young-Dupré equation

$$\boldsymbol{n} \cdot \boldsymbol{n_1} = \frac{\sigma_{sg} - \sigma_{sl}}{\sigma_{lg}} \equiv \cos\alpha, \tag{1.4}$$

which relates the surface normals $\boldsymbol{n}, \boldsymbol{n_1}$ and surface tensions of the solid-liquid σ_{sl}, solid-gas σ_{sg} and liquid-gas $\sigma_{lg} \equiv \sigma$ interfaces to the contact-angle α, as shown in

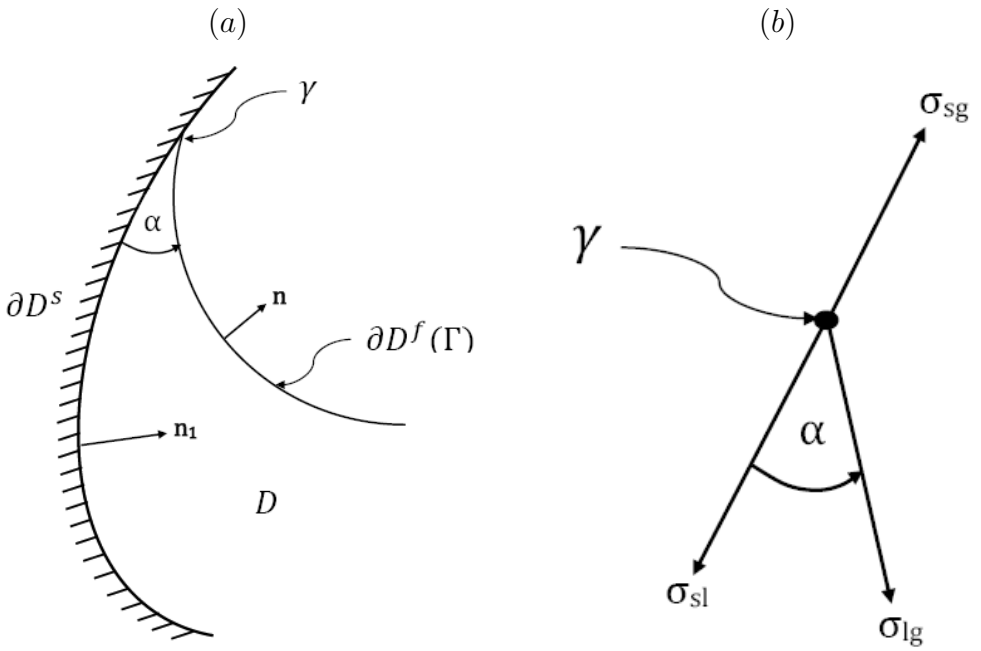

Figure 1.1: Three-phase contact-line: (a) definition sketch and (b) force balance on contact-line.

figure 1.1(b). The contact-angle is a macroscopic quantity specified by the material properties of the three-phase contact-line.

The disturbance energy associated with a deviation y ($\delta\boldsymbol{x}$ in figure 1.2) from the equilibrium surface configuration is proportional to the second variation

$$\frac{1}{\sigma}\delta^2 U = \int_\Gamma \left[-\left(\kappa_1^2+\kappa_2^2\right)\, y - \Delta_\Gamma y\right] y + \int_\gamma \left(\frac{\partial y}{\partial e} + \chi y\right) y, \tag{1.5}$$

which is conveniently decomposed into its respective interface Γ and contact-line γ contributions (Myshkis *et al.*, 1987). Here Δ_Γ is the Laplace-Beltrami operator,

$$\Delta_\Gamma y \equiv \frac{1}{\sqrt{g}}\frac{\partial}{\partial u^\alpha}\left(\sqrt{g}g^{\alpha\beta}\frac{\partial y}{\partial u^\beta}\right), \tag{1.6}$$

$g_{\alpha\beta} \equiv \boldsymbol{x}_\alpha \cdot \boldsymbol{x}_\beta$ is the surface metric, and χ is related to the contact-angle α and normal curvatures (defined in Kreyszig, 1991) of the interface k and surface-of-

support $\bar{k}$,

$$\chi \equiv \frac{k\cos\alpha - \bar{k}}{\sin\alpha}. \tag{1.7}$$

Stability of the equilibrium surface is determined by the sign of the second variation (1.5) and can be greatly influenced by the disturbance class to which the interface is subject. In particular the two types of contact-line disturbance that have no associated disturbance energy are of particular interest(c.f. figure 1.2). The first satisfies

$$\frac{\partial y}{\partial e} + \chi y = 0 \quad [\gamma], \tag{1.8}$$

and preserves the static contact-angle α in accordance with the Young-Dupré equation (1.4) and is termed the 'natural disturbance' (c.f. figure 1.2(a)). The natural contact-line condition (1.8) represents the linearization of the Young-Dupré equation (1.4) about the angle α. Equation (1.8) is derived in Appendix A. The second has a 'pinned' contact-line

$$y = 0 \quad [\gamma], \tag{1.9}$$

as shown in figure 1.2(b). When the equilibrium surface is subject to either of the aforementioned disturbances, stability is uniquely determined by the sign of the eigenvalue λ of the boundary value problem

$$-\Delta_\Gamma y - \left(\kappa_1^2 + \kappa_2^2\right) y = \lambda y, \tag{1.10}$$

with stability assured if $\lambda > 0$.

With regards to dynamic stability, one method frequently used to study small interface disturbances of a fluid subject to capillarity, is to manipulate the hydrodynamic equations into an eigenvalue problem via a normal mode expansion ($\mathrm{e}^{\lambda t}$). Following the analysis of Davis (1980), a disturbance energy balance will be derived by manipulating the linearized hydrodynamic field equations. To begin, consider an incompressible, viscous fluid occupying an arbitrary domain D, bounded by a

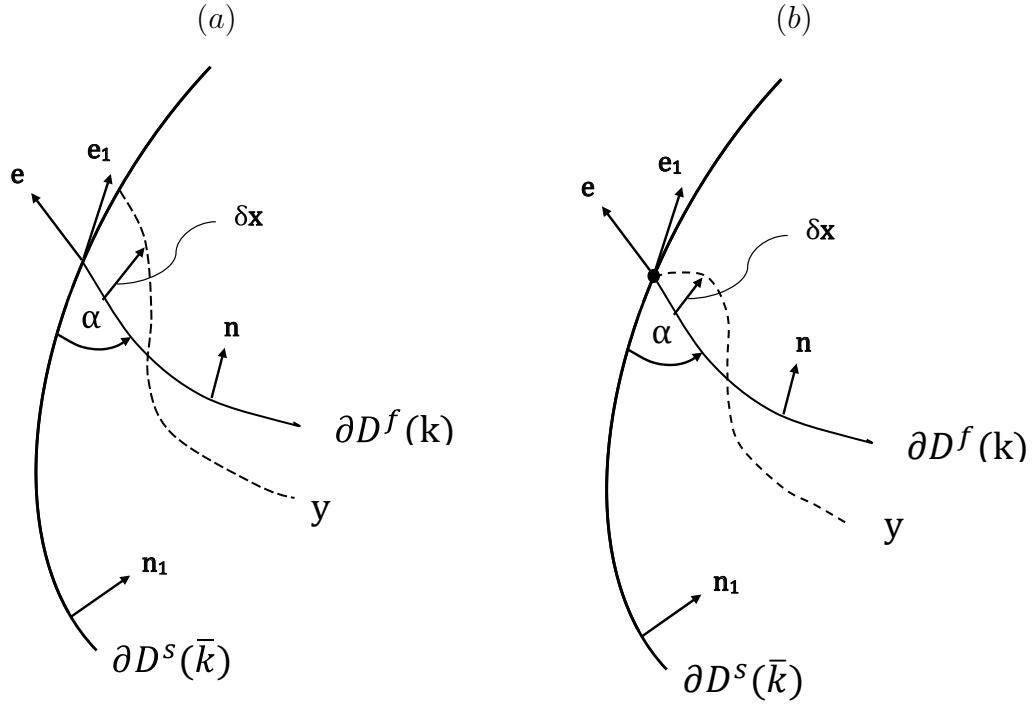

Figure 1.2: Disturbance classes: (a) fixed contact-angle (natural) and (b) fixed contact-line (pinned).

surface-of-support ∂D^s and an interface ∂D^f (Γ) of constant surface tension, as in figure 1.3. Given a velocity field $\boldsymbol{v}$, interface disturbance y and growth rate λ, the time-independent, dimensionless field equations are written as

$$\lambda \boldsymbol{v} = \boldsymbol{\nabla} \cdot \mathbf{T} \quad [D], \tag{1.11a}$$

$$\boldsymbol{\nabla} \cdot \boldsymbol{v} = 0 \quad [D], \tag{1.11b}$$

$$\boldsymbol{v} \cdot \boldsymbol{n} = \lambda y \quad [\partial D^f], \tag{1.11c}$$

$$\mathbf{T} \cdot \boldsymbol{n} = (2H)_\epsilon \, \boldsymbol{n} \quad [\partial D^f], \tag{1.11d}$$

$$\boldsymbol{v} = \mathbf{0} \quad [\partial D^s]. \tag{1.11e}$$

Equations (1.11a) and (1.11b) represent the linearized Navier-Stokes and continuity equations, respectively. A kinematic condition (1.11c) relates the normal velocity of the fluid to the interface disturbance there. Similarly, the balance of normal

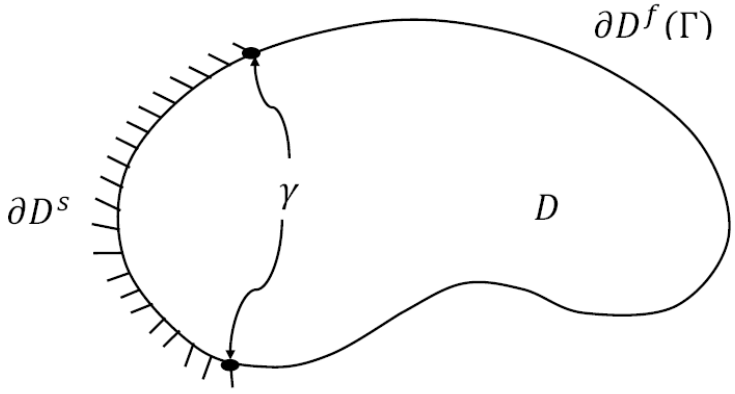

Figure 1.3: Schematic of an arbitrary fluid domain bound by a free surface ∂D^f and surface-of-support ∂D^s.

stresses at the free surface is represented by the Young-Laplace equation (1.11d). Here the pressure p from (1.3) is replaced in (1.11d) with the full stress tensor $\mathbf{T}$,

$$\mathbf{T} = -p\mathbf{1} + \hat{\mu}\mathbf{D}, \tag{1.12a}$$

$$\mathbf{D} \equiv \boldsymbol{\nabla}\boldsymbol{v} + (\boldsymbol{\nabla}\boldsymbol{v})^t, \tag{1.12b}$$

with $\hat{\mu}$ a non-dimensional viscosity parameter. Lastly, a no-slip condition (1.11e) is necessitated at the support surface.

An 'energy-like' balance equation is derived by taking the dot product of the linearized Navier-Stokes equations (1.11a) with $\boldsymbol{v}$,

$$\lambda \int_D |\boldsymbol{v}|^2 = \int_{\partial D} \boldsymbol{v} \cdot \mathbf{T} \cdot \boldsymbol{n} - \int_D \boldsymbol{\nabla}\boldsymbol{v} : \mathbf{T}. \tag{1.13}$$

The Helmholtz decomposition theorem allows one to decompose the velocity field $\boldsymbol{v} = \boldsymbol{B} + \boldsymbol{\nabla}\phi$ into a rotational $\boldsymbol{B}$ and irrotational $\boldsymbol{\nabla}\phi$ part (Joseph, 2006). Using this decomposition, one can manipulate the disturbance energy balance into

$$\int_{\partial D^f} \left(\lambda^2\phi + \lambda\hat{\mu}\boldsymbol{n} \cdot \mathbf{D} \cdot \boldsymbol{n}\left[1 + (\boldsymbol{B})_n / (\boldsymbol{v})_n\right] - (2H)_\epsilon\right) y = 0, \tag{1.14}$$

which is recognized as a functional eigenvalue problem on the interface disturbance y and takes the form of a damped harmonic oscillator

$$\lambda^2 M + \lambda \Phi + K = 0, \tag{1.15}$$

with

$$M \equiv \int_{\partial D^f} \phi \, y, \; \Phi \equiv \hat{\mu} \int_{\partial D^f} \boldsymbol{n} \cdot \mathbf{D} \cdot \boldsymbol{n} \left[1 + \frac{(\boldsymbol{B})_n}{(\boldsymbol{v})_n} \right] y, \; K \equiv - \int_{\partial D^f} (2H)_\epsilon \, y. \tag{1.16}$$

The dissipation is strictly positive $\Phi > 0$ and seen to be stabilizing when the discriminant of (1.15) is examined. Although the dissipation Φ of the disturbance energy balance (1.14) is amenable to a variety of approximations, the irrotational approximation $\boldsymbol{v} = \boldsymbol{\nabla} \phi$ of the inviscid limit ($\hat{\mu} = 0$) is of particular interest. In this limit, integral (1.14) reduces to the governing integro-differential equation,

$$-\Delta_\Gamma \left(\frac{\partial \phi}{\partial n} \right) - \left(\kappa_1^2 + \kappa_2^2 \right) \left(\frac{\partial \phi}{\partial n} \right) = -\lambda^2 \phi, \tag{1.17}$$

which is augmented with a boundary condition on the contact line γ. Dynamic stability is determined from the sign of λ^2, with interface oscillations for $\lambda^2 < 0$ and instability when $\lambda^2 > 0$. One should note that the structure of the static (1.10) and dynamic (1.17) boundary value problems are identical, but the dynamic problem is supplemented by the no-penetration condition (1.11e) on the surface-of-support. As such, static stability can be recovered from the dynamic formulation by setting the growth rate to zero.

In most studies, solution of the governing hydrodynamic equations (1.11) relies heavily on computationally-intensive approaches for all but the simplest geometries. One of the primary goals of this work is to re-formulate the disturbance energy balance (1.17) within a functional analysis framework, where the extension to constrained interfaces is straightforward and the computations are tractable. This formalism is used as an apparatus to study a number of related problems.

1.3 Organization of thesis

The content of this dissertation is conveniently organized into two types of problems, all related to constrained interfaces. **Chapters 2-4** focus on immobile or 'pinned' contact-lines and the extent-of-wetting contact, while **Chapters 5-7** are concerned with the effect of volume and wetting conditions on the three-phase contact-line.

Chapter 2 considers the axisymmetric oscillations of an inviscid spherical drop pinned on a latitudinal circle-of-contact. The effect of pinning the drop is to shift the frequencies of the unconstrained drop (Lord Rayleigh, 1879) and modify the mode shapes according to the location of the circle-of-contact, as well as introduce a new low-frequency eigenmode. Here the center-of-mass motion, important in application, is partitioned amongst all the eigenmodes but the low-frequency mode is its principal carrier. A large portion of the content of Chapter 2 appears in an article by Bostwick & Steen (2009). **Chapter 3** extends the work of the previous chapter in analyzing the oscillations of a viscous liquid drop immersed in an immiscible fluid and constrained by an axisymmetric spherical-belt. Here the interface is the union of a surface-of-support and two independent free surfaces, which are coupled by the incompressibility condition and allowed to 'communicate' or exchange volume under the constraint. To address the transition from free to support-surface along the drop interface, a modified set of shear boundary conditions, which make use of an indicator function, are proposed. As the size of the spherical-belt constraint increases from a pinned circle-of-contact, an ambiguity in a standard definition of mode number is observed at a critical belt-size, which is interpreted from both a mathematical and physical perspective by using a perturbed volume embedding.

In **Chapter 4** the stability of constrained cylindrical interfaces, partially supported by a cylindrical cup-like solid, is considered. This liquid cylinder is subject to dynamic capillary instability, including Plateau-Rayleigh break-up. The influence of the extent-of-constraint on the dispersion relation and modal structures is reported. In the extreme, the support reduces to a wire, aligned axially, and just touching the interface. From prior work (Davis, 1980), this constraint is known to stabilize the Plateau-Rayleigh limit by some 13%, whereas the wave-number of maximum growth and characteristic break-up time are estimated here. The constraint is then bent in-plane to add a weak secondary curvature to the now nearly-cylindrical base-state. This is referred to as the torus-lift of the cylinder. The static stability of these toroidal equilibria, calculated using a perturbation approach, shows that the position of constraint is crucial - constraint can stabilize (outside) or destabilize (inside). The combined influence of secondary curvature and wire constraint on the Plateau-Rayleigh limit is tracked. Finally, attention is restricted to constraints that yield a lens-like cylindrical meniscus. For these lenses, the torus-lift is used as apparatus along with a symmetrization procedure to prove a large-amplitude static stability result. The content of Chapter 4 has been largely disseminated in an article by Bostwick & Steen (2010).

Chapter 5 is focused on the stability of the sessile drop under a number of contact-line conditions, including a moving contact-line modeled by a continuous contact-angle against speed relationship. The problem is parameterized by azimuthal wave-number l, volume via the static contact-angle α (wetting) and the boundary conditions on the three-phase contact-line, which can be controlled by a spreading parameter Λ. Although the majority of motions are oscillatory, an instability is found that is related to 'walking' or translational motion of the drop. Cataloging this instability may be of great importance to a number of coating

processes. As a limiting case, a hemispherical drop given a fixed contact-angle disturbance has characteristic oscillation frequencies, which are degenerate with respect to azimuthal wave-number much like the Bohr model of the atom is degenerate with respect to angular momentum quantum number. This degeneracy can be attributed to the configurational symmetry of the hemispherical base-state and is broken by smoothly varying either i) the volume or ii) the spreading condition. Application of the former allows one to make an analogy between the spectrum of these 'broken' states and the filling order of the periodic table by energy levels, while simultaneously utilizing both degeneracy breaking mechanisms may help to explain mode crossing behavior related to a contact-line instability observed experimentally (Vukasinovic *et al.*, 2007).

Chapter 6 is concerned with the instabilities of the static rivulet and their classification. More specifically, allowable interface disturbances are decomposed into the varicose and sinuous mode types, which are classified by their symmetry or anti-symmetry about the vertical mid-plane, respectively. As regards stability, the varicose mode is the more unstable mode type and has dispersion relations that exhibit behavior typical of capillary instability or Plateau-Rayleigh break-up. That is, there exists a fastest growing shape that is distinguished by a non-trivial axial wave-number $k_m \neq 0$. Alternatively, the sinuous mode that preserves the static contact-angle exhibits a different type of instability, which is not characteristic of Plateau-Rayleigh break-up. The instability mode shape is characterized by $k_m = 0$, has no axial dependence and may be relevant to rivulet meandering.

Lastly, the static stability of the catenoid, under a number of contact-line conditions, is computed using a 'bounding' technique in **Chapter 7**. In lieu of computing the second variation explicitly, elementary results from the calculus

of variations are used on a critical functional, obtained from the extreme-value theorem, to generate a sufficient condition for stability using only the geometric properties of the equilibrium shape. This approximate method recovers well-known results to a great degree of accuracy and is used to generate new ones regarding the fixed contact-angle disturbance class, which is destabilizing when compared to a fixed contact-line disturbance. In fact, the entire family of catenoids are unstable to constant pressure, fixed contact-angle disturbances. This method also delivers stability bounds for the general axisymmetric liquid bridge with pinned contact-lines. Although the stability bounds obtained are only approximations, the results presented here are almost surprisingly accurate when compared to existing literature, while the amount of work required to obtain them has been greatly reduced when compared to traditional stability calculations.

Each chapter is intended to be self-contained and concludes with a succinct summation of the results from that chapter.

CHAPTER 2

OSCILLATIONS OF A PINNED LIQUID DROP

The content of this chapter has been largely disseminated in Bostwick & Steen (*Phys. Fluids.* (2009), *vol.* 21, *p.* 032108)

2.1 Introduction

It is well-known that a plucked liquid drop will oscillate, reflecting a competition between inertia and surface tension (capillary action). The study of small, inviscid, free oscillations of an isolated, spherical drop is attributed to Lord Rayleigh (1879). The Rayleigh frequencies of a drop immersed in a second fluid are given by

$$\omega_n^2 = \frac{n(n-1)(n+1)(n+2)}{(n+1)\rho_i + n\rho_e}\frac{\sigma}{R^3} \tag{2.1}$$

where σ, ρ_i, ρ_e and R are surface tension, fluid drop density (interior), density of fluid of immersion (exterior) and the radius of the un-deformed drop, respectively. The Rayleigh mode shapes are given by the Legendre polynomials (see Lamb, 1932). The $n = 0$ and $n = 1$ modes are zero frequency modes which can be attributed to conservation of volume and translational invariance, respectively. In practice, the smallest non-zero frequency mode is important, because this mode is typically the first to be excited. The lowest non-zero mode corresponds to $n = 2$ for Rayleigh oscillations. Interested in low-gravity applications, Trinh & Wang (1982) have experimentally verified (2.1). These results, which are valid for small perturbations, have been extended to moderate amplitude oscillations by Tsamopoulos & Brown (1983). They use domain constrained perturbations and a Poincaré-Lindstedt expansion to report corrections to both mode shape and frequency at second order in amplitude for both droplets and bubbles.

More recently, attention has been paid to spherical fluid drops under a variety of constraints, because of applications such as inkjet printing, crystal growth and light focusing using liquid lenses (Kuiper & Hendriks, 2004; Lopez *et al.*, 2005; Lopez & Hirsa, 2008). Strani & Sabetta (1984, 1988) have considered the linear oscillations of a drop in partial contact with a spherical bowl for both the inviscid and viscous cases. The unperturbed shape is a single spherical drop resting on a spherical support, similar to the contact a golf ball makes with a tee. They find that an additional low frequency vibrational mode was present ($n = 1$), in comparison with isolated drops where it is zero (2.1). This low frequency mode has been attributed to oscillatory motion of the center-of-mass which arises due to breaking of the translational invariance of the drop. More recent works report observations of center-of-mass motion of constrained drops. For example, Basaran & DePaoli (1994) report oscillatory center-of-mass motion of pendant drops, while Bian *et al.* (2003) also report a low frequency slosh mode for a fluid constrained to a cylindrical tube. In addition, Courty *et al.* (2006) show that the 'translational' mode is important for contact times of bouncing spherical droplets. One should note that in all the aforementioned studies, the free surface is a simply-connected domain.

In contrast, Theisen *et al.* (2007) consider a liquid over-filling a small cylindrical hole, drilled in a flat plate, in such a way that a droplet protrudes on either side of the plate. The top droplet is subjected to air-pressure disturbances from a loudspeaker setting the droplet-droplet system into motion. Theisen *et al.* model the system as spherical-cap drops coupled through a length L of liquid and predict the center-of-mass motion. They compare the predicted frequencies for small-amplitude motions against experiment, where the agreement is reasonable. However, non-spherical shapes are common for initial large-amplitude deformations

and the model breaks down. The model developed here predicts such higher modes and may be expected to be relevant to the experiments in the limit $L \to 0$ (*see* Results). The droplet-droplet configuration is important to various applications, such as *grab-and-release* applications, where liquid is pumped into the small droplet to form a liquid bridge against a substrate (grab) and then withdrawn from the droplet to break from the substrate (release) (Vogel *et al.*, 2005). Additionally, in spherical-cap liquid lens applications, the focal length (radius-of-curvature) of the liquid lens can be quickly and continuously varied for use in an optical micro-lens device (Kuiper & Hendriks, 2004; Lopez *et al.*, 2005; Zhang *et al.*, 2003, 2004).

The natural axisymmetric oscillations of an inviscid liquid drop, constrained by a latitudinal circle-of-contact, are considered here. This work is intended to be an extension of the inviscid study of Strani & Sabetta (1984), where the key difference is that the domain of the free surface has two components rather than a single component. An integro-differential boundary value problem, which governs the linearized motion of the free surface, is derived. The governing equation is then re-formulated as a functional eigenvalue equation on linear operators, which could be used to re-produce the results of Rayleigh and Strani & Sabetta. The respective problems differ only by the boundary conditions which must be enforced, or the type of 'allowable' disturbance to which the interface is subject.

In the case of an isolated fluid drop (Rayleigh), the relevant boundary conditions on the free surface deformation require the perturbations to be physical, or bounded, at the north and south poles ($\theta = 0, \pi$). For the Strani & Sabetta problem, the interface deformation must vanish on the bowl-of-contact, in addition to being bounded at the north pole ($\theta = 0$). In both cases, the resulting problems are well-posed two-point boundary value problems. However, pinning the fluid drop

on a circle-of-contact gives rise to an additional boundary condition on the free surface perturbation. This condition, in addition to requiring disturbances to be bounded at the poles, defines a three point boundary-value problem, thus making the problem over-determined and unlike the standard two point boundary value problem.

A spectral method is used to compute the oscillation frequencies/mode shapes of the functional eigenvalue problem. The additional boundary condition at the pinned circle-of-contact is incorporated into the solution via a constrained function space. Judicious choice of linear combinations of Legendre polynomials allows one to generate basis functions which obey all boundary and integral conditions. and equivalently span the constrained function space. The Legendre polynomials, or eigenfunctions that correspond to eigenfrequencies (2.1), form a complete set and are chosen because of the spherical symmetry of the problem. A series solution is constructed from this constrained function space and then used to reduce the functional eigenvalue equation to standard matrix form, using the standard L_2 inner product.

The pinned circle-of-contact constraint introduces the low frequency center-of-mass mode, as well as modifies the higher frequency modes, according to the position of the constraint. In general, the higher-order mode shapes have an associated center-of-mass motion. That is, the center-of-mass motion partitions predominantly to but not solely to the lowest-frequency mode. Higher mode shapes carry part of the center-of-mass motion and the fraction carried depends on the position of the constraint.

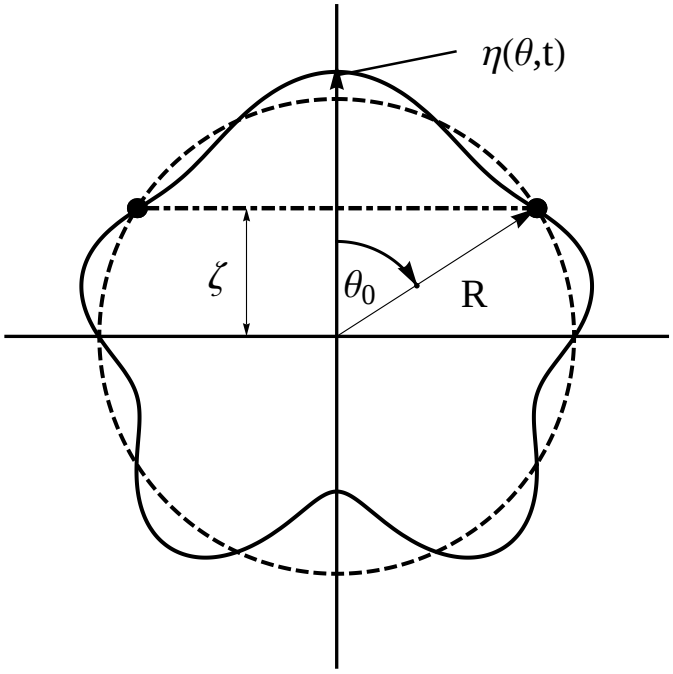

Figure 2.1: Definition sketch for the pinned liquid drop.

2.2 Mathematical formulation

The static equilibrium shape of the droplet is a sphere of radius R, which is pinned on a latitudinal circle-of-contact specified by θ_0, as shown in the definition sketch (figure 2.1). The domain is the combined region internal to and external to the droplet, $D \equiv D^i \cup D^e$,

$$D^i \equiv \{(r,\theta)\,|0 \le r \le R, 0 \le \theta \le \pi\}\,, \tag{2.2a}$$

$$D^e \equiv \{(r,\theta)\,|R \le r \le \infty, 0 \le \theta \le \pi\}\,, \tag{2.2b}$$

where no domain perturbation is needed for linear problems. The sub-domains are separated by an interface $\partial D \equiv \partial D^f \cup \partial D^s$, defined as the union of a free surface and a surface-of-support,

$$\partial D^f \equiv \{(r,\theta)\,|r = R,\, \theta \ne \theta_0\}\,, \tag{2.3a}$$

$$\partial D^s \equiv \{(r,\theta)\,|r = R,\, \theta = \theta_0\}\,. \tag{2.3b}$$

The interface is given a small, time-dependent, axisymmetric disturbance of the form $\eta(\theta, t)$. The inner and outer fluids are inviscid and incompressible, while the flow is assumed to be irrotational and the effect of gravity is neglected.

2.2.1 Dynamic equations

The flow is assumed to be irrotational, therefore the velocity field may be written as $\boldsymbol{v} = -\nabla\Psi$. Additionally, the assumption of fluid incompressibility dictates the velocity potential Ψ must satisfy Laplace's equation on the domain, written in a spherical coordinate system as

$$\nabla^2\Psi = \sin\theta\frac{\partial}{\partial r}\left(r^2\frac{\partial\Psi}{\partial r}\right) + \frac{\partial}{\partial\theta}\left(\sin\theta\frac{\partial\Psi}{\partial\theta}\right) = 0 \ \ [D]. \tag{2.4}$$

The pressure field is defined by the linearized Bernoulli equation,

$$p = p_0 + \rho\frac{\partial\Psi}{\partial t} \ \ [D], \tag{2.5}$$

valid in both sub-domains. Henceforth, to distinguish between sub-domains, superscripts will be used for field quantities and subscripts for material properties. Accordingly, ρ_i and ρ_e will represent the density of the internal and external fluids, respectively, while p^i and p^e are the internal and external pressures, and so forth.

The linearized kinematic condition on the free surface relates the radial velocity to the surface deflection there,

$$\frac{\partial\Psi}{\partial r} = -\frac{\partial\eta}{\partial t} \ \ [\partial D^f]. \tag{2.6}$$

Similarly, the no-penetration condition on the pinned circle-of-contact requires the radial velocity amplitude to vanish,

$$\frac{\partial\Psi}{\partial r} = -\frac{\partial\eta}{\partial t} = 0 \ \ [\partial D^s]. \tag{2.7}$$

A perturbed interface, held by uniform surface tension σ, generates pressure gradients, which is described by the normal stress boundary condition

$$p^i - p^e = \sigma \nabla \cdot \hat{n}, \tag{2.8}$$

or Young-Laplace equation for inviscid fluids (Drazin, 1981). Equivalently, the pressure difference across the interface is balanced by the surface tension times the mean curvature of the disturbed interface. In the limit of small deflection, $|\eta|/R << 1$, the mean curvature evaluates to the term in the square brackets,

$$p^i - p^e = \sigma \left[\frac{2}{R} - \frac{1}{R^2} \left(\frac{1}{\sin\theta} \frac{\partial}{\partial \theta} \left(\sin\theta \frac{\partial \eta}{\partial \theta} \right) + 2\eta \right) \right], \tag{2.9}$$

which holds on the free part of the interface ∂D^f.

As the fluid is assumed to be incompressible, the interface perturbation is constrained by a conservation of volume condition,

$$\int_0^\pi \eta(\theta) \sin\theta \, \mathrm{d}\theta = 0. \tag{2.10}$$

2.3 Reduced system

The mathematical model is reduced in the standard way by the use of normal modes,

$$\Psi(r, \theta, t) = \phi(r, \theta) \mathrm{e}^{i\omega t}, \tag{2.11a}$$

$$\eta(\theta, t) = iy(\theta) \mathrm{e}^{i\omega t}, \tag{2.11b}$$

where the surface disturbance is taken $\pi/2$ out of phase with respect to the radial component of velocity (2.11b), consistent with the kinematic condition (2.6). Normal modes (2.11) are substituted into the governing hydrodynamic equations

(2.4)-(2.10) to generate a reduced problem on the new functions ϕ and y;

$$\nabla^2\phi = 0 \quad [D], \tag{2.12a}$$

$$\omega\left(\rho_i\phi^i - \rho_e\phi^e\right) = -\frac{\sigma}{R^2}\left[\frac{1}{\sin\theta}\frac{\partial}{\partial\theta}\left(\sin\theta\frac{\partial y}{\partial\theta}\right) + 2y\right] \quad \left[\partial D^f\right], \tag{2.12b}$$

$$\frac{d\phi}{dr} = \omega y \quad \left[\partial D^f\right], \tag{2.12c}$$

$$\frac{d\phi}{dr} = \omega y = 0 \quad [\partial D^s], \tag{2.12d}$$

$$\int_0^\pi y(\theta)\sin\theta\,\mathrm{d}\theta = 0, \tag{2.12e}$$

which is recognized as an eigenvalue problem on allowable interface perturbations.

2.3.1 Velocity potential solution

The reduced velocity potential ϕ obeys Laplace's equation on the domain and (2.12a,2.12c) is recognized as a standard Neumann type boundary value problem. Introducing the coordinate transformation $\mu = \cos\theta$, separation of variables and the method of Frobenius may be used to find a standard solution,

$$\phi^i(r,\mu) = \omega R\left(\xi_0 + \sum_{k=1}^{\infty}\frac{\xi_k}{k}\frac{r^k}{R^k}P_k(\mu)\right), \tag{2.13a}$$

$$\phi^e(r,\mu) = -\omega R\left(\sum_{k=1}^{\infty}\frac{\xi_k}{k+1}\frac{R^{k+1}}{r^{k+1}}P_k(\mu)\right), \tag{2.13b}$$

where

$$\xi_k = \frac{(y,P_k)}{(P_k,P_k)},\ (P_k,P_k) = \frac{2}{2k+1}.$$

Here (f,g) is the standard inner product of square integrable functions on the domain $\mu \in (-1,1)$,

$$(f,g) = \int_{-1}^{1} f(\mu)\,g(\mu)\,\mathrm{d}\mu. \tag{2.14}$$

One should note that (2.13) is a general solution for an arbitrary surface perturbation.

2.3.2 Surface deformation

The balance of capillary and inertial pressures is represented by (2.12b) and is expanded using the new coordinate μ to give

$$\frac{d}{d\mu}\left(\left(1-\mu^2\right)\frac{dy}{d\mu}\right)+2y=-\frac{\rho_i\omega R^2}{\sigma}\left[\phi^i(R,\mu)-\frac{\rho_e}{\rho_i}\phi^e(R,\mu)\right]. \tag{2.15}$$

The velocity potential solution (2.13) is used to reduce the inhomogeneous differential equation (2.15) to an integro-differential equation

$$(1-\mu^2)\frac{d^2y}{d\mu^2}-2\mu\frac{dy}{d\mu}+2y=-\lambda^2\left[\sum_{k=1}^{\infty}\left(\frac{1}{k}+\frac{\rho_e}{\rho_i}\frac{1}{k+1}\right)\frac{(y,P_k)}{(P_k,P_k)}P_k\right], \tag{2.16}$$

governing the free surface deformation, where $\lambda^2\equiv\rho_i\omega^2R^3/\sigma$ is the scaled eigenfrequency.

Boundary/Integral conditions

Allowable solutions of (2.16) necessarily satisfy the following boundary conditions. All solutions must be bounded at the north and south poles

$$y(\pm1)-\text{bounded}. \tag{2.17}$$

The no-penetration condition (2.12d) on the pinned circle-of-contact reduces to a zero-amplitude perturbation

$$y(\zeta)=0, \tag{2.18}$$

with $\zeta\equiv\cos\theta_0$. Additionally, the conservation of volume constraint (2.12e) reduces to

$$\int_{-1}^{1}y\left(\mu\right)\mathrm{d}\mu=0. \tag{2.19}$$

Equations (2.16)-(2.19) represent the reduced eigenvalue problem on the free surface perturbation.

2.4 Solution method

To compute the characteristic oscillation frequencies and corresponding mode shapes, it is productive to frame the integro-differential equation as an operator equation,

$$K\left[y\right] + \lambda^2 M\left[y\right] = 0, \tag{2.20}$$

with the linear operators defined via (2.16) as

$$K\left[y\right] \equiv (1-\mu^2)\frac{d^2}{d\mu^2}y - 2\mu\frac{d}{d\mu}y + 2y, \tag{2.21a}$$

$$M\left[y; \frac{\rho_e}{\rho_i}\right] \equiv \sum_{k=1}^{\infty}\left(\frac{1}{k} + \frac{\rho_e}{\rho_i}\frac{1}{k+1}\right)\frac{(y, P_k)}{(P_k, P_k)}P_k. \tag{2.21b}$$

The operators K and M are self-adjoint and M is a positive operator, while ρ_e/ρ_i is the density ratio and may be treated as a parameter. If the functions y are restricted to boundary conditions (2.17) and the volume constraint (2.19), then the eigenvalue problem corresponds to the classical Rayleigh problem. Solution gives Legendre polynomials as eigenfunctions, which are the Rayleigh modes, and eigenvalues which correspond to the Rayleigh frequencies (2.1).

Alternatively, the problem may be posed as a variational one following a standard Rayleigh-Ritz procedure (Segel, 1987). The required input to the Ritz method is a set of functions, which span a predetermined function space. The strategy employed will be to construct a constrained function space that incorporates the additional boundary condition (2.18) on the pinned circle-of-contact. Notice that this restriction does not affect the velocity potential solution (2.13), since this a general solution to the Neumann boundary value problem for an arbitrary surface disturbance. Finally, a series solution to (2.20) is sought using appropriately chosen basis functions that span the constrained function space.

2.4.1 Constrained function space

A set of functions which span the constrained function space is derived here. The idea is to construct basis functions $h_k(\mu)$ satisfying (2.17), (2.18) and (2.19). Then a solution of the following form is sought,

$$y(\mu) = \sum_{k=1} f_k h_k(\mu). \tag{2.22}$$

The procedure is straightforward but some details of the steps involved are offered.

To construct the function space, begin by assuming a test function of the form

$$g(\mu) = \sum_{i=0}^{N} c_i P_i(\mu). \tag{2.23}$$

The Legendre polynomials $P_i(\mu)$ are used because they form a complete, orthonormal set on the domain and they identically satisfy the boundedness condition (2.17).

Consider the conservation of volume condition (2.19) first. Substitution of the test function $g(\mu)$ into (2.19) gives

$$\int_{-1}^{1} g(\mu)\mathrm{d}\mu = c_0 \int_{-1}^{1} P_0(\mu)\mathrm{d}\mu + c_1 \int_{-1}^{1} P_1(\mu)\mathrm{d}\mu + \cdots + c_N \int_{-1}^{1} P_N(\mu)\mathrm{d}\mu = 0. \tag{2.24}$$

Since $\int_{-1}^{1} P_i(\mu)\mathrm{d}\mu = 0$ for all $i \neq 0$ (MacRobert, 1967), the only contribution from (2.24) is the first term and $c_0 = 0$ is determined.

Next, enforcing the no-penetration condition (2.18) requires

$$g(\zeta) = c_1 P_1(\zeta) + c_2 P_2(\zeta) + \cdots + c_N P_N(\zeta) = 0. \tag{2.25}$$

This algebraic equation may be interpreted as the inner product between a fixed vector and the unknown coefficient vector $[c_1, c_2, ...c_N]$. Equivalently, it says there are $N-1$ linearly independent coefficient $N-1$ dimensional vectors that solve

(2.25). In other words, there are $N-1$ basis functions, parameterized by the location of the pinned circle-of-contact ζ, and conveniently written as

$$v_k(\mu) = P_k(\mu) - \frac{P_k(\zeta)}{P_1(\zeta)} P_1(\mu),\ k = 2, 3, \cdots, N. \tag{2.26}$$

It is readily verified that these functions satisfy (2.17), (2.18), and (2.19). As stated above, $N-1$ such functions span the reduced space (space with constraint incorporated) or, alternatively, if one function in the direction of the constraint is appended, these N functions will span the original unconstrained space.

The basis functions (2.26) are linearly independent but they are not orthonormal. For efficiency in computations, it is convenient to work with an orthonormal set. The last step is to use a Gram-Schmidt procedure on the set of functions v_k to deliver orthonormal functions, h_k, renumbered $k = 1, 2, \cdots N-1$. This step is done using symbolic computer algebra.

2.4.2 Reduction to matrix form

The variational approach of Rayleigh-Ritz generates a set of algebraic equations from the truncated solution series expansion,

$$y(\mu) = \sum_{k=1}^{N-1} f_k h_k(\mu). \tag{2.27}$$

Note that this is an order $N-1$ approximation in the constrained space but an order N approximation in the unconstrained space. That is, the surface perturbation has $N-1$ degrees-of-freedom, all orthogonal to the constraint direction (the N^{th} dimension).

The operator equation (2.20) is reduced to a matrix equation

$$K_{ij} f_j = -\lambda^2 M_{ij} f_j, \tag{2.28}$$

by taking inner products with the basis functions,

$$K_{ij} \equiv \int_{-1}^{1} K\left[h_i\right] h_j \mathrm{d}\mu, \quad M_{ij} \equiv \int_{-1}^{1} M\left[h_i\right] h_j \mathrm{d}\mu. \tag{2.29}$$

For example, the $1j$ position is the projection onto the j^{th} basis function, when the 1^{st} basis function is applied to the operator. Solutions of (2.28) determine the eigenvalues λ_n^2 and the eigenvectors $\hat{f}^{(n)}$, from which the eigenfunctions y_n are readily constructed by applying the eigenvector coefficients $\hat{f}_k^{(n)}$ to the orthonormal basis functions h_k,

$$y_n(\mu) = \sum_{k=1}^{N-1} \hat{f}_k^{(n)} h_k(\mu). \tag{2.30}$$

As the eigenfunctions are determined only up to a constant, the final step is to fix that constant by specifying

$$\hat{y}_n = \frac{y_n}{\max\left(|y_n(-1)|, |y_n(1)|\right)}. \tag{2.31}$$

This scaling is reminiscent of the Rayleigh eigenfunctions where a similar scaling is applied to the north pole only ($\mu = 1$). The scaling used here is with respect to the maximum displacement at either pole ($\mu = \pm 1$) because, unlike the Legendre polynomials (Rayleigh eigenfunctions), the eigenfunctions are neither symmetric nor antisymmetric about the equator and because the norm on the eigenfunctions is inherited from the norm on the Legendre polynomials.

A number of consistency checks on the computational results are performed, as well as a comparison of limiting cases with previous results from the literature. These will be discussed in the next section. Another check uses the self-adjoint nature of the operator K. The null space of K is found to be $P_1(\mu)$, which has a node at $\zeta = 0$, thus satisfying the pinned condition (2.18). The Fredholm alternative applied to (2.20) requires that the right hand side, $\lambda^2 M\left[y\right]$, be orthogonal to

the nullspace of K; that is,

$$\big(P_1(\mu), -\lambda^2 M\,[h_j]\big) = 0 \tag{2.32}$$

where

$$M\,[h_j] \equiv \sum_{k=1} \left(\frac{1}{k} + \frac{\rho_e}{\rho_i}\frac{1}{k+1}\right) \left[\frac{(h_j(\mu), P_k(\mu))}{(P_k(\mu), P_k(\mu))}\right] P_k(\mu).$$

In accordance with the positive definite structure of M, the term in the brackets on the right hand side is non-zero, which requires that $\lambda^2 = 0$. Computational results show that the $n = 1$ eigenfrequency tends to zero when the circle-of-contact tends to the equator of the fluid drop ($\zeta = 0$), consistent with the Fredholm alternative requirement.

2.5 Results

The vibrational frequencies and respective mode shapes of the constrained fluid drop are computed. The scaled frequencies λ_n^2 for the first three modes are plotted in figure 2.2 as a function of the location of the circle-of-contact ζ, for $\rho_e/\rho_i = 0$. As could be anticipated, the frequencies are symmetric with respect to the pin location, $\lambda_n^2(\zeta) = \lambda_n^2(-\zeta)$. For reference, the corresponding Rayleigh frequencies (R in the legend) are plotted as horizontal lines. The frequency of the constrained problem is never lower than that of the unconstrained problem (Griffel, 1985), with equality achieved whenever the constraint falls on a node of the corresponding Rayleigh mode (Legendre polynomial). This is to be anticipated since the constraint is satisfied 'naturally' in the latter case. What is not anticipated is that the constrained frequency can more than double the Rayleigh frequency for certain pin locations. For example, pinning the $n = 2$ mode at the equator raises the frequency from 8 to 22.

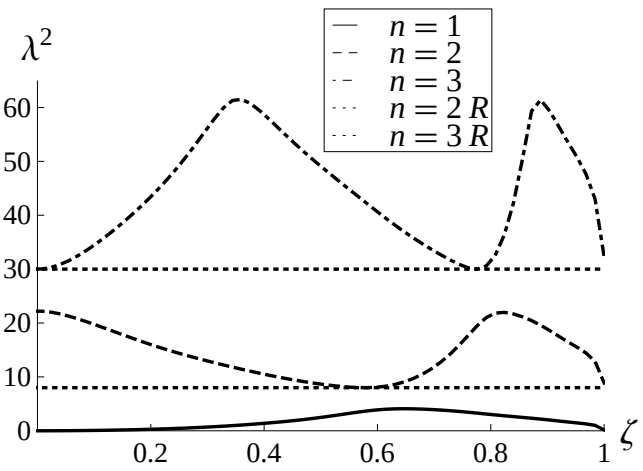

Figure 2.2: Eigenfrequency against pin location ($\rho_e/\rho_i = 0$).

Much like the local minimums of figure 2.2 which occur at 'natural' pin locations, the local maximums occur at 'unnatural' pin locations with respect to the 'unconstrained' Rayleigh modes. The definition of an 'unnatural' pin location becomes apparent when the eigenfrequencies and eigenmodes are computed. The results presented here were obtained with a 13 term expansion, which gives convergence of the first three eigenfrequencies to within 0.1% for all pin locations. The rate of convergence depends upon the pin location. For example, the $n = 2$ mode shows convergence to the prescribed tolerance (0.1%) using only 5 terms for $\zeta = -0.557$, a 'natural' location for this mode. On the other hand, if the drop is pinned at the equator, the $n = 2$ mode converges to the prescribed tolerance using 10 terms. If one desires the eigenfrequency and mode shape for a high wavenumber, say $n = 20$, the number of terms necessary in the expansion is of the order 30. However, the recursive nature of the Gram-Schmidt procedure makes it very computationally intensive to generate 30 orthonormal basis functions; this is the step that computationally limits the approach.

Figure 2.2 also shows that pinning the drop introduces a low frequency mode

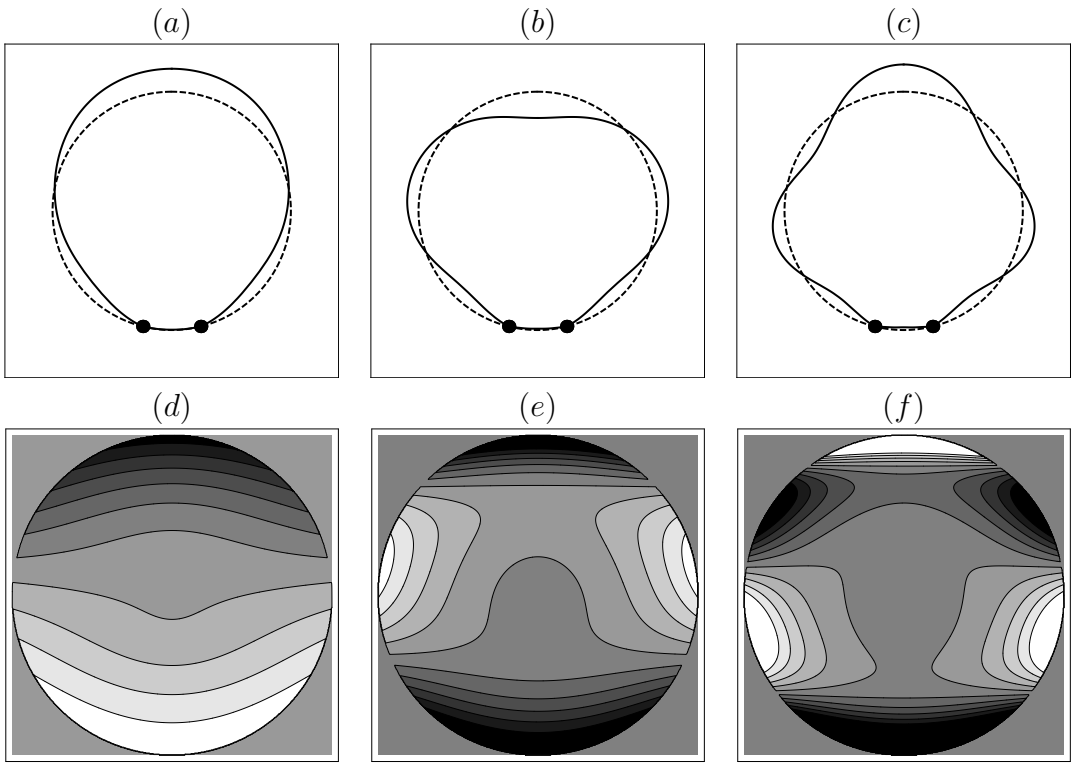

Figure 2.3: Eigenmode (a, b, c) and velocity potential (d, e, f) for $\zeta = -0.99$. Mode $n = 1$ (a, d), $n = 2$ (b, e) and $n = 3$ (c, f).

$(n = 1)$ not present in the unconstrained Rayleigh problem. This mode has been reported previously by Strani & Sabetta (1984), among others. The Strani study considered a drop in partial contact with a spherical cap support, remarking that the new mode 'tends to a zero-frequency rigid displacement' as the constrained portion of the surface vanishes. The Strani limit of the contact region shrinking to a point $(\theta \to \pi)$ coincides with the limit of the circle shrinking to either pole $(\zeta \to -1)$. These results agree with Strani's in this common limit and both results tend to the corresponding frequencies (2.1). Mode shapes and velocity potentials for this case are shown in figure 2.3.

Another special pinning location is the equator. For the Rayleigh problem, all odd modes have a node at $\mu = 0$. Therefore, when $\zeta = 0$, all odd constrained

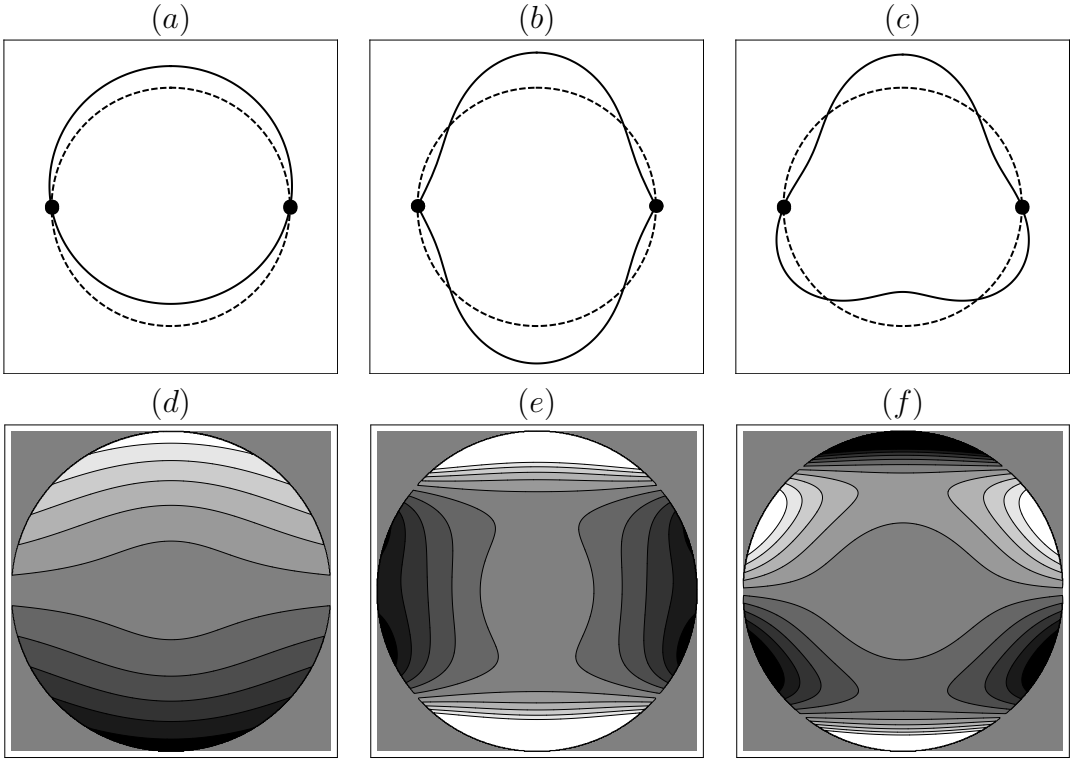

Figure 2.4: Eigenmode (a, b, c) and velocity potential (d, e, f) for $\zeta = 0$. Mode $n = 1$ (a, d), $n = 2$ (b, e) and $n = 3$ (c, f).

frequencies correspond to odd Rayleigh frequencies. The mode shapes for $n = 1$ and $n = 3$, $P_1(\mu)$ and $P_3(\mu)$, respectively, are shown in figure 2.4 above the corresponding velocity potentials. Figure 2.5 shows the first three eigenfunctions for $\zeta = -0.557$, which is the location of a node for $P_2(\mu)$. Not surprisingly, the $n = 2$ mode shape corresponds to $P_2(\mu)$.

2.5.1 Decomposition of eigenmodes

In view of the completeness of the Legendre polynomials, any shape can be decomposed into a weighted sum of $P_n(\mu)$. These weights, for the mode shapes shown in figures 2.3, 2.4, and 2.5 are computed for reference. A given eigenmode $\hat{y}_n(\mu)$ may

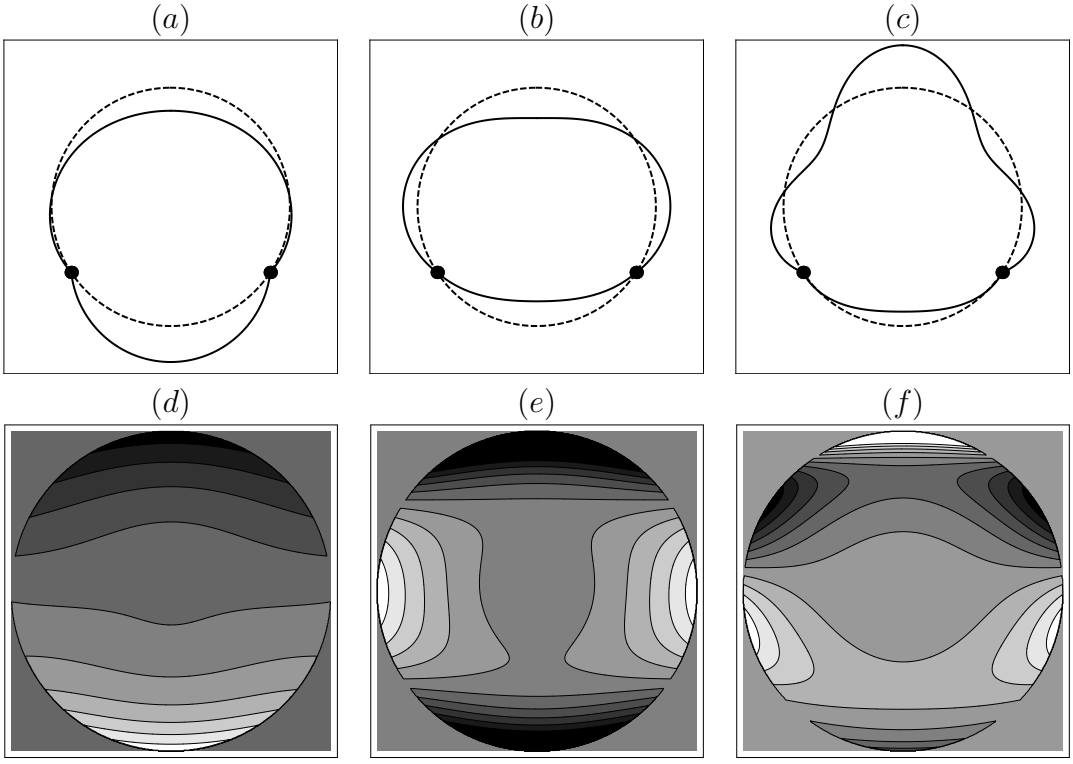

Figure 2.5: Eigenmode (a, b, c) and velocity potential (d, e, f) for $\zeta = -0.557$. Mode $n = 1$ (a, d), $n = 2$ (b, e) and $n = 3$ (c, f).

be decomposed into the Rayleigh modes as follows,

$$\hat{y}_n(\mu) = \sum_{k=1}^{\infty} b_k P_k(\mu), \tag{2.33}$$

with

$$b_k = \frac{(\hat{y}_n, P_k)}{(P_k, P_k)} = \frac{2k+1}{2} (\hat{y}_n, P_k) \,. \tag{2.34}$$

Shown below is the decomposition of the first four eigenmodes into the first 8 coefficients of the 13 term expansion, for the pin locations used to generate figures 2.3-2.5.

Rayleigh decomposition for $\zeta = -0.99$

n	b_1	b_2	b_3	b_4	b_5	b_6	b_7	b_8
1	0.784	0.321	-0.160	0.108	-0.080	0.061	-0.048	0.038
2	-0.084	0.804	0.383	-0.188	0.127	-0.095	0.073	-0.057
3	-0.031	0.128	-0.783	-0.453	0.206	-0.136	0.100	-0.076
4	0.015	-0.056	0.152	-0.719	-0.511	0.212	-0.135	0.097

Rayleigh decomposition for $\zeta = 0.001$

n	b_1	b_2	b_3	b_4	b_5	b_6	b_7	b_8
1	0.999	0.001	0	0	0	0	0	0
2	0	0.644	-0.008	0.523	0.002	-0.214	-0.001	0.132
3	0	0.004	0.991	0.006	0	-0.002	0	0.001
4	0	-0.104	0	0.589	-0.028	0.570	0.002	-0.222

Rayleigh decomposition for $\zeta = -0.557$

n	b_1	b_2	b_3	b_4	b_5	b_6	b_7	b_8
1	0.488	-0.072	0.312	-0.189	0.018	0.084	-0.085	0.023
2	0.034	0.928	0.064	-0.034	0.003	0.014	-0.014	0.004
3	0.039	0.010	-0.619	-0.499	0.028	0.108	-0.101	0.026
4	-0.027	-0.006	0.177	-0.482	-0.476	-0.377	0.269	-0.062

2.5.2 Center-of-mass motion

Although a number of authors have reported the low frequency $n = 1$ mode, most have incorrectly labeled this mode as a center-of-mass mode. Here the definition

of the center-of-mass is used to decompose the eigenmodes into center-of-mass motion, from which one can calculate how this motion partitions amongst mode shapes.

The center-of-mass resides on the z-axis, due to the assumed axisymmetry of perturbations. Hence, one may define the center-of-mass of a given perturbation $\eta(\theta, t)$ in the standard way as

$$\begin{aligned} m z_{cm} = \int z \, \mathrm{d}m &= 2\pi\rho \int_0^{\pi} \int_0^{r} r^3 \sin(\theta)\cos(\theta) \, \mathrm{d}r \, \mathrm{d}\theta \\ &= \frac{\rho\pi}{2} \int_0^{\pi} r^4 \sin(\theta)\cos(\theta) \, \mathrm{d}\theta, \end{aligned} \tag{2.35}$$

where the radial perturbation coordinate is defined as

$$r = R\left(1 + \epsilon\eta(\theta, t)\right) \tag{2.36}$$

with

$$r^4 = R^4 \left(1 + \epsilon\eta(\theta, t)\right)^4 = R^4 \left[1 + \epsilon\left(4\eta(\theta, t)\right) + \cdots\right]. \tag{2.37}$$

Likewise, the center-of-mass coordinate may be expanded as

$$z_{cm} = \left(z_{cm}\right)_0 + \epsilon \left(z_{cm}\right)_1 + \cdots . \tag{2.38}$$

Expanding (2.35) in ϵ gives

$$\begin{aligned} m\left[\left(z_{cm}\right)_0 + \epsilon\left(z_{cm}\right)_1 + \cdots\right] = \frac{\rho\pi R^4}{2} &\int_0^{\pi} \sin(\theta)\cos(\theta) \, \mathrm{d}\theta \\ + \epsilon 2\pi\rho R^4 &\int_0^{\pi} \eta(\theta, t) \sin(\theta)\cos(\theta) \, \mathrm{d}\theta. \end{aligned} \tag{2.39}$$

Using $\mu = \cos(\theta)$, $m = \rho\frac{4}{3}\pi R^3$ and equating terms of the same order we find

$$\left(z_{cm}\right)_0 = 0, \tag{2.40a}$$

$$\left(z_{cm}\right)_1 = \frac{3}{2} R\left(\eta_n(\mu, t), P_1(\mu)\right). \tag{2.40b}$$

Finally, one can use the definition of $\eta_n(\mu, t)$ as an eigenmode,

$$\eta_n(\mu, t) = i\mathrm{e}^{i\omega_n t}\hat{y}_n(\mu), \tag{2.41}$$

to show the scaled center-of-mass motion is

$$\frac{(z_{cm})_1}{R} = \frac{3}{2} i \mathrm{e}^{i\omega_n t} \left(\hat{y}_n, P_1\right). \tag{2.42}$$

For the Rayleigh problem, the $n = 1$ mode has zero frequency and is correctly associated with the linearized center-of-mass motion of the drop (2.1). The imposed constraint, fixed in the laboratory frame, breaks the translational invariance to typically yield a non-zero frequency for the center-of-mass motion. As such, the center-of-mass motion for the Rayleigh modes is completely determined by the $n = 1$ mode and the higher order mode shapes are effectively decoupled for motion of the center-of-mass. In contrast, there is no such simple partition for constrained motions.

Of particular interest is in what role the center-of-mass plays in the higher modes that are reported here. To that end, the contribution of the center-of-mass motion (z_{cm}) to any mode is found to be, $(z_{cm})/R$=3/2 $i\mathrm{e}^{i\omega_n t}$ $(\hat{y}_n, P_1)$. Understanding this contribution is of utmost importance in applications such as ink-jet printing where generating large excursions of the center-of-mass often correlates with pinch-off of droplets. Despite the fact that this analysis is restricted to small-amplitude motions, such linear results are known to often carry through to nonlinear behavior.

The center-of-mass is found to oscillate at the eigenfrequency ω_n with a contribution to the eigenmode $(\hat{y}_n, P_1)$. Figure 2.6 shows the decomposition $(z_{cm})_n = (\hat{y}_n, P_1)$ as a function of pinning location, which shows the $n = 1$ mode carries the majority of the center-of-mass motion, but not all of it. The higher mode shapes are also accompanied by an associated motion of the center-of-mass, thereby coupling the translation and oscillatory Rayleigh modes. Courty *et al.* (2006) have postulated that this coupling might explain the discrepancy between experimental (Richard *et al.*, 2002) and theoretical pre-factor values for contact

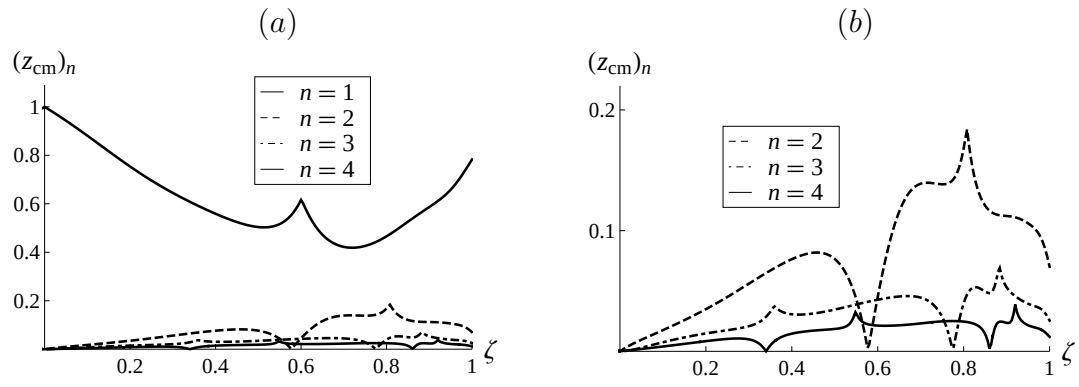

Figure 2.6: Center-of-mass motion contribution to eigenmodes as a function of pin location ζ.

and impact times for droplet bouncing. While it may be convenient to view the $n = 1$ mode as a center-of-mass mode, it is clearly an approximation, at best.

Although the $n = 1$ mode carries the majority of the center-of-mass motion, the ordering of the center-of-mass decomposition for the $n > 1$ modes is not preserved with pin location (figure 2.6 (b)). For example, the $n = 2$ mode carries less center-of-mass motion than the $n = 3$ or $n = 4$ mode for a pin location near $\zeta = 0.557$ (the node of $P_2(\mu)$). For a fixed initial deformation amplitude and/or kinetic energy, suppose one would like to excite a preferred mode to get the greatest extension of the center-of-mass in order to encourage a pinch-off of a certain volume, say. Figure 2.6 provides a guide as how to choose the optimal pin location for such behavior.

2.5.3 Extension to a double pinned fluid drop

One feature of the spectrum shown in figure 2.2 are the regions of inaccessible frequency space, such as $22 < \lambda^2 < 30$. As has been demonstrated, the discrete

spectrum of the free drop may be broken through the introduction of a pinned circle-of-contact. This observation leads one to believe these gaps in frequency space could be filled by introducing another pinned circle-of-contact, or the entire frequency space could be accessible.

The analysis outlined previously can be extended to the case of a double-pinned spherical fluid drop, where the locations of the pinned circles-of-contact are defined as ζ_1 and ζ_2. To proceed, (2.17)-(2.19) are augmented with a boundary condition on the radial velocity amplitude or equivalently the perturbation amplitude at the second pinned circle-of-contact. Now, the boundary/integral conditions to be satisfied are:

$$y(\zeta_1) = 0, \tag{2.43a}$$

$$y(\zeta_2) = 0, \tag{2.43b}$$

$$\int_{-1}^{1} y\,(\mu)\,\mathrm{d}\mu = 0. \tag{2.43c}$$

By the same reasoning as section 4, a set of basis functions are constructed which obey all necessary conditions and then used to form an approximate solution to the integro-differential operator equation. Again, begin by assuming a test function of the form,

$$g(\mu) = \sum_{i=0}^{N} c_i P_i(\mu). \tag{2.44}$$

As was the case for the single pinned circle-of-contact, (2.43c) requires $c_0 = 0$. Next, substituting (2.44) into (2.43a,2.43b) gives

$$g(\zeta_1) = c_1 P_1(\zeta_1) + c_2 P_2(\zeta_1) + \cdots + c_N P_N(\zeta_1), \tag{2.45a}$$

$$g(\zeta_2) = c_1 P_1(\zeta_2) + c_2 P_2(\zeta_2) + \cdots + c_N P_N(\zeta_2), \tag{2.45b}$$

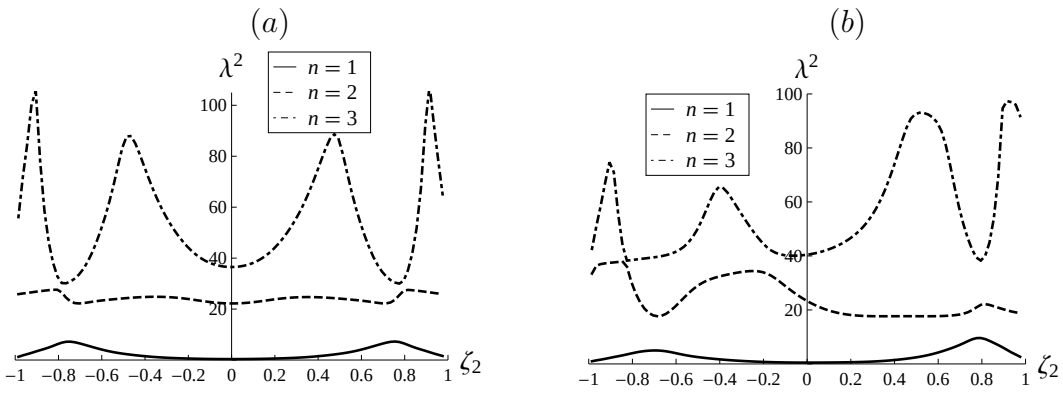

Figure 2.7: Frequency against second pin location ζ_2, while holding the first pin location (a) $\zeta_1 = 0.01$ and (b) $\zeta_1 = 0.15$ fixed.

or equivalently

$$\begin{bmatrix} P_1(\zeta_1) & P_2(\zeta_1) & \cdots & P_N(\zeta_1) \\ P_1(\zeta_2) & P_2(\zeta_2) & \cdots & P_N(\zeta_2) \end{bmatrix} \begin{bmatrix} c_1 \\ \vdots \\ c_N \end{bmatrix} = \begin{bmatrix} 0 \\ 0 \end{bmatrix}. \tag{2.46}$$

It can be shown that the solution of (2.46) gives $N-2$ linearly independent basis functions,

$$\begin{aligned} v_n(\mu) = P_n(\mu) - \frac{P_n(\zeta_1)}{P_1(\zeta_1)} P_1(\mu) - \frac{(P_1(\zeta_1)P_n(\zeta_2) - P_n(\zeta_1)P_1(\zeta_2))}{(P_1(\zeta_1)P_2(\zeta_2) - P_2(\zeta_1)P_1(\zeta_2))} P_2(\mu) \\ + \frac{P_2(\zeta_1)}{P_1(\zeta_1)} \frac{(P_1(\zeta_1)P_n(\zeta_2) - P_n(\zeta_1)P_1(\zeta_2))}{(P_1(\zeta_1)P_2(\zeta_2) - P_2(\zeta_1)P_1(\zeta_2))} P_1(\mu) \end{aligned} \tag{2.47}$$

which satisfy (2.43a)-(2.43c). Again the Gram-Schmidt procedure is applied to these linearly independent functions to generate a set of orthonormal functions, which are applied to the operator equation (2.20) to reduce the problem to a truncated set of algebraic equations.

Shown in figures 2.7,2.8 are the computed vibrational frequencies as a function of the second pin location ζ_2, while holding the first pin location ζ_1 fixed. As postulated, the introduction of the second pinned circle-of-contact leads to the filling

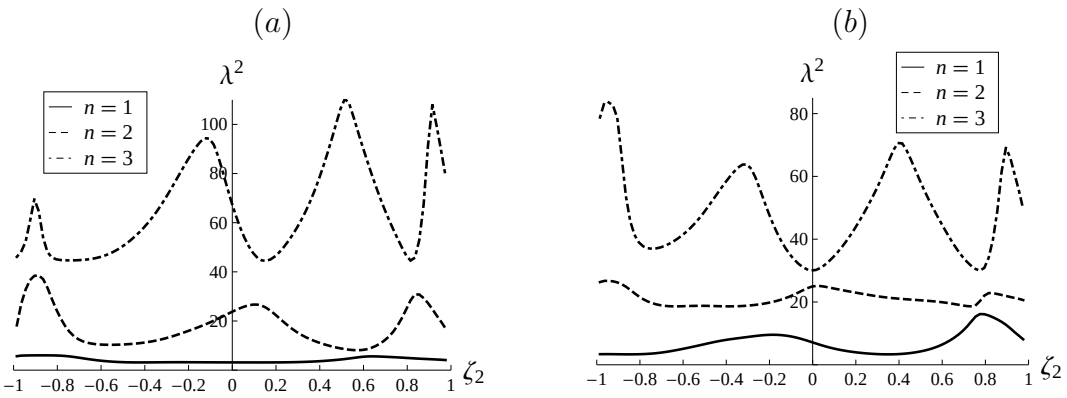

Figure 2.8: Frequency against second pin location ζ_2, while holding the first pin location (a) $\zeta_1 = -0.5$ and (b) $\zeta_1 = -0.7$ fixed.

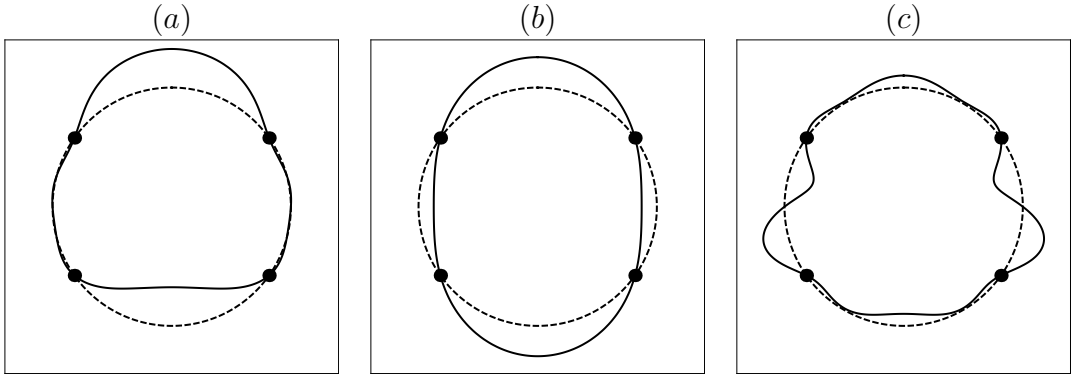

Figure 2.9: Eigenmodes (a) $n = 1$ (b) $n = 2$ and (c) $n = 3$ with pin locations $\zeta_1 = -.55, \zeta_2 = 0.55$.

of the frequency space, previously inaccessible with only one circle-of-contact, as shown in figure 2.2. Likewise, sample mode shapes are given in figures 2.9-2.11.

2.5.4 Density variation

The above results have illustrated the behavior for $\rho_e = 0$. Results for other density ratios are readily computed. Increasing the ratio of outer to inner density (ρ_e/ρ_i) is found to decrease the eigenfrequencies compared to the case of an isolated fluid

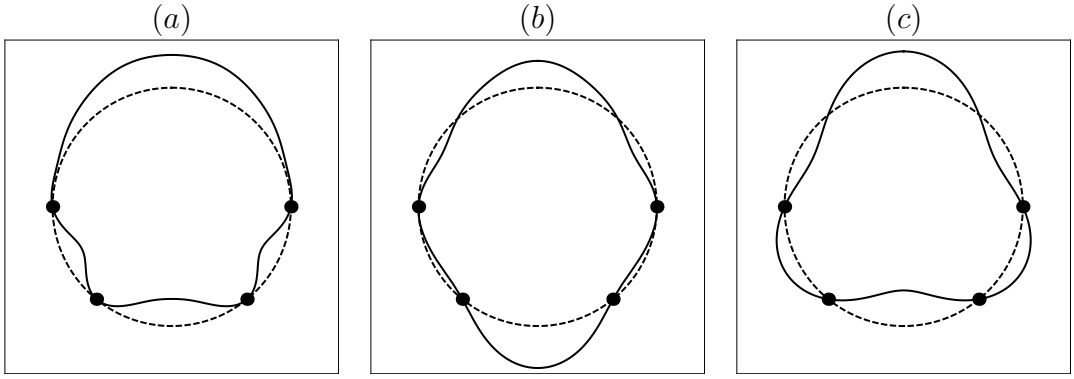

Figure 2.10: Eigenmodes (a) $n = 1$ (b) $n = 2$ and (c) $n = 3$ with pin locations $\zeta_1 = -0.775, \zeta_2 = 0.001$.

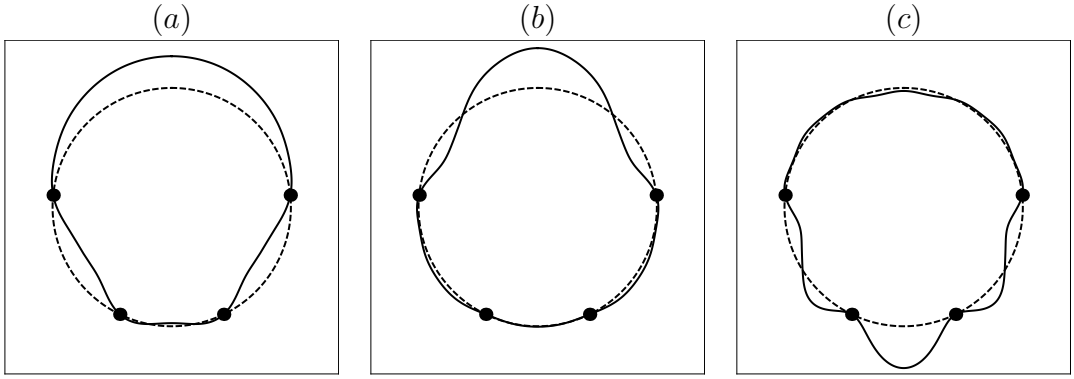

Figure 2.11: Eigenmodes (a) $n = 1$ (b) $n = 2$ and (c) $n = 3$ with pin locations $\zeta_1 = -0.91, \zeta_2 = 0.1$.

drop ($\rho_e = 0$). To illustrate, let $\lambda^2_{n,0}$ denote the n^{th} eigenfrequency for $\rho_e = 0$ and λ^2_n be the eigenfrequency for $\rho_e \neq 0$. Using the definition of λ^2, define $\Omega^2 \equiv \lambda^2_{n,0}/\lambda^2_n$ as the ratio of the eigenfrequency for an isolated drop to the eigenfrequency for $\rho_e \neq 0$. The computed Ω^2 against (ρ_e/ρ_i) is shown in figure 2.12. It is seen that a non-zero outer density has a greater effect on the higher frequency modes, which is consistent with the numerical results of Strani & Sabetta for varying density ratios in the common limit, $\zeta \to -1$ (figure 2.12).

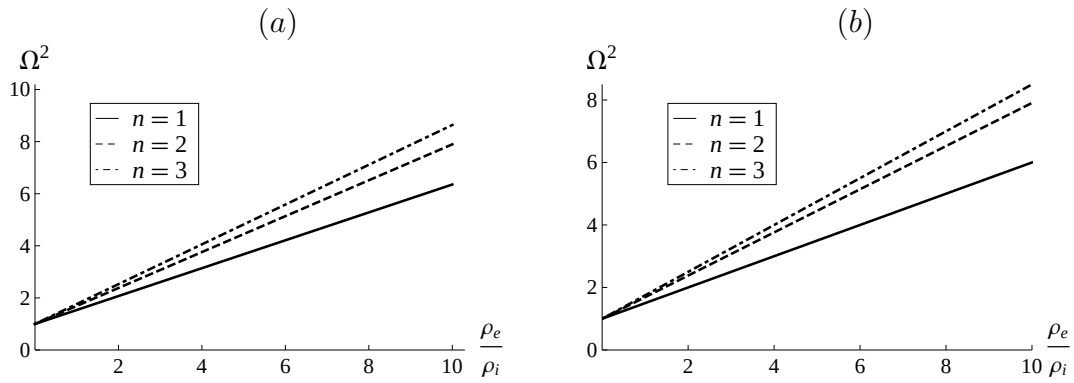

Figure 2.12: Density variation in eigenmodes for a drop pinned on the (a) south pole $\zeta = -0.99$ and (b) equator $\zeta = 0$.

2.6 Concluding remarks

The classic Rayleigh problem can be posed as a variational problem for a quadratic functional, where the minimization is taken over functions that satisfy conditions (2.17) and (2.19). This is referred to as the unconstrained problem. The integro-differential equation governing the motion of the free surface has been formulated as an operator equation (2.20), which represents the corresponding Euler-Lagrange equation, obtained by requiring the first variation to vanish. As an extension to the unconstrained Rayleigh problem, candidate functions have been restricted to be pinned on a latitudinal circle-of-constraint (2.18). Implementation of the Rayleigh-Ritz variational approach allows one to show that the frequency of the constrained problem cannot decrease relative to the unconstrained one (Griffel, 1985). The eigenvalues and eigenfunctions of the constrained problem that have been presented here are consistent with these bounds.

One motivation for this study is to compare against predictions of the spherical-cap model. Theisen *et al.* (2007) restrict to spherical-cap shapes in considering the dynamics of the center-of-mass motion of two droplets coupled through a tube.

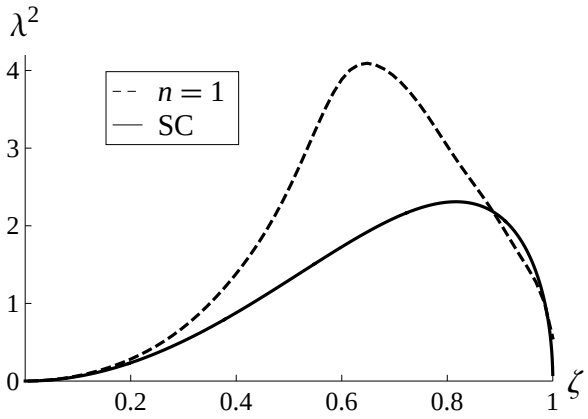

Figure 2.13: Frequency versus pin location: Spherical cap (SC) and $n = 1$ mode.

In the limit of zero tube length, the system reduces to two spherical caps coupled along a common circle-of-contact. When the two caps are complementary pieces of a sphere, the equilibrium state under consideration corresponds to a sphere with a latitudinal circle-of-constraint, or the problem treated here. Among other results, they report frequency of oscillation of small-amplitude motions as it depends on ζ. The frequency of the computed $n = 1$ mode shows a qualitatively similar dependence on ζ as the spherical-cap model (Figure 2.13). For example, both give an oscillation frequency of zero when $\zeta = 0$ and $\zeta = 1$ and have a single maximum near $\zeta = 0.7$. However, there is quantitative discrepancy between the frequencies, which can be traced to the different shapes allowed near the circle-of-contact. For the spherical caps, the tangent to the interface from below and from above the pinning latitude must be discontinuous (except for equilibrium shapes). Whereas, the formulation developed here does not allow a singularity in curvature, which precludes discontinuous slopes. Thus, the spherical cap shape may reasonably capture the observed frequencies for finite non-zero tube lengths but will likely fail quantitatively for sufficiently short tubes.

These issues are illustrated in figure 2.14. A snapshot of the two coupled drops,

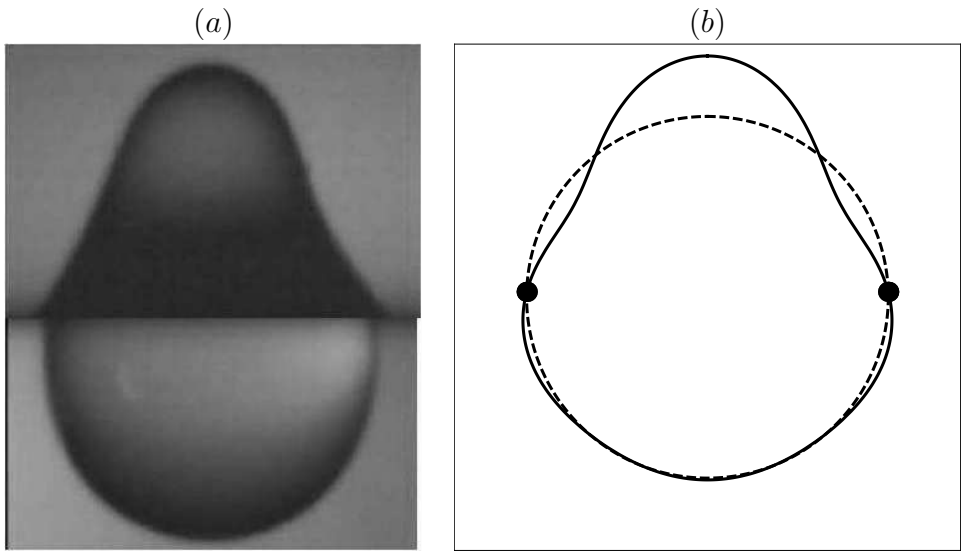

Figure 2.14: Comparison with experiment (a) experiment and (b) $n = 2$ eigenmode for $\zeta = 0.05$.

digitally modified to remove the tube, is seen in figure 2.14(a).[1] Figure 2.14(b) shows the $n = 2$ computed eigenmode, for a pin location deviating slightly away from the equator to account for small gravitational effects on the static equilibrium shape. This qualitative comparison is acceptable if one ignores the behavior near the contact-line. The photo shows different apparent contact angles for the top and bottom interfaces, a feature especially apparent at the right side where the top contact-line has evidently de-pinned. Furthermore, comparison near the contact-line, photo against computation, shows a different curvature. In addition, it should be noted that, in the computed shape, the tangents at the contact-line appear dissimilar at this scale but are actually smooth, consistent with the discussion of the previous paragraph. Because of the contact-line issues and the influence of the tube, quantitative comparison with the experiments is precluded. The point here is to elucidate these issues.

[1]The image from experiment in figure 2.14 (a) was taken from high-speed video recording of oscillation experiments done in the Hirsa Laboratory at RPI (reported in Theisen *et al.* (2007))

A practical question regarding the computations presented here is whether there is a preferred way to excite the system to get the greatest extension of the center-of-mass, say, for a fixed constraint position and initial deformation amplitude. Clearly, the $n = 1$ mode carries the majority of the center-of-mass motion, but the excursion of the $n = 2, 3, \cdots$ modes may be surprising. One might expect the lower order modes to carry more of the center-of-mass than the higher order modes, considering that the velocity fields for the higher order modes are more localized on the surface (*see* Velocity Potentials). To the contrary, for certain pin locations, it is seen that the higher modes carry more of the center-of-mass motion. For these pin locations, to get the greatest extension of the center-of-mass, one should preferentially excite particular modes.

Additionally, this analysis has been extended to include a second pinned circle-of-contact. By introducing the second pinning circle, it is shown that the frequency gaps seen in figure 2.2 begin to fill, as shown in figures 2.7,2.8. That is, according to figure 2.2, there is no pinning location to give a scaled frequency between 22 and 30. Effectively, by adding a second constraint, one can choose a pin location to achieve any desired frequency.

A goal of this work is to extend Strani & Sabetta's analysis to include 'belts' of restricted deformation on the sphere. That is, suppose one wishes to pin the interface between latitudes 50° and 70°. This can be done by adding a finite number of circular pinning constraints, from which the spherical bowl constraint considered by Strani is recovered with a sufficient number of closely placed pinning circles.

CHAPTER 3

VISCOUS OSCILLATIONS OF A FLUID DROP UNDER SPHERICAL-BELT CONSTRAINT

3.1 Introduction

Liquid drops, held by surface tension, are known to assume spherical shapes at equilibrium. When perturbed, an isolated inviscid drop will oscillate with characteristic frequency and mode shape, given by Lord Rayleigh (1879) in the limit of small interface deformation. The Rayleigh frequencies, which will be referred to as the 'unconstrained' problem, have discrete spectrum (2.1) and corresponding mode shapes given by the Legendre polynomials, $P_n(\cos\theta)$. This theoretical result has been verified experimentally for immiscible drops by Trinh & Wang (1982) and free drops in microgravity by Wang *et al.* (1996).

Many fluids do not obey the inviscid assumption and dissipate energy, giving rise to attenuated drop oscillation amplitudes. To extend the work of Lord Rayleigh, Lamb (1932) has computed the viscous dissipation for the free drop under the assumption of irrotational motion and in the limit of small kinematic viscosity ν to show the amplitude of oscillation is damped like $\exp(-\kappa t)$, with

$$\kappa = \frac{\nu}{R^2}(n-1)(2n+1). \tag{3.1}$$

Likewise, Padrino *et al.* (2007) have extended Lamb's result to report viscous corrections to the oscillation frequencies of the isolated drop in the irrotational limit. In addition, they compare the irrotational dissipation approximation and viscous potential flow theory to the exact solution of the linear theory obtained by Prosperetti (1980*b*). Both methods use a potential flow approximation, but differ in

how viscosity enters the governing equations. Viscous potential flow introduces viscosity to the normal stress balance on the interface, while the irrotational dissipation approximation evaluates the viscous dissipation in the mechanical energy equation using the irrotational potential flow solution. The irrotational dissipation approximation is shown to be quite satisfactory for small viscosities.

Finite viscous effects, as they relate to the free drop problem, have been investigated by Reid (1960) for an isolated drop in a vacuum. In the large viscosity limit, Chandrasekhar (1961) has established boundaries between oscillatory and aperiodic motion. Miller & Scriven (1968) have derived a dispersion relationship for immiscible drops, whose interface may or may not have elastic properties. Prosperetti (1980*b*) has computed the spectrum of immiscible viscous drops using a normal mode analysis. This result was later verified numerically by Basaran (1992). In contrast to the standard normal mode analysis, Prosperetti has also studied the initial-value problem for viscous drops and identified three-phases of evolution: the first phase is characterized by irrotational flow, the second phase has vorticity generated at the drop surface diffusing into the bulk and the final phase being the least-damped normal mode (Prosperetti, 1980*a*,*c*).

The study of constrained fluid drops is predominantly motivated by applications, such as drop atomization (James *et al.*, 2003*a*,*b*; Vukasinovic *et al.*, 2007) and liquid lens focusing (Lopez & Hirsa, 2008; Lopez *et al.*, 2005), to name a few. Most relevant to the problem considered here are the spherical constraints used in the works of Strani & Sabetta (1984, 1988), Theisen *et al.* (2007) and Bostwick & Steen (2009). Strani & Sabetta (1984) consider the linear oscillations of a drop in partial contact with a 'spherical-bowl' in the inviscid limit by using a Green's function approach to derive an integral eigenvalue equation, which is

then reduced to a set of linear algebraic equations by a Legendre series expansion. They report a new low-frequency mode, not present for isolated drops, and exponential eigenfrequency growth as the size of the spherical-bowl is increased from a point to a fully captured sphere. Similarly, Bauer & Chiba (2004, 2005) have also investigated spherical 'bowl-like' constraints for inviscid and viscous captured drops by approximating finite-sized constraints with a large number of point-wise constraints.

Theisen *et al.* (2007) study moderate amplitude spherical cap oscillations of a drop pinned on a circle-of-contact, and report low frequency center-of-mass motions. The spherical cap model was reasonably accurate when compared against small amplitude disturbances in their droplet-droplet experiment, but for large initial disturbances, higher order mode shapes were shown to persist. To model these higher order mode shapes, Bostwick & Steen (2009) analyzed the linear oscillations of a drop constrained by a latitudinal circle-of-contact and report a shift in the characteristic frequencies compared to the unconstrained drop, as well as the low frequency $n = 1$ mode. Their analysis utilizes a Rayleigh-Ritz procedure and chosen function spaces that necessitated continuous contact angles across the circle-of-contact constraint, whereas the droplet-droplet experiments exhibit discontinuous contact angles. This issue, among others, will be addressed here.

A drop constrained by a spherical-belt (c.f. figure 3.1) has an interface that is decomposed into one surface-of-support and two independent free surfaces, which may exchange volume through the underlying fluid consistent with the incompressibility condition. An integro-differential boundary value problem, governing the free surface deformations of a drop constrained by a spherical-belt is derived and formulated as a functional eigenvalue equation on linear operators, which takes

the form of a damped-harmonic oscillator. A solution to the eigenvalue problem is found using the variational procedure of Rayleigh-Ritz on a constrained function space, constructed to satisfy the no-penetration condition on the surface-of-support and appropriately couple the deformations of the two free surfaces according to volume conservation. In contrast to the unconstrained free drop, the shear boundary conditions change along the drop interface depending upon the type of surface, either free or supported. To address this issue, a set of modified shear boundary conditions, valid on the entire interface, are proposed and validated in the appropriate limits. While the inviscid frequencies may be computed from a standard eigenvalue problem, the viscous frequencies are determined from a nonlinear characteristic equation, because the viscous dissipation operator is nonlinear in the eigenvalue. The viscous frequencies are shown to bifurcate from complex to real eigenvalues, corresponding to under-damped to over-damped motion, at a critical value of viscosity. Higher order mode shapes are shown to bifurcate at smaller viscosities, because of strong relative motion among fluid elements, or large viscous dissipation.

A limiting case of this analysis is the pinned circle-of-contact constraint, employed in Chapter 2. Here, in contrast, the interface may have a discontinuous contact-angle across the pinned constraint. By comparing the computed frequencies, one learns that a pinned drop would always prefer to have a discontinuous contact-angle, except when the circle-of-contact is placed at a 'natural' pin location. A 'natural' pin location is defined as a 'node' or zero of the unconstrained eigenmode. This preference is especially pronounced at 'unnatural' pin locations, observed qualitatively in the droplet-droplet experiment and an essential feature of the spherical-cap model (Theisen *et al.*, 2007).

Eigenfrequencies are readily computed as a function of spherical-belt size and location. As the size of the constraint is increased from a pinned circle-of-contact, the mode shapes are shown to qualitatively change their character by increasing their number of 'nodes', or zeroes of the corresponding eigenfunctions, while preserving the numerical ordering of the eigenvalues at a critical belt size. In addition, the mode shape that transfers the most volume between disjoint surfaces also changes at these points.

This chapter begins by defining the linearized hydrodynamic field equations and relevant boundary conditions for the viscous problem, from which the equation of motion for the drop interface is derived and formulated as an eigenvalue problem on linear operators. The functional eigenvalue equation is reduced to a truncated set of linear algebraic equations using a Rayleigh-Ritz procedure on a constrained function space. The eigenvalues/eigenmodes are then computed from a characteristic equation, nonlinear in material properties and the size/location of the constraint. The chapter concludes by offering some remarks on the computational results.

3.2 Mathematical formulation

Consider an unperturbed spherical droplet of radius R, constrained by a spherical-belt given through the polar angle $\theta_1 \leq \theta \leq \theta_2$ in spherical coordinates, as shown in the definition sketch (c.f. figure 3.1). The drop interface is disturbed by time-dependent free surface perturbations, $\eta_1(\theta, t)$ and $\eta_2(\theta, t)$, which are assumed to be axisymmetric and small. No domain perturbation is needed for linear problems, thus the domain is the combination of the region internal to and external to the

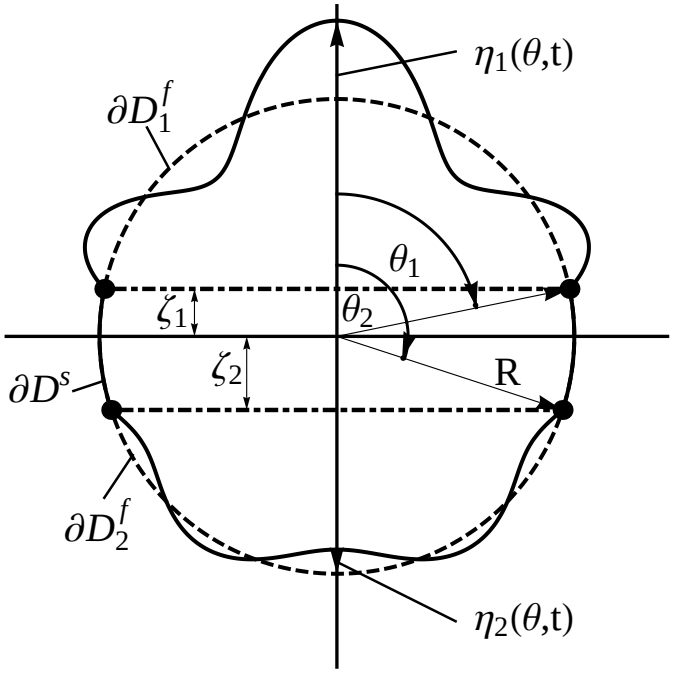

Figure 3.1: Definition sketch of a drop constrained by a spherical-belt.

static droplet;

$$D^i \equiv \{(r,\theta) \mid 0 < r \leq R, 0 \leq \theta \leq \pi\}, \tag{3.2a}$$

$$D^e \equiv \{(r,\theta) \mid R < r < \infty, 0 \leq \theta \leq \pi\}, \tag{3.2b}$$

$$D \equiv D^i \cup D^e. \tag{3.2c}$$

The interface separating the interior and exterior fluids is defined as the union of two free surfaces and one surface-of-support;

$$\partial D_1^f \equiv \{(r,\theta) \mid r = R, 0 \leq \theta \leq \theta_1\}, \tag{3.3a}$$

$$\partial D_2^f \equiv \{(r,\theta) \mid r = R, \theta_2 \leq \theta \leq \pi\}, \tag{3.3b}$$

$$\partial D^s \equiv \{(r,\theta) \mid r = R, \theta_1 \leq \theta \leq \theta_2\}, \tag{3.3c}$$

$$\partial D \equiv \partial D_1^f \cup \partial D_2^f \cup \partial D^s. \tag{3.3d}$$

The inner and exterior fluids are viscous and incompressible and the effect of gravity is neglected.

3.2.1 Field equations

The field equations, governing the motion of the fluid, are written via a velocity field $\boldsymbol{u}$ and pressure P. An incompressible fluid necessarily has a divergence-free velocity field,

$$\boldsymbol{\nabla} \cdot \boldsymbol{u} = 0. \tag{3.4}$$

The linear momentum balance on a material volume gives the linearized Navier-Stokes equation

$$\rho \frac{\partial \boldsymbol{u}}{\partial t} = -\boldsymbol{\nabla} P - \mu \boldsymbol{\nabla} \times \boldsymbol{\nabla} \times \boldsymbol{u}, \tag{3.5}$$

where the material properties, ρ and μ, are the fluid density and kinematic viscosity, respectively. Applying the curl to (3.5) gives the balance of angular momentum

$$\rho \frac{\partial \boldsymbol{\Omega}}{\partial t} = -\mu \, \boldsymbol{\nabla} \times \boldsymbol{\nabla} \times \boldsymbol{\Omega}, \tag{3.6}$$

with the vorticity $\boldsymbol{\Omega}$ defined as

$$\boldsymbol{\Omega} \equiv \boldsymbol{\nabla} \times \boldsymbol{u}. \tag{3.7}$$

3.2.2 Velocity field definition

The velocity field for axisymmetric flows is written in spherical coordinates as

$$\boldsymbol{u} = u_r \left(r, \theta, t\right) \boldsymbol{e}_r + u_\theta \left(r, \theta, t\right) \boldsymbol{e}_\theta. \tag{3.8}$$

In accordance with the velocity field (3.8), the vorticity is

$$\boldsymbol{\Omega} = \Omega \left(r, \theta, t\right) \boldsymbol{e}_\phi = \frac{1}{r} \left[u_\theta + r \frac{\partial u_\theta}{\partial r} - \frac{\partial u_r}{\partial \theta} \right] \boldsymbol{e}_\phi. \tag{3.9}$$

3.2.3 Reduced system

Substitution of normal modes

$$
\begin{aligned}
&u_r(r,\theta,t) = v_r(r,\theta)\,\mathrm{e}^{-\gamma t}, \quad u_\theta(r,\theta,t) = v_\theta(r,\theta)\,\mathrm{e}^{-\gamma t},\\
&\Omega(r,\theta,t) = \omega(r,\theta)\,\mathrm{e}^{-\gamma t}, \quad P(r,\theta,t) = p(r,\theta)\,\mathrm{e}^{-\gamma t},\\
&\eta(\theta,t) = y(\theta)\,\mathrm{e}^{-\gamma t},
\end{aligned}
\tag{3.10}
$$

into (3.4)-(3.7) delivers a reduced set of field equations,

$$\boldsymbol{\nabla}\cdot\boldsymbol{v} = 0, \tag{3.11a}$$

$$\rho\gamma\boldsymbol{v} = \boldsymbol{\nabla}p + \mu\boldsymbol{\nabla}\times\boldsymbol{\nabla}\times\boldsymbol{v}, \tag{3.11b}$$

$$\rho\gamma\boldsymbol{\omega} = \mu\boldsymbol{\nabla}\times\boldsymbol{\nabla}\times\boldsymbol{\omega}, \tag{3.11c}$$

$$\boldsymbol{\omega} = \boldsymbol{\nabla}\times\boldsymbol{v}, \tag{3.11d}$$

valid in both interior and exterior domains. Here γ is the complex growth rate.

3.2.4 Boundary/Integral conditions

The no-slip and no-penetration conditions for viscous fluids requires

$$v_\theta^{i,e}(R,\theta) = 0 \;\; [\partial D^s], \tag{3.12a}$$

$$v_r^{i,e}(R,\theta) = 0 \;\; [\partial D^s], \tag{3.12b}$$

on the surface-of-support, while continuity of tangential velocity and shear stress

$$v_\theta^i(R,\theta) = v_\theta^e(R,\theta) \;\; \left[\partial D_1^f, \partial D_2^f\right], \tag{3.13a}$$

$$\tau_{r\theta}^i(R,\theta) = \tau_{r\theta}^e(R,\theta) \;\; \left[\partial D_1^f, \partial D_2^f\right], \tag{3.13b}$$

is enforced on the free surfaces. The linearized kinematic condition relates the radial velocity to the surface deformation there

$$v_r^i\left(R,\theta\right) = v_r^e\left(R,\theta\right) = -\gamma y(\theta) \quad \left[\partial D_1^f, \partial D_2^f\right], \tag{3.14}$$

and the difference in normal stress across the interface is balanced by the surface tension σ times the linearized curvature of the surface perturbation

$$\tau_{rr}^i\left(R,\theta\right) - \tau_{rr}^e\left(R,\theta\right) = -\sigma\left[\frac{1}{R^2}\left(\frac{1}{\sin\theta}\left(\sin\theta\, y_{,\theta}\right)_{,\theta} + 2y\right)\right]. \tag{3.15}$$

The integral form of the incompressibility condition (3.4) constrains the interface perturbation to be volume conserving,

$$\int_0^\pi y\left(\theta\right)\sin\theta\,\mathrm{d}\theta = 0. \tag{3.16}$$

The fluids are assumed to be Newtonian, where the components of stress are related to the velocity field components. In spherical coordinates, these relationships are

$$\tau_{r\theta} = \tau_{\theta r} = \mu\left[\frac{\left(v_r\right)_{,\theta}}{r} + r\left(\frac{v_\theta}{r}\right)_{,r}\right], \tag{3.17a}$$

$$\tau_{rr} = -p + 2\mu\left(v_r\right)_{,r}. \tag{3.17b}$$

3.2.5 Velocity field decomposition

The Helmholtz decomposition theorem (e.g. Joseph, 2006) states that the velocity field may be decomposed as the sum of rotational and irrotational fields. The vorticity field is solenoidal and therefore may be written as the curl of a vector potential $\boldsymbol{B}$

$$\boldsymbol{\omega} = \boldsymbol{\nabla}\times\boldsymbol{B}, \tag{3.18}$$

where for axisymmetric flows with non-trivial interface deflection (Chandrasekhar, 1961),

$$\boldsymbol{B} = B\left(r,\theta\right)\boldsymbol{e}_r. \tag{3.19}$$

Given (3.18), the velocity field is decomposed as

$$\boldsymbol{v} = \boldsymbol{B} + \boldsymbol{\nabla}\Psi, \tag{3.20}$$

with the scalar field Ψ defined as the velocity potential. Let $x \equiv \cos(\theta)$, then the velocity field components are

$$\boldsymbol{v} = \left(B + \frac{\partial\Psi}{\partial r}\right)\boldsymbol{e}_r + \left(\frac{1}{r}\left(1-x^2\right)^{1/2}\frac{\partial\Psi}{\partial x}\right)\boldsymbol{e}_\theta. \tag{3.21}$$

Similar to the field quantities, the vector and velocity potentials are expanded with normal modes

$$B\left(r,x,t\right) = T_n\left(r\right)P_n\left(x\right)\mathrm{e}^{-\gamma t}, \quad \Psi\left(r,x,t\right) = \phi_n\left(r\right)P_n\left(x\right)\mathrm{e}^{-\gamma t}, \tag{3.22}$$

where $P_n(x)$ is the n^{th} Legendre polynomial.

3.2.6 Velocity field governing equations

The rotational field (3.19) satisfies the vorticity equation (3.11c). Substituting the normal mode (3.22) into (3.11c) generates an equation governing $T_n(r)$

$$\frac{\mu}{\rho}\frac{d^2T_n}{dr^2} + \gamma T_n - \frac{\mu}{\rho}\frac{n\left(n+1\right)}{r^2}T_n = 0. \tag{3.23}$$

The velocity potential ϕ is chosen such that the incompressibility condition (3.11a) is satisfied. Substituting (3.21,3.22) into (3.11a) results in an inhomogeneous equation for $\varphi_n(r)$

$$\nabla^2\left(\phi_n\left(r\right)P_n\left(x\right)\right) = -\frac{1}{r^2}\frac{d}{dr}\left(r^2T_n\right)P_n\left(x\right). \tag{3.24}$$

A general solution for the velocity field (3.20) is constructed by solving (3.23,3.24).

Equations (3.11)–(3.16) form an eigenvalue problem on the interface deformation $y(x)$. Before solving the fully viscous problem, it will be instructive to first consider the inviscid limit.

3.3 Inviscid solution method

An integro-differential eigenvalue equation, governing the interface deflection, is derived in this section. To compute the spectrum of eigenvalues and corresponding mode shapes, the integro-differential equation is formulated as a functional equation on linear operators, which is reduced to a set of linear algebraic equations by a Rayleigh-Ritz variational procedure. The necessary input to such a procedure is a predetermined function space, which is constructed to satisfy the no-penetration condition on the surface-of-support and to couple the independent free surface perturbations, η_1 and η_2, according to the incompressibility condition (3.16). Equivalently, the two free surfaces are allowed to 'communicate' across the spherical-belt constraint through the underlying fluid, subject to the conservation of volume constraint. The eigenfrequencies/modes are computed using standard numerical routines from a truncated set of linear algebraic equations.

3.3.1 Velocity potential solution

In the inviscid limit, the velocity field is described by the velocity potential, which satisfies Laplace's equation

$$\nabla^2 \left(\phi_n(r) P_n(x)\right) = \left[\frac{1}{r^2}\left(r^2 \frac{d\phi_n}{dr}\right) - n\left(n+1\right)\phi_n\right] P_n(x) = 0 \quad [D]. \tag{3.25}$$

The kinematic condition takes the form

$$v_r = \frac{\partial \phi}{\partial r} = -\gamma y\left(x\right) \quad \left[\partial D_1^f, \partial D_2^f\right], \tag{3.26a}$$

$$v_r = \frac{\partial \phi}{\partial r} = -\gamma y\left(x\right) = 0 \quad \left[\partial D^s\right]. \tag{3.26b}$$

To satisfy (3.25,3.26), consider the three surfaces as one interface and restrict the interface perturbations to be functions which vanish on the support (3.3c). Equation (3.26b) will be satisfied by construction for such functions, which are called 'admissible'. Equations (3.25,3.26) are then recognized as a standard Neumann type boundary-value problem, whose solution is given by (Arfken & Weber, 2001)

$$\phi^i(r,x) = -\gamma R \sum_{n=1}^{\infty} \frac{d_n}{n}\left(\frac{r}{R}\right)^n P_n\left(x\right), \tag{3.27a}$$

$$\phi^e\left(r,x\right) = \gamma R \sum_{n=1}^{\infty} \frac{d_n}{n+1}\left(\frac{R}{r}\right)^{n+1} P_n\left(x\right), \tag{3.27b}$$

where

$$d_n \equiv \frac{\left(y, P_n\right)}{\left(P_n, P_n\right)}. \tag{3.28}$$

Here (f,g) is the inner product of square integrable functions on the domain $x \in (-1,1)$,

$$\left(f,g\right) = \int_{-1}^{1} f(x) g(x)\, \mathrm{d}x. \tag{3.29}$$

3.3.2 Pressure

The pressure field, valid for small oscillations, is governed by the Bernoulli equation

$$p = p_0 + \rho\gamma\phi \quad [D], \tag{3.30}$$

where p_0 is the static pressure required to maintain the undisturbed spherical shape of the drop. For vanishing viscosity μ, the normal stress boundary condition (3.15) relates the difference in pressure across the interface to the local curvature there

$$p^i - p^e = \sigma \left[\frac{1}{R^2} \left(1 - x^2\right) y_{xx} - 2xy_x + 2y \right]. \tag{3.31}$$

3.3.3 Operator equation

Evaluating the pressure from (3.30) at the drop surface and substituting into (3.31) results in an integro-differential operator equation governing allowable interface deformations,

$$\left(1 - x^2\right) y_{xx} - 2xy_x + 2y = \frac{\rho_i \gamma^2 R^3}{\sigma} \left[\sum_{k=1}^{\infty} \left(\frac{1}{k} + \frac{\rho_e}{\rho_i} \frac{1}{k+1} \right) d_k P_k(x) \right]. \tag{3.32}$$

Additionally, the interface deformation y must satisfy the following boundary/integral conditions;

$$y(\pm 1) - \text{bounded}, \tag{3.33a}$$

$$\int_{-1}^{1} y(x)\, \mathrm{d}x = 0, \tag{3.33b}$$

$$y\left(\zeta_1 \leq x \leq \zeta_2\right) = 0, \tag{3.33c}$$

$$y(\zeta_1) = 0, \tag{3.33d}$$

$$y(\zeta_2) = 0, \tag{3.33e}$$

with $\zeta_1 \equiv \cos(\theta_1)$ and $\zeta_2 \equiv \cos(\theta_2)$.

Equations (3.33c–3.33e) enforce the no-penetration condition on the surface-of-support, while (3.33b) requires the perturbation to be volume conserving, necessary for incompressible fluids. Equation (3.33a) guarantees the interface deformation is physical.

There is no dissipation in inviscid fluids for interfaces that are pinned, therefore the growth rate γ is purely imaginary. Let $\underline{\gamma = i\omega}$ and define $\underline{\lambda^2 \equiv \rho_i \omega^2 R^3/\sigma}$. To solve the eigenvalue problem (3.32,3.33), the integro-differential equation is formulated as an operator equation

$$K\left[y\right] = \lambda^2 M\left[y\right], \tag{3.34}$$

where

$$K\left[y\right] \equiv \left(1-x^2\right)\frac{d^2y}{dx^2} - 2x\frac{dy}{dx} + 2y \tag{3.35}$$

is a self-adjoint differential operator and

$$M\left[y;\frac{\rho_e}{\rho_i}\right] \equiv -\left[\sum_{k=1}^{\infty}\left(\frac{1}{k}+\frac{\rho_e}{\rho_i}\frac{1}{k+1}\right)\left(\frac{2k+1}{2}\right)\left(\int_{-1}^{1} y\,P_k\,\mathrm{d}x\right)P_k(x)\right] \tag{3.36}$$

is a positive-definite integral operator. Here the density ratio ρ_e/ρ_i is a material parameter.

3.3.4 Rayleigh-Ritz method

The eigenvalue equation (3.34) is posed as a variational one, using Rayleigh-Ritz formalism, whereby the eigenvalues are computed by minimizing the following functional,

$$\lambda^2 = \min\frac{\left(K\left[y\right],y\right)}{\left(M\left[y\right],y\right)},\ \ y \in S \tag{3.37}$$

over a given function space S. Some details of the theory will be presented here, while a thorough discussion can be found in e.g. Segel (1987).

Given n orthonormal basis functions $\psi_j(x)$, which span the function space S, the variational problem is reduced to a set of linear algebraic equations from which the eigenvalues/vectors are computed. A solution is constructed as a linear combination of the orthonormal basis functions,

$$y(x) = \sum_{j=1}^{n} a_j \psi_j(x). \tag{3.38}$$

Equation (3.38) is applied to the functional (3.37) and minimized with respect to the coefficients a_j, subject to the constraint $(y, y) = 1$. The resulting set of linear equations are written as

$$K_{ij} a_j = \lambda^2 M_{ij} a_j \tag{3.39}$$

with

$$K_{ij} \equiv \int_{-1}^{1} K[y_i] y_j \, \mathrm{d}x, \;\; M_{ij} \equiv \int_{-1}^{1} M[y_i] y_j \, \mathrm{d}x. \tag{3.40}$$

Equation (3.39) is solved using standard numerical techniques. Given an eigenvalue $\lambda^{2(k)}$ and eigenvector $a_j^{(k)}$, the corresponding eigenfunction is

$$y^{(k)}(x) = \sum_{j=1}^{n} a_j^{(k)} \psi_j(x). \tag{3.41}$$

3.3.5 Constrained function space

To use the Rayleigh-Ritz procedure on equation (3.34), a function space that satisfies (3.33) is constructed. To begin, consider a piecewise test function

$$f(x) = \begin{cases} f_1(x) & -1 \le x \le \zeta_1 \\ 0 & \zeta_1 \le x \le \zeta_2 \\ f_2(x) & \zeta_2 \le x \le 1, \end{cases} \tag{3.42}$$

subject to the following conditions;

$$\int_{-1}^{\zeta_1} f_1(x)\,\mathrm{d}x + \int_{\zeta_2}^{1} f_2(x)\,\mathrm{d}x = 0, \tag{3.43a}$$

$$f_1(\zeta_1) = 0, \tag{3.43b}$$

$$f_2(\zeta_2) = 0. \tag{3.43c}$$

By construction, the test function (3.42) satisfies (3.33c) and therefore the no-penetration condition (3.26b). The functions $f_1(x)$ and $f_2(x)$ are the deformations of the respective free surfaces and are completely independent, except for coupling via the conservation of volume constraint (3.43a). The perturbation is single-valued, which dictates that its amplitude must vanish on the boundaries of the spherical-belt constraint (3.43b,3.43c).

To construct functions that satisfy (3.43), assume the free surface perturbations take the form;

$$f_1(x) = \sum_{k=0}^{N} c_k P_k(x),\;\; f_2(x) = \sum_{k=0}^{N} d_k P_k(x). \tag{3.44}$$

Substitution of (3.44) into (3.43) gives

$$c_0 \int_{-1}^{\zeta_1} P_0\,\mathrm{d}x + \cdots + c_N \int_{-1}^{\zeta_1} P_N\,\mathrm{d}x + \cdots + d_N \int_{\zeta_2}^{1} P_N\,\mathrm{d}x = 0, \tag{3.45a}$$

$$c_0 P_0(\zeta_1) + c_1 P_1(\zeta_1) + \cdots + c_N P_N(\zeta_1) = 0, \tag{3.45b}$$

$$d_0 P_0(\zeta_2) + d_1 P_1(\zeta_2) + \cdots + d_N P_N(\zeta_2) = 0, \tag{3.45c}$$

which is a set of 3 algebraic equations on the coefficients c_k and d_k

$$\begin{bmatrix} \int_{-1}^{\zeta_1} P_0(x)\mathrm{d}x & \cdots & \int_{-1}^{\zeta_1} P_N(x)\mathrm{d}x & \int_{\zeta_2}^{1} P_0(x)\mathrm{d}x & \cdots & \int_{\zeta_2}^{1} P_N(x)\mathrm{d}x \\ P_0(\zeta_1) & \cdots & P_N(\zeta_1) & 0 & \cdots & 0 \\ 0 & \cdots & 0 & P_0(\zeta_2) & \cdots & P_N(\zeta_2) \end{bmatrix} [\boldsymbol{c}] = [\boldsymbol{0}]\,. \tag{3.46}$$

There are $2(N+1) - 3 = 2N - 1$ linearly independent coefficient vectors that solve (3.46) and equivalently $2N - 1$ linearly independent basis functions $\xi_k(x)$

which solve (3.43). To use the Rayleigh-Ritz procedure, an orthonormal set of functions is needed. This step is done using Gram-Schmidt orthogonalization and a computer algebra package. The orthonormal basis functions inherit the properties of the linearly independent basis functions, such as identically satisfying the boundary/integral conditions (3.33). Finally, a solution series, which spans the constrained function space, is constructed using the orthonormal basis functions $\psi_k(x)$ as

$$y(x) = \sum_{k=1}^{2N-1} a_k \psi_k(x). \tag{3.47}$$

3.4 Inviscid results

The solution series (3.47) is used to reduce the operator equation (3.34), via a Rayleigh-Ritz procedure, to a standard eigenvalue problem. The eigenfrequencies/modes, as they depend upon ρ_e/ρ_i, ζ_1 and ζ_2, are then computed from (3.39). Setting $N = 7$ for computation shows eigenvalue convergence to within 0.1% for the results presented here. Equivalently, 13 terms are used in the solution series (3.47) with a resolution of 8 terms on each free surface.

The formalism developed here can be specialized to a pinned latitudinal circle-of-contact constraint by setting $\zeta_1 = \zeta_2$. In contrast to the pinned spherical drop considered in Chapter 2, a broader class of allowable solutions, which are less restrictive and accommodate discontinuous contact angles across the pinned circle-of-contact, are considered. Stated differently, in Chapter 2 the problem was idealized as a single free surface with solutions that necessarily have a continuous contact-angle across the circle-of-contact, whereas in the present study we treat the two free surfaces as independent, giving rise to solutions with a discontinu-

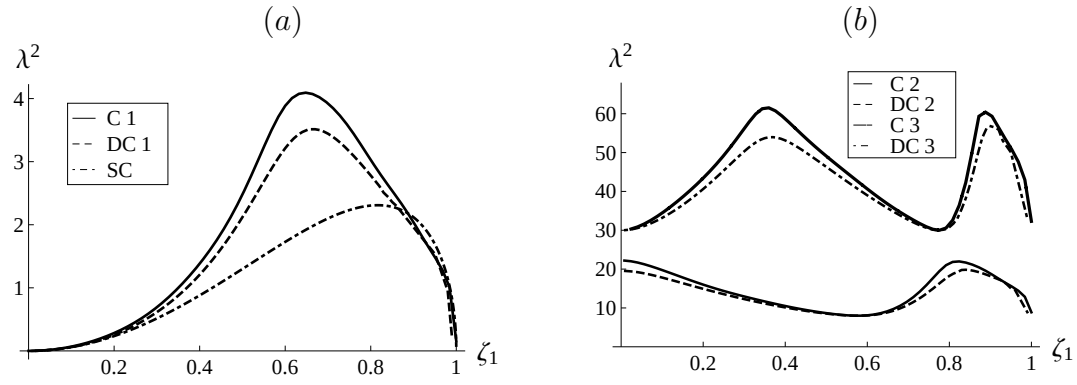

Figure 3.2: Frequency (λ^2) comparison between continuous (C), discontinuous (DC) and spherical cap (SC) perturbations for a pinned circle-of-contact ($\zeta_1 = \zeta_2$) with (a) $n = 1$ (b) $n = 2, 3$.

ous contact-angle. As seen in figure 3.2, which plots the eigenfrequency λ^2 vs. pin location ζ_1 for $\rho_e/\rho_i = 0$, the continuous contact-angle frequencies (C) are always larger than the corresponding discontinuous frequencies (DC), with equality achieved at local minima. Here the frequencies are symmetric with respect to the pin location, $\lambda_n^2(\zeta) = \lambda_n^2(-\zeta)$, and the value of the local minima correspond to the 'unconstrained' Rayleigh frequencies (2.1) for mode number n. These minima are termed 'natural' pin locations and specified by the 'nodes' or zeroes of the corresponding unconstrained mode shapes. As seen from the computed mode shapes of figures 3.3(a, c), the equator is a natural pin location for the odd mode shapes. Likewise, a pin location out-of-phase with respect to the unconstrained mode shapes is analogously called 'unnatural' and may be associated with the local maxima of figure 3.2. For example, consider the $n = 2$ mode shape shown in figure 3.3(b). This mode clearly shows a discontinuous contact-angle for a drop pinned at the equator. Using the variational problem interpretation, one could say a perturbed liquid drop would generally prefer to oscillate with a discontinuous contact-angle across the pinned circle-of-contact.

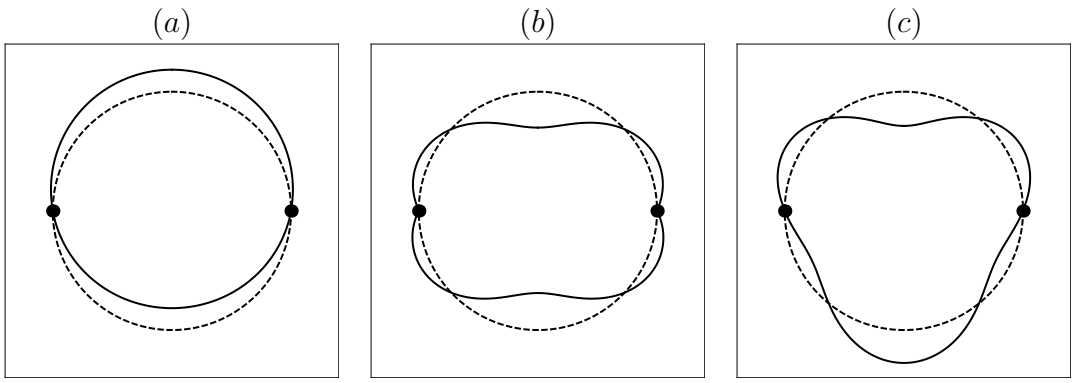

Figure 3.3: Mode shapes (a) $n = 1$ (b) $n = 2$ (c) $n = 3$ for a drop with pinned circle-of-contact located at the equator ($\zeta_1 = \zeta_2 = 0$).

One goal in generalizing to disjoint free surfaces with discontinuous contact angles is to compare the low-frequency $n = 1$ mode to the spherical cap model of Theisen *et al.* (2007). In the preceeding chapter, a snapshot is provided of the corresponding experiments to clearly show the different apparent contact angles across the constraint. Figure 3.2(a) compares the spherical cap model (SC) with the $n = 1$ frequency from the continuous (C) and discontinuous (DC) contact-angle analysis. As shown, the qualitative behavior is similar in each analysis, but the discontinuous model most closely resembles the spherical cap model, which can be directly attributed to the larger class of solutions for this model.

The spherical-cap behavior of the $n = 1$ mode shape, shown in figures 3.4(a) and 3.5(a), persists for finite-sized spherical-belt constraints. Additionally, the $n \neq 1$ mode shapes of figures 3.4,3.5 show rich behavior, illustrating different ways that the two free surfaces communicate across the constraint. For example, the mode shapes of figures 3.4(b),3.4(c) and 3.5(b) display spherical-cap behavior on one free surface and higher-order shapes on the other. This leads one to believe that eigenmodes may be excited where one free surface is relatively 'inactive' compared to the second free surface. Alternatively, figure 3.5(c) demonstrates that higher-

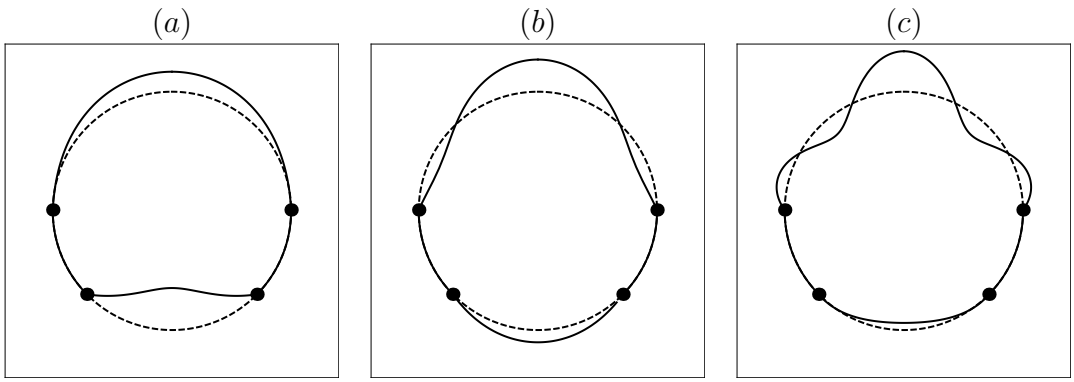

Figure 3.4: Mode shapes (a) $n = 1$ (b) $n = 2$ (c) $n = 3$ with spherical-belt constraint $\zeta_1 = -0.7, \zeta_2 = 0$.

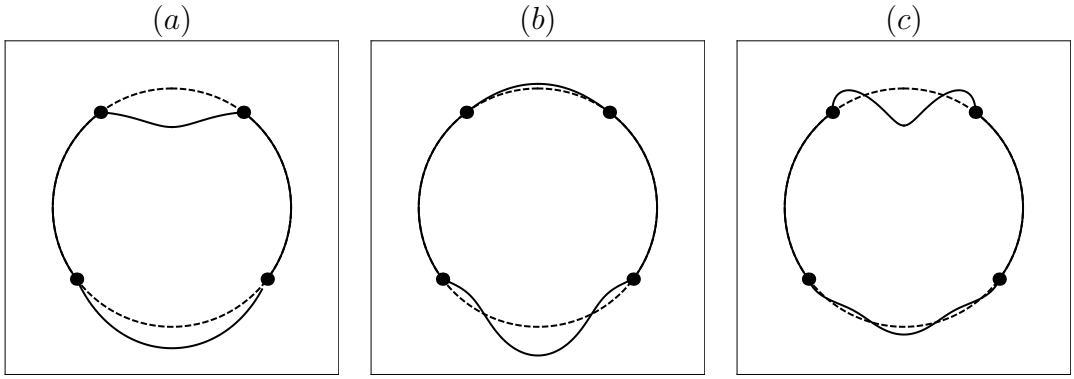

Figure 3.5: Mode shapes (a) $n = 1$ (b) $n = 2$ (c) $n = 3$ with spherical-belt constraint $\zeta_1 = -0.6, \zeta_2 = 0.8$.

order shapes can occur on both free surfaces.

Strani & Sabetta (1984) have shown that increasing the size of their spherical-bowl constraint leads to exponential growth of the eigenfrequency. To examine the effect of constraint size, the first five eigenfrequencies are plotted in figure 3.6 as a function of the second pin location ζ_2, while holding the first pin location ζ_1 fixed. The frequency growth is monotonic with constraint size, but there are certain well-defined plateaus or 'dead zones', where a further increase in belt-size has no substantial influence on the frequencies themselves. In these regions, no ap-

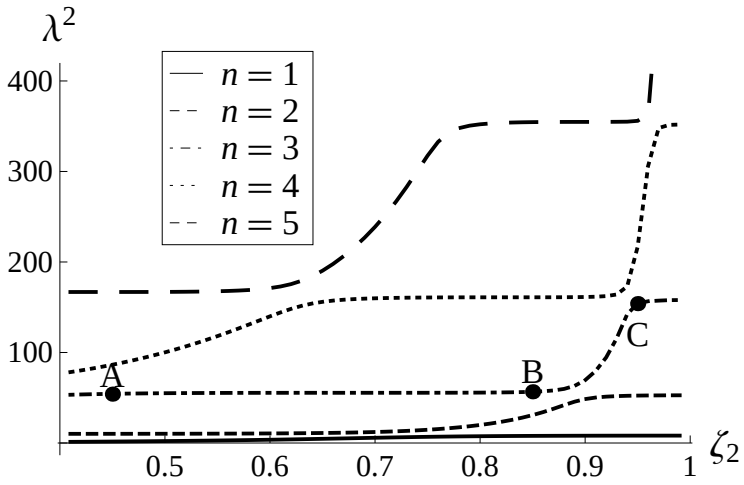

Figure 3.6: Frequency λ^2 against second pin location ζ_2, while holding $\zeta_1 = 0.4$.

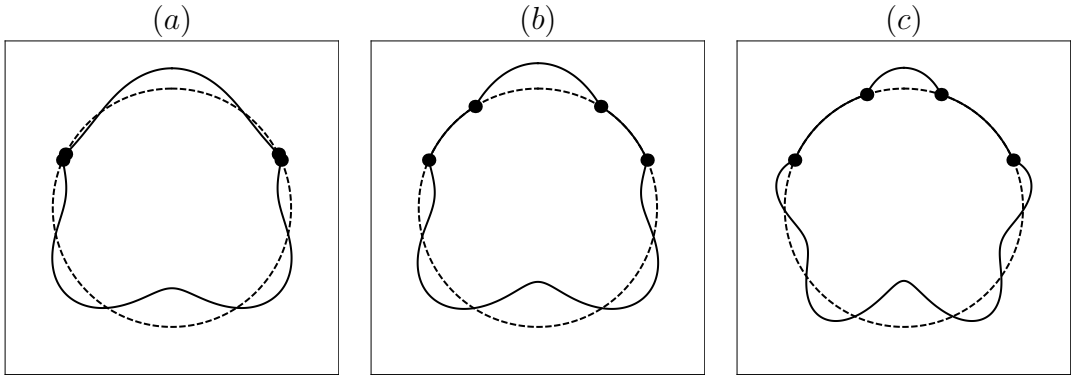

Figure 3.7: Mode shape ($n = 3$) at (a) point A($\zeta_1 = 0.4, \zeta_2 = 0.45$) ($b$) point B($\zeta_1 = 0.4, \zeta_2 = 0.85$) ($c$) point C($\zeta_1 = 0.4, \zeta_2 = 0.95$) of Figure 3.6.

preciable change in mode shape is observed. Alternatively, one might say that one belt-size appears to be no more desirable than the next. As such, figures 3.7(a, b) show only a slight variation in the $n = 3$ mode shape, despite the drastic difference in constraint size. Figure 3.6 also displays accelerated eigenfrequency growth in particular regions. In these regions, one surface seems relatively inactive, while the other is actively changing its character (e.g. number of nodes) to

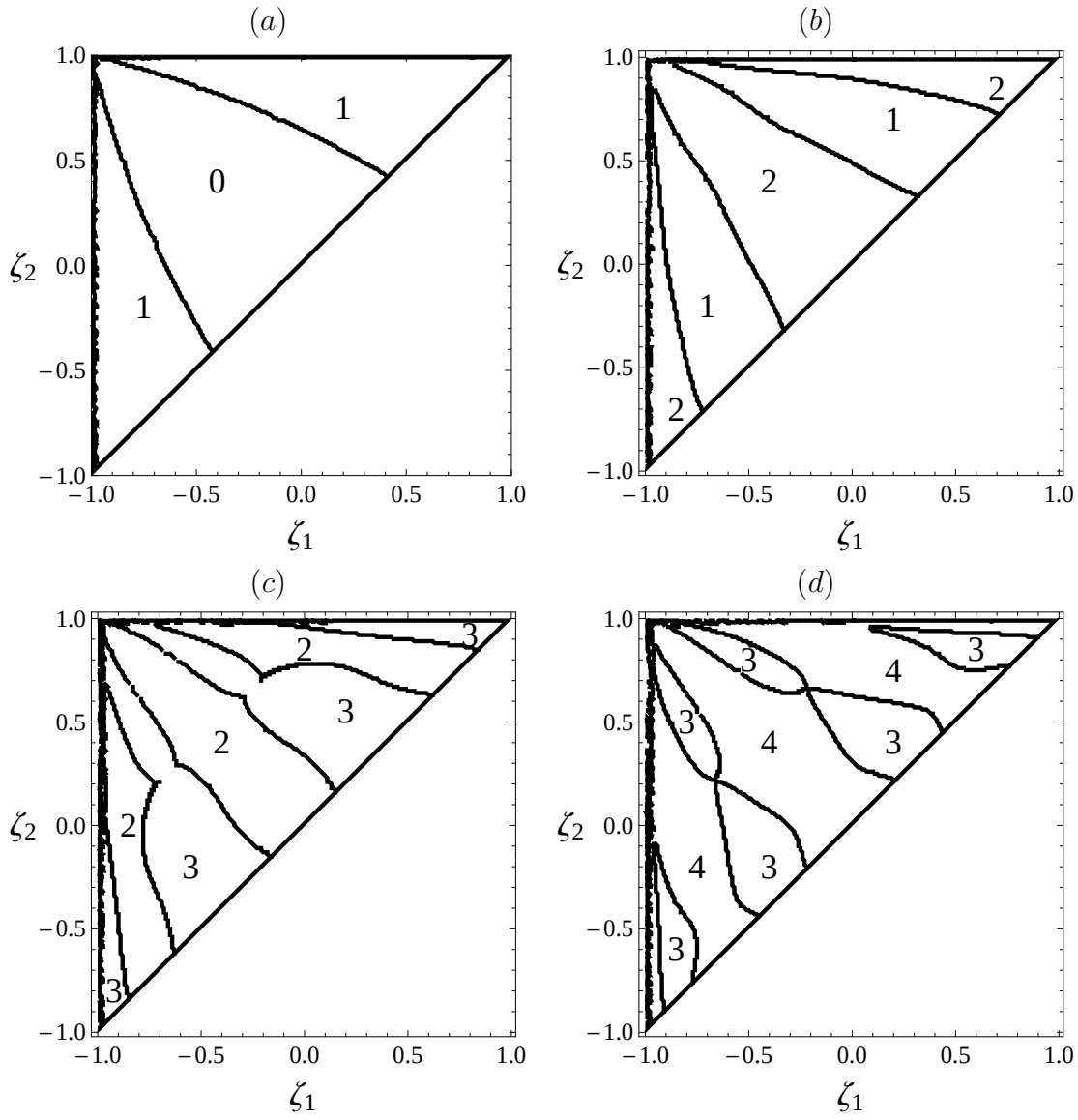

Figure 3.8: Geometric index (engineering) of mode (a) $n = 1$, (b) $n = 2$, (c) $n = 3$ and (d) $n = 4$, against ζ_1 and ζ_2.

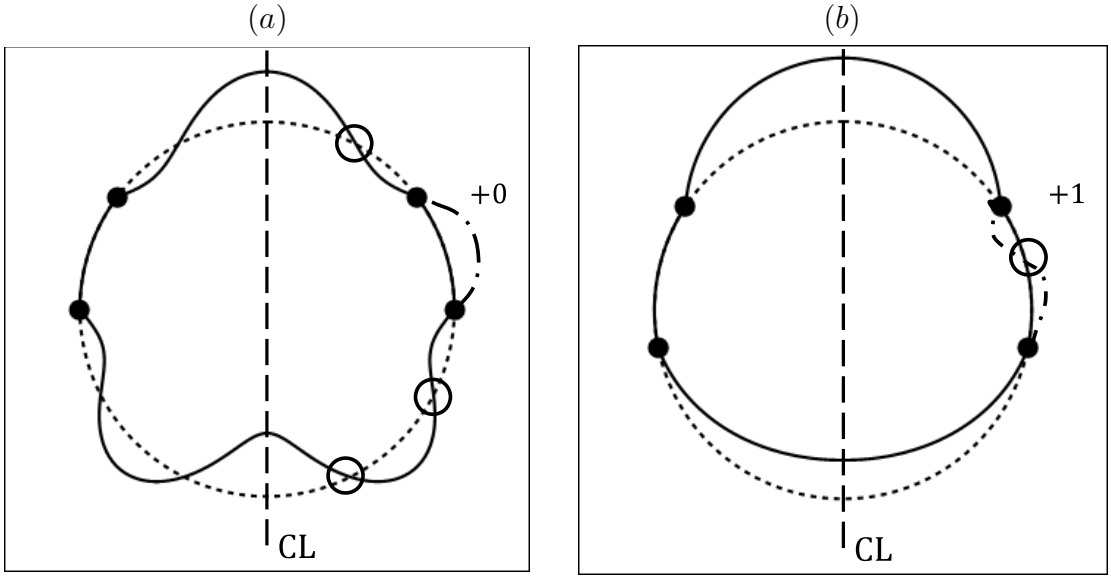

Figure 3.9: Geometric index: comparison between the engineering and mathematical interpretation.

fit the given constraint. These changes are tracked in figure 3.7, which plots the $n = 3$ mode shape at points A, B, C of the $n = 3$ curve from figure 3.6. The transition from figure 3.7(b) to figure 3.7(c) occurs when the $n = 2$ and $n = 3$ curves of figure 3.6 cross. More definitively, such a point is identified mathematically by the eigenvalue's algebraic and geometric multiplicity of two and one, respectively. The defining feature of the coalescence point is qualitative and associated with a change in the number of nodes of the corresponding mode shape, despite preserving the numerical ordering of eigenvalues. One can monitor node-creation or-destruction by defining a geometric index of a given mode shape as the number of times the disturbed shape intersects the undisturbed shape. The boundaries of the spherical-belt constraint are not included in this definition, which will be referred to as the 'engineering index'. The index can be defined on the half-drop, because of the axisymmetry assumption (c.f. figure 3.9). The engineering index, as it depends upon the geometry of the spherical belt, is shown in figure 3.8 for

the first four modes. In unconstrained problems, the spectral ordering of eigenvalues and number of nodes of the respective mode shape are coincident, as for the unconstrained Rayleigh modes. The constrained nature of the problem considered here distorts this ordering, whereby the mode shape associated with the third numerical eigenvalue may have less than three nodes for a fixed constraint. The ambiguity in ordering occurs at the coalescence points of figure 3.6 and is tracked using the engineering index in figure 3.8. To reconcile this ambiguity, one can define a new geometric index to account for the possibility of a virtual node within the spherical-belt constraint. This interpretation is termed the 'mathematical index'. Specifically, if the amplitude of the linear disturbance has opposite sign on either side of the spherical-belt, continuity requires the existence of an additional 'virtual' node within the spherical-belt constraint (c.f. figure 3.9(b)). In this case, *the mathematical index is simply the engineering index plus one.* Alternatively, when the disturbance has the same sign on both sides of spherical-belt then there does not exist a virtual node and *the engineering and mathematical index are coincident* (c.f. figure 3.9(a)). The mathematical index is identical to the numerical order of the respective frequency and is thus unambiguous with respect to the classical ordering of mode shapes. In addition, the mathematical index reduces to the index of the Rayleigh modes in the limit of a pinned circle-of-contact ($\zeta_1 = \zeta_2$).

Another distinguishing feature of figure 3.6 is that horizontal asymptotes connect dead regions of different mode number. The asymptotes are lines of constant λ^2, whose numerical value is given by the corresponding eigenfrequency for the drop constrained by a spherical bowl (Strani & Sabetta, 1984), whose size $1 - \zeta_1$ is set by fixing ζ_1 and taking the limit $\zeta_2 \to 1$. Furthermore, *if one connects each successive point of coalescence, the resulting curve is well-defined and exponential.* As this curve is traversed, one can monitor node creation.

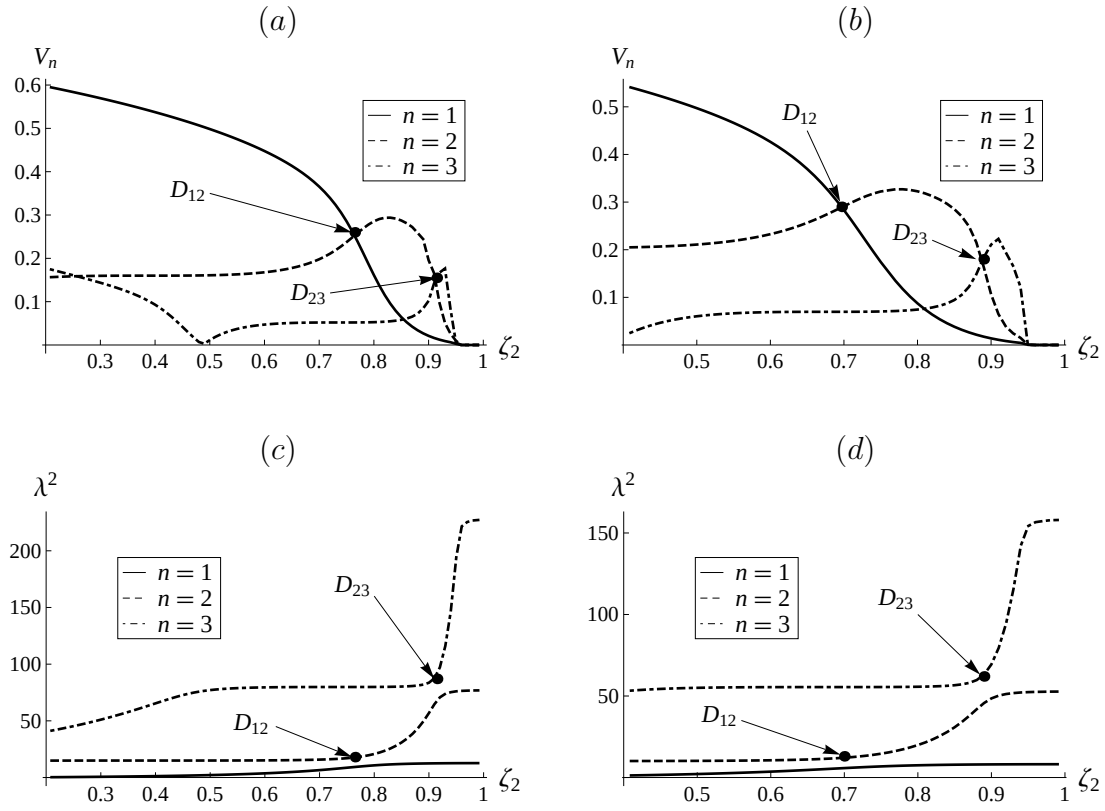

Figure 3.10: Perturbed volume V_n (a, b) and frequency λ^2 (c, d) vs. ζ_2 for fixed (a),(c) $\zeta_1 = 0.2$ and (b),(d) $\zeta_1 = 0.4$.

Physically, these crossings may be located by examining the perturbed volume exchange between disjoint interfaces for a given mode shape $y^{(n)}$, defined as

$$V_n \equiv \int_{\zeta_2}^{1} y^{(n)}(x)\,\mathrm{d}x. \tag{3.48}$$

Figures 3.10$(a), (b)$ plot the perturbed volume exchanged V_n as a function of the second pin location ζ_2, while holding the first pin location ζ_1 fixed. From these figures, one can identify D_{12} and D_{23} as crossing points, where the primary volume-carrying mode-shape changes from $n = 1$ to $n = 2$ and $n = 2$ to $n = 3$, respectively. As shown in figures 3.10(c, d), which plots frequency λ^2 vs. ζ_2 for fixed ζ_1, such points are precisely the coalescence points, which were previously defined mathematically. To summarize, at transition point $D_{n(n+1)}$ the $n + 1$ mode shape adds

another node and becomes the primary volume carrier, taking volume from the n mode shape.

3.4.1 Perturbed-volume embedding

To further investigate the role of volume-exchange amongst disjoint interfaces, consider an arbitrary domain, bound by two free surfaces and subject to the following constraint

$$\int_{\partial D_1^f} y_1 = C, \quad \int_{\partial D_2^f} y_2 = -C. \tag{3.49}$$

Here, a perturbed volume C is exchanged between interfaces, while total volume is conserved, in accordance with the assumption of fluid incompressibility. As the governing equations can be derived from a variational approach, one may incorporate the constraints (3.49) into an augmented functional

$$\begin{aligned} F\left[y_1, y_2; \mu_1, \mu_2\right] = &\int_{\partial D_1^f} \left(\lambda_1 M\left[y_1\right] + K\left[y_1\right] + \mu_1\right) y_1 \\ &+ \int_{\partial D_2^f} \left(\lambda_2 M\left[y_2\right] + K\left[y_2\right] + \mu_2\right) y_2 \end{aligned} \tag{3.50}$$

through the Lagrange multipliers μ_1, μ_2. This formulation is completely equivalent to the solution method employed previously. It utilizes an embedding to enforce incompressibility, whereas previously this condition was explicitly satisfied through the construction of the constrained function space. As mentioned above, the surface disturbance may be defined in a piecewise manner by decomposing the bounding surface into the union of the free surfaces and surface-of-support, $\partial D \equiv \partial D_1^f \cup \partial D_2^f \cup \partial D^s$. Using this decomposition, in conjunction with a continuity condition on the surface-of-support, one can independently vary the free surface disturbances y_1, y_2, giving rise to the form of (3.50). Stationary values of the augmented functional are solutions of the corresponding Euler-Lagrange

equations

$$\lambda_1 M[y_1] + K[y_1] + \mu_1 = 0, \quad \lambda_2 M[y_2] + K[y_2] + \mu_2 = 0, \tag{3.51}$$

where the Lagrange multipliers may be interpreted physically as the constant pressure applied at each respective interface, requisite to displace a volume C. To enforce the constraint (3.49) (i.e. embed the perturbed volume), integrate the Euler-Lagrange equations (3.51) over the respective undisturbed free surface to specify μ_1, μ_2. The following Euler-Lagrange equations result,

$$k_1[y_1] = -\lambda_1 m_1[y_1; C], \; k_2[y_2] = -\lambda_2 m_2[y_2; C]. \tag{3.52}$$

The structure of the governing equations is reminiscent of a system of weakly-coupled oscillators and shows that the respective interfaces oscillate with an effective spring constant

$$k_1[y_1] \equiv K[y_1] - \frac{\int_{\partial D_1^f} M^{-1}[K[y_1]]}{\int_{\partial D_1^f} M^{-1}[1]}, \quad k_2[y_2] \equiv K[y_2] - \frac{\int_{\partial D_2^f} M^{-1}[K[y_2]]}{\int_{\partial D_2^f} M^{-1}[1]}, \tag{3.53}$$

and effective mass, parameterized by C and given by

$$m_1[y_1; C] \equiv M[y_1] - \frac{C}{\int_{\partial D_1^f} M^{-1}[1]}, \quad m_2[y_2; C] \equiv M[y_2] + \frac{C}{\int_{\partial D_2^f} M^{-1}[1]}. \tag{3.54}$$

One may independently compute the oscillation frequencies $\lambda_1(C), \lambda_2(C)$, as they depend upon the perturbed volume C, from (3.52). However, the interfaces are coupled through the fluid domain, which requires the frequencies to be in phase, $\lambda = \lambda_1(C^*) = \lambda_2(C^*)$, at a critical perturbed volume C^*. Accordingly, each mode shape exchanges a characteristic perturbed volume C^* between disjoint free surfaces.

The perturbed-volume embedding can be used to provide useful information regarding the eigenvalue degeneracy mentioned earlier. Namely, by specifying the perturbed-volume makes the eigenvalue problem well-posed, as opposed to the

under-specified standard two-point boundary-value problem. Accordingly, mode shapes with the same perturbed volume are necessarily identical by uniqueness, giving rise to degenerate eigenvalues, as shown in figures $3.10(a), (b)$. Additionally, the perturbed volume C can be viewed as a measure of 'communication' between free surfaces. A non-trivial perturbed volume implies the disjoint surfaces are in communication, while mode shapes with zero perturbed volume exchange are essentially de-coupled.

3.5 Viscous solution method

The equation governing the interface deflection of a *viscous* drop is derived and formulated as an operator equation in this section. The no-penetration condition (3.12b) is satisfied by restricting the interface perturbations to the constrained function space derived previously. However, the 'shear' boundary conditions (3.12a),(3.13a) and (3.13b) change from no-stress (free) to no-slip (supported). To address this issue, a modified set of boundary conditions are proposed. A normal mode analysis with the modified boundary conditions allows one to derive the viscous operator equation, which depends upon a viscosity parameter ϵ, the ratio of inner to exterior densities ρ, the ratio of inner to exterior viscosities μ, and a support size parameter. The operator equation is solved for both a viscous drop in a vacuum and an inviscid fluid (bubble) immersed in a viscous liquid. A general operator equation for an immiscible viscous drop is given in Appendix B. Unlike the inviscid limit, the eigenvalues are computed from a characteristic equation with eigenvalues appearing nonlinearly.

3.5.1 Vector potential solution

The vector potential solution of (3.23) is given by

$$T_n^i(r) = \left(\frac{r}{R}\right)^{1/2} T_n^i(R) \frac{J_{n+1/2}\left(z^i\right)}{J_{n+1/2}\left(Z^i\right)}, \;\; T_n^e(r) = \left(\frac{r}{R}\right)^{1/2} T_n^e(R) \frac{H^{(1)}_{n+1/2}\left(z^e\right)}{H^{(1)}_{n+1/2}\left(Z^e\right)}, \quad (3.55)$$

where

$$z^{i,e} \equiv r\left(\gamma \frac{\rho_{i,e}}{\mu_{i,e}}\right)^{1/2}, \;\; Z^{i,e} \equiv R\left(\gamma \frac{\rho_{i,e}}{\mu_{i,e}}\right)^{1/2}, \quad (3.56)$$

and $J_n(z)$ and $H_n^{(1)}(z)$ are the appropriate Bessel functions (standard notation used, Arfken & Weber, 2001).

3.5.2 Velocity potential solution

Equation (3.24) is solved using variation-of-parameters for the velocity potential,

$$\begin{aligned} \phi_n^{i,e}(r) = &\left[\alpha_n^{i,e} - \frac{n+1}{2n+1}\int_R^r \frac{T_n^{i,e}(s)}{s^n}\,\mathrm{d}s\right] r^n \\ &+ \left[\beta_n^{i,e} - \frac{n}{2n+1}\int_R^r s^{n+1} T_n^{i,e}(s)\,\mathrm{d}s\right] r^{-(n+1)}. \end{aligned} \quad (3.57)$$

The velocity potential is finite as $r \to 0$ and $r \to \infty$, which requires

$$\beta_n^i = -\frac{n}{2n+1}\int_0^R s^{n+1} T_n^i(s)\,\mathrm{d}s = -\frac{n}{2n+1}\frac{T_n^i(R)}{\mathcal{J}_{n+3/2}\left(Z^i\right)} R^{n+2} \quad (3.58)$$

and

$$\alpha_n^e = \frac{n+1}{2n+1}\int_R^\infty \frac{T_n^e(s)}{s^n}\,\mathrm{d}s = \frac{n+1}{2n+1}\frac{T_n^e(R)}{\mathcal{H}_{n-1/2}\left(Z^e\right)} R^{-(n-1)}, \quad (3.59)$$

where

$$\mathcal{J}_n\left(z\right) \equiv z\frac{J_{n-1}\left(z\right)}{J_n\left(z\right)}, \;\; \mathcal{H}_n\left(z\right) \equiv z\frac{H^{(1)}_{n+1}\left(z\right)}{H^{(1)}_n\left(z\right)} \quad (3.60)$$

are fractional Bessel functions (again standard notation, Arfken & Weber, 2001).

3.5.3 Pressure

The pressure is found by substituting (3.22) into (3.11b) to give

$$p = p_0 + \rho\left(\gamma\phi_n - \frac{\mu}{\rho}\frac{dT_n}{dr}\right)P_n(x). \tag{3.61}$$

Using the vector and velocity potential solutions (3.55,3.57), the pressure evaluated on the surface is

$$p^i(R) = p_0^i - \left[(n+1)\,\mu_i\frac{T_n^i(R)}{R} + \frac{\rho_i R\gamma^2}{n}d_n\right]P_n(x), \tag{3.62a}$$

$$p^e(R) = p_0^e + \left[(n)\mu_e\frac{T_n^e(R)}{R} + \frac{\rho_e R\gamma^2}{n+1}d_n\right]P_n(x). \tag{3.62b}$$

3.5.4 Boundary conditions

As with the other field quantities, the interface perturbation is expanded as

$$y(x) = d_n P_n(x), \quad d_n \equiv \frac{(y, P_n)}{(P_n, P_n)}. \tag{3.63}$$

Using (3.21) and (3.63), the linearized kinematic condition (3.14) is reduced to

$$T_n^i(R) + \frac{d\phi_n^i}{dr}\Big|_{r=R} = -\gamma d_n,\ T_n^e(R) + \frac{d\phi_n^e}{dr}\Big|_{r=R} = -\gamma d_n. \tag{3.64}$$

As in the inviscid limit, equation (3.64) is valid on the entire interface, and the no-penetration condition (3.12b) is satisfied by restricting candidate functions to an appropriately chosen function space. To simplify (3.64), use the velocity potential solution (3.57) to obtain

$$\alpha_n^i = \frac{n+1}{n}R^{-(2n+1)}\beta_n^i - \frac{\gamma}{n}R^{-(n-1)}d_n, \quad \beta_n^e = \frac{n}{n+1}R^{2n+1}\alpha_n^e + \frac{\gamma}{n+1}R^{n+2}d_n. \tag{3.65}$$

with β_n^i and α_n^e given by (3.58) and (3.59), respectively.

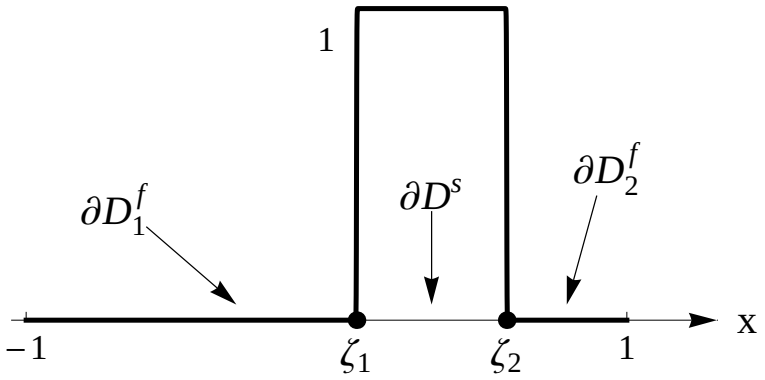

Figure 3.11: Indicator function $\Gamma(x, \zeta_1, \zeta_2\ )$

The remaining unknowns, $T_n^i(R)$ and $T_n^e(R)$, are found from the shear boundary conditions; (3.12a),(3.13a) and (3.13b). These boundary conditions are valid on specified parts of the interface and are not amenable to standard analysis. To resolve this issue, a new set of boundary conditions are proposed. On the drop interface, the following boundary conditions are introduced as equivalent to (3.12a),(3.13a) and (3.13b);

$$v_\theta^i|_{r=R} = v_\theta^e|_{r=R}, \tag{3.66a}$$

$$\left(\tau_{r\theta}^i - \tau_{r\theta}^e\right)|_{r=R}\left[1 - \Gamma\left(x, \zeta_1, \zeta_2\right)\right] = C\Gamma\left(x, \zeta_1, \zeta_2\right) v_\theta^i|_{r=R}. \tag{3.66b}$$

Here $\Gamma(x, \zeta_1, \zeta_2)$ is an indicator function, which is active on the surface-of-support and inactive on the free surfaces (c.f. figure 3.11),

$$\Gamma(x, \zeta_1, \zeta_2) \equiv H(x - \zeta_1) - H(x - \zeta_2), \tag{3.67}$$

where $H(x)$ is the Heaviside step function. The constant C, which has units of $[viscosity]/[length]$, will be determined when the problem is scaled.

3.5.5 Viscous operator equation

The viscous operator equation is derived from the normal stress boundary condition (3.15)

$$-p^i + 2\mu_i \frac{\partial v_r^i}{\partial r}\Big|_{r=R} + p^e - 2\mu_e \frac{\partial v_r^e}{\partial r}\Big|_{r=R} = -\sigma \left[\frac{1}{R^2}\left(\left(1-x^2\right) y_{xx} - 2xy_x + 2y\right)\right],$$

which can be written as

$$\begin{aligned}\left[\left(\frac{\rho_e}{n+1} + \frac{\rho_i}{n}\right)\gamma^2 R + 2\left(n-1\right)\left(n+2\right)\left(\mu_i - \mu_e\right)\frac{\gamma}{R}\right] d_n \\ + n\left(n+2\right)\mu_e \frac{T_n^e\left(R\right)}{R} - \left(n-1\right)\left(n+1\right)\mu_i \frac{T_n^i\left(R\right)}{R} \\ = -\sigma/R^2\left[\left(1-x^2\right) y_{xx} - 2xy_x + 2y\right],\end{aligned} \tag{3.68}$$

with $T_n^i(R)$ and $T_n^e(R)$ determined from the modified boundary conditions (3.66). This is done in Appendix B.

The following scalings are introduced,

$$\gamma^* \equiv \sqrt{\frac{\rho_i R^3}{\sigma}}\gamma, \quad \epsilon_{i,e} \equiv \frac{\mu_{i,e}}{\sqrt{\rho_{i,e} R \sigma}}, \quad \mu \equiv \frac{\mu_e}{\mu_i}, \quad \rho \equiv \frac{\rho_e}{\rho_i}. \tag{3.69}$$

A product of the modified boundary conditions is a 'shape' factor

$$L_n = \left(\int_{-1}^{1} \left(P_n^{(1)}(x)\right)^2 \Gamma(x, \zeta_1, \zeta_2)\, \mathrm{d}x\right)\left(\frac{2n+1}{2}\frac{(n-1)!}{(n+1)!}\right), \tag{3.70}$$

which is a measure of the relative size of the surface-of-support. Here $P_n^{(1)}(x)$ is the n^{th} Legendre polynomial of order one (MacRobert, 1967).

Drop in vacuum

A viscous drop in a vacuum corresponds to the limiting case $\mu_e \to 0$ and $\rho_e \to 0$. In this limit, the viscous drop operator equation is given by

$$\gamma^{*2} M_d\left[y\right] + \gamma^* \Phi_d\left[y; \gamma^*, \epsilon_i\right] + K\left[y\right] = 0. \tag{3.71}$$

The differential operator

$$K[y] \equiv \left(1-x^2\right) y_{xx} - 2xy_x + 2y \tag{3.72}$$

is associated with the curvature and acts as a restoring force (same as equation (3.35)), while the positive-definite inertia operator is defined as

$$M_d[y] \equiv \sum_{n=1} \frac{1}{n} d_n P_n(x). \tag{3.73}$$

Viscous effects are controlled by the dissipation operator

$$\Phi_d[y;\gamma^*,\epsilon_i] \equiv -\epsilon_i \sum_{n=1} \left[2(n-1)(n+2) + (n-1)(n+1) T_n^i(R)\right] d_n P_n(x) \tag{3.74}$$

where

$$T_n^i(R) = \left[\frac{2(n-1)/n - \epsilon_i A_n/n}{\left(2/\mathcal{J}_{n+3/2}(X^i) - 1\right) + \epsilon_i A_n/\mathcal{J}_{n+3/2}(X^i)}\right] \tag{3.75}$$

and

$$A_n \equiv L_n/(1-L_n);\ X^i \equiv (\gamma^*/\epsilon_i)^{1/2}. \tag{3.76}$$

Bubble in viscous medium

A similar operator equation is derived for a bubble, the limit $\mu_i \to 0$ and $\rho_i \to 0$ in equation (3.68),

$$\gamma^{*2} M_b[y] + \gamma^* \Phi_b[y;\gamma^*,\epsilon_e] + K[y] = 0 \tag{3.77}$$

where the curvature operator is defined in (3.72) and the inertia operator for a bubble as

$$M_b[y] \equiv \sum_{n=1} \frac{1}{n+1} d_n P_n(x). \tag{3.78}$$

The bubble dissipation operator is given by

$$\Phi_b[y;\gamma^*,\epsilon_e] \equiv -\epsilon_e \sum_{n=1} \left[-2(n-1)(n+2) + n(n+2) T_n^e(R)\right] d_n P_n(x). \tag{3.79}$$

with

$$T_n^e(R) = -\left[\frac{2(n+2)/(n+1) - \epsilon_e\ A_n/(n+1)}{\left(2/\mathcal{H}_{n-1/2}(X^e) - 1\right) + \epsilon_e A_n/\mathcal{H}_{n-1/2}(X^e)}\right] \tag{3.80}$$

and

$$A_n \equiv L_n/(1-L_n);\ X^e \equiv (\gamma^*/\epsilon_e)^{1/2}. \tag{3.81}$$

Immiscible viscous drop in viscous medium

The operator equation for an immiscible viscous drop is given in Appendix B.

3.5.6 Viscous operator solution

The operator equations (3.71) and (3.77) are nonlinear in the eigenvalue and reduced to a set of algebraic equations using a Rayleigh-Ritz procedure with the function space (3.47) derived in section 3.3.5. The resulting matrix equation is parameterized by the viscosity parameter ϵ and the boundaries of the belted constraint, ζ_1 and ζ_2, via the indicator function $\Gamma(x, \zeta_1, \zeta_2)$. The eigenvalues/eigenmodes are then computed from a nonlinear characteristic equation, found by taking the determinant of the matrix equation.

3.6 Viscous results

The viscous eigenvalues/modes for the drop and bubble, as they depend upon the viscosity parameter ϵ, are the roots of a nonlinear characteristic equation and computed using a variant of the secant method. As with the inviscid limit, 13 terms are used in the solution series (3.47), with a resolution of $N = 7$ Legendre

polynomials on each free surface, to derive the characteristic equations from the Rayleigh-Ritz procedure. As the viscosity parameter ϵ is varied, the eigenvalues bifurcate from complex to strictly real. The motion transitions from under-damped to over-damped.

3.6.1 Checks on viscous solution

A number of checks are performed to verify both the numerical routine as well as the modified boundary conditions (3.66). First, consider the limiting case of a pinned circle-of-contact constraint, $\zeta_2 \to \zeta_1$. In this limit, the 'shape' factor (3.70) tends to zero and the operator equations (3.71,3.77) can be manipulated into the functional equivalent of the Prosperetti (1980*b*) equations for the unconstrained drop. The modified boundary conditions (3.66) are equivalent to the boundary conditions for an unconstrained drop, provided the no-penetration condition (3.12b) is satisfied, which can be accomplished by constructing the appropriate function space. The no-slip condition cannot be satisfied in this limit, which implies 'slip' across the circle-of-contact.

A second check is performed in the limit $\zeta_1 \to -1$, where the spherical-belt constraint is equivalent to the spherical-bowl constraint analyzed by Strani & Sabetta (1988). Figure 3.12 plots the real and imaginary parts of the first three eigenfrequencies as a function of the viscosity parameter ϵ_i for a drop in a vacuum with spherical-bowl constraint. The $n = 2, 3$ eigenvalues bifurcate from complex to real at a critical value of the viscosity parameter, which is smaller for the $n = 3$ mode as compared with the $n = 2$ mode, because there is stronger relative motion between fluid elements as the mode number increases. As can be seen from figure 3.13, which plots the viscous frequencies for a bubble pinned on the south pole

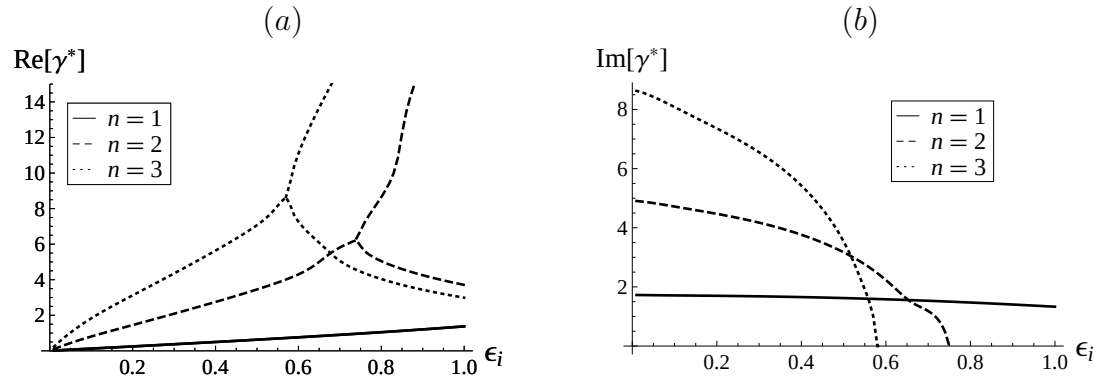

Figure 3.12: Decay rate (a) $\mathrm{Re}[\gamma^*]$ and oscillation frequency (b) $\mathrm{Im}[\gamma^*]$ against viscosity parameter ϵ_i for a viscous drop with spherical-bowl support ($\zeta_1 = -1, \zeta_2 = -0.8$).

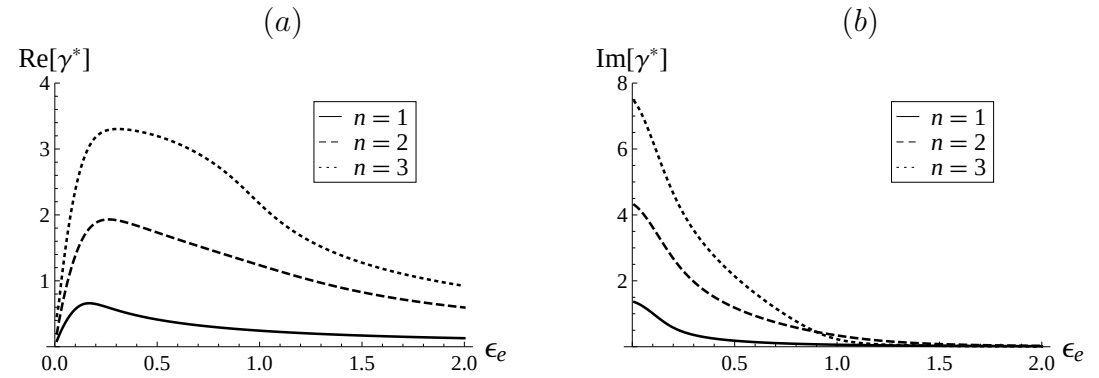

Figure 3.13: Decay rate (a) $\mathrm{Re}[\gamma^*]$ and oscillation frequency (b) $\mathrm{Im}[\gamma^*]$ against viscosity parameter ϵ_e for a bubble pinned at the south pole ($\zeta_1 = -1, \zeta_2 = -0.99$).

($\zeta_1 = -1, \zeta_2 = -0.99$), the transition from under-damped to over-damped motion does not occur for the bubble. Figures 3.12 and 3.13 are in excellent agreement with the results of Strani & Sabetta (1988).

Finally, a spherical-belt constraint is chosen and the complex frequencies are computed for the drop and bubble in figures 3.14 and 3.15, respectively. For reference, the drop mode-shapes for this constraint are plotted in figure 3.16. The

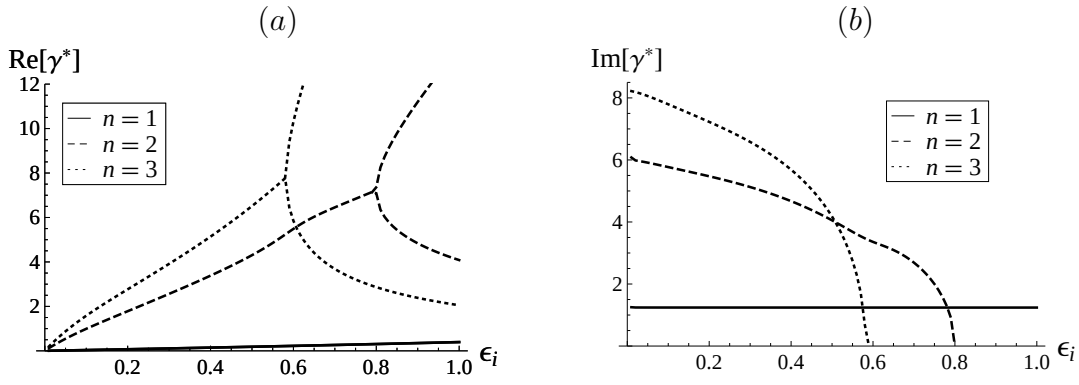

Figure 3.14: Decay rate (a) $\mathrm{Re}[\gamma^*]$ and oscillation frequency (b) $\mathrm{Im}[\gamma^*]$ against viscosity parameter ϵ_i for a drop with spherical-belt support ($\zeta_1 = -0.2, \zeta_2 = 0.4$).

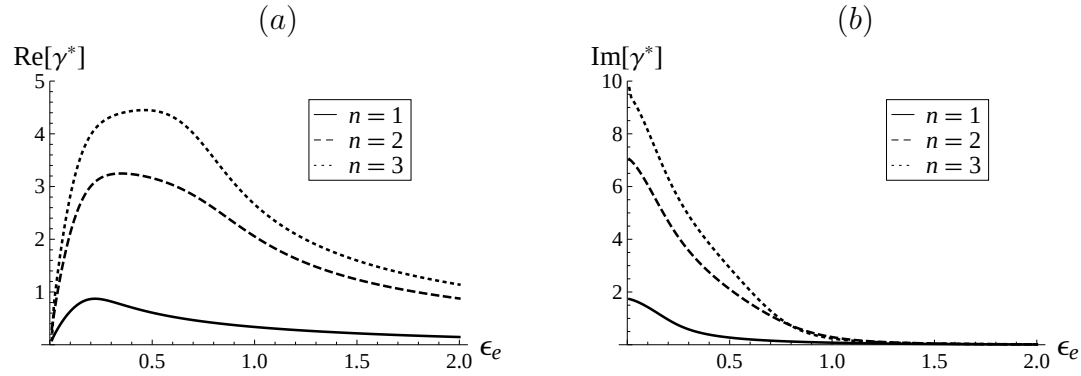

Figure 3.15: Decay rate (a) $\mathrm{Re}[\gamma^*]$ and oscillation frequency (b) $\mathrm{Im}[\gamma^*]$ against viscosity parameter ϵ_e for a bubble with spherical-belt support ($\zeta_1 = -0.2, \zeta_2 = 0.4$).

dissipation arising from relative fluid motion is very apparent when one compares the growth rate of the $n = 1$ mode to the $n = 2, 3$ modes in figure 3.14, where the magnitude is much more pronounced for large mode numbers. To illustrate, consider figure 3.16 which shows very little relative motion for the $n = 1$ mode shape as compared with the $n = 2, 3$ modes.

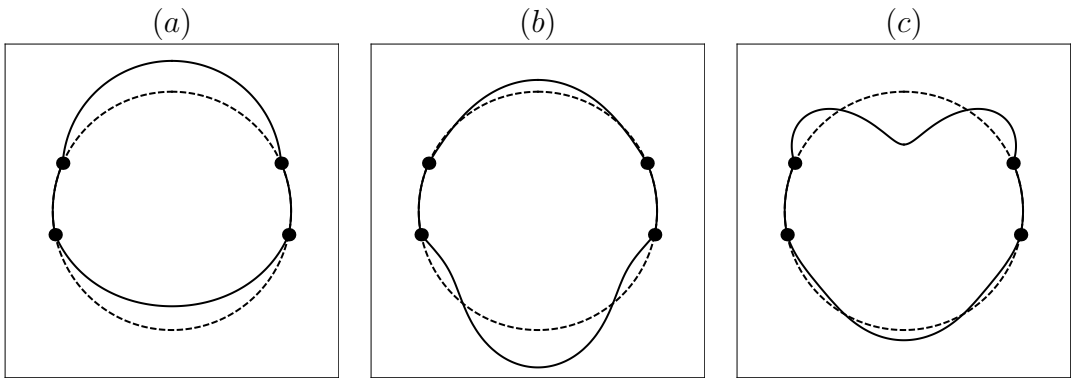

Figure 3.16: Mode shapes (a) $n = 1$ (b) $n = 2$ (c) $n = 3$ for a drop with spherical-belt support ($\zeta_1 = -0.2, \zeta_2 = 0.4$).

3.7 Concluding remarks

The linear oscillations of an immiscible, viscous fluid drop, held by surface tension and supported with a spherical-belt constraint has been considered here. The integro-differential equation governing the interface deformation is formulated as an eigenvalue problem on linear operators. A solution is generated using the variational procedure of Rayleigh-Ritz on a constrained function space. To construct the constrained function space, one can define the interface as the union of the two free and one surface-of-support and restrict 'allowable' solutions to appropriately chosen candidate functions. At this level of generality, the free surface deformations are independent and allowed to communicate, or exchange volume through the region beneath the surface-of-support, but coupled by a conservation of volume constraint.

The formalism developed here treats the two free surfaces independently and allows one to seek solutions in a broad class of functions, giving rise to the possibility of a discontinuous contact-angle across a pinned circle-of-contact constraint, in contrast to Chapter 2, where the contact-angle is necessarily continuous. Compar-

ing the inviscid eigenfrequencies from both studies reveals the drop typically has a discontinuous contact-angle (c.f. figure 3.2). A comparison is made between the spherical-cap model of Theisen *et al.* (2007) and the $n = 1$ 'slow' frequency mode shown figure 3.2(a), where the quantitative agreement is improved by generalizing to discontinuous contact angles.

As the size of the spherical-belt constraint is increased, there are mode crossings, as shown in figure 3.6. These are multiplicities, where two mode share the same frequency. Physically, it has been shown that a transition happens, where the primary volume-carrying mode-shape changes. At these critical belt sizes, the numerical ordering of the eigenvalues is preserved, but the number of 'nodes' or engineering index of the corresponding mode shape changes, in contrast to the classical theory of unconstrained linear operators, where these are coincident. The engineering index, as it depends upon the geometry of the spherical-belt constraint, is shown in figure 3.8. Mathematically, crossings are characterized by an eigenvalue with algebraic and geometric multiplicity of one and two, respectively. Clearly, the presence of the constraint distorts the classical ordering of modes by their index. To address this, an alternative definition of the index is used, whereby there is the possibility of a 'virtual' node within the spherical-belt constraint. The mathematical index reduces to the Rayleigh index.

A perturbed volume embedding is used in conjunction with the variational form of the governing equations to provide useful information with regards to the eigenvalue degeneracy. Namely, it has been shown that coupled, disjoint interfaces oscillate with an effective mass, similar to a system of weakly coupled linear oscillators. Additionally, mode-shapes with equal perturbed-volume exchange correspond to the eigenfrequency degeneracy.

The functional analytic approach used for the inviscid drop has also been used in formulating the viscous operator equation. A set of modified boundary conditions (3.66), valid on the entire interface, were introduced and validated. An indicator function (3.67) is used to track the transition from no-shear to no-slip along the interface. Introduction of the modified boundary conditions allows one to derive the operator equations (3.71) and (3.77), which are reduced to a set of linear algebraic equations and give rise to a nonlinear characteristic equation for the complex eigenvalue γ^*. The eigenvalue solutions bifurcate from complex to real solutions, or under-damped to over-damped motion, at a critical value of the viscosity parameter ϵ for a viscous drop. No such qualitative behavior change occurs for the bubble in a viscous medium and under-damped periodic motion persists. The higher mode-number solutions have a smaller critical viscosity parameter, because these mode shapes have stronger relative motion among fluid elements and equivalently stronger viscous dissipation. As the size of the spherical-belt shrinks, it has been shown that 'slip' occurs across the pinned circle-of-contact. The modified boundary conditions and the results presented here have been validated against previous literature (Strani & Sabetta, 1988; Prosperetti, 1980*b*).

While this work focused on non-trivial interface dynamics of a viscous drop, there exists shear/rotational wave solutions of the governing equations, if one would consider an additional vector potential generating a radial component of vorticity. The extension to these aperiodic motions is straightforward and the methodology is sketched in Appendix C.

CHAPTER 4

STABILITY OF CONSTRAINED CYLINDRICAL INTERFACES AND THE TORUS-LIFT OF PLATEAU-RAYLEIGH

The content of this chapter has been largely disseminated in Bostwick & Steen (*J. Fluid Mech.* (2010), *vol.* 647, *pp.* 201-219)

4.1 Introduction

A cylindrical interface holds an underlying liquid in static equilibrium and is subject to dynamic capillary instability, including Plateau-Rayleigh break-up. Plateau (1863) found instability of the liquid cylinder for lengths longer than the base-state circumference by comparing surface areas of both the disturbed and undisturbed base-state shapes, the well-known Plateau limit. Plateau went on to *incorrectly* interpret this limit as predicting the size of drop resulting from the instability. Extending the work of Plateau, Lord Rayleigh (1879) formulated the linearized hydrodynamic equations and calculated the growth rate as it depends on disturbance wave-number and *correctly* interpreted the wave-number of maximum growth rate from this dispersion relation as giving a good approximation to the final drop size. The Plateau limit is recovered from the Rayleigh result by putting growth rate to zero. Probably for this reason, the Plateau limit is sometimes referred to as the Plateau-Rayleigh limit.

The stability and/or dynamics of constrained cylindrical interfaces are important in a number of applications including coating and casting processes, low-gravity liquid containment, and two-phase heat transfer. For example, in planar-flow melt spinning molten metal is held by surface tension between a stationary

nozzle and a moving substrate (Steen & Karcher, 1997). The upstream meniscus is nearly cylindrical and is part of a full meniscus which takes the shape of a distorted torus. In fact, Rayleigh oscillations of an inviscid sphere capture the wavelength of a defect frozen into the ribbon-product (Byrne *et al.*, 2006). The constrained toroidal geometry used here is potentially relevant to the drop impact problem of Renardy *et al.* (2003), where a toroidal rim, attached to a thin liquid sheet is formed after impact. Similarly, the formation of Edgerton crowns, or the 'crown-splash problem, result from instability of toroidal rims (Deegan *et al.*, 2008).

The stability of cylindrical interfaces constrained by wetting contact with a cylindrical cup of circular cross-section is considered here, figure 4.1. The interface is pinned at contact-lines along the edges of the solid support. The polar angle of contact θ_s defines the extent of the cylindrical-cup constraint. First, using the dynamic approach for inviscid liquids, the modes of instability and dispersion relations are calculated for $0 < \theta_s < 2\pi$, extending previous results obtained by the static approach, much as Rayleigh extended the Plateau result. Next, the cylindrical interface is bent in-plane and required to wet a toroidal-cup constraint, thereby introducing a weak secondary curvature. That is, toroidal interfaces near the cylindrical limit are considered. Unlike the cylinder, the torus is not an equilibrium shape but there exists a near-torus equilibrium shape whose cross-sections are deformed circular arcs. Using a perturbation approach, the static stability of these base-states is calculated, showing that the constraint can either stabilize or destabilize depending on its inside or outside position. Moreover, in the case of stabilization, a base-shape is identified for which the destabilization of the secondary curvature just cancels the stabilization by the wire constraint. That is, the Plateau limit is lifted to the torus. Finally, using the static approach on the torus-lift of

the cylinder, it will be shown that $\theta_s = \pi$ bounds a stability window, where here stability is to *finite-amplitude* disturbances. The argument uses a symmetrization procedure that goes back to Steiner (1882).

It is well-known that constraints can dramatically influence the stability of the Plateau-Rayleigh problem, which is relevant to capillary jets, liquid bridges, columns, ridges and fillet beads, among others. There exists a large volume of literature focused on the static stability of capillary interfaces and the most relevant to this study are mentioned here. Majumbar & Michael (1976) obtain the static stability of a cylindrical meniscus pinned along a horizontal slot, while studying pendant drops. Brown & Scriven (1980) consider the exactly-cylindrical fillet for constant-pressure as well as constant-volume disturbances and report static stability. Langbein (1990) treats the static stability of cylindrical interfaces constrained to wet a V-groove, considering liquid in positions both inside and outside the groove. Roy & Schwartz (1999) also study liquids that partially wet cylindrical 'containers' of a variety of cross-sectional shapes, including planar, V-groove, circular, and elliptical. Their static stability analysis of the circular-arc cross-section base-state recover results of the previous studies and also treat some new substrate geometries. May & Lowry (2008) propose helical and double-helical wire constraints (pinning locus) to support liquid columns and calculate the static stability of resulting interfaces, which may or may not be nearly-cylindrical. Other static stability results can be found in Michael (1981), who has reviewed the static approach.

Despite the fact that static stability results can be recovered from the dynamic approach, the existing literature with regards to dynamic stability calculations is sparse. One such example is given by Myshkis *et al.* (1987) (Section 5.3.4),

who sketches one solution approach for vibrations of an ideal liquid underlying a cylindrical meniscus supported by a V-groove with convex circular bottom, all for natural boundary conditions (contact-angle of $\pi/2$). No dispersion relations or eigenmodes are presented, but static results are recovered: axial disturbances are unstable at half the Plateau-Rayleigh limit and planar disturbances for base-state interfaces greater than semi-circular. In a study of moving contact-lines and rivulets, Davis (1980); Weiland & Davis (1981) considers the stability of a static rivulet of circular-arc cross-section on a horizontal plate. The Davis (1980) study of static rivulets conveniently frames this study even though the moving contact-line is not of interest.

Using the dynamic approach, Davis manipulates the linearized hydrodynamic equations into a balance equation for the 'disturbance energy', from which static stability results are obtained. For example, the boundaries of the instability window for the rivulet with pinned contact-lines is a function of scaled axial wavenumber α and given by

$$\alpha_c^2 = 1 - \frac{\pi^2}{(2\pi - \theta_s)^2}. \tag{4.1}$$

The limiting case of $\theta_s = 0$ corresponds to a cylindrical interface touching the plane along a generator line and yields an upper boundary of $\alpha_c = (3/4)^{1/2}$ (note that the Plateau limit $\alpha_c = 1$ cannot be recovered from (4.1) because of differences in the class of disturbances admitted). In contrast, $\theta_s > \pi$ is a lens-like cylindrical interface resting on a parallel plane; this case is seen to be stable to all lengths. Davis' stability limits recover the constant-volume limits of Brown & Scriven (1980) and Majumbar & Michael (1976), as expected. In the present study, the disturbance energy equations posed by Davis are solved in the case of an inviscid fluid to obtain explicit dispersion relations as well as eigenmode structures for both natural and pinned axial end-plane conditions.

Studies of stability to finite-amplitude disturbances must account for nonlinear effects and, for free boundary problems, the further complication of changes in connectivity. Since any free surface can be plucked to a shape that is nearly pinched off, there are always finite-amplitude disturbances that do not return to the base-state. Restrictions on the size and type of disturbances for finite-amplitude stability results are then to be expected. The characterization of such disturbances depends on the Steiner symmetrization procedure. Whenever the symmetrization is possible, it delivers static stability to a class of finite-size disturbances. When symmetrization is not possible, no conclusion can be made. The problem considered is defined by the radius of the cylinder and its axial extent, the polar extent of the cylindrical-cup constraint, and the fill-ratio of the liquid. A comprehensive treatment would study how results depend on fill-ratio. To keep the focus on ideas and main results, the role of fill-ratio has been suppressed. For the dynamics, full-cylinder volumes (fill-ratio of unity) are considered, while for the torus results the role of volume will be addressed when it appears. For the symmetrization results, volumes such that shape meets the support with common tangent are assumed, although generalization to other volumes clearly would be straightforward.

In the sections that follow, the governing equations are formulated and reduced to linear-operator form, from which a solution is constructed using a Rayleigh-Ritz procedure on a constrained function space. Growth rates and eigenmode structures are then reported. Second, the cylinder is lifted to the torus and the focus is on wire constraints. Unlike the perfect cylinder, the location of the wire constraint affects the stability. Next, symmetrization is used to establish a finite-amplitude stability result for lens-like cylindrical interfaces. Finally, some concluding remarks are offered.

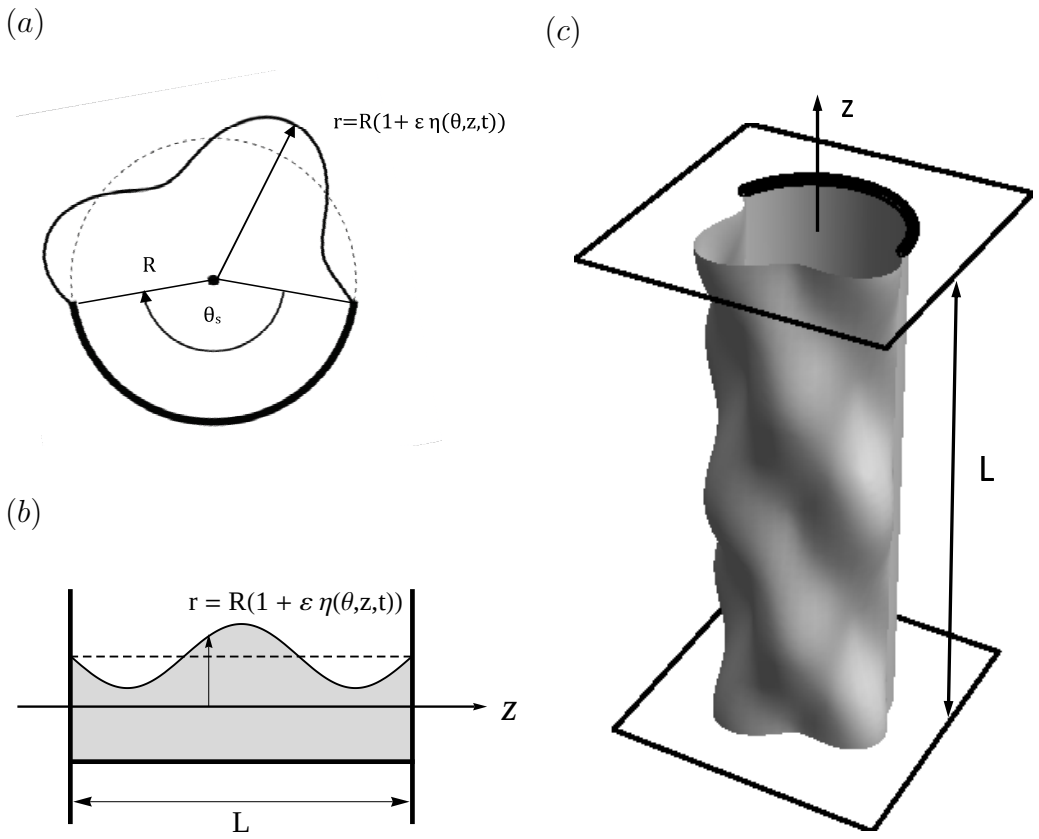

Figure 4.1: Constrained cylindrical interface definition sketch: (a) cross-section with solid support (thick) (b) axial-section with interface pinned at endpoints and (c) 3D view, with sample disturbed interface.

4.2 Formulation of dynamical problem

A cylindrical interface of radius R and axial length L is constrained by a cylindrical-cup solid support, of polar extent $0 \leq \theta \leq \theta_s$ in cylindrical coordinates (r, θ, z), as shown in figure 4.1. The domain of the liquid bridge,

$$D \equiv \{(r, \theta, z) \mid 0 < r \leq R, 0 \leq \theta \leq 2\pi, 0 \leq z \leq L\}, \tag{4.2}$$

is bounded by a free surface (4.3a), the cylindrical-cup support (4.3b) and two solid, parallel end-planes (4.3c);

$$\partial D^f \equiv \{(r,\theta,z) \,|\, r = R, \theta_s \leq \theta \leq 2\pi, 0 \leq z \leq L\}, \tag{4.3a}$$

$$\partial D_1^s \equiv \{(r,\theta,z) \,|\, r = R, 0 \leq \theta \leq \theta_s, 0 \leq z \leq L\}, \tag{4.3b}$$

$$\partial D_2^s \equiv \{(r,\theta,z) \,|\, r = R, 0 \leq \theta \leq 2\pi, z = 0, L\}, \tag{4.3c}$$

$$\partial D^{int} \equiv \partial D^f \cup \partial D_1^s. \tag{4.3d}$$

Additionally, it is also instructive to define the interface as the union of the free surface and cylindrical-cup support (4.3d). The fluid of immersion has no inertia and applies a constant pressure on the interface, while the effect of gravity is assumed to be negligible.

The interface of this incompressible, inviscid fluid is given a small time-dependent disturbance of the form $\eta(\theta, z, t)$. Two classes of end-plane boundary conditions (4.3c) are considered. The first is the 'natural' boundary condition, equivalent to an infinitely-periodic interface, for which the contact-line is free to move with contact-angle $\pi/2$,

$$\left.\frac{\partial \eta}{\partial z}\right|_{z=0,L} = 0, \tag{4.4}$$

while the second is a pinned contact-line

$$\left.\eta\right|_{z=0,L} = 0. \tag{4.5}$$

Furthermore, the linearized interface disturbance is constrained by the integral form of the incompressibility condition, which requires the disturbance to be volume conserving

$$\int_0^L \int_0^{2\pi} \eta\,(\theta, z)\; \mathrm{d}\theta\, \mathrm{d}z = 0. \tag{4.6}$$

4.2.1 Hydrodynamic equations

The flow is assumed to be irrotational and incompressible. Therefore, the velocity field is described by a velocity potential, $\boldsymbol{v} = -\boldsymbol{\nabla}\Psi$, which satisfies Laplace's equation on the domain,

$$\nabla^2\Psi(r,\theta,z,t) = \frac{1}{r}\frac{\partial}{\partial r}\left(r\frac{\partial\Psi}{\partial r}\right) + \frac{1}{r^2}\frac{\partial^2\Psi}{\partial\theta^2} + \frac{\partial^2\Psi}{\partial z^2} = 0 \quad [D]\,. \tag{4.7}$$

The kinematic condition

$$v_r = -\frac{\partial\Psi}{\partial r} = -\frac{\partial\eta}{\partial t} \quad \left[\partial D^f\right] \tag{4.8}$$

relates the radial component of the velocity to the free surface deflection there. Similarly, the no-penetration condition on the surfaces of support require

$$v_r = -\frac{\partial\Psi}{\partial r} = 0 \quad [\partial D_1^s]\,, \tag{4.9a}$$

$$v_z = -\frac{\partial\Psi}{\partial z} = 0 \quad [\partial D_2^s]\,. \tag{4.9b}$$

The pressure field in the fluid domain is determined from the linearized Bernoulli equation

$$p = p_0 + \rho\frac{\partial\Psi}{\partial t} \quad [D]\,, \tag{4.10}$$

where ρ is the fluid density and p_0 is the static pressure required to maintain the fluid's static interface shape. Deviations from equilibrium surface configurations generate pressure gradients, and equivalently capillary-driven flows, described by the Young-Laplace equation,

$$p/\sigma = 2H \equiv \kappa_1 + \kappa_2 \quad \left[\partial D^f\right], \tag{4.11}$$

which relates the principal curvatures, κ_1 and κ_2, of an interface held by surface tension σ to the pressure there. Accordingly, a constant pressure is the criteria for static equilibrium, such as $p_0 = \sigma/R$ for a cylinder.

4.2.2 Normal-mode reduction

The motion of an inviscid fluid, whose cylindrical interface is held by surface tension is governed by the linearized field equations (4.6)-(4.11), which can be reduced to an eigenvalue problem through the use of normal modes. To begin, normal modes

$$\Psi\left(r,\theta,z,t\right)=\phi\left(r,\theta,z\right)\mathrm{e}^{\gamma t},\ \eta\left(\theta,z,t\right)=y\left(\theta,z\right)\mathrm{e}^{\gamma t} \tag{4.12}$$

are substituted into (4.7)-(4.9) to produce a boundary value problem for ϕ

$$\nabla^2\phi(r,\theta,z)=\frac{1}{r}\frac{\partial}{\partial r}\left(r\frac{\partial\phi}{\partial r}\right)+\frac{1}{r^2}\frac{\partial^2\phi}{\partial\theta^2}+\frac{\partial^2\phi}{\partial z^2}=0\quad[D]\,, \tag{4.13a}$$

$$v_r=-\frac{\partial\phi}{\partial r}=-\gamma y(\theta,z)\quad\left[\partial D^f\right], \tag{4.13b}$$

$$v_r=-\frac{\partial\phi}{\partial r}=0\quad[\partial D_1^s]\,, \tag{4.13c}$$

$$v_z=-\frac{\partial\phi}{\partial z}=0\quad[\partial D_2^s]\,. \tag{4.13d}$$

To solve (4.13), consider boundary conditions (4.13b) and (4.13c) as a single boundary condition on the interface (4.3d) and restrict the 'interface' disturbances to have no amplitude on the surface-of-support (4.3b). Such constrained interface disturbances satisfy the no-penetration condition (4.13c) by construction and the solution to (4.13) is given by

$$\phi(r,\theta,z)=-\sum_{m=1}^{\infty}\sum_{l=0}^{\infty}\gamma\frac{2}{\pi^2 m}\frac{I_l\left(\frac{m\pi}{L}r\right)}{I_l'\left(\frac{m\pi}{L}R\right)}\cos\left(\frac{m\pi}{L}z\right)\xi_l\left[B_{lm}\cos\left(l\theta\right)+C_{lm}\sin\left(l\theta\right)\right], \tag{4.14}$$

where

$$\xi_l\equiv\begin{cases}1/2 & l=0\\ 1 & l\neq 0,\end{cases} \tag{4.15a}$$

$$B_{lm}\equiv\int_0^L\int_0^{2\pi}y\left(\theta,z\right)\cos\left(\frac{m\pi}{L}z\right)\cos\left(l\theta\right)\mathrm{d}\theta\,\mathrm{d}z, \tag{4.15b}$$

$$C_{lm}\equiv\int_0^L\int_0^{2\pi}y\left(\theta,z\right)\cos\left(\frac{m\pi}{L}z\right)\sin\left(l\theta\right)\mathrm{d}\theta\,\mathrm{d}z, \tag{4.15c}$$

and I_l is the modified Bessel function of the first kind.

Given the velocity potential solution (4.14) and the normal mode reduction of (4.10,4.11), one may equate the capillary pressure from (4.11) to the inertial pressure from (4.10), evaluated at the interface (4.3d), to give

$$\gamma\left[-\frac{y}{R^2}-\frac{y_{\theta\theta}}{R^2}-y_{zz}\right]=\rho_i\gamma\phi|_{r=R}, \tag{4.16}$$

which is recognized as an integro-differential equation governing the motion of the interface.

4.2.3 Reduction to operator equation

The integro-differential equation (4.16) is reduced to a problem on the polar component of the interface disturbance $y(\theta,z)$ for natural (4.4), and pinned (4.5) end conditions.

Natural wetting condition on endplate

To enforce the natural endpoint condition (4.4), a series solution

$$y\left(\theta,z\right)=\sum_{k=1}^{\infty}A_k\left(\theta\right)\cos\left(k\frac{\pi z}{L}\right), \tag{4.17}$$

is used to reduce (4.16) to an integro-differential eigenvalue problem on $A_k(\theta)$,

$$A_k^{''}+\left(1-\alpha^2\right)A_k=\lambda^2\frac{1}{\alpha\pi}\sum_{l=0}^{\infty}\mathcal{I}_l\left(\alpha\right)\xi_l\left[B_l\cos\left(l\theta\right)+C_l\sin\left(l\theta\right)\right], \tag{4.18}$$

with

$$\lambda^2 \equiv \rho\gamma^2 R^3/\sigma, \tag{4.19a}$$

$$\alpha \equiv k\pi R/L, \tag{4.19b}$$

$$\mathcal{I}_l(\alpha) \equiv I_l(\alpha)/I_l'(\alpha), \tag{4.19c}$$

$$B_l \equiv \int_0^{2\pi} A_k(\theta)\cos(l\theta)\,\mathrm{d}\theta,\ C_l \equiv \int_0^{2\pi} A_k(\theta)\sin(l\theta)\,\mathrm{d}\theta. \tag{4.19d}$$

Equation (4.18) is recast as an eigenvalue problem on linear operators

$$K^n[A_k;\alpha] = \lambda^2 M^n[A_k;\alpha], \tag{4.20a}$$

$$K^n[A_k;\alpha] \equiv A_k'' + \left(1-\alpha^2\right)A_k, \tag{4.20b}$$

$$M^n[A_k;\alpha] \equiv \frac{1}{\alpha\pi}\sum_{l=0}^{\infty}\mathcal{I}_l(\alpha)\,\xi_l\,[B_l\cos(l\theta)+C_l\sin(l\theta)]. \tag{4.20c}$$

Pinned condition on endplate

An analogous operator equation is derived for the pinned endpoint condition (4.5) using a solution series of the form;

$$y(\theta,z) = \sum_{k=1}^{\infty} A_k(\theta)\sin\left(k\frac{2\pi z}{L}\right). \tag{4.21}$$

Substitution of (4.21) into (4.16) produces an integro-differential equation on $A_k(\theta)$, parameterized by axial wave-number k, aspect ratio $\hat{\alpha} \equiv \pi R/L$ and formulated as an eigenvalue problem

$$K^p[A_k;\hat{\alpha},k] = \lambda^2 M^p[A_k;\hat{\alpha},k], \tag{4.22a}$$

$$K^p[A_k;\hat{\alpha},k] \equiv A_k'' + \left(1-(2k\hat{\alpha})^2\right)A_k, \tag{4.22b}$$

$$M^p[A_k;\hat{\alpha},k] \equiv \sum_{m-odd}\frac{64}{\pi^3 m\hat{\alpha}}\left(\frac{k^2}{4k^2-m^2}\right)\times \sum_{l}\mathcal{I}_l(m\hat{\alpha})\,\xi_l\,[B_l\cos(l\theta)+C_l\sin(l\theta)]. \tag{4.22c}$$

Unlike (4.20a), the pinned operator equation (4.22a) is parameterized by the aspect ratio $\hat{\alpha}$ and discrete axial wave-number k.

No-penetration auxiliary condition

Solutions of the natural/pinned operator equations are required to satisfy the incompressibility (4.6) and no-penetration (4.13c) conditions. The solution series for the natural (4.17) and pinned (4.21) endpoint conditions were chosen to satisfy the incompressibility condition (4.6). However, to ensure the no-penetration condition (4.13c), equations (4.20a) and (4.22a) are augmented with the following restriction,

$$A_k(\theta) = 0, \;\; 0 \leq \theta \leq \theta_s. \tag{4.23}$$

This auxiliary condition (4.23) is satisfied by restricting candidate solutions of (4.20a) and (4.22a) to an appropriately chosen function space.

4.2.4 Solution of operator equations

The Rayleigh-Ritz procedure for linear operators (Segel, 1987) is used to solve the natural (4.20a) and pinned (4.22a) operator equations, which have the same structural form. The necessary input to such a procedure is a set of orthonormal basis functions, which span a predetermined function space.

Constrained function space

To construct the constrained function space, begin by considering candidate functions of the form

$$A_k(\theta) = \begin{cases} 0 & 0 \leq \theta \leq \theta_s \\ h(\theta) & \theta_s \leq \theta \leq 2\pi. \end{cases} \tag{4.24}$$

By definition, functions of the form (4.24) satisfy (4.23). To ensure the interface perturbation $A_k(\theta)$ is single-valued, the following conditions are placed on the free surface deformation $h(\theta)$,

$$h(\theta_s) = 0,\ h(2\pi) = 0. \tag{4.25}$$

Next, assume the free surface deformation $y(\theta)$ may be expressed as

$$h(\theta) = \sum_{j=0}^{N} b_j \cos(j\theta) + c_j \sin(j\theta). \tag{4.26}$$

Substituting (4.26) into (4.25) gives

$$\begin{bmatrix} 1 & \cos(\theta_s) & \cdots & \cos(N\theta_s) & \sin(\theta_s) & \cdots & \sin(N\theta_s) \\ 1 & 1 & \cdots & 1 & 0 & \cdots & 0 \end{bmatrix} \begin{bmatrix} b_0 \\ \vdots \\ c_N \end{bmatrix} = \begin{bmatrix} 0 \\ 0 \end{bmatrix}, \tag{4.27}$$

or a set of algebraic equations on the coefficients of the test function series (4.26). There exists $2N-1$ coefficient vectors that solve (4.27), or $2N-1$ linearly independent functions of the form (4.26) that solve (4.25). The Gram-Schmidt orthogonalization procedure and a computer algebra package are used to convert the linearly independent basis functions into a set of orthonormal functions $\{\psi_j(\theta)\}$, which span the constrained function space. For reference, a sample test function ψ is shown in figure 4.2.

Rayleigh-Ritz method

Finally, a solution series

$$A_k(\theta) = \sum_{j=1}^{2N-1} a_j \psi_j(\theta), \tag{4.28}$$

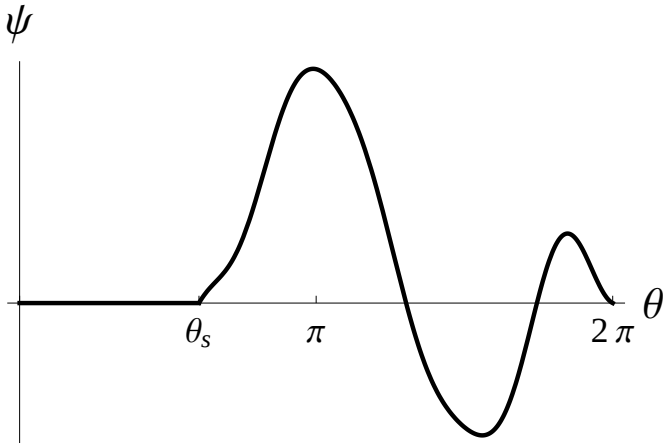

Figure 4.2: Sample orthonormal basis function $\psi(\theta)$

constructed from the orthonormal basis functions ψ_j is used to reduce the eigenvalue operator equation of form $K\left[A_k\right] = \lambda^2 M\left[A_k\right]$ to a matrix equation,

$$K_{ij} a_j = \lambda^2 M_{ij} a_j, \tag{4.29a}$$

$$K_{ij} \equiv \int_0^{2\pi} K\left[\psi_i\right] \psi_j \, \mathrm{d}\theta; \;\; M_{ij} \equiv \int_0^{2\pi} M\left[\psi_i\right] \psi_j \, \mathrm{d}\theta. \tag{4.29b}$$

The eigenvalues and eigenvectors of (4.29a) are readily computed using standard numerical routines. Eigenvalues and eigenvectors are specified by integer pairs $[l, k]$, the polar and axial wave-numbers, and both depend on the continuous aspect ratio $\pi R/L$. The polar wave-number is simply the number of intersections plus one of the disturbed circle with undisturbed circle (c.f. Figure 4.7). Given an eigenvector $a_j^{(r)}$ of (4.29a), the corresponding eigenfunction is

$$A_k^{(r)}(\theta) = \sum_{j=1}^{2N-1} a_j^{(r)} \psi_j(\theta). \tag{4.30}$$

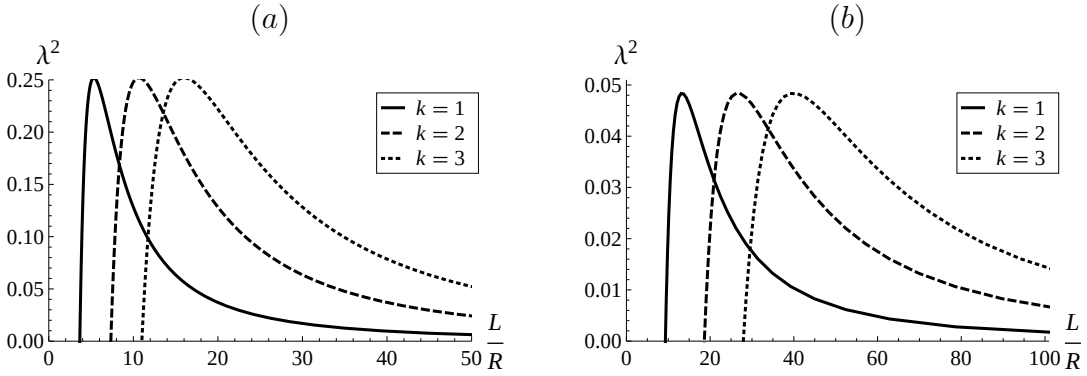

Figure 4.3: Growth rate of most unstable polar mode $[1, k]$ vs. aspect ratio L/R (a) for $\theta_s = 0.01$ with natural conditions and (b) for $\theta_s = 2.0$ for pinned conditions.

4.3 Results for a constrained cylindrical interface

The eigenvalues/eigenmodes of the operator equations (4.20a) and (4.22a) are computed using standard numerical routines for a fixed constraint size θ_s. All eigenvalues presented here show convergence to within 0.1%, when 13 terms ($N = 7$) have been used in the solution series (4.28).

The eigenvalues for the most unstable ($\lambda^2 > 0$) polar mode ($l = 1$) depend on the aspect ratio as shown in figure 4.3, for various axial wave-numbers k. As seen from the natural operator (4.20a), L/R and k are not independent and the separate curves collapse onto a single curve by scaling. In contrast, because L/R and k appear separately in the pinned operator (4.22a), they appear to be independent but the same scaling also collapses the curves in figure 4.3(b) so, in fact, they are not independent.

Relative to the natural end-plane constraint, the pinned end-plane constraint always increases static stability α_c by a factor of two, which is shown for the

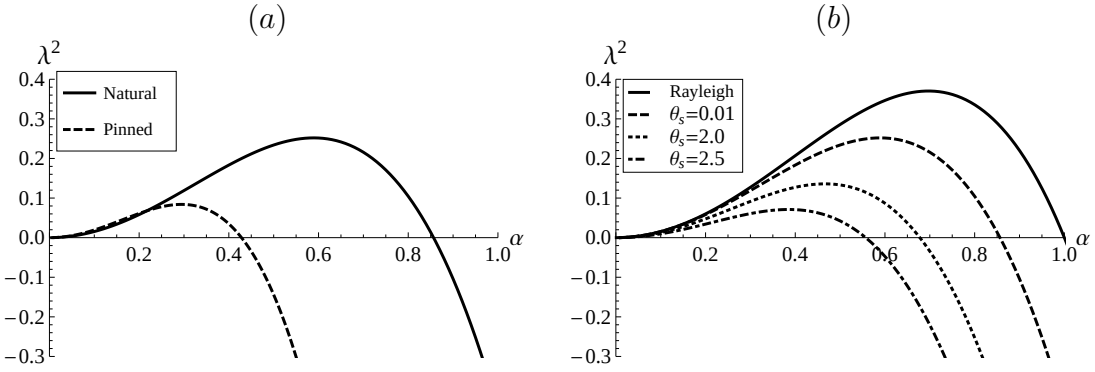

Figure 4.4: Dispersion relation of $l = 1$ modes (a) for $\theta_s = 0.01$ with natural and pinned conditions and (b) for varying θ_s for natural conditions. Rayleigh dispersion, for reference.

touching wire in figure 4.4(a). Increasing the extent of polar constraint also always stabilizes, as shown for the natural conditions in figure 4.4(b). These static stability results are summarized in figure 4.5. The curve for natural end conditions on figure 4.5(a) recovers equation (4.1) and could be read off figure 4.4(b). The pinned curve on figure 4.5(a) is the natural curve scaled by a factor of two. This relationship between the pinned and natural stability limits is seen again in figure 4.5(b), which plots the static limit as it depends on the length and polar constraints, the so-called stability envelope. There, the $k = 1$ pinned and $k = 2$ natural curves collapse to a single curve and the $k = 1$ pinned and $k = 1$ natural curves differ by a factor of two. Indeed, the four curves of figure 4.5(b) all collapse onto a single curve. They have plotted separately to compare directly to the natural end-constraint results of Brown & Scriven (1980), with which they are in agreement. The convergence of eigenvalue/eigenmodes and the recovery of a range of static stability results are tests that validate the computations.

Each dispersion relation seen in figure 4.4 exhibits a fastest growing mode with corresponding aspect ratio which, following Rayleigh, can be interpreted as an es-

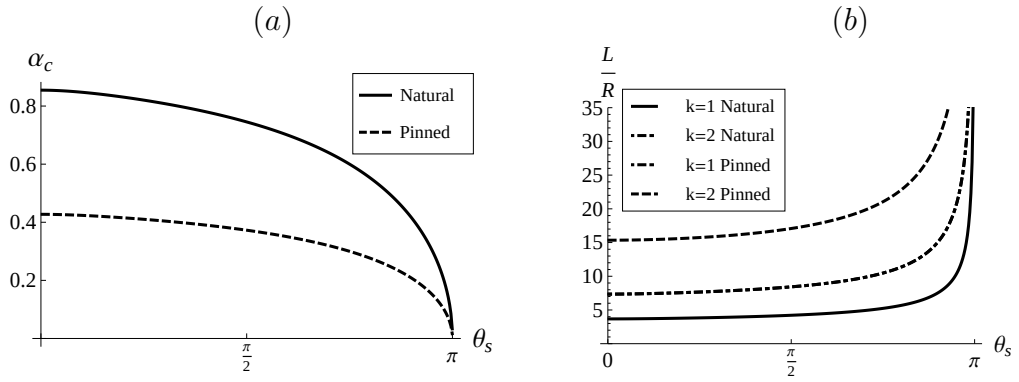

Figure 4.5: Static stability against polar constraint θ_s measured by (a) wave-number α_c or (b) envelope of stable L/R (below curve).

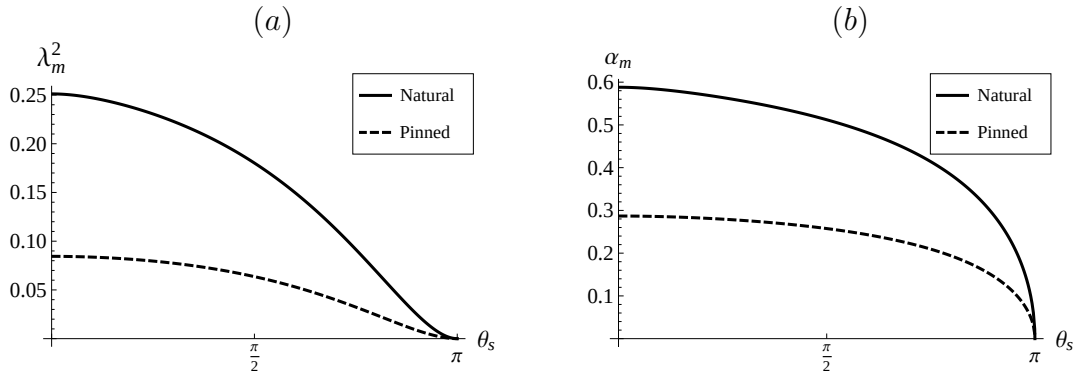

Figure 4.6: (a) Growth rate λ_m^2 and (b) wave-number α_m against polar constraint for fastest growing mode.

timate for the bead size which results from the breakup instability. Figure 4.4(b) shows that the maximum growth rates of the unstable modes are smaller than that for the corresponding unconstrained Rayleigh jet ($\lambda_{Ray}^2 = 0.343$). The Rayleigh dispersion relation is plotted for reference. Figure 4.6 summarizes the maximum growth rates (fig. 4.6(a)) and corresponding aspect ratios (fig. 4.6(b)) as they depend on extent-of-support. Figure 4.7(a) illustrates the mode shape of a pinned-end disturbance, unstable when unconstrained, but stabilized by a cup that is 63.7% of the critical cup (π). For the same constraint, figure 4.7(b) shows the

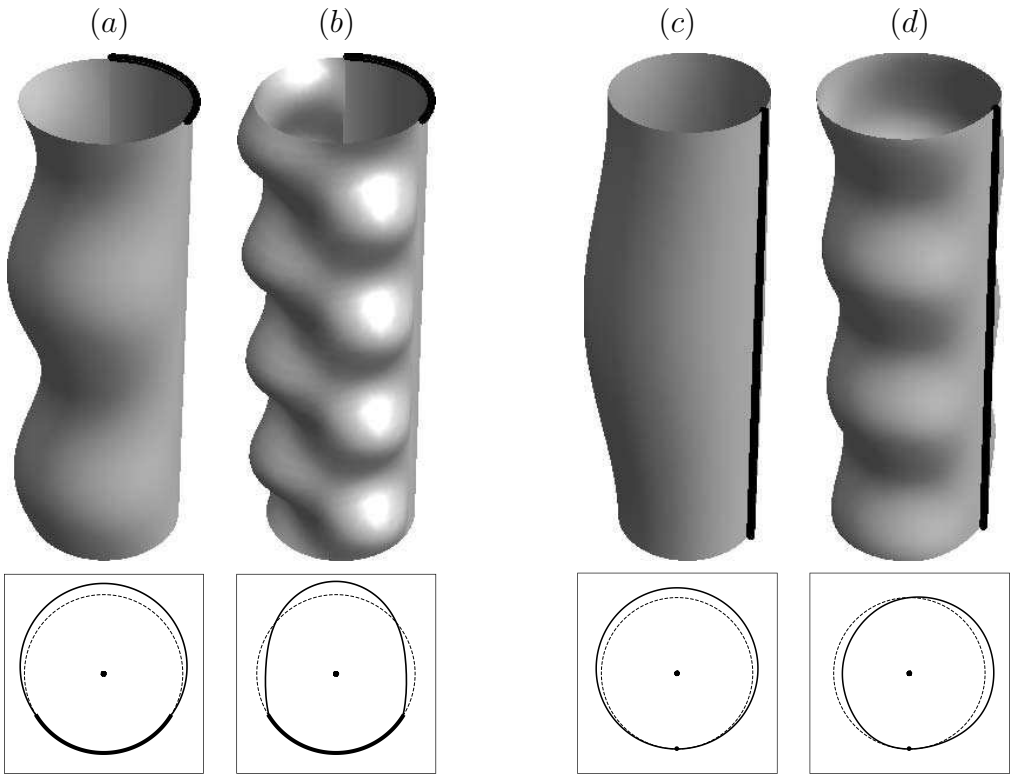

Figure 4.7: Modes $[l, k]$ in 3D and polar projection for $L/R = 2\pi$ with (a, b) $\theta_s = 2.0$ and pinned conditions for (a) [1,1] and (b) [3,2] and (c, d) $\theta_s = 0.01$ and natural conditions for (c) [1,1] and (d) [2,3].

stable $[3, 2]$ vibrational mode. Increasing the polar constraint stabilizes, as mentioned. However, slower growing unstable modes remain and such a mode shape is illustrated in figure 4.7(c) for natural-end conditions in the presence of a wire constraint. For reference, figure 4.7(d) shows the $[2, 3]$ vibrational mode (stable) for a wire constraint.

Explicit knowledge of the inertia operator $M[y]$ is needed to determine the spectrum of the eigenvalue problem (4.29a), but is not necessary to show static stability, provided one can show $(M[y; \alpha], y) > 0$ for $y \neq 0$. Indeed, if $M[y; \alpha]$ is positive definite, the curvature operator $K[y; \alpha]$ determines the sign of the eigenvalues and may be used to determine the static stability limit α_c. Positive-definiteness

of M is straightforward to show and the argument is sketched. Applying Green's first identity to the velocity potential $\phi(\mathbf{x})$ on the domain D, results in an integral over the domain and its boundary,

$$\int_{\partial D} \phi \left(\nabla\phi \cdot \mathbf{n}\right) \mathrm{d}S = \int_{D} \left[\phi\nabla^2\phi + \nabla\phi \cdot \nabla\phi\right] \mathrm{d}V. \tag{4.31}$$

The domain integral is evaluated using $\nabla^2\phi = 0$. The boundary integral is evaluated using $\phi|_{\partial D} = M\,[y]$, which follows from the linearized Bernoulli equation, and using $\nabla\phi \cdot \mathbf{n} = y$, which follows from the kinematic condition.

For the axial and polar constraints considered so far, narrowing the class of disturbances enhances stability. Next, the class of equilibrium states is enlarged to show that, relative to the cylindrical cap interface, constraint can be stabilizing or destabilizing.

4.4 Lifting the cylinder to the torus

The torus with surface-of-revolution constraint is of interest, c.f. figure 4.8. The torus is described using a standard parametric representation (Kreyszig, 1991),

$$x = (R + a\cos\theta)\cos\varphi,\ \ y = (R + a\cos\theta)\sin\varphi,\ \ z = a\sin\theta. \tag{4.32}$$

The torus is a near-cylinder for $\epsilon \equiv a/R \ll 1$ and, in the limit $\epsilon \to 0$, a cylinder with axial periodicity. An in-plane bending of the constraint introduces a secondary curvature, controlled by ϵ. A straightforward calculation of the mean curvature H of the torus (4.32) shows that it varies with θ according to $a(2H) = 1+\epsilon(\cos\theta/(1+\epsilon\cos\theta))$. A non-constant mean curvature does not satisfy the Young-Laplace law and, hence, the torus surface is not in capillary equilibrium. However, for the near-cylindrical torus, a near-toroidal shape can be found that is an equilibrium shape

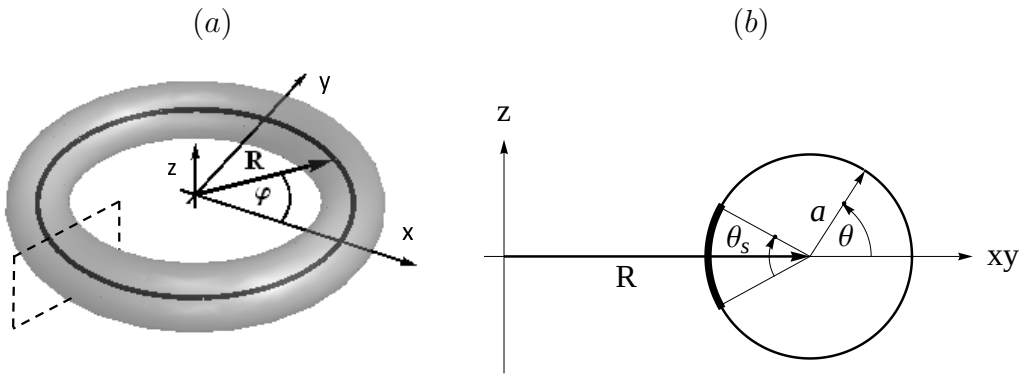

Figure 4.8: Torus sketch in (a) 3D view and in (b) polar view with cup support (thick line).

provided that the shape is constrained. It turns out that such a constraint must be symmetric about the $z = 0$ mid-plane. For this reason, constraints symmetric about the mid-plane and subtending an angle θ_s are considered. The constraints in focus are directly analogous to those considered for the cylinder. This constraint is either 'inside' (as in figures 4.8 and 4.10(b)) or 'outside' (as in figure 4.9(b)) relative to the origin. In the limiting case $\theta_s = 0$, the constraint is a wire. In the further limit of $\epsilon = 0$, the perfect cylinder is recovered and the distinction between inside and outside is lost.

The family of near-toroidal equilibrium shapes is referred to as the 'torus-lift of the cylinder'; the family is parameterized by ϵ. The torus-lift is of interest for two different kinds of results, both regarding static stability. First, the stability of the torus-lift to small disturbances for the case of inner and outer wire constraints is calculated. This suffices to demonstrate the destabilizing and stabilizing nature of the inner and outer constraints, respectively. Second, Steiner symmetrization on the torus-lift is applied to cylindrical lens-like shapes ($\theta_s > \pi$) to demonstrate stability to finite-amplitude disturbances. The limiting case $\theta_s = \pi$ is seen to be a 'hard' stability boundary.

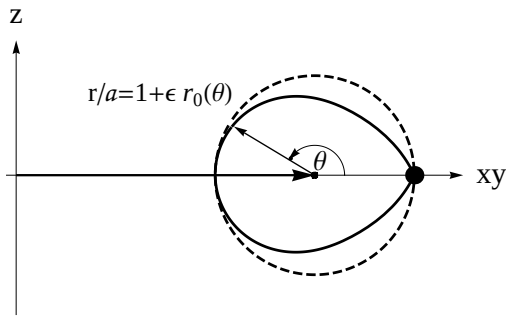

Figure 4.9: Torus equilibrium shape $r_0(\theta)$ with unit-circle (dotted) for reference.

4.4.1 Near-toroidal equilibrium shapes

Lengths can be scaled by a so small deformations take the form (c.f. figure 4.8),

$$r/a = 1 + \epsilon r_0(\theta). \tag{4.33}$$

Here, in view of the mean curvature of the perfect torus, shapes depending only on θ are anticipated. The strategy is to seek near-toroidal shapes that just cancel the curvature of the torus. At order ϵ, the near-cylindrical and near-toroidal curvatures are found to be $\cos\theta/a$ and $-(r_0 + r_0^{''})/a$, respectively. Hence, to this order, equilibrium is maintained provided,

$$r_0^{''} + r_0 = \cos\theta. \tag{4.34}$$

Solution to (4.34) is given by

$$r_0\,(\theta) = 1/2\;(\theta - \pi)\sin\theta, \tag{4.35}$$

where boundary conditions symmetric about the mid-plane corresponding to the outer wire constraint have been enforced. This particular shape, which has a corner at the wire ($\theta = 0, 2\pi$), is shown in figure 4.9. The corner may be shifted from the outer to the inner position by redefining the polar surface coordinate $\theta \to \theta - \pi$ and using an alternative solution to (4.34), $r_0 = 1/2(\theta - \pi)\sin(\theta - \pi)$.

Note that a slightly larger class of solutions would be obtained by adding a constant to the right-hand-side of (4.34). This corresponds to allowing near-toroidal equilibrium shapes with 'constant' mean-curvatures, of a different 'constant' than the cylinder. Physically, this amounts to an adjustment of the volume of liquid. In summary, if one demands that the volume of the equilibrium shape be the same as that of the corresponding near-cylindrical shape, it can be arranged, although there is no fundamental reason to do so. Finally, volumes can be easily calculated by Pappus' theorem knowing the centroid of the plane figure and its planar area.

4.4.2 Stability of near-toroidal equilibrium shapes

The equilibrium shape is perturbed by an amount δ of the form $r_1(\theta, \varphi)$

$$r/a = 1 + \epsilon r_0 + \delta r_1(\theta)\, \mathrm{e}^{iq\varphi}, \tag{4.36}$$

where q is the toroidal azimuthal wave-number. The disturbance must remain smaller than the deviation from the cylinder, $\delta \ll \epsilon$. Note that the disturbance preserves volume of the equilibrium state.

Static stability of the base-state is determined by the order δ deviation of the mean curvature. This deviation, as it depends on ϵ, is formulated as an operator

$$\begin{aligned} K[r_1; \alpha, \epsilon] \equiv (2H)_\delta = &\left[(1+\epsilon\cos\theta)^2 + \epsilon^2\cos\theta - \alpha^2\right] r_1 \\ &\mp\epsilon\sin\theta\,(1+\epsilon\cos\theta)\, r_1' + (1+\epsilon\cos\theta)^2 r_1'' - \epsilon^2 (1+\epsilon\cos\theta)^2 F[\theta], \end{aligned} \tag{4.37}$$

where $\alpha = qa/R$ is the scaled wave-number and

$$F[\theta] \equiv \frac{1}{16}\left[-3 - (\theta-\pi)^2 + \left((\theta-\pi)^2 - 13\right)\cos 2\theta + 14\,(\theta-\pi)\sin 2\theta\right]. \tag{4.38}$$

Allowable solutions of (4.37) are subject to the no-penetration condition along the wire constraint,

$$r_1(\theta = 0, 2\pi) = 0. \tag{4.39}$$

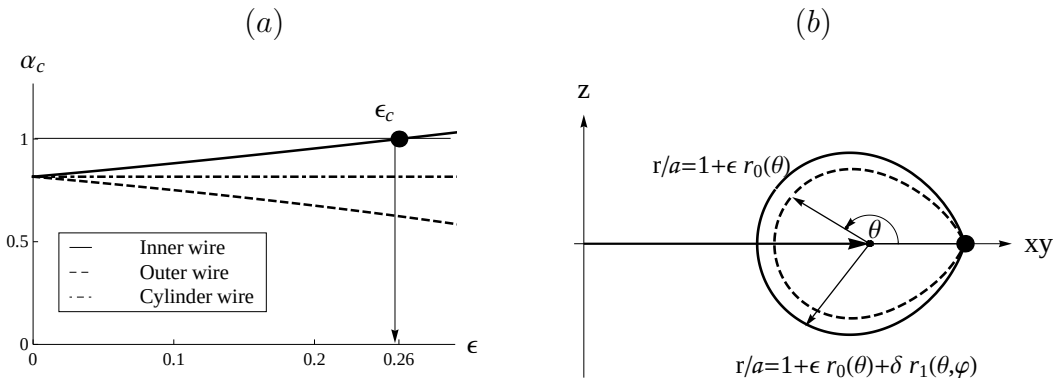

Figure 4.10: Stability of toroidal equilibrium shapes showing (a) static limit α_c against deviation from cylinder ϵ and (b) typical destabilizing mode shape, with equilibrium shape (dotted) for reference.

The $\mp$ signs in (4.37) denote a torus with an outer or inner wire constraint, respectively.

Static stability is determined by the sign of the curvature operator $(K[y;\alpha],y)$, where the surface disturbance y belongs to an appropriate function space. Allowable surface disturbances to the torus must satisfy (4.39), which are structurally identical to the free surface disturbances of the cylinder with a wire constraint. Therefore, the solution series (4.28) derived earlier can be used as the input to the Rayleigh-Ritz procedure on the curvature operator (4.37) for the torus. Also note that, the curvature operator (4.37) reduces to the curvature operator for the cylinder (4.20b) in the limit $\epsilon \to 0$.

Given α and ϵ, the spectrum of $K[r_1;\alpha,\epsilon] = \lambda^2 r_1$ is readily computed using the Rayleigh-Ritz procedure. For secondary curvature ϵ, the critical wave-number α_c is computed by iterating over α and locating where the unstable eigenvalue changes sign.

Figure 4.10(a) plots the critical wave-number vs. secondary curvature for a torus with a wire constraint placed on the inner and outer extrema, while fig-

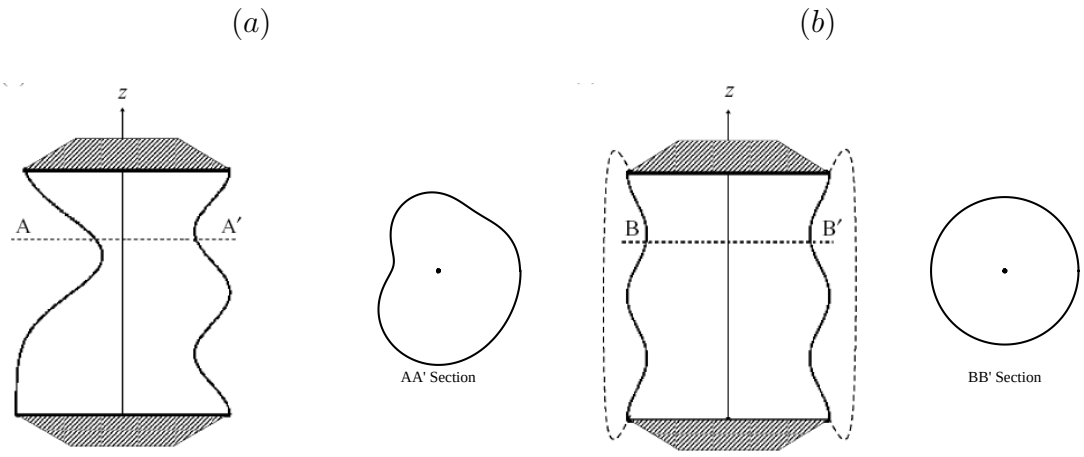

Figure 4.11: Symmetrization of general shape proceeds from (a) non-circular slice AA′ to (b) circular slice BB′ with reassembly to axisymmetric shape.

ure 4.10(b) displays the polar projection of the instability mode shape. As shown in figure 4.10(a), the location of the wire constraint can have either a stabilizing (outer pin) or destabilizing (inner pin) effect, when compared to the wire-constrained cylinder. For the inner pin, as the secondary curvature increases, a cancelation occurs at $\epsilon_c = 0.26$, where the destabilizing effect of the secondary curvature exactly cancels the stabilization of the wire inherited from the cylinder. The toroidal equilibrium shape of this size with inner wire constraint will have precisely the Plateau-Rayleigh limit. The validity of the expansion to ϵ_c and beyond is plausible in view of the linear dependence seen in figure 4.10(a) but has not been investigated further.

4.4.3 Symmetrization and large-amplitude stability of the lens meniscus

To illustrate symmetrization and its relationship to stability, consider a liquid bridge spanning end-plates where it is pinned along circular contact-lines, figure 4.11. Symmetrization starts with the non-symmetric shape, figure 4.11(a) and ends with the axisymmetric shape, figure 4.11(b). First, take a 'constant z' cut to obtain the plane figure of section AA$'$. This AA$'$ figure encloses a planar area. The perimeter of this figure is then minimized, for fixed planar area, to obtain a circle, section BB$'$. This circle is then reassembled with the circles from other sections, aligning centers, to yield the axisymmetric shape, figure 4.11(b). Symmetrization establishes a mapping from non-axisymmetric to axisymmetric shapes. Gillette & Dyson (1972) proved that this mapping preserves volume while decreasing surface-area. One should note that their proof doesn't preclude shape differences of finite amplitude. They applied their result to small non-axisymmetric disturbances to conclude that for axisymmetric bridge base-states, single-valued in radial coordinate, it is sufficient to consider axisymmetric disturbances when testing for stability. That is, if an equilibrium configuration is statically unstable to a non-axisymmetric disturbance, then it is unstable to an axisymmetric disturbance.

Note that the procedure fails if the disturbance section AA$'$ is not simply-connected. Such sections certainly occur for base-states that are multiple-valued in radius, as for the dotted shape in figure 4.11(b) with slice taken above the top plate. Shapes with tangents to the endplates are the limiting shapes, known as the 'rotund limit' (Russo & Steen, 1986). Separate analysis assuming small amplitudes have shown that, beyond the rotund limit, non-axisymmetric disturbances are in fact destabilizing (Slobozhanin *et al.*, 1997). Hence, failure of the procedure

corresponds to a sharp bound. Finally, note that the procedure succeeds even with a solid internal boundary, such as a rod spanning the endplates, as long as the base-state and disturbances maintain a fully-wetted internal boundary. This occurs, of course, since it is increases/decreases in the liquid/gas surface area only that alter the energy. To use the Gillette & Dyson result for cylindrical interfaces, the cylinder is lifted to the torus.

Symmetrization of the liquid bridge uses a cylindrical coordinate system and takes plane slices orthogonal to the generator axis, which shall be denoted the *symmetrization-axis*, (c.f. figure 4.1). Symmetrization can proceed if the slices yield a simply-connected planar figure. This occurs precisely when starting with a single-valued volume-enclosing shape. This motivates the notion of finite-amplitude 'admissible' interfaces – interfaces that are single-valued in the radial direction relative to the symmetrization-axis. To obtain stability results, both base-state and disturbances must be admissible.

The equilibrium interfaces of the torus-lift family are admissible for $\theta_s > \pi$ and a range of volumes. These are lens-like meniscus shapes. Recall the Gillette & Dyson result: symmetrization maps non-axisymmetric shapes onto axisymmetric shapes of the same volume but with lesser surface area (GD reduction theorem). This applies directly to the torus-lift. Hence, to obtain stability to general volume-preserving admissible disturbances, it is *sufficient to consider axisymmetric disturbances,* relative to the symmetrization axis. These are the most dangerous. This reduces the full 3D problem to a 2D planar one. Of course, the reduction fails for multiple-valued base-states; these do occur for $\theta_s < \pi$ and a filling ratio of unity. It should be noted that volume, an independent parameter, is taken to be the filling volume here. The filling-volume is that volume whose equilibrium shape meets the

constraint at the contact-line tangentially. Clearly, for a fixed $\theta_s < \pi$, there will be a range of volumes (low) that have single-valued and a range (modest to high) that have double-valued equilibrium shapes.

Symmetrization of the torus-lift can deliver *general* large-amplitude stability results in the limit of the cylindrical-lens meniscus, figure 4.12. That is, in the cylindrical limit $\epsilon = 0$, the toroidal equilibrium shapes reduce to cylindrical cap shapes and, for $\theta_s > \pi$, these are cylindrical lenses. The GD reduction theorem applies to each $\epsilon > 0$ and thus holds in the limit $\epsilon = 0$. The toroidal equilibrium shape is relatively stable to axisymmetric disturbances (finite-amplitude, admissible, volume-preserving) and, hence, the cylindrical lens is relatively stable to disturbances varying in parallel cross-sections, figure 4.12(a). It is left to show that the lens is also relatively stable to disturbances in the transverse plane. his follows by choosing a new symmetrization axis – the axis of the cylindrical meniscus – for which slices are transverse cross-sections, figure 4.12(a), and applying the GD theorem again. One then concludes that disturbances with variations along parallel cross-sections are most dangerous. Together, the results from orthogonal symmetrization procedures, delivers the result; the cylindrical lens is stable to general large-amplitude volume-preserving admissible disturbances. It remains to state this result formally.

Disturbance class. *'Admissible' interface shapes are those with parallel and transverse cross-sections that are simply-connected.* (An equivalent definition is those shapes that are single-valued in the radial coordinate, relative to both symmetrization axes; that is, both parallel and transverse slices give single-valued shapes.)

Figure 4.12(b) illustrates a large-amplitude disturbance (transverse section)

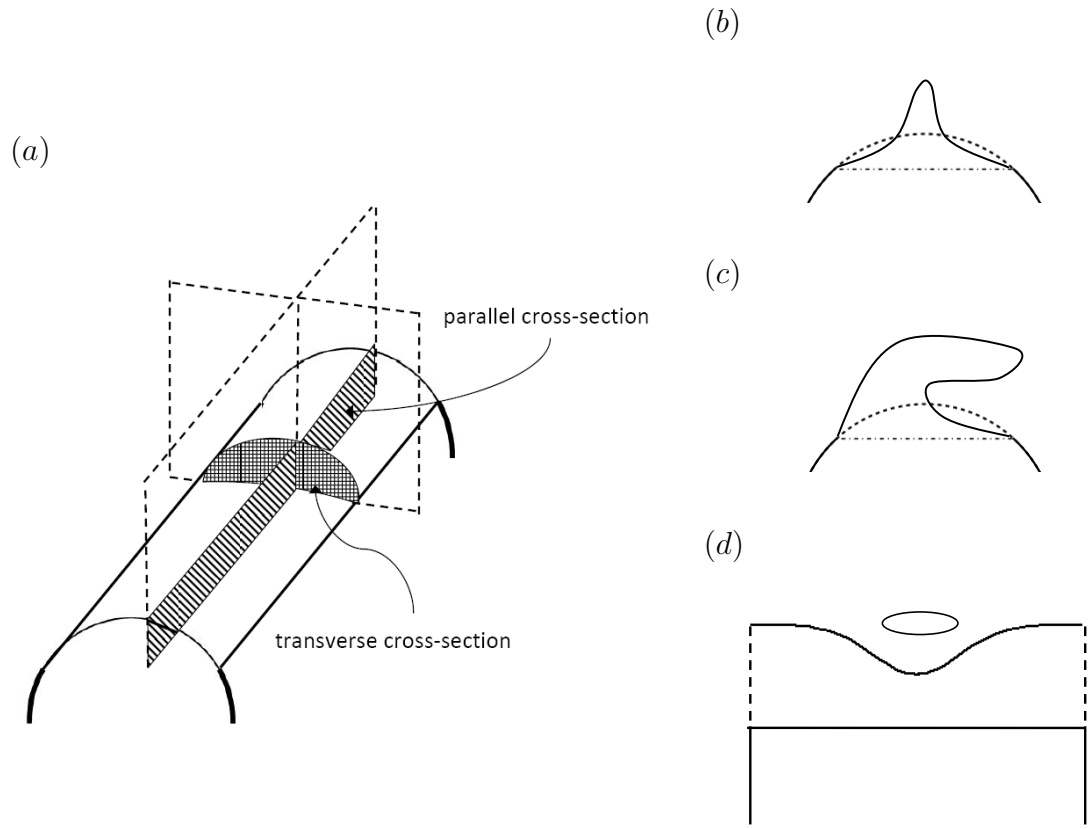

Figure 4.12: Symmetrization of lens meniscus using (a) parallel and transverse cross-sectional slices in 3D view; sketches of large-amplitude disturbances that are (b) admissible (in transverse section), or (c, d) inadmissible (c) in transverse section, (d) in parallel section.

that is admissible while figures 4.12(c, d) give orthogonal views of an inadmissible disturbance.

Theorem 1 *The cylindrical interface of cylindrical volume, constrained by solid support $\theta_s > \pi$ with pinned contact-lines, is statically stable to arbitrarily large volume-preserving disturbances as long as the disturbances are admissible and preserve wetted area-of-contact with the solid support.*

This theorem is proved by observing that i) the GD reduction theorem applies to large-amplitude disturbances, ii) the GD reduction applies to the lens-like toroidal equilibrium states (inside constraint), iii) the toroidal azimuthal coordinate becomes the cylindrical axial coordinate in the cylindrical limit of the torus, and that iv) the GD reduction also applies with the toroidal axial coordinate as symmetrization axis. In summary, the cylindrical lens base-state admits symmetrization in two orthogonal directions, by which it is found to be globally stable to admissible disturbances. Theorem 1 says that $\theta_s > \pi$ is *sufficient* for stability of the cylindrical interface while the linear stability results in the literature show that $\theta_s \geq \pi$ is also *necessary* for stability since, for $\theta_s < \pi$, small disturbances that destabilize have been exhibited.

4.5 Concluding remarks

Constraint tends to stabilize, whether via end-plane (axial) or lateral-cup (polar). To the extent that a constraint narrows the class of disturbances to which a base-state is subject, this stands as a principle. In going from the natural to the pinned end-plane conditions, the instability window is narrowed by a factor of two no matter the extent of the cup constraint. Likewise, in going from the unconstrained cylinder (Plateau-Rayleigh) to the cylinder touching a wire, the instability window is narrowed by 13%. Increasing θ_s narrows the instability window further until it disappears at $\theta_s = \pi$ and beyond which it remains closed. In contrast, bending the cup constraint into a torus configuration can either stabilize or destabilize depending on whether the cup is placed on the inside or outside of the bend. Bending creates two new families of equilibrium states. For each member of these families, increasing the constraint will enhance stability, while relative to the constrained

cylinder the new family can be more or less stable. It has been shown how the destabilization of bending curvature can cancel the stabilization of the wire to yield the same critical value as occurs for the Plateau-Rayleigh instability. All these are small-amplitude static results.

The torus-lift of the cylinder allows one to prove a large-amplitude stability result for cylindrical lens interfaces ($\pi < \theta_s < 2\pi$). Large disturbances, just so they are single-valued, are statically stable. This may provide important insight for application. For example, one way to discourage multiple-valued disturbances is to limit the liquid volume. Furthermore, as a tool for obtaining finite-amplitude results, the symmetrization technique may well be useful to a broader class of interfacial stability problems.

As regards dynamics, the disturbance equations posed by Davis (1980) are solved in the special case of an inviscid liquid when the liquid is pinned along the edges of the circular-cup and of a volume that just fills the circular section. An integro-differential equation has been derived for both natural and pinned axial constraints. The governing equation is formulated as an eigenvalue problem on linear operators, from which a solution is constructed using a Rayleigh-Ritz procedure. The eigenvalues/eigenmodes are dependent upon the polar constraint and have been computed from a truncated set of linear algebraic equations using standard numerical routines.

The lens-like interfaces are always stable; only oscillatory motions occur. For the drop-like interfaces, only the eigenmode with smallest polar wave-number $l = 1$ exhibits instability and that for a range of axial wave-numbers. The polar constraint stabilizes axial wave-numbers that are unstable for the Plateau-Rayleigh cylinder, as mentioned. The constraint also slows the growth rate of the unsta-

ble modes but the slowing of growth rates does not scale in the same manner as the static limit stabilization. For example, the disturbance with fastest growth rate for the natural end-point conditions grows nearly three times as fast as that of the corresponding pinned end-point mode. The cylinder-against-a-wire illustrates the influence of constraint. Compared to Rayleigh break-up, the fastest growing disturbance is 18% longer suggesting about a 6% increase in final droplet size. What might be easier to distinguish in experiment is that the characteristic time to break-up is nearly 40% longer for the wire constraint as compared to the unconstrained Rayleigh break-up.

CHAPTER 5

STABILITY OF THE SESSILE DROP: CONTACT-LINE DYNAMICS AND SYMMETRY BREAKING

5.1 Introduction

The natural oscillations of the sessile drop are of fundamental interest in a number of industrial applications, such as coating processes, ink-jet printing and spray-cooling via drop-atomization. In contrast to the free drop, which has been studied extensively since the time of Lord Rayleigh (1879), the existing literature on the sessile drop is sparse and particularly so for analytical-based solution methods. This occurs because supported drops possess less symmetry than free drops. Many authors have extended the pioneering work of Lord Rayleigh, who considered the linear oscillations of an incompressible, inviscid free drop. Lamb (1932) has used the irrotational solution to compute the dissipation and equivalently the decay-rate of free viscous drops. Much later, the viscous correction to the oscillation frequency under the irrotational assumption was reported by Padrino *et al.* (2007). They compare the spectrum of the free viscous drop computed using the irrotational approximation to that using viscous potential flow theory (Joseph, 2006). In the limit of small viscosities, the irrotational approximation is shown to be quite satisfactory and compares well with the exact solution of the linearized viscous problem proposed by Miller & Scriven (1968) and computed by Prosperetti (1980*b*). The aforementioned results have assumed the interface disturbances are small. With regards to finite-amplitude disturbances, Tsamopoulos & Brown (1983) use a domain perturbation method to show that the characteristic frequencies of the free drop decrease with the square of the amplitude in the moderate-amplitude regime.

Trinh & Wang (1982) have shown experimentally that a further increase in amplitude can lead to drop break-up. This has been verified numerically by Lundgren & Mansour (1988), who use a boundary-integral method to identify the large-amplitude states that precede this type of break-up. In general, large amplitude oscillations are handled using computational-based approaches, such as those developed by Patzek *et al.* (1991) for inviscid free drops.

Interest in the dynamics of supported drops, in contrast to free drops in zero-gravity environments, can be attributed to a number of terrestrial applications. One of the first works in the subject was the experimental study of Rodot *et al.* (1979), who were concerned with characterizing the frequency and mode shape of the supported drop as a function of the material parameters and support geometry. This investigation was followed by the theoretical study of Strani & Sabetta (1984, 1988), who considered both inviscid and viscous drops under an idealized spherical-bowl constraint. Here the choice of support-surface greatly simplifies the analysis. They use a Green's function approach and a Legendre series expansion to reduce the governing equation to a standard algebraic eigenvalue problem. Similarly, Bauer & Chiba (2004, 2005) have considered the same problem but model the spherical-bowl support as a large number of point-wise constraints in order to compute the drop's frequency spectrum. Ganan & Barerro (1990) use the Green's function expansion technique of Strani & Sabetta (1984) to analyze the linearized dynamics of captive drops and bridges. Their numerical-based method is able to handle gravitational effects and has been verified against experiment, which they also perform. In contrast to isolated drops, supported drops require a model for the three-phase contact-line. The aforementioned studies have made the common assumption that the interface has an immobile or 'pinned' contact-line.

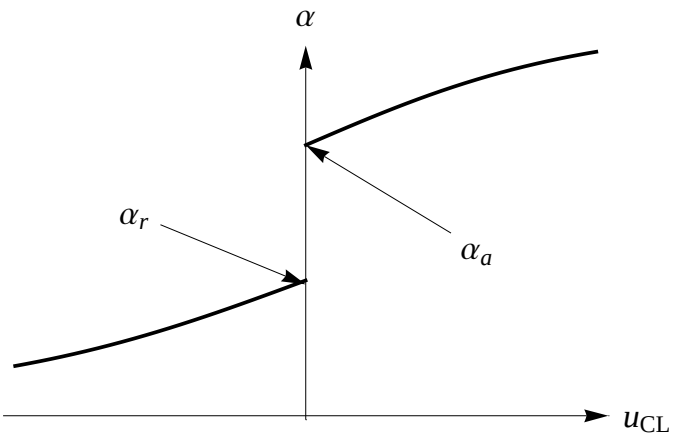

Figure 5.1: Typical experimental relationship between contact-angle α and contact-line speed u_{CL}, which also shows the advancing α_a and receding α_r static contact-angle ($u_{CL} \to 0$).

The dynamics of the moving contact-line are not as straightforward. One has to establish the appropriate constitutive laws there (Dussan, 1979). As observed experimentally, the typical relationship between the contact-angle α and contact-line speed u_{CL} is shown in figure 5.1. The ambiguity in the static contact-angle ($u_{CL} \to 0$) is referred to as contact-angle hysteresis. More precisely, in many physical systems there exists a range of contact angles $\alpha \in [\alpha_r, \alpha_a]$ where no contact-line motion is observed. Here α_a and α_r are related to the material properties of the advancing/receding contact-line, respectively. Figure 5.1 has served as the basis for a number of theoretical studies on moving contact-lines and a few of the most relevant studies will be mentioned here. In a series of studies on moving contact-lines with application to fluid rivulets, Davis *et al.* assume that the contact-angle depends *smoothly* on the contact-line speed, $\alpha = G(u_{CL})$. They establish linear stability bounds for a number of base-states (Davis, 1980; Weiland & Davis, 1981; Young & Davis, 1987). Contact-angle hysteresis is excluded here because of assumptions on the smoothness of G. In a study of capillary-gravity waves of a

planar interface, Hocking (1987*b*) introduced the following contact-line condition

$$\frac{\partial \eta}{\partial t} = \begin{cases} \Theta_a \left(\xi - \xi_a \right), & \xi > \xi_a \\ 0, & \xi_r < \xi < \xi_a \\ \Theta_r \left(\xi - \xi_r \right), & \xi < \xi_r, \end{cases} \tag{5.1}$$

which does allow for contact-angle hysteresis, despite the assumption that the interface perturbation η is small. The 'Hocking' condition relates the linearized contact-line speed $\partial \eta / \partial t$ to the deviation in contact-angle from its equilibrium value $\xi = \xi(\eta)$, which itself is a function of the interface disturbance η. Here Θ_a, ξ_a and Θ_r, ξ_r are parameters related to the material properties; and the wetting and spreading conditions of the advancing/receding contact lines, respectively. When the deviation in contact-angle ξ exceeds the critical interval $\xi \in [\xi_r, \xi_a]$, contact-line motion ensues. Hocking (1987*a*) has shown that in the absence of contact-angle hysteresis $\xi_a = \xi_r$, (5.1) reduces to

$$\frac{\partial \eta}{\partial t} = \Theta \xi. \tag{5.2}$$

Similarly, the linearized version of the constitutive law adopted by Davis ($\alpha = G(u_{CL})$) can be written as

$$\xi = \Lambda \frac{\partial \eta}{\partial t}. \tag{5.3}$$

In this common limit, the contact-line conditions (5.2,5.3) are related through the interpretation of the spreading parameters $\Theta = 1/\Lambda$. For the purposes of this chapter, the Davis interpretation (5.3) will be used in analyzing the dynamic contact-line.

As regards the dynamics of drops in contact with a planar support, Lyubimov *et al.* (2004, 2006) study free and forced oscillations of the sessile drop with a hemispherical base-state for both vertical and horizontal forcing. By exploiting the

symmetry of the base-state, they are able to compute the frequency spectrum under a linearized Hocking boundary condition (5.2). Fayzrakhmanova & Straube (2009) implement the full Hocking condition (5.1) via numerical integration to study the stick-slip dynamics and frequency response caused by contact-angle hysteresis of the forced hemispherical drop. In the absence of base-state symmetry, one generally turns to a more computationally-based method. Finite-element methods have been employed by Basaran *et al.* to study the finite-amplitude natural oscillations of pendant drops (Basaran & DePaoli, 1994), as well as the forced oscillations of supported drops with application to drop ejection (Wilkes & Basaran, 2001) and hysteretic response (Wilkes & Basaran, 1999), which was reported experimentally by DePaoli *et al.* (1995). In another numerical study, James *et al.* (2003*a*) developed a Navier-Stokes solver to capture drop ejection phenomenon of forced sessile drops.

Recently, there has been a growing interest in the dynamics of sessile drops under external forcing with an emphasis on the wetting conditions at the three-phase contact-line and their motion. In drop atomization experiments, James *et al.* (2003*b*) observed a hierarchy of instabilities for the sessile drop forced by a piezoelectrically-driven diaphragm. A more detailed investigation of these instabilities are given in Vukasinovic *et al.* (2007). A brief synopsis of the experimental observations is given here.

To begin, a sessile drop with pinned contact-lines is placed on a vibrating diaphragm and a frequency sweep is performed for fixed forcing-amplitude until resonance is observed or an axisymmetric interface disturbance is born. The frequency is then locked and the forcing amplitude is increased. At a critical forcing amplitude, the contact-line de-pins and an azimuthal instability is triggered

along the contact-line. A further increase in the forcing amplitude results in the azimuthal wave propagating upwards until it consumes the entire drop interface. This time-dependent state is called the 'lattice mode'. Finally, drop atomization is observed at larger values of forcing amplitude. The azimuthal instability triggered by the contact-line motion (de-pinning) will be discussed later.

In a similar study of mechanically-vibrated sessile drops, Noblin *et al.* (2004) focused on the transition from a pinned to free contact-line and the acceleration necessary to overcome the contact-angle hysteresis. Extending their previous work, Noblin *et al.* (2005) showed that at sufficiently high accelerations an azimuthal instability called the 'triplon mode' is generated in large fluid puddles. Once again, this instability is triggered once the contact-angle hysteresis is overcome and the contact-line de-pins. These modes and the instability observed in Vukasinovic *et al.* (2007) exhibit subharmonic resonances, which are characteristic of Faraday waves (Faraday, 1831). A thorough review of the parametrically-driven Faraday wave instability is given by Miles & Henderson (1990).

As an alternative to vertical forcing, the sessile drop subject to in-plane (horizontal) forcing exhibits another set of intriguing phenomenon. The first being a set of mode shapes that are odd or anti-symmetric about the vertical mid-plane. These types of shapes are not possible under the assumption of axisymmetry, but have been observed by Daniel *et al.* (2004) for sessile drops in forced oscillation on chemically-treated gradient surfaces. In addition, they also observe translational motion of drops that have overcome the hysteretic barrier or have mobile (unpinned) contact-lines. A study of both horizontal and vertical forcing by Noblin *et al.* (2009) has shown that this translational motion can be directionally controlled. Surprisingly, Brunet *et al.* (2009) have shown that under external forcing

a sessile drop can overcome the influence of gravity and be driven *up* a sloped incline against gravity. A fundamental understanding of the wetting conditions that give rise to these types of motions are of importance to micro-fluidic technology and coating processes.

In this chapter, the small oscillations of the sessile drop under a number of contact-line conditions are analyzed. Specifying the boundary conditions on the three-phase contact-line sets the disturbance class to which the drop interface is subject. The disturbances considered here fall into two categories and are termed i) 'kinematic' or ii) 'dynamic'. Kinematic disturbances have no 'contact-line disturbance energy' associated with their motions, while a dynamic disturbance can dissipate energy. A kinematic disturbance either i) preserves the drop's static contact-angle (natural) or ii) has fixed contact-lines (pinned). The dynamic disturbance relates 'field' quantities by a postulated constitutive law valid on the three-phase contact-line. More specifically, the dynamic contact-angle is related to the contact-line speed via a spreading parameter.

A dynamic stability analysis is performed, whereby the linearized hydrodynamic equations, governing the interfacial motion of the inviscid sessile drop, are formulated as a functional eigenvalue-problem on linear operators. The functional equation is solved using one of two equivalent formulations, referenced as the 'forward' or 'inverse' problem. Both problems are reduced to a set of algebraic equations by the variational procedure of Rayleigh-Ritz. The frequency spectrum for the kinematic disturbances, fixed contact-angle and fixed contact-line, are computed by solving the inverse problem. An ad hoc solution method is used for the contact-line speed condition, which exploits the structure of the second variation of surface energy and utilizes select results from the 'natural' disturbance class.

This problem is parameterized by azimuthal wave-number l, the static contact-angle α (equivalently volume) and the boundary conditions by a spreading parameter Λ. Although the majority of the sessile drop motions are oscillatory, there does exists an instability related to the natural disturbance for a range of contact angles ($90^\circ < \alpha < 180^\circ$) that define the super-hemispherical base-state. The characteristic feature of this instability is an advancing contact-line, which is accelerating relative to the receding contact-line, thereby transferring mass from one side of the drop to the other. There is no such mechanism to resist this motion and the droplet 'walks' along the supported surface. Cataloging this instability may be of great importance in coating processes and microfluidic applications, where control of the translational motion of fluid droplets is desirable.

The sessile drop with hemispherical base-state ($\alpha = 90^\circ$) is a special case, since it possesses some additional symmetry. It has characteristic oscillation frequencies that are degenerate with respect to azimuthal wave-number for the natural disturbance class. To 'break' this symmetry, one can either i) change the static contact-angle of the base-state, $\alpha \neq 90^\circ$ or ii) introduce new boundary conditions $\Lambda \neq 0$. Pinning the drop's contact lines lifts this degeneracy $\Lambda \to \infty$. There exists a range of frequencies for fixed polar wave-number k which depend upon azimuthal wave-number. The frequency range is approximately 10% for the pinned hemispherical base-state and can be increased significantly by varying the static contact-angle. Here, for a given polar wave-number k, the mode shapes with largest azimuthal wave-number l have a greater oscillation frequency in comparison to the low azimuthal wave-number shapes. This directional breaking persists for super-hemispherical base-states ($\alpha > 90^\circ$), where the high azimuthal wave-number shapes have the larger oscillation frequencies. In contrast, for the sub-hemispherical base-states ($\alpha < 90^\circ$), the oscillation frequency decreases as the

azimuthal wave-number increases. The magnitude of the frequency range increases as the volume deviates from hemispherical. In fact, for large deviations there is the possibility for mode crossings, parameters at which two mode shapes share the same frequency. An analogy can be made between the mode-crossing phenomenon and the 'filling' of the periodic table by energy levels. In addition to modal crossings controlled by the base-state volume, they can be controlled by the contact-line speed condition. This type of mode crossing possibly can be used to explain instabilities observed experimentally (Vukasinovic *et al.*, 2007).

The utility of the contact-line speed condition is that by varying the spreading parameter Λ, one can smoothly 'deform' the problem between the two kinematic disturbances, natural ($\Lambda \to 0$) and pinned ($\Lambda \to \infty$). Application of the contact-line speed condition shows that at finite values of Λ, the oscillation frequencies are damped, despite viscosity being zero. The lower-order mode shapes dissipate the most energy over an oscillation cycle, unlike bulk viscous effects where the higher-order modes dissipate more energy. This behavior can be understood using the interpretation of the spreading parameter as a measure of the mobility of the contact-line. According to this constitutive law, effective dissipation is related to contact-line motion. Lower-order mode shapes have larger contact-line motions, thus, one would expect their dissipation to be larger according to this constitutive law. Similarly, the sub-hemispherical drops have contact lines that are more mobile, in comparison to the super-hemispherical ones and equivalently dissipate more energy. In the super-hemispherical limit $\alpha \to 180^\circ$ (non-wetting), the contact lines are essentially immobile and the distinction between the natural and pinned disturbance is lost, resulting in frequencies that are indistinguishable.

In the following sections the mathematical problem associated with the small

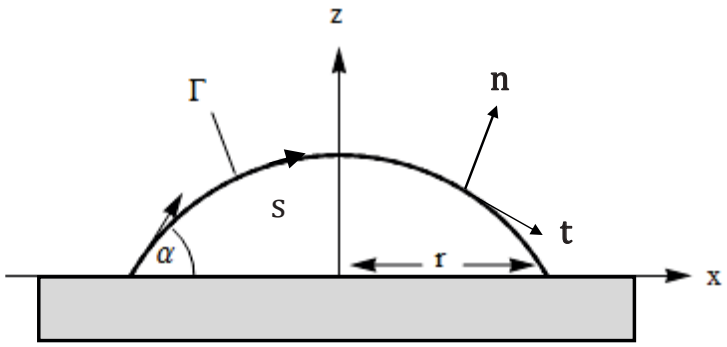

Figure 5.2: Sessile drop equilibrium shape in polar view showing vectors normal $\boldsymbol{n}$ and tangential $\boldsymbol{t}$ to the surface Γ.

deformations of the sessile drop is formulated. The disturbance classes are defined and the governing equations are reduced via a normal mode expansion to a functional eigenvalue equation. The frequency spectrum is computed from a set of algebraic equations, which results from the implementation of the Rayleigh-Ritz procedure. The oscillation frequencies and/or growth rates depend upon the static contact-angle α, azimuthal wave-number l and spreading parameter Λ. The dependence of the spectrum on these parameters is discussed and some concluding remarks are offered.

5.2 Mathematical formulation

The sessile drop is a surface of constant mean curvature H and equivalently a static equilibrium according to the Young-Laplace equation

$$\frac{p}{\sigma} = \kappa_1 + \kappa_2 \equiv 2H, \tag{5.4}$$

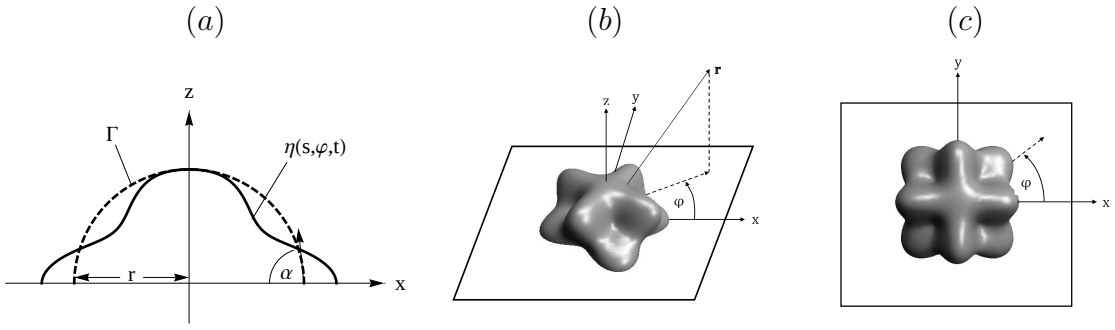

Figure 5.3: Definition sketch with unperturbed Γ (dashed) and perturbed interface η (solid) in (a) polar cross-section and three-dimensional (b) perspective and (c) top views.

which relates the principal curvatures, κ_1 and κ_2, to the pressure p there. This equilibrium surface Γ may be defined parametrically as

$$X(s,\varphi;\alpha) = -\frac{1}{\sin(\alpha)}\sin(s)\cos(\varphi), \tag{5.5a}$$

$$Y(s,\varphi;\alpha) = -\frac{1}{\sin(\alpha)}\sin(s)\sin(\varphi), \tag{5.5b}$$

$$Z(s;\alpha) = \frac{1}{\sin(\alpha)}\left(\cos(s)-\cos(\alpha)\right), \tag{5.5c}$$

using arc-length $s \in [-\alpha, \alpha]$ and azimuthal angle $\varphi \in [0, 2\pi]$ as generalized surface coordinates. As depicted in figure 5.2, the equilibrium surface is scaled by its base radius r and parameterized by contact-angle α. Thus, the scaled drop volume is given by

$$V/r^3 = \left(\frac{\pi}{3}\right)\frac{2-3\cos\alpha+\cos^3\alpha}{\sin^3\alpha}. \tag{5.6}$$

The interface is given a small perturbation $\eta(s,\varphi,t)$ (c.f. figure 5.3). No domain perturbation is needed for small deformations, thus the droplet domain

$$D \equiv \{(x,y,z)|\ 0 \le x \le X(s,\varphi;\alpha),\ 0 \le y \le Y(s,\varphi;\alpha),\ 0 \le z \le Z(s;\alpha)\} \tag{5.7}$$

is bounded by a free surface ∂D^f ($\equiv \Gamma$) of uniform surface tension σ, and a planar surface-of-support ∂D^s;

$$\partial D^f \equiv \{(x,y,z)\,|\,x = X(s,\varphi;\alpha),\ y = Y(s,\varphi;\alpha),\ z = Z(s;\alpha)\}, \quad (5.8a)$$

$$\partial D^s \equiv \{(x,y,z)\,|\,z = 0\}. \quad (5.8b)$$

The droplet is immersed in a passive gas and the effect of gravity is neglected.

5.2.1 Hydrodynamic field equations

The fluid is incompressible and the flow is assumed to be irrotational. Therefore, the velocity field may be described as $\boldsymbol{v} = \boldsymbol{\nabla}\Psi$, where the velocity potential Ψ satisfies Laplace's equation

$$\nabla^2\Psi = 0 \quad [D] \quad (5.9)$$

on the drop domain. Additionally, the velocity potential satisfies the no-penetration condition

$$\boldsymbol{\nabla}\Psi \cdot \hat{\boldsymbol{z}} = 0 \quad [\partial D^s] \quad (5.10)$$

on the surface-of-support and a (linearized) kinematic condition

$$\frac{\partial\Psi}{\partial n} = -\frac{\partial\eta}{\partial t} \quad [\partial D^f] \quad (5.11)$$

on the free surface, which relates the normal velocity to the perturbation amplitude there. In the limit of small interface deflection and in accordance with potential flow theory, the pressure field is expressed by the linearized Bernoulli equation

$$p = \varrho\frac{\partial\Psi}{\partial t} \quad [D], \quad (5.12)$$

where ϱ is the fluid density. Finally, deviations from the equilibrium surface Γ generate pressure gradients, and thereby flows, according to the Young-Laplace

equation

$$p/\sigma = -\Delta_\Gamma \eta - \left(\kappa_1^2 + \kappa_2^2\right) \eta \;\; [\partial D^f]. \tag{5.13}$$

Here the Laplace-Beltrami operator Δ_Γ and principal curvatures κ_1, κ_2 are defined on the equilibrium surface and Δ_Γ is given below by eqn. (5.17).

The hydrodynamic field equations (5.9)-(5.13) govern the motion of an inviscid fluid, whose spherical-cap interface is given a small disturbance. Formally, the field equations must be augmented with a boundary condition on the three-phase contact-line to form a well-posed system of partial differential equations. Alternatively, one needs to specify the disturbance class to which the interface is subject.

5.3 Derivation of functional eigenvalue equation

To study the interfacial motion of the sessile drop, the hydrodynamic equations are reduced via a normal mode expansion. The resulting eigenvalue problem is then formulated as a functional equation on linear operators, from which the characteristic frequencies and corresponding mode-shapes are readily computed.

5.3.1 Normal-mode reduction

Normal modes

$$\eta(s, \varphi, t) = y(s) \mathrm{e}^{i\omega t} \mathrm{e}^{il\varphi}, \;\; \Psi(\boldsymbol{x}, t) = \phi(\rho, \theta) \mathrm{e}^{i\omega t} \mathrm{e}^{il\varphi}, \tag{5.14}$$

are applied to the field equations (5.9)-(5.13) to generate the following eigenvalue problem,

$$\frac{1}{\rho^2}\frac{\partial}{\partial\rho}\left(\frac{\partial\phi}{\partial\rho}\right)+\frac{1}{\rho^2\sin\theta}\frac{\partial}{\partial\theta}\left(\sin\theta\frac{\partial\phi}{\partial\theta}\right)-\frac{l^2}{\rho^2\sin^2\theta}\phi=0\ \ [D], \tag{5.15a}$$

$$\frac{\partial\phi}{\partial n}=0\ \ [\partial D^s], \tag{5.15b}$$

$$\frac{\partial\phi}{\partial n}=-i\omega y\ \ [\partial D^f], \tag{5.15c}$$

$$-\Delta_\Gamma\frac{\partial\phi}{\partial n}-\left(\kappa_1^2+\kappa_2^2\right)\frac{\partial\phi}{\partial n}+l^2\left(\frac{\sin^2(\alpha)}{\sin^2(s)}\right)\frac{\partial\phi}{\partial n}=\lambda^2\phi\ \ [\partial D^f], \tag{5.15d}$$

$$\int_\Gamma\frac{\partial\phi}{\partial n}=0, \tag{5.15e}$$

$$\lambda^2\equiv\frac{\varrho\omega^2r^3}{\sigma}. \tag{5.15f}$$

The problem is parameterized by the azimuthal wave-number l. Equation (5.15a) is Laplace's equation written in spherical coordinates (ρ,θ), (5.15b) is the no-penetration condition on the support surface, (5.15c) is the kinematic condition and (5.15e) is recognized as the integral form of the incompressibility condition or a volume conservation constraint. The dynamic pressure balance across the free surface is represented by (5.15d) with the principal curvatures given by

$$\kappa_1=\kappa_2=\sin(\alpha). \tag{5.16}$$

The Laplace-Beltrami operator

$$\Delta_\Gamma y\equiv\frac{1}{\sqrt{g}}\frac{\partial}{\partial u^\alpha}\left(\sqrt{g}g^{\alpha\beta}\frac{\partial y}{\partial u^\beta}\right) \tag{5.17}$$

is defined by functions y on the equilibrium surface. Here the definition of the surface metric

$$g_{\alpha\beta}\equiv\boldsymbol{x}_\alpha\cdot\boldsymbol{x}_\beta=\begin{pmatrix}\csc^2(\alpha) & 0\\ 0 & \left(\csc(\alpha)\sin(s)\right)^2\end{pmatrix},\ \ g=\left(\sin(s)\csc^2(\alpha)\right)^2, \tag{5.18}$$

allows one to write (5.15d) as

$$\left(\frac{\partial\phi}{\partial n}\right)''+\cot(s)\left(\frac{\partial\phi}{\partial n}\right)'+\left(2-\frac{l^2}{\sin^2(s)}\right)\left(\frac{\partial\phi}{\partial n}\right)=-\frac{\lambda^2}{\sin^2(\alpha)}\phi, \tag{5.19}$$

where differentiation is with respect to the arc-length coordinate, $' = d/ds$.

5.3.2 Operator formalism

This integro-differential equation governs the motion of the interface and may be formulated as a operator equation using one of two alternative representations.

Forward problem

The first formulation uses the interface deflection $\partial\phi/\partial n$ as the unknown function, giving rise to the following operator equation

$$K\left[\frac{\partial\phi}{\partial n};l\right] = -\hat{\lambda}^2 M\left[\frac{\partial\phi}{\partial n}\right], \quad \hat{\lambda}^2 \equiv \frac{\lambda^2}{\sin^2(\alpha)}, \tag{5.20}$$

which is referred to as the forward problem. Here M is an integral operator representative of the fluid inertia and K a differential operator related to the curvature,

$$M\left[\frac{\partial\phi}{\partial n}\right] \equiv \phi, \tag{5.21a}$$

$$K\left[\frac{\partial\phi}{\partial n};l\right] \equiv \left(\frac{\partial\phi}{\partial n}\right)'' + \cot(s)\left(\frac{\partial\phi}{\partial n}\right)' + \left(2 - \frac{l^2}{\sin^2(s)}\right)\left(\frac{\partial\phi}{\partial n}\right). \tag{5.21b}$$

To proceed with this formulation, one must construct a sufficiently general solution to the boundary value problem

$$\nabla^2\psi = 0 \ \ [D], \quad \frac{\partial\psi}{\partial n} = f_k \ \ [\partial D^f]. \tag{5.22}$$

Equivalently, given a surface deformation f_k, one needs to compute the corresponding velocity potential ψ_k, in accordance with the inertia operator (5.21a). In general, for all but the simplest of geometries, solution of this Neumann-type

boundary value problem requires a computationally intensive approach, such as a boundary integral method.

Inverse problem

Alternatively, one may use the velocity potential ϕ as the unknown function and define the inverse problem

$$M^{-1}[\phi] = -\hat{\lambda}^2 K^{-1}[\phi; l], \tag{5.23}$$

which follows directly from (5.19). Here the integro-differential nature of the governing equation persists, with

$$M^{-1}[\phi] \equiv \frac{\partial \phi}{\partial n} \tag{5.24}$$

the differential operator and K^{-1} an integral operator, inversely related to the curvature operator K defined in (5.21b). As with the forward problem, the primary difficulties associated with the inverse problem are related to the integral operator. Specifically, construction of the inverse operator K^{-1} depends on the parametrization of the equilibrium surface and may or may not be analytically tractable.

Forward vs. Inverse problem

The two representations defined here are completely equivalent, but each has their respective difficulties. In the forward problem, one has to construct a sufficiently general solution to Laplace's equation with Neumann boundary conditions. In most cases, this is analytically intractable. Likewise, one must construct the

Green's function to the differential curvature operator to proceed with the inverse operator formalism. By specifying the relevant boundary conditions on the three-phase contact-line, the disturbance class to which the interface is subject is set and one may proceed with the most relevant operator formulation, either the forward or inverse problem. While the inverse problem is seen to be more tractable in general, the forward problem has an attractive variational structure that can be exploited.

5.3.3 Contact-line conditions

To compute the spectrum of the eigenvalue problem (5.15), one needs to specify the disturbance class, via boundary conditions on the three-phase contact-line. Namely, 'allowable' solutions are decomposed into two distinct classes, kinematic or dynamic, as mentioned above. Kinematic disturbances depend solely on the interface deflection, whereas dynamic disturbances are related to 'dynamic' field quantities, such as the contact-line speed. To ensure the boundary-value problem is well-posed mathematically, the kinematic and dynamic boundary conditions are augmented with the following restriction,

$$\left.\frac{\partial \phi}{\partial n}\right|_{s=0} - \text{bounded}, \tag{5.25}$$

a necessary conditions to guarantee the interface disturbance is physical.

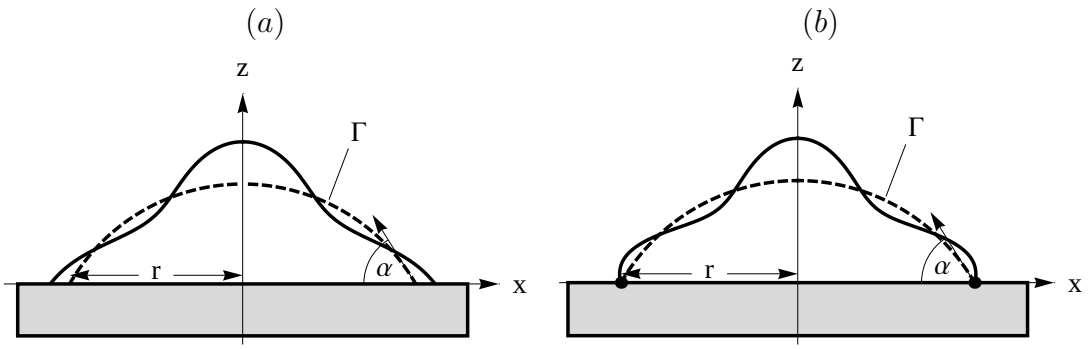

Figure 5.4: Kinematic disturbances classes for the sessile drop: (a) natural and (b) pinned contact-line.

Natural

The first type of kinematic disturbance is shown in figure 5.4(a) and preserves the static contact-angle α in accordance with

$$\frac{\partial}{\partial s}\left(\frac{\partial \phi}{\partial n}\right) + \cos(\alpha)\frac{\partial \phi}{\partial n} = 0\Big|_{s=\alpha}, \tag{5.26}$$

and is termed the 'natural' boundary condition. A more thorough derivation of the natural contact-line condition (A.9) is given in Appendix A.

Pinned

The second class of kinematic disturbance is shown in figure 5.4(b) and has 'pinned' contact-lines,

$$\frac{\partial \phi}{\partial n}\Big|_{s=\alpha} = 0. \tag{5.27}$$

As noted by Courant & Hilbert (1953) for the general boundary-value problem, the pinned contact-line is the most restrictive perturbation as the size of its function space of allowable disturbances is the smallest.

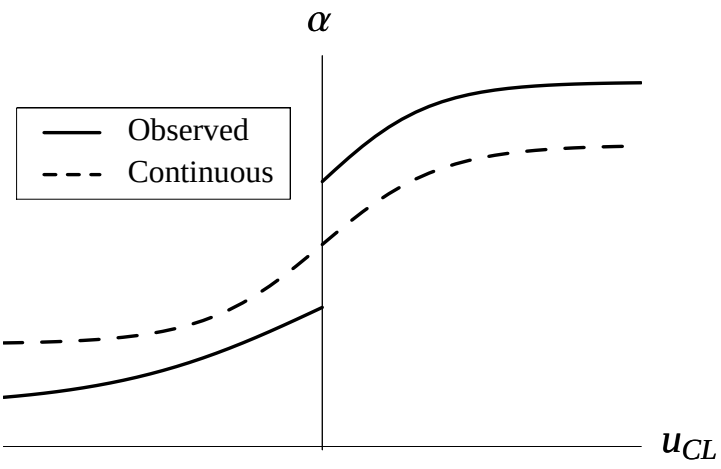

Figure 5.5: Typical contact-line behavior observed (solid) and the continuous constitutive law model (dashed) imposed here.

Dynamic contact-line

The dynamic contact-line condition follows by assuming that the contact-angle depends smoothly on the contact-line speed through the function f (c.f. figure 5.5),

$$\alpha + \epsilon\hat{\alpha} = f\left(0 + \epsilon\, i\omega \left(\frac{\partial\phi}{\partial n}\right)\right). \tag{5.28}$$

This postulated constitutive law is inversely related to the Hocking contact-line speed condition, which assumes that the contact-line speed is proportional to the deviation from the static contact-angle (mentioned above). The variation in contact-angle

$$\hat{\alpha} = i\omega\, f'(0)\, \left(\frac{\partial\phi}{\partial n}\right) \tag{5.29}$$

found from linearizing (5.28) is applied to (A.9), which results in the following boundary condition

$$\frac{\partial}{\partial s}\left(\frac{\partial\phi}{\partial n}\right) + \cos(\alpha)\left(\frac{\partial\phi}{\partial n}\right) = i\omega\Lambda \left(\frac{\partial\phi}{\partial n}\right)\Big|_{s=\alpha}, \quad \Lambda \equiv f'(0). \tag{5.30}$$

Here $1/\Lambda$ is a measure of the mobility of the contact-line, which is used as a parameter which can smoothly change the boundary condition from natural to

pinned. This is sometimes called a 'homotopy' parameter. In the limit $\Lambda \to 0$, (5.30) reduces to the natural condition (fully mobile) and $\Lambda \to \infty$ corresponds to the pinned contact-line condition (immobile). It should be noted that contact-angle hysteresis is not allowable here by linearization of (5.28).

5.4 Solution method for kinematic disturbances

As stated earlier, the spectrum of the operator equation (5.19) may be computed by either the forward or inverse method. This choice depends upon the imposed disturbance class. Here the inverse method will be used for the kinematic disturbances, whereas it is advantageous to analyze the contact-line speed condition by the forward method.

5.4.1 Inverse-operator construction

The two kinematic disturbances, either natural or pinned, are structurally similar and their respective inverse operators are derived simultaneously. To use the inverse operator formalism, one must construct the integral operator

$$K^{-1}\left[\phi\right](x) = \int_b^1 G\left(x, y; l\right) \phi\left(y\right) \mathrm{d}y, \tag{5.31}$$

which is simply the Green's function or fundamental solution of the curvature operator (5.21b),

$$G\left(x, y; l\right) = \begin{cases} \xi(l) y_1(y; l) \left[\frac{\tau_2(l)}{\tau_1(l)} y_1(x; l) - y_2(x; l)\right] & b < x < y < 1 \\ \xi(l) y_1(x; l) \left[\frac{\tau_2(l)}{\tau_1(l)} y_1(y; l) - y_2(y; l)\right] & b < y < x < 1. \end{cases} \tag{5.32}$$

Here the coordinate transformation $x \equiv \cos(s)$ has been used in the Green's function, which is parameterized by azimuthal wave-number l and the transformed contact-angle $b \equiv \cos(\alpha)$. The functions y_1 and y_2 belong to the kernel of the curvature operator K and are given by:

$$y_1(x;0) = P_1(x), \quad y_2(x;0) = Q_1(x), \tag{5.33a}$$

$$y_1(x;1) = P_1^{(1)}(x), \quad y_2(x;1) = Q_1^{(1)}(x), \tag{5.33b}$$

$$y_1(x;l \geq 2) = (x+l)\left(\frac{1-x}{1+x}\right)^{l/2},$$

$$y_2(x;l \geq 2) = \frac{(x+l)}{2l\,(l^2-1)}\left(\frac{1+x}{1-x}\right)^{l/2}, \tag{5.33c}$$

where P_1, Q_1 and $P_1^{(1)}, Q_1^{(1)}$ are the order 0 and 1 Legendre functions of index 1, respectively. Similarly, the scale factor is given by

$$\xi(l) \equiv \begin{cases} 1/2 & l = 1 \\ 1 & l \neq 1, \end{cases} \tag{5.34}$$

while the parameters τ_1 and τ_2 are related to the contact-line boundary conditions and expressed as

$$\tau_1^{(n)} = y_1'(b;l) + \frac{b}{\sqrt{1-b^2}} y_1(b;l), \quad \tau_2^{(n)} = y_2'(b;l) + \frac{b}{\sqrt{1-b^2}} y_2(b;l), \tag{5.35}$$

for the natural and

$$\tau_1^{(p)} = y_1(b;l), \quad \tau_2^{(p)} = y_2(b;l) \tag{5.36}$$

pinned contact-line disturbance classes, respectively.

Axisymmetric operator equation $(l = 0)$

Volume must be conserved by (5.15e) for this incompressible fluid. To satisfy this condition, recall that the velocity potential ϕ is defined up to an arbitrary constant

C, which allows one to write (5.23) as

$$\frac{\partial \phi}{\partial n}(x) = -\hat{\lambda}^2 \left[C \int_b^1 G(x,y;0)\mathrm{d}y + \int_b^1 G(x,y;0)\phi(y)\mathrm{d}y \right]. \tag{5.37}$$

Integrating (5.37) along the equilibrium surface and enforcing (5.15e) uniquely determines this constant

$$C = -\frac{\int_b^1\int_b^1 G(x,y;0)\phi(y)\mathrm{d}y\mathrm{d}x}{\int_b^1\int_b^1 G(x,y;0)\mathrm{d}y\mathrm{d}x}. \tag{5.38}$$

Finally, the functional eigenvalue equation for the axisymmetric disturbance class is written as

$$\frac{\partial \phi}{\partial n}(x) = \hat{\lambda}^2 \left[\frac{\int_b^1\int_b^1 G(x,y;0)\phi(y)\mathrm{d}y\mathrm{d}x}{\int_b^1\int_b^1 G(x,y;0)\mathrm{d}y\mathrm{d}x} \int_b^1 G(x,y;0)\mathrm{d}y - \int_b^1 G(x,y;0)\phi(y)\mathrm{d}y \right], \tag{5.39}$$

with volume conserved for all ϕ.

Azimuthal-dependent operator equation ($l \neq 0$)

Unlike the axisymmetric operator equation (5.39), the volume conservation constraint (5.15e) is naturally satisfied for interface disturbances with azimuthal wavenumber $l \geq 1$. Thus, the corresponding operator equation is given by

$$\frac{\partial \phi}{\partial n}(x) = -\hat{\lambda}^2 \left[\int_b^1 G(x,y;l)\phi(y)\mathrm{d}y \right]. \tag{5.40}$$

5.4.2 Rayleigh-Ritz

Stationary values of the operator equations (5.39,5.40) are the characteristic oscillation frequencies of the sessile drop, provided the no-penetration condition (5.15b) is satisfied. This can be accomplished through proper selection of the potential

functions ϕ. Once these basis functions are selected, a Rayleigh-Ritz procedure is used to reduce the operator equation into a standard algebraic eigenvalue equation. The method is sketched here, while a more thorough illustration of the method is given in Segel (1987). To begin, the eigenvalues λ of the operator equation

$$B\left[y\right] = \lambda A\left[y\right] \tag{5.41}$$

are the stationary values of the functional

$$\lambda = \min \frac{(B[y], y)}{(A[y], y)}, \quad y \in S, \tag{5.42}$$

where S is a predetermined function space. A solution series,

$$y = \sum_{i=1} c_i y_i, \tag{5.43}$$

constructed from functions $y_i \in S$ are applied to the functional (5.42) and minimized with respect to the coefficients c_i to generate a set of algebraic equations

$$\sum_{j=1} \left(b_{ij} - \lambda a_{ij}\right) c_j = 0, \tag{5.44a}$$

$$b_{ij} \equiv \int B[y_i]\, y_j, \tag{5.44b}$$

$$a_{ij} \equiv \int A[y_i]\, y_j, \tag{5.44c}$$

from which the eigenvalues may be computed.

Axisymmetric operator $(l = 0)$

The necessary input for the Rayleigh-Ritz procedure is a solution series

$$\phi = \sum_{j=1}^{N} a_j \phi_j, \tag{5.45}$$

constructed from basis functions ϕ_j. These functions are applied to (5.39) and inner products are taken to generate a set of linear algebraic equations

$$\sum_{j=1}^{N} \left(m_{ij} - \hat{\lambda}^2 \kappa_{ij} \right) a_j = 0, \tag{5.46}$$

which have matrix elements

$$m_{ij} \equiv \int_b^1 \left(\frac{\partial \phi_i}{\partial n} \right) (\phi_j) \, \mathrm{d}x, \quad \kappa_{ij} \equiv \left[\frac{G_{0i} G_{j0}}{G_{00}} - G_{ij} \right], \tag{5.47}$$

with

$$\begin{aligned} G_{ij} \equiv & \left[\int_b^1 y_1(x;0) \phi_i(x) \mathrm{d}x \right] \left[\int_b^1 \left(\frac{\tau_2}{\tau_1} y_1(x;0) - y_2(x;0) \right) \phi_j(x) \mathrm{d}x \right] \\ & + \int_b^1 y_1(x;0) \phi_i(x) \int_x^1 y_2(y;0) \phi_j(y) \mathrm{d}y \mathrm{d}x \\ & - \int_b^1 y_2(x;0) \phi_i(x) \int_x^1 y_1(y;0) \phi_j(y) \mathrm{d}y \mathrm{d}x. \end{aligned} \tag{5.48}$$

Allowable solutions of functional (5.39) necessarily satisfy the hydrodynamic field equations (5.15). Recall, volume conservation (5.15e) has been satisfied by proper selection of the constant C and the contact-line conditions are incorporated into the Green's function (5.32), but the no-penetration condition (5.15b) has yet to be satisfied. This can be accomplished through proper selection of the basis functions

$$\phi_j(\rho, \theta) = \rho^{2j} P_{2j} (\cos \theta), \tag{5.49}$$

given here in spherical coordinates, ρ and θ, and chosen to be harmonic, as required by (5.15a). Here P_{2j} is the Legendre polynomial of degree $2j$. The normal derivatives of the basis functions (5.49), evaluated on the equilibrium surface, are expressed as

$$\begin{aligned} \frac{\partial \phi_j}{\partial n} \equiv \boldsymbol{\nabla} \phi_j \cdot \boldsymbol{n} = & 2j P_{2j} (\cos \theta) (-\sin s \sin \theta + \cos s \cos \theta) (\rho)^{2j-1} \\ & + \sin \theta P'_{2j} (\cos \theta) (\sin s \cos \theta + \cos s \sin \theta) (\rho)^{2j-1}, \end{aligned} \tag{5.50}$$

using mixed coordinates for efficiency in presentation. The basis functions (5.49) and their normal derivatives (5.50) are defined on the equilibrium surface through the following coordinate transformation,

$$\rho \equiv \sqrt{X^2+Y^2+Z^2}, \;\; \cos\theta \equiv \frac{Z}{\sqrt{X^2+Y^2+Z^2}}, \;\; \sin\theta \equiv \sqrt{\frac{X^2+Y^2}{X^2+Y^2+Z^2}}, \tag{5.51}$$

which relates spherical coordinates, whose origin is centered on the surface-of-support, to the arc-length coordinate. Here $X = X(s)$, $Y = Y(s)$, $Z = Z(s)$ have been defined in (5.5). Finally, the basis functions (5.49) are applied to (5.47) to generate a set of algebraic equations (5.46), from which the characteristic oscillation frequencies are computed.

Azimuthal operator ($l \neq 0$)

An analogous solution series

$$\phi^{(l)} = \sum_{j=l}^{l+N} a_j \phi_j^{(l)} \tag{5.52}$$

is used to compute the stationary values of the functional (5.40), as they depend upon the azimuthal wave-number l. As before, the basis functions $\phi_j^{(l)}$ are applied to (5.40) and inner products are taken to generate the matrix equation

$$\sum_{j=l}^{l+N} \left(m_{ij}^{(l)} - \hat{\lambda}^2 \kappa_{ij}^{(l)} \right) a_j = 0 \tag{5.53}$$

with

$$m_{ij}^{(l)} \equiv \int_b^1 \left(\frac{\partial \phi_i^{(l)}}{\partial n} \right) \left(\phi_j^{(l)} \right) \mathrm{d}x \tag{5.54}$$

and

$$\frac{\kappa_{ij}^{(l)}}{\xi(l)} \equiv \left[\int_b^1 y_1(x;l)\phi_i^{(l)}(x)\,\mathrm{d}x\right]\left[\int_b^1 \left(\frac{\tau_2}{\tau_1}y_1(x;l) - y_2(x;l)\right)\phi_j^{(l)}(x)\,\mathrm{d}x\right] + \int_b^1 y_1(x;l)\phi_i^{(l)}(x)\int_x^1 y_2(y;l)\phi_j^{(l)}(y)\mathrm{d}y\mathrm{d}x - \int_b^1 y_2(x;l)\phi_i^{(l)}(x)\int_x^1 y_1(y;l)\phi_j^{(l)}(y)\mathrm{d}y\mathrm{d}x. \tag{5.55}$$

As stated earlier, volume conservation (5.15e) is naturally satisfied for interface disturbances with a non-trivial ($l \neq 0$) azimuthal wave-number. Hence, the basis functions

$$\phi_j^{(l)}(\rho,\theta) = \rho^j P_j^{(l)}(\cos\theta) \tag{5.56}$$

are used to generate the matrix elements (5.54,5.55). Here $P_j^{(l)}$ is the Legendre function of order l and degree j. The following restriction on the polar j and azimuthal l wave-umbers is needed to ensure the no-penetration conditions is satisfied: $l + j =$ even. Additionally, a consistency condition requires $j \geq l$. Thus, the sum in (5.52) runs from l to $l+N$. These conditions are a result of well-known properties of the Legendre functions $P_j^{(l)}$ (MacRobert, 1967).

The normal derivatives of the basis functions (5.56) on the equilibrium surface are given by

$$\frac{\partial\phi_j^{(l)}}{\partial n} \equiv \boldsymbol{\nabla}\phi^{(l)}\cdot\boldsymbol{n} = 2jP_{2j}^{(l)}(\cos\theta)\left(-\sin s\sin\theta + \cos s\cos\theta\right)(\rho)^{2j-1} + \sin\theta P_{2j}^{'(l)}(\cos\theta)\left(\sin s\cos\theta + \cos s\sin\theta\right)(\rho)^{2j-1}. \tag{5.57}$$

As before, to define the basis functions (5.56) and their normal derivatives (5.57) on the equilibrium surface, one uses the coordinate transformation (5.51) and the parametric representation of the equilibrium surface (5.5).

5.4.3 Results for kinematic disturbances

The eigenvalues $\lambda_{k,l}$ of (5.46,5.53), as they depend upon the contact-angle α and azimuthal wave-number l, have been computed using a resolution of $N = 10$ basis functions in the solution series (5.45,5.52) for both natural and pinned disturbance classes. Computations show this particular truncation exhibits relative error of 0.1% for the first three eigenfrequencies. The eigenfunction or velocity potential associated with the eigenfrequency $\lambda_{k,l}$ and corresponding eigenvector $a_j^{(k,l)}$ is given by

$$\phi^{(k,l)}(x) = \sum_{j=l}^{l+N} a_j^{(k,l)} \phi_j^{(l)}(x). \tag{5.58}$$

Here eigenfrequencies/vectors are distinguished by polar k and azimuthal l wave-numbers. Similarly, the mode shape or interface deformation related to this potential function is expressed as

$$y^{(k,l)}(x) = \sum_{j=l}^{l+N} a_j^{(k,l)} \left(\frac{\partial \phi_j^{(l)}}{\partial n} \right)(x). \tag{5.59}$$

Low azimuthal wave-number $l = 0, 1$

To distinguish between kinematic disturbance classes, figure 5.6 plots frequency $\lambda_{k,l}$ against contact-angle α for $l = 0, 1$ azimuthal wave-number. Here the natural frequency is always smaller than the corresponding pinned case, which could have been anticipated considering the fixed contact-angle disturbance is the 'natural' disturbance for the sessile drop. Sample mode shapes are given in figures 5.7,5.8 for pinned and natural disturbances, respectively. Recall that the mode shapes are effectively normalized by the metric inherited from the denominator in the Rayleigh-Ritz ratio–that is, per unit 'inertia.'

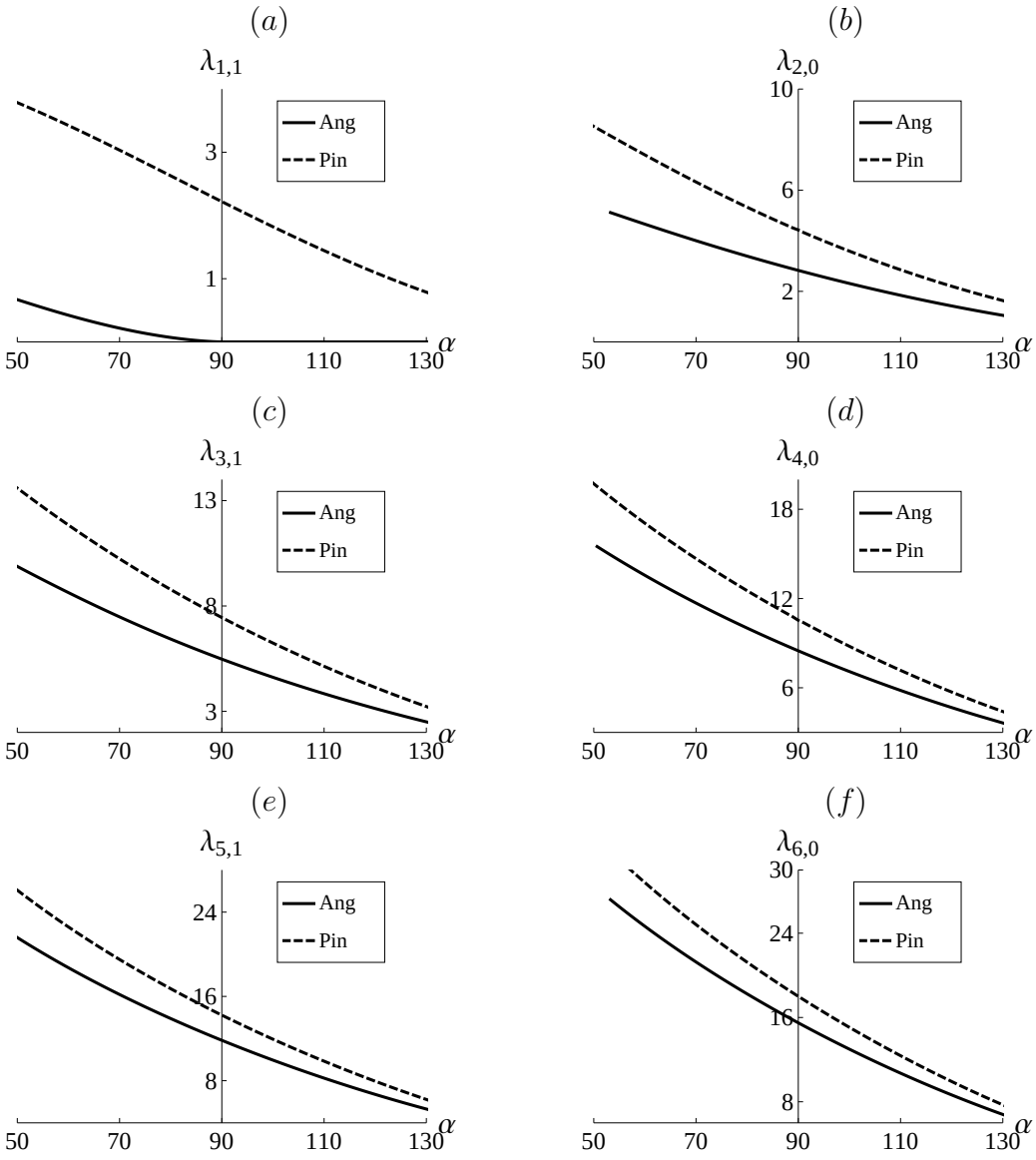

Figure 5.6: Frequency $\lambda_{k,l}$ against contact-angle α for natural (Ang) and pinned (Pin) modes $[k,l]$ with low azimuthal wave-number $l = 0, 1$: (a) $[1,1]$, (b) $[2,0]$, (c) $[3,1]$, (d) $[4,0]$, (e) $[5,1]$, and (f) $[6,0]$. Here $\mathrm{Im}[\lambda_{1,1}] = 0$ in all cases except $\alpha > 90°$ (c.f. figure 5.10). Note that the scalings of the frequency axis are different from (a) to (f).

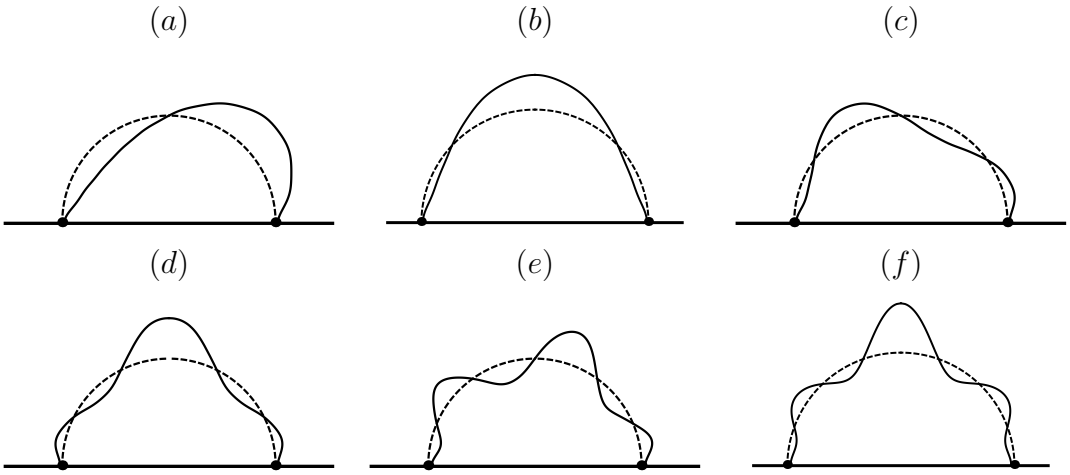

Figure 5.7: Pinned mode shapes $[k, l]$ for hemispherical base-state $\alpha = 90°$: (a) $[1, 1]$, (b) $[2, 0]$, (c) $[3, 1]$, (d) $[4, 0]$, (e) $[5, 1]$, and (f) $[6, 0]$ (polar view).

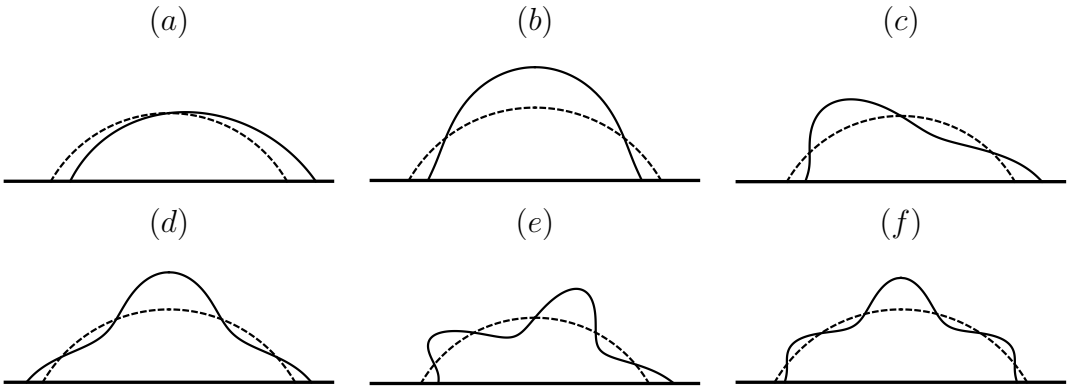

Figure 5.8: Natural mode shapes $[k, l]$ for sub-hemispherical base-state $\alpha = 60°$: (a) $[1, 1]$, (b) $[2, 0]$, (c) $[3, 1]$, (d) $[4, 0]$, (e) $[5, 1]$, and (f) $[6, 0]$ (polar view).

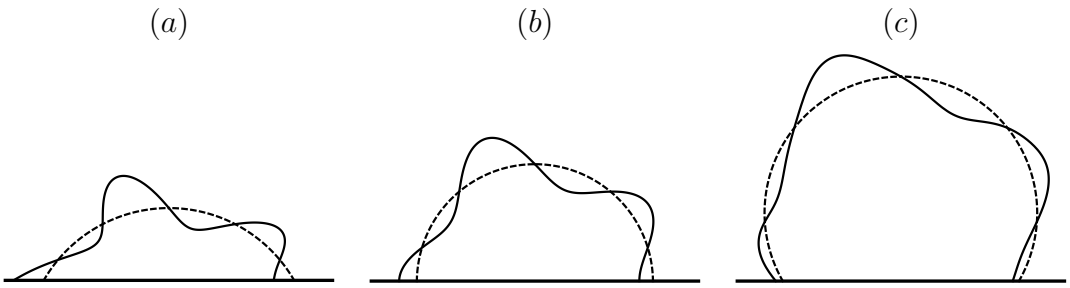

Figure 5.9: Contact-line mobility of the natural mode shape $[k, l] = [5, 1]$ for contact-angle (a) 60°, (b) 90°, and (c) 120°.

As the static contact-angle $\alpha \to 180°$ or in the limit of the drop touching the support plane along an infinitesimal generating circle, the frequencies for the two kinematic disturbances are indistinguishable. In this limit, the natural disturbance class degenerates into the pinned disturbance. To explain, one can compare the characteristic motion around the contact-line for the natural disturbance class to show that the super-hemispherical $\alpha > 90°$ drops has a relatively immobile contact-line that is essentially fixed, while the contact-line of the sub-hemispherical $\alpha < 90°$ drop is much more mobile. This feature is evident from figure 5.9, which plots the $k, l = 5, 1$ natural mode shape for three different base-states. Here the interface displacement around the contact-line is larger and more pronounced for the sub-hemispherical drop in comparison to the super-hemispherical drop. In fact, the displacement of the contact-line for the natural mode shape with polar wave-number k decreases as the static contact-angle increases from 0° to 180°, where the displacement is zero or the contact-line is fixed.

In addition to the static contact-angle, contact-line displacement is greatly influenced by the polar wave-number k. Consider the displacement of the interface at the contact-line for the natural mode shapes shown in figure 5.8, which is seen to decrease as the polar wave-number increases. This contact-line behavior is

characteristic of the natural disturbance class and is independent of static contact-angle. One could have also inferred that contact-line mobility decreases with polar wave-number by examining the relative difference $(\lambda_p - \lambda_n)/\lambda_p$ between the natural (λ_n) and pinned (λ_p) frequencies, which may be used as a measure of contact-line displacement (mobility). For example, the $k, l = 6, 0$ mode for the hemispherical drop ($\alpha = 90°$) has a relative frequency difference of 11%, which compares to a difference of 42% for the $k, l = 2, 0$ mode. A small difference in frequency (measure) indicates the contact-line is essentially pinned and one cannot distinguish between the natural and pinned disturbance. With regards to the example mentioned above, one may conclude that the $k, l = 6, 0$ mode has a much smaller contact-line displacement than the $k, l = 2, 0$ mode. Similarly, one could use this interpretation for figure 5.6 to conclude that the mode shapes for the super-hemispherical base-states have relatively immobile contact-lines.

As might have been anticipated, the natural $k, l = 1, 1$ mode for the hemispherical base-state has zero-frequency and corresponds to a rigid, horizontal translation of the drop's center-of-mass. This motion is analogous to the zero-frequency mode of the drop pinned on an equatorial circle-of-contact and likewise can be attributed to the additional symmetry inherent in the hemispherical base-state (Field *et al.*, 1991). One can prove that the oscillation frequency of this mode shape is necessarily zero. The proof is sketched here. To begin, the function $P_1^{(1)}(x)$ is a fundamental solution of the curvature operator (5.21b) and uniquely satisfies the natural boundary conditions (5.26) for this base-state. Therefore, this function belongs to the kernel of (5.21b). It is also straightforward to show that the 'inertia' operator (5.21a) is positive definite. Thus, applying the Fredholm alternative for linear operators to this particular mode shape delivers $\lambda_{1,1}^2 = 0$.

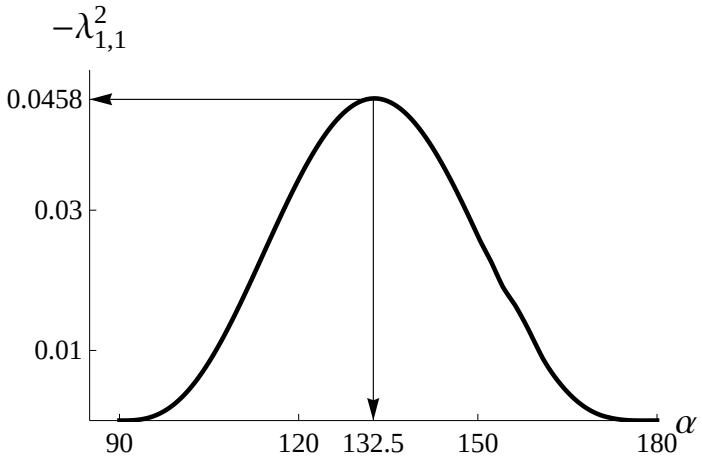

Figure 5.10: Instability growth rate $-\lambda_{1,1}^2$ against contact-angle α for a sessile drop subject to a natural disturbance, exhibiting a maximum growth rate ($-\lambda_{1,1}^2 = 0.0458$) at $\alpha = 132.5°$.

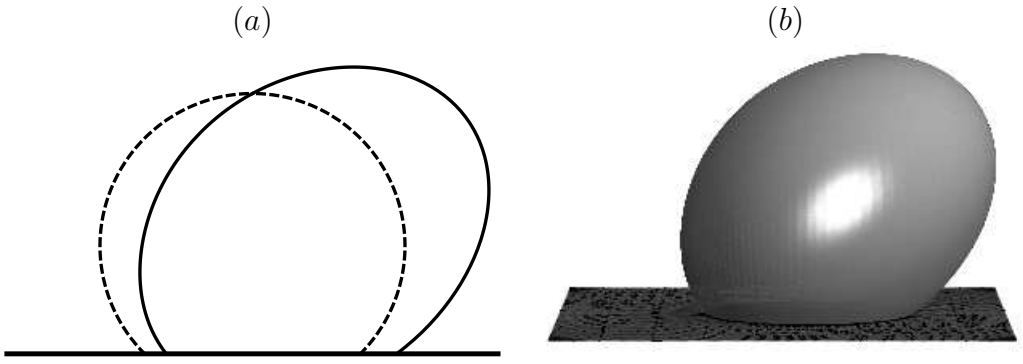

Figure 5.11: Typical instability mode shape $[1, 1]$ with contact-angle $\alpha = 120°$ in (a) polar and (b) three-dimensional views.

'Walking' instability

In addition to a number of oscillatory mode shapes, the sessile drop exhibits instability ($\lambda^2 < 0$) to the natural disturbance class for the super-hemispherical base states; that is, those in the range of contact angles $90° < \alpha < 180°$. Figure 5.10, which plots the square of the instability growth rate $-\lambda_{1,1}^2$ against static

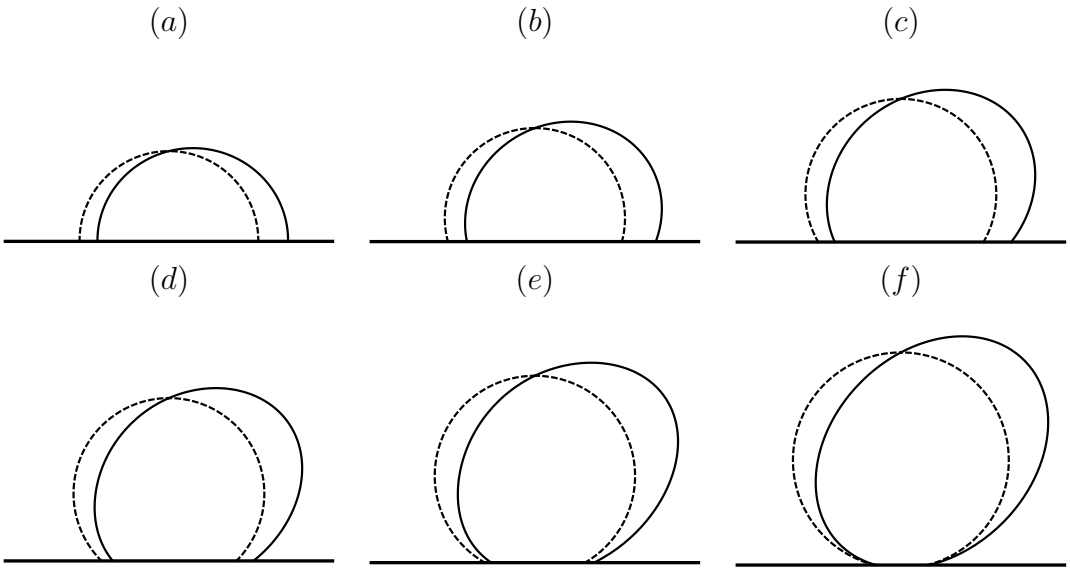

Figure 5.12: Instability mode shape $[1, 1]$ with contact-angle (a) 91°, (b) 105°, (c) 120°, (d) 135°, (e) 150°, and (f) 170° in polar view.

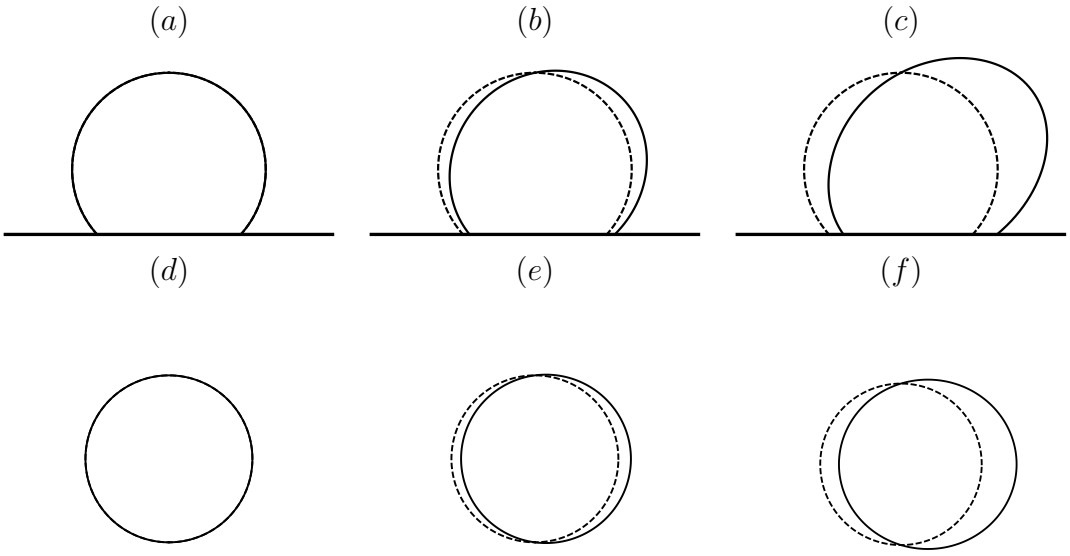

Figure 5.13: Time series of the instability mode shape with largest growth rate ($-\lambda_{1,1}^2 = 0.0458$): (a, b, c) polar view and (d, e, f) contact-line footprint at time (a, d) $t = 0$, (b, e) $t = T/2$ and (c, f) $t = T$ ($\alpha = 132.5°$). Here T represents the time it takes to disturb the interface by a given amplitude ($T = 1.226$ in this figure).

contact-angle α, shows that the maximum growth rate ($-\lambda_{1,1}^2 = 0.0458$) occurs at $\alpha = 132.5°$. Typical unstable mode shapes are shown in figures 5.11 & 5.12. Here the disturbed shape (solid) has been made to intersect the undisturbed shape (dashed) at its apex (north pole) as a convention, although there is no fundamental reason to do so (c.f. figure 5.12). The characteristic feature of this instability is an advancing contact-line, which is accelerating relative to its corresponding receding contact-line, thereby displacing mass from one side of the drop to the other, as shown in figure 5.13. To illustrate, figure 5.13(b) demonstrates how the contact-line footprint deforms from a circle into an ellipse as the instability evolves in time. Forcing the contact-lines to be 'pinned' naturally suppresses the instability and the possibility of 'walking', while generating oscillatory motion for all contact angles (c.f. figure 5.6(a)).

Instability occurs when the perturbed state has a lower potential energy than the corresponding base-state. To investigate the nature of this instability, one can start with the second variation of potential energy (c.f. eqn. 1.5),

$$\delta^2 U = -\int_b^1 \left[\left(\left(1-x^2\right) y' \right)' + \left(2 - \frac{1}{1-x^2} \right) \right] y \, \mathrm{d}x, \tag{5.60}$$

and integrate by parts using the natural boundary condition (5.26) to obtain

$$\delta^2 U = \int_b^1 \left[\left(1-x^2\right) \left(y'\right)^2 - \left(2 - \frac{1}{1-x^2} \right) y^2 \right] \mathrm{d}x + b\sqrt{1-b^2}\, y^2(b), \tag{5.61}$$

with $b \equiv \cos\alpha$. This equivalent form of the total disturbance energy E_t may be decomposed into two interfacial energies (E_1, E_2) and one contact-line energy (E_3),

$$E_t = E_1 + E_2 + E_3 \tag{5.62a}$$

$$E_1 \equiv \int_b^1 \left[\left(1-x^2\right) \left(y'\right)^2 + \left(\frac{1}{1-x^2} \right) y^2 \right] \mathrm{d}x \tag{5.62b}$$

$$E_2 \equiv -\int_b^1 2\, y^2 \mathrm{d}x \tag{5.62c}$$

$$E_3 \equiv b\sqrt{1-b^2}\, y^2(b). \tag{5.62d}$$

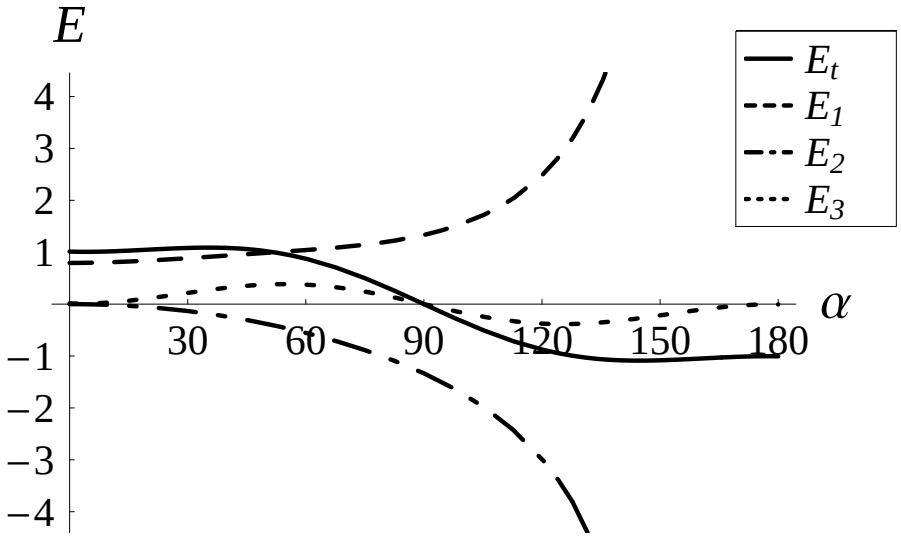

Figure 5.14: Decomposition of disturbance energy (E) against contact-angle α for the $[1, 1]$ instability mode.

Here the interfacial energy E_1 is a positive-definite (stabilizing) measure of the gradients in mean-curvature of the perturbed surface, while E_2 is negative-definite (destabilizing) and represents the tendency of a volume of liquid to form an isolated spherical drop (minimal energy state). In contrast, the contact-line energy E_3 can either stabilize ($E_3 > 0$) or destabilize ($E_3 < 0$), depending upon the geometry of the base-state. Contrast with the case of the rivulet reported by Davis (1980). See also, Chapter 6.

Of course, a linear analysis cannot reveal what configuration that an instability will finally lead to, but one may speculate that the instability reported here will cause the drop to walk along the surface-of-support because of the following mechanism. Figure 5.14, which plots the decomposition of disturbance energy (5.62) for the instability mode shape y, shows that both interfacial (E_2) and contact-line (E_3) terms drive the instability. The interfacial energy E_2 is always destabilizing and its associated instability mechanism has been mentioned above. In contrast, the

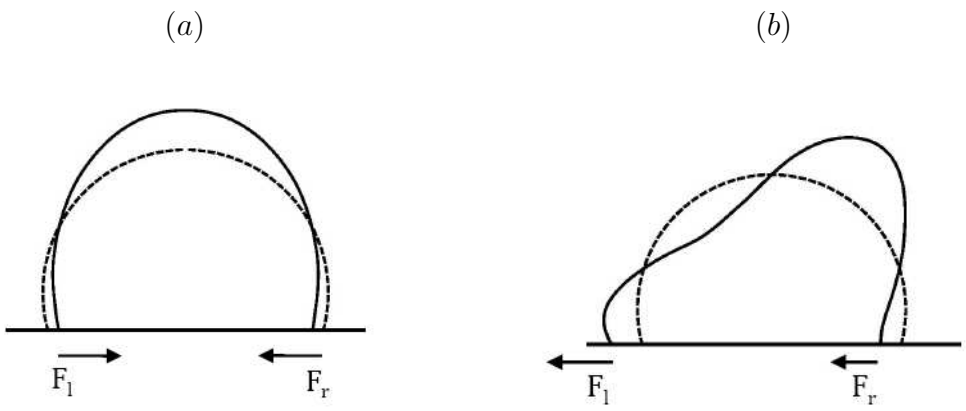

Figure 5.15: Visualization of the left (F_l) and right (F_r) constraint force at the contact-line for the natural mode shapes with (a) even and (b) odd symmetry about the vertical mid-plane.

contact-line energy E_3 is destabilizing for the range of contact angles that exhibit instability ($90° < \alpha < 180°$). Here energy is supplied to the drop from the contact-line by a 'virtual' force acting at the contact-line that does work on the drop. To explain the origins of this force, consider the natural boundary condition, which preserves the static contact-angle, as an auxiliary constraint on the drop motion. An arbitrary (unconstrained) interface disturbance does not satisfy the static force balance at the contact-line or preserve the static contact-angle and is therefore not in equilibrium. Thus, to maintain the static contact-angle during deformation, a constraint force must be applied on the contact-line. This constraint force is typical of problems with an auxiliary condition and may or may not have a net effect on the drop. For example, if the disturbance is mirror-symmetric (even) about the vertical mid-plane (c.f. figure 5.15(a)), the constraint forces from the left (F_l) and right (F_r) contact lines produce no net force on the drop, because they have equal magnitude and act in opposite directions. On the contrary, disturbances with odd-symmetry (c.f. figure 5.15(b)) can generate a net force, because

the constraint forces from the advancing and receding contact-line act in the same direction. This net force drives the 'walking' instability and also explains why the instability mode shape is the sole carrier of the drop's horizontal center-of-mass motion.

High azimuthal wave-number $l \geq 2$

Lastly, one can examine the role of azimuthal wave-number l on the characteristic frequencies and mode shapes for the kinematic disturbance classes. The mode shapes are decomposed into three categories and are conveniently distinguished by their wave-number pair $[k, l]$ using standard terminology for the spherical harmonics (MacRobert, 1967); i) zonal, ii) sectoral, and iii) tesseral. Zonal shapes ($l = 0$) are axisymmetric and do not intersect the undisturbed shape along a longitudinal line. On the contrary, sectoral mode shapes ($k = l$) have no latitudinal crossings, except if the contact lines are pinned. Mode shapes associated with all other wave-number pairs are referred to as tesseral. Given a natural mode shape with wave-number pair $[k, l]$, there are precisely $2l$ longitudinal and $k - l$ latitudinal crossings or intersections of the undisturbed shape. For the sectoral and tesseral mode shapes, there is necessarily a crossing at the north pole that has not been counted. The pinned mode shapes have two additional latitudinal crossings, because the support plane lies along a constant latitude. To illustrate, mode shapes from the three categories are plotted in figures 5.16 & 5.17 for natural and pinned contact-line disturbances, respectively.

With regards to oscillation frequencies, figure 5.18 shows that the natural frequencies of polar wave-number k are degenerate with respect to azimuthal wave-number l for the hemispherical base-state $\alpha = 90°$. Varying the static contact-angle

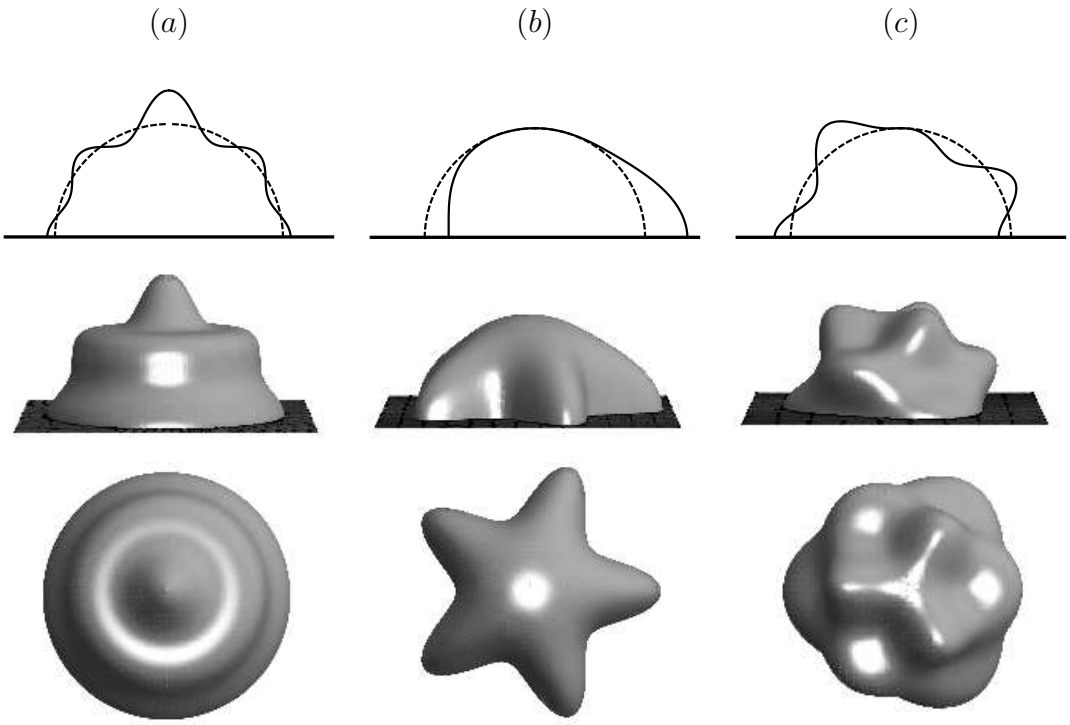

Figure 5.16: Natural mode shapes $[k, l]$ in polar and three-dimensional side/top views for (a) zonal $[8, 0]$, (b) sectoral $[5, 5]$, and (c) tesseral $[7, 3]$ disturbances for $\alpha = 90°$.

α or volume breaks this degeneracy. Here frequencies for the sub-hemispherical $\alpha < 90°$ base-states decrease with increasing azimuthal wave-number. The opposite is true for the super-hemispherical $\alpha > 90°$ base-states. As shown, the relative frequency difference between the zonal $l = 0$ and sectoral $l = k$ mode shapes can be large. For example, the frequency difference between the $k, l = 4, 0$ and $k, l = 4, 4$ mode shapes approaches 100% for the base-state $\alpha = 50°$ subject to natural disturbances. Although the magnitude may be surprising, the difference in frequencies is not completely unexpected. Recall that the sectoral mode shape has the fewest number of latitudinal crossings or 'nodes', has the greatest contact-line mobility and is therefore the preferred disturbance by sub-hemispherical base-states. In contrast, super-hemispherical base-states favor less mobile contact lines

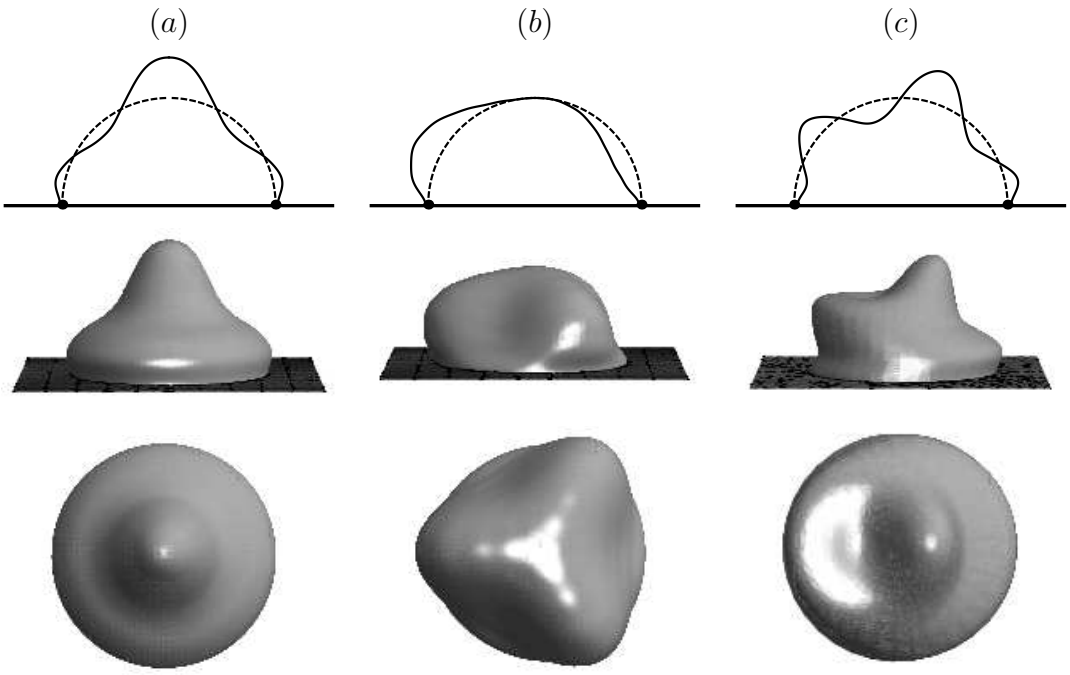

Figure 5.17: Pinned mode shapes $[k, l]$ of the hemispherical base-state $\alpha = 90°$ in polar and three-dimensional side/top views for (a) zonal $[4, 0]$, (b) sectoral $[3, 3]$, and (c) tesseral $[5, 1]$ disturbances.

and zonal mode shapes are to be expected. The qualitative behavior of the two types of kinematic disturbance are similar, but there are a couple of distinctions. The first and most apparent difference is the magnitude of the pinned contact-line frequency splitting between the zonal and sectoral mode shapes, which is much smaller than the corresponding frequency range for the natural disturbance class. The size of this splitting can be seen in figure 5.19, which plots the pinned frequencies against static contact-angle. Another interesting feature of figure 5.19 is that the azimuthal wave-number degeneracy of the hemispherical base-state has been eliminated. The relationship between this degeneracy and the symmetry of the system are intimately connected and will be expanded upon further in the following section.

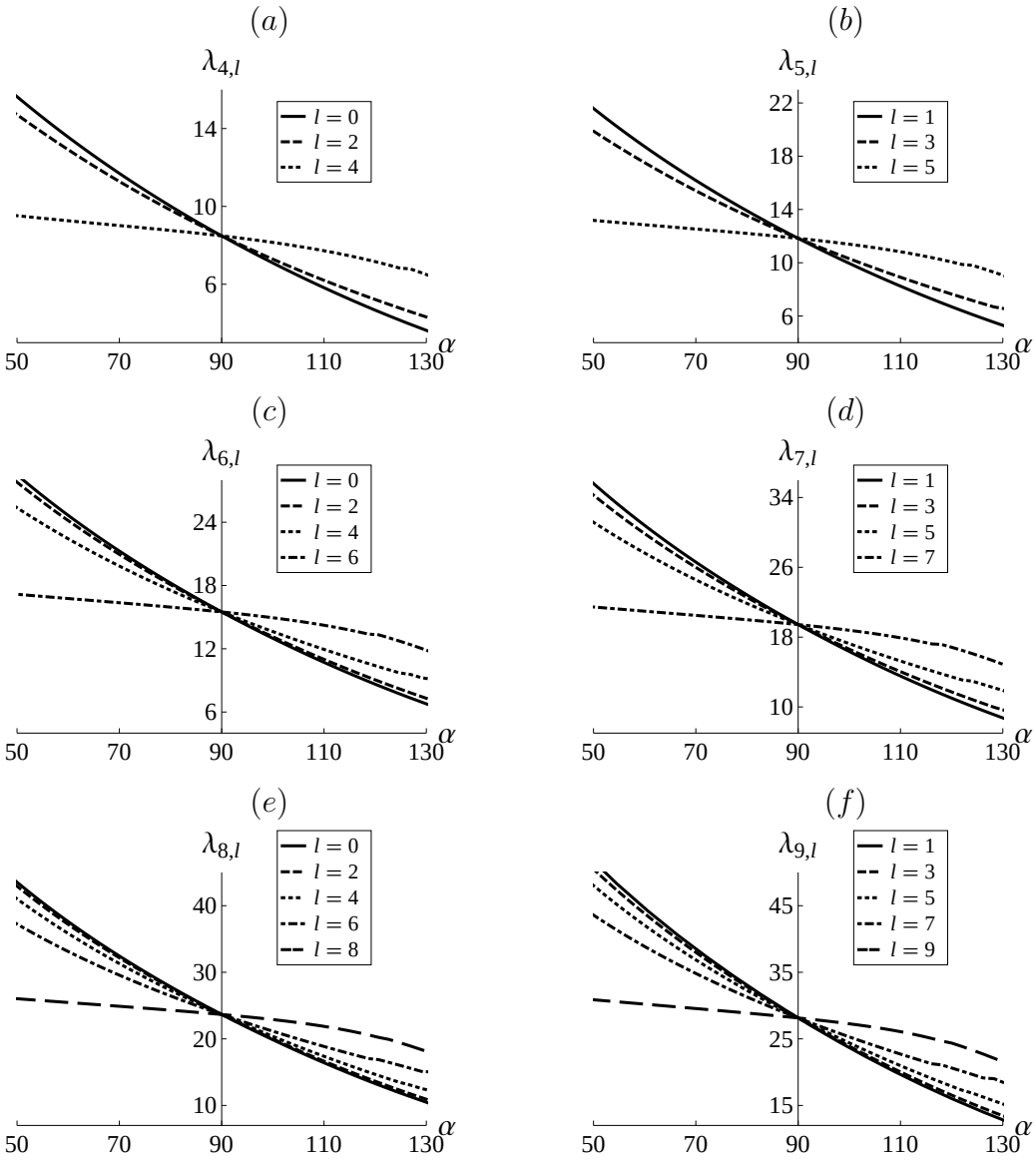

Figure 5.18: Natural frequency $\lambda_{k,l}$, as it depends upon azimuthal wave-number l, against contact-angle α for fixed polar wave-number (a) $k = 4$, (b) $k = 5$, (c) $k = 6$, (d) $k = 7$, (e) $k = 8$, and (f) $k = 9$.

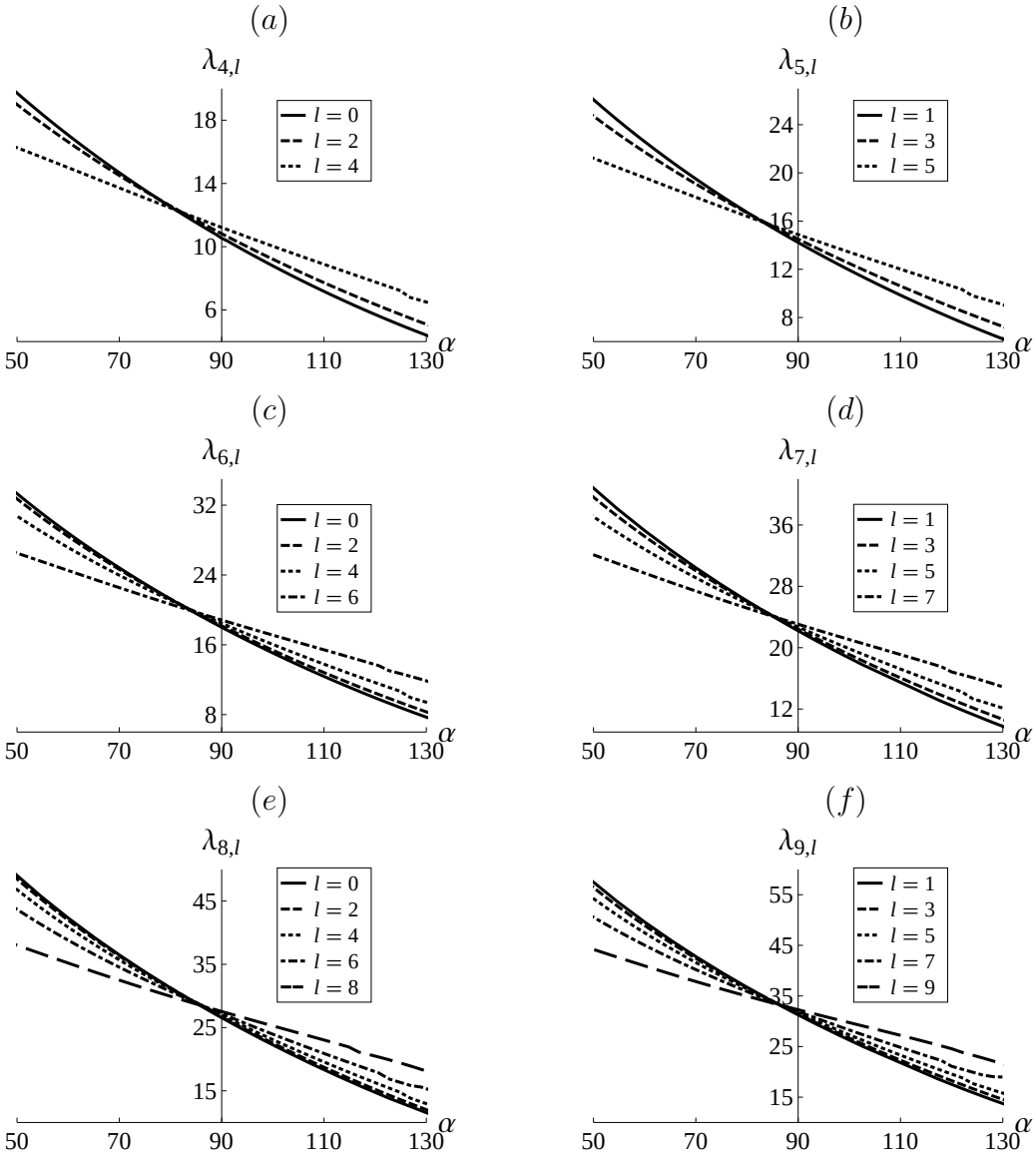

Figure 5.19: Pinned frequency $\lambda_{k,l}$, as it depends upon azimuthal wave-number l, against contact-angle α for fixed polar wave-number (a) $k = 4$, (b) $k = 5$, (c) $k = 6$, (d) $k = 7$, (e) $k = 8$, and (f) $k = 9$.

5.5 Solution method for contact-line speed relation

In principle, the inverse method could be used to satisfy the dynamic contact-line condition (5.30), but this formulation gives rise to an integral operator with the eigenvalue parameter in its kernel, which is notorious for computational instability (e.g. Walter, 1973). To circumvent this issue, select results from the natural disturbance class are utilized and the structure of the variational problem associated with (5.19) is exploited. Essentially this is an ad hoc approach. It will be shown that contact-angle variation associated with the contact-line speed condition (5.30) is a purely dissipative process.

5.5.1 Operator construction

By exploiting the structure of the variational problem associated with (5.19), the reduced operator equation is cast in a particularly advantageous form. Namely, the second variation of surface energy is given by

$$\delta^2 U = -\int_\Gamma \left(\left(\kappa_1^2 + \kappa_2^2\right) \frac{\partial \phi}{\partial n} + \Delta_\Gamma \frac{\partial \phi}{\partial n} \right) \frac{\partial \phi}{\partial n} + \int_\gamma \left(\frac{\partial}{\partial s}\left(\frac{\partial \phi}{\partial n}\right) + \cos(\alpha) \frac{\partial \phi}{\partial n} \right) \frac{\partial \phi}{\partial n}, \tag{5.63}$$

which is comprised of free surface Γ and contact line γ contributions. The Euler-Lagrange equations associated with this second variation give rise to the hydrodynamic boundary value problem (5.15d) for the natural disturbance class. It is clear from the contact-line contribution to (5.63) that the fixed contact-angle condition (5.26) is the 'natural' boundary condition, as there is no contact-line energy associated with these motions. Thus, the natural disturbances are seen to be the true minimizers of the functional eigenvalue problem (5.20) and the function space

spanned by these orthogonal mode shapes form a complete set.

5.5.2 Hybrid Ritz method

Recall that the necessary input to the Rayleigh-Ritz procedure is a set of functions which span a pre-determined function space. Thus, in implementing the forward method on the operator equation (5.20) one could choose to use the complete set of natural mode shapes $y^{(j,l)}$, defined in (5.59), as the basis functions in the requisite solution series

$$\frac{\partial \phi^{(l)}}{\partial n} = \sum_{j=l}^{l+N} c_j y^{(j,l)}(x). \tag{5.64}$$

By construction, volume is conserved according to (5.15e) for this particular set of functions. Application of the forward method requires the computation of the velocity potential corresponding to the respective interface perturbation. As stated earlier, this proves a daunting task for most geometries, including the spherical cap geometry used here. However, judicious choice of the solution series (5.64) can completely eliminate this difficulty. To explain, recall that application of the inverse method to the operator equation (5.23) results in eigenfunctions (5.58) that are identified as velocity potentials, with the corresponding interface disturbance (5.59). That is, the eigenfunction (5.58) is a velocity potential ϕ that generates an interface disturbance $y \propto \partial\phi/\partial n$ as defined in (5.59). Equivalently, one could say the *known* interface disturbance $y^{(j,l)}$ generates the *known* velocity potential $\phi^{(j,l)}$. This solves precisely the difficulty mentioned above: compute the velocity potential for a given interface disturbance in a relatively simple manner. Of course the question remains, why choose the natural mode shapes as the basis functions for the solution series (5.64)? As stated earlier, the fixed contact-angle disturbances are the 'natural' disturbances and the space which they span is the largest and

least restrictive (see Courant & Hilbert, 1953; Lanczos, 1986; Segel, 1987).

Finally, the set of algebraic equations which result from the application of the Rayleigh-Ritz procedure to the forward problem are written as

$$\sum_{j=l}^{l+N} \left[K_{ij}^{(l)} + \frac{i\omega}{\sqrt{1-b^2}} \Phi_{ij}^{(l)} + \frac{\omega^2}{1-b^2} M_{ij}^{(l)} \right] c_j = 0, \tag{5.65}$$

with matrix elements

$$K_{ij}^{(l)} \equiv \int_b^1 \left(\left(1-x^2\right) y_{xx}^{(i,l)} - 2x y_x^{(i,l)} + \left(2 - \frac{l^2}{1-x^2} \right) y^{(i,l)} \right) y^{(j,l)} \mathrm{d}x, \tag{5.66a}$$

$$\Phi_{ij}^{(l)} \equiv \Lambda \, y^{(i,l)}(b) \, y^{(j,l)}(b), \tag{5.66b}$$

$$M_{ij}^{(l)} \equiv \int_b^1 \phi^{(i,l)} y^{(j,l)} \mathrm{d}x. \tag{5.66c}$$

As evident from the damped harmonic oscillator structure of (5.65), contact-angle variation controlled by the spreading parameter Λ in (5.66b) is a purely dissipative process.

5.5.3 Results

The oscillation frequencies are computed as the roots of the characteristic equation resulting from (5.65) for a given truncation N. Given a static contact-angle α and spreading parameter Λ, computations show that a truncation of $N = 12$ terms in the solution series (5.64) is sufficient to generate relative error of 0.1% for the first three frequencies. The mode shapes corresponding to these frequencies are then given by

$$\psi^{(k,l)} = \sum_{j=l}^{l+N} c_j^{(k,l)} y^{(j,l)}, \tag{5.67}$$

where $c_j^{(k,l)}$ is the respective coefficient eigenvector with polar k and azimuthal l wave-numbers.

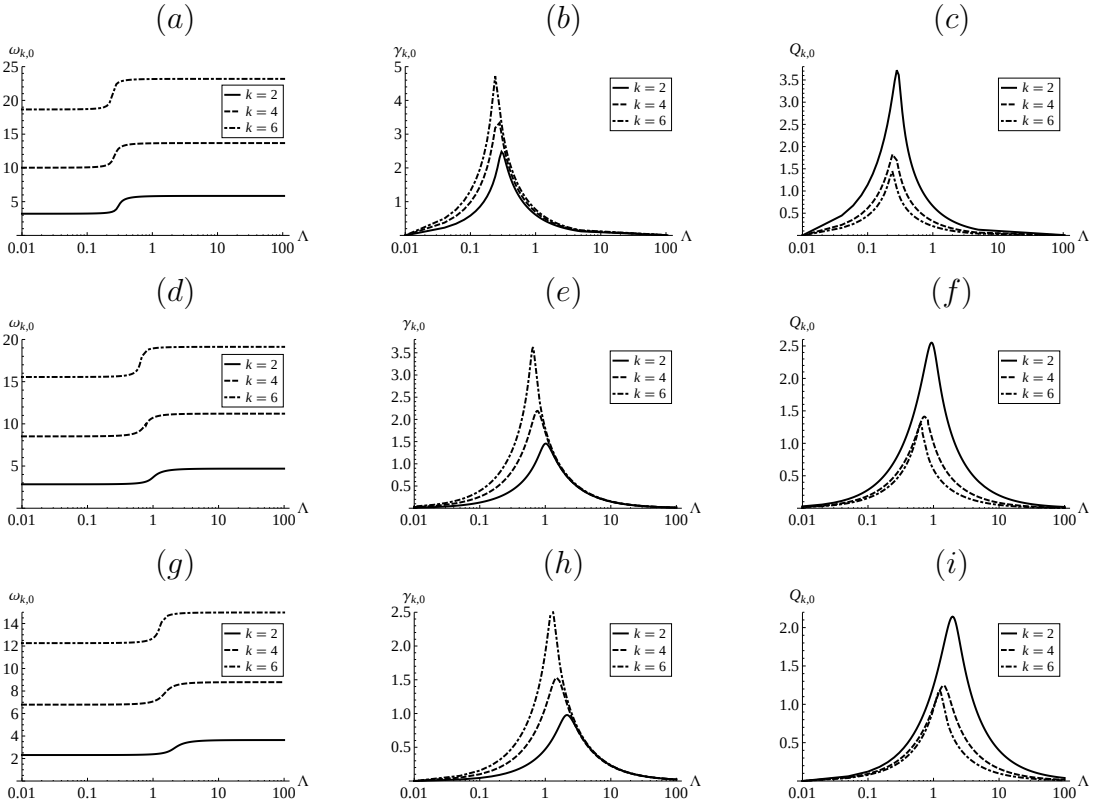

Figure 5.20: Oscillation frequency $\omega_{k,0}$ (a, d, g), decay rate $\gamma_{k,0}$ (b, e, h) and effective dissipation $Q_{k,0}$ (c, f, i) as a function of the spreading parameter Λ for a contact-angle (a, b, c) $\alpha = 75°$, (d, e, f) $\alpha = 90°$ and (g, h, i) $\alpha = 105°$.

Effective dissipation

The spreading parameter Λ is a measure of the mobility of the contact-line and can also be used to smoothly vary the boundary conditions on the three-phase contact-line, thereby, changing the disturbance class from natural ($\Lambda \to 0$) to pinned contact-line ($\Lambda \to \infty$). The postulated constitutive law (5.28), which assumed the dynamic contact-angle was a function of contact-line speed gave rise to the contact-line speed boundary condition (5.30) and finally the variational form of the governing equations (5.65), from which it has been shown that contact-angle

variation is a purely dissipative process controlled by the spreading parameter. The complex frequencies $\lambda = -\gamma + i\omega$ are computed from (5.65) as a function of the spreading parameter Λ for the axisymmetric ($l = 0$) mode shapes in figure 5.20. Here in both the natural ($\Lambda \to 0$) and pinned ($\Lambda \to \infty$) limits, no energy is dissipated for such motions, while for finite values of the spreading parameter, it is the high polar wave-number mode shapes that have the largest decay rate $\gamma_{k,0}$. A similar decay rate relationship, $\gamma \propto (k-1)(2k+1)$, has been derived from bulk viscous effects for the isolated spherical drop by Lamb (1932). That is, the decay rate increases monotonically with polar wave-number k. However, if one uses the damped-harmonic oscillator structure of (5.65) and related formalism to define the effective dissipation over an oscillation cycle as

$$Q_{k,l} \equiv 2\pi \frac{\gamma_{k,l}}{\omega_{k,l}}, \tag{5.68}$$

the results may be surprising. For reference, the dissipation due to bulk viscous effects for the spherical fluid drop is given by $Q_{k,l} \propto \sqrt{k}$.

As shown in figure 5.20(c, f, i), which plots the effective dissipation $Q_{k,0}$ for the axisymmetric mode shapes ($l = 0$) as a function of the spreading parameter Λ, it is the low polar wave-number modes that dissipate the most energy. This can be directly attributed to the contact-line mobility, which was discussed in a prior section. Recall that the motion of the contact-line was most pronounced for the low polar wave-number mode shapes. Thus, if the dissipation mechanism for this constitutive law is the contact-line mobility, it stands to reason that the low wave-number mode shapes will dissipate the most energy. Computational results substantiate this interpretation. Furthermore, it has been established in a previous section that contact-line mobility of the natural disturbance class decreases as the static contact-angle increases. To wit, figures 5.20(c) and 5.20(i) plot the effective dissipation $Q_{k,0}$ vs. spreading parameter Λ for a sub-hemispherical ($\alpha = 75°$) and

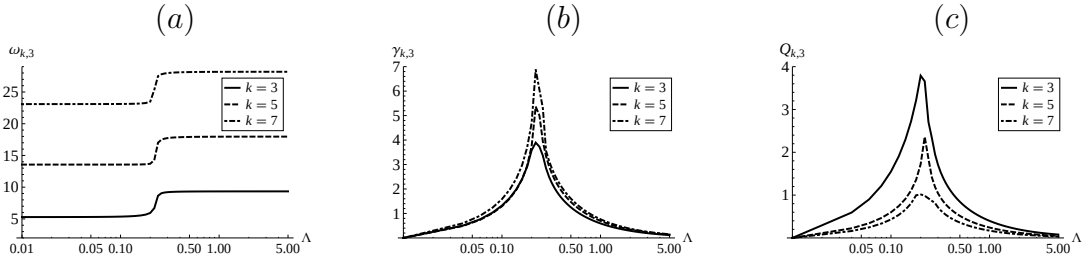

Figure 5.21: Oscillation frequency $\omega_{k,3}$ (a), decay rate $\gamma_{k,3}$ (b) and effective dissipation $Q_{k,3}$ (c) as a function of the spreading parameter Λ for contact-angle $\alpha = 75°$ and azimuthal wave-number $l = 3$.

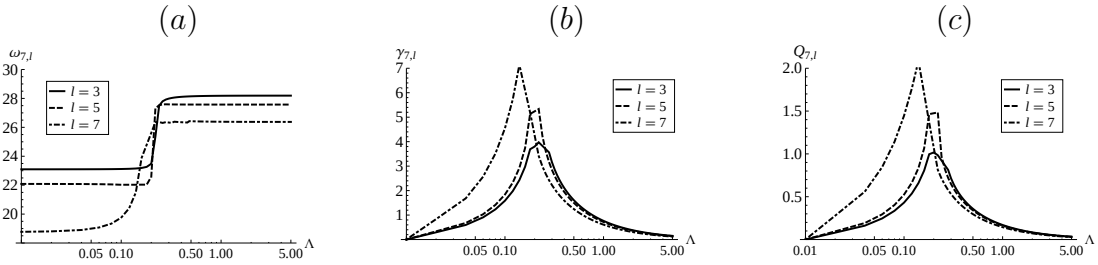

Figure 5.22: Oscillation frequency $\omega_{7,l}$ (a), decay rate $\gamma_{7,l}$ (b) and effective dissipation $Q_{7,l}$ (c) as a function of the spreading parameter Λ for contact-angle $\alpha = 75°$ and polar wave-number $k = 7$.

super-hemispherical ($\alpha = 105°$) base-state, respectively. Unsurprisingly, the mode shapes with smaller contact-angle α dissipate the most energy, as they have the more mobile contact lines, consistent with the interpretation of this constitutive law. For these comparisons, recall that the kinetic energy of the disturbance is normalized via the denominator in Rayleigh-Ritz quotient.

Large relative dissipation of energy by the low polar wave-number modes is not unique to the axisymmetric $l = 0$ disturbance class and persists for mode shapes of all non-zero azimuthal wave-number. This feature of the contact-line speed condition is independent of static contact-angle and is corroborated by figure 5.21, which plots the complex frequencies and effective dissipation as a function of the

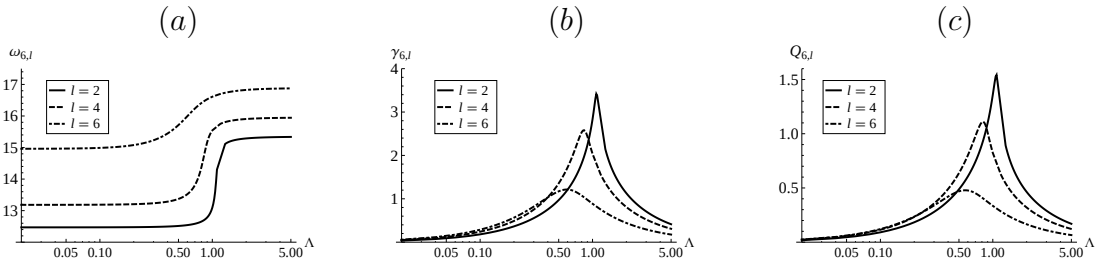

Figure 5.23: Oscillation frequency $\omega_{6,l}$ (a), decay rate $\gamma_{6,l}$ (b) and effective dissipation $Q_{6,l}$ (c) as a function of the spreading parameter Λ for contact-angle $\alpha = 105^\circ$ and polar wave-number $k = 6$.

spreading parameter for a drop with sub-hemispherical base state $\alpha = 75^\circ$ and fixed azimuthal wave-number $l = 3$. Alternatively, one can fix the polar wave-number k and analyze the effect of azimuthal wave-number l. To that end, figures 5.22 & 5.23 plot the complex frequency and effective dissipation against spreading parameter Λ for the sub-hemispherical $\alpha = 75^\circ$ base-state with $l = 7$ and super-hemispherical $\alpha = 105^\circ$ base-state with $l = 6$, respectively. Here no universal statement can be made with regards to the dissipation of an arbitrary mode shape with fixed polar wave-number. At different values of the spreading parameter, the mode shape that dissipates the largest amount of energy may change. For example, figure 5.23(c) shows that for spreading parameters $\Lambda = 0.5$ and $\Lambda = 1$, the $[6, 4]$ and $[6, 2]$ modes have the largest effective dissipation, respectively. However, the maximal effective dissipation over the range of spreading parameters is sensitive to the static contact-angle and equivalently the volume of the base-state. For fixed polar wave-number k, the mode shape of maximal dissipation has either the largest or smallest possible azimuthal wave-number for the sub-hemispherical and super-hemispherical base-states, respectively.

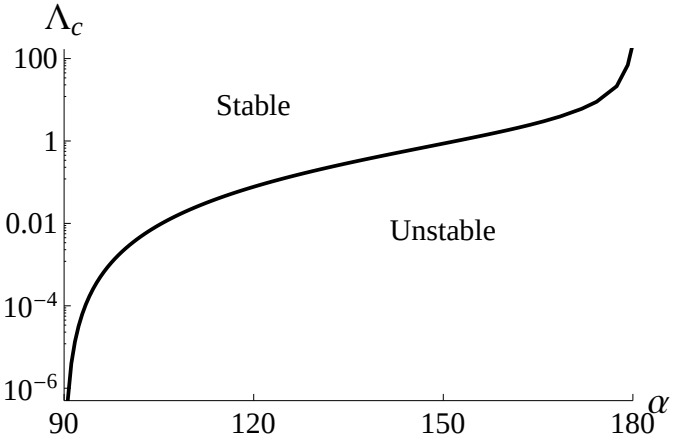

Figure 5.24: Stability diagram for the $[k, l] = [1, 1]$ mode: critical spreading parameter Λ_c against contact-angle α.

'Walking' instability

The effective dissipation, which results from the dynamic contact-line condition, can suppress the instability that the $[1, 1]$ mode exhibits for the super-hemispherical base-states (c.f. figure 5.10). To explain, recall that instability results when the perturbed state has a lower energy than the base-state. The base-state may be stabilized if there exists a mechanism to counteract this energy difference, such as the effective dissipation from the dynamic contact-line condition, which is controlled by the spreading parameter Λ. Figure 5.24 plots the critical spreading parameter Λ_c, where the base-state is neutrally stable or the dissipation exactly balances the energy difference, against the static contact-angle α. In the singular limit $\alpha \to 180°$, where the scaling radius shrinks to zero and the natural disturbance degenerates into a pinned contact-line, the instability window remains open (c.f. figure 5.24) despite the small instability growth rate observed in this limit (c.f. figure 5.10). Here the stabilizing ($E > 0$) effective dissipation (5.66b) tends to zero and cannot overcome the destabilizing disturbance energy ($E_t < 0$) seen in

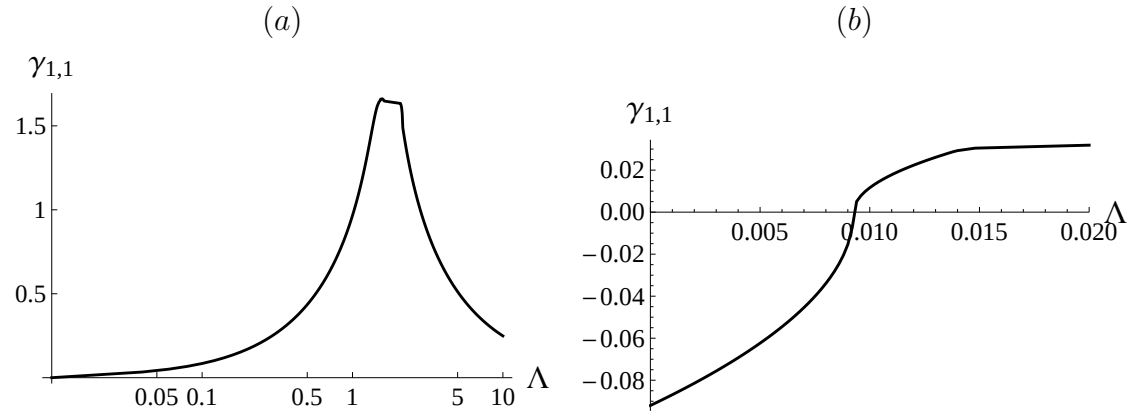

Figure 5.25: Complex frequency $\lambda = -\gamma + i\omega$ for the $[1,1]$ mode: (a) decay rate $\gamma_{1,1} > 0$ and (b) instability growth rate $\gamma_{1,1} < 0$ as a function of the spreading parameter Λ for contact-angle $\alpha = 105°$. See figure 5.27 (a) for corresponding oscillation frequency $\omega_{1,1}$.

figure 5.14. With regards to growth rate, the effective dissipation is a monotonically increasing function of the spreading parameter Λ, therefore the maximum instability growth rate corresponds to $\Lambda = 0$. As such, the maximum growth rate as a function of the contact-angle is shown in figure 5.10. A typical transition from instability $\gamma < 0$ to damped oscillations $\gamma > 0$ for the $[1,1]$ mode is shown in figure 5.25.

Symmetry breaking

As stated earlier, the natural mode shapes are degenerate with respect to azimuthal wave-number for the hemispherical drop. This occurs for the hemispherical base-state because it possesses more configurational symmetry than the other base-states and symmetries are known to produce degeneracies via Noether's theorem. The variational formulation of this problem is consistent with Noether's theorem and degeneracies in the hemispherical limit are to be expected. As shown earlier in

figures 5.18 & 5.19, this degeneracy is lifted by either i) pinning the contact lines or ii) by 'breaking' the configurational symmetry of the base-state. The degeneracy breaking mechanism for ii) is straightforward, while an interpretation of i) is more subtle. To elucidate, one can examine the second variation of surface energy (5.63) and more specifically the 'disturbance' energy associated with the contact-line motion (i.e. the second integral in (5.63)). Interface perturbations that have no related contact-line disturbance 'energy' are deemed 'natural' and necessarily satisfy the 'natural' boundary conditions for the system. For the sessile drop, the natural disturbance preserves the static contact-angle of the sessile drop. Implicit in Noether's theorem is the assumption that the boundary conditions associated with the second variation of energy are the 'natural' ones. Therefore, to lift the degeneracy associated with the hemispherical base-state one can introduce small deviations to the natural boundary conditions.

The utility of the contact-line speed condition (5.30) is that one can lift the degeneracy of the hemispherical drop by smoothly varying the spreading parameter Λ. Figure 5.26 plots the computed oscillatory frequency $\omega_{k,l}$ vs. spreading parameter Λ for the hemispherical base-state ($\alpha = 90°$). As expected, the degeneracy persists in the natural limit $\Lambda = 0$, is broken at some finite value of spreading parameter and stays broken until the pinned contact-line limit is reached at $\Lambda \to \infty$. For fixed polar wave-number k, the mode shapes with largest azimuthal wave-number $l = k$ have the greatest frequency in the pinned contact-line limit, because they have the smallest number of polar nodes, which makes it difficult to satisfy the pinned contact-line condition. To illustrate this phenomenon, sample mode shapes are shown in figures 5.16 & 5.17. Also, one can quantify the degree to which the degeneracy is lifted by analyzing the relative difference in frequencies between mode shapes of equal polar wave-number but differing azimuthal wave-

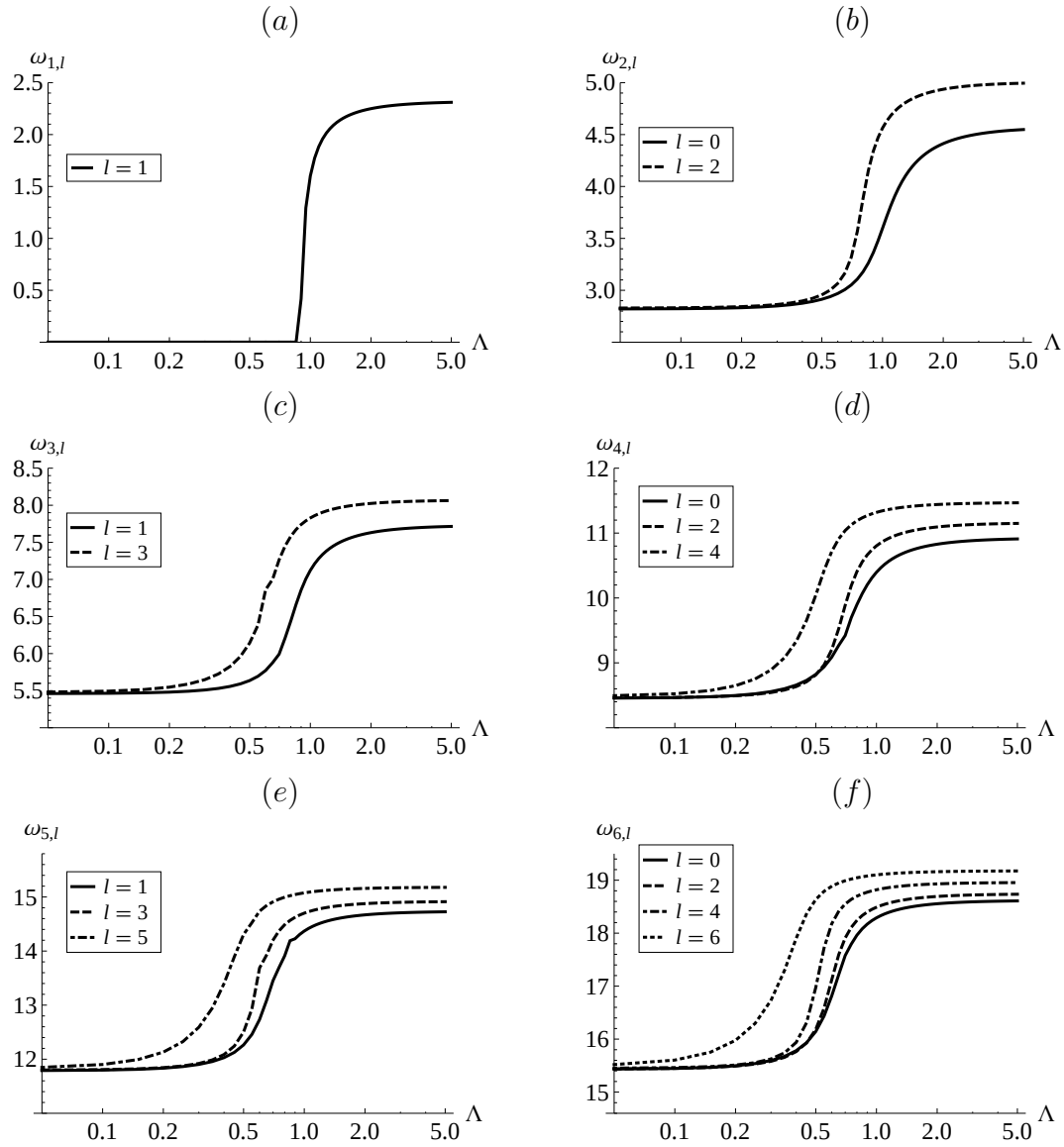

Figure 5.26: Oscillation frequency $\omega_{k,l}$, as it depends upon azimuthal wave-number l, against spreading parameter Λ for the hemispherical ($\alpha = 90°$) base-state with polar wave-number (a) $k = 1$, (b) $k = 2$, (c) $k = 3$, (d) $k = 4$, (e) $k = 5$, and (f) $k = 6$.

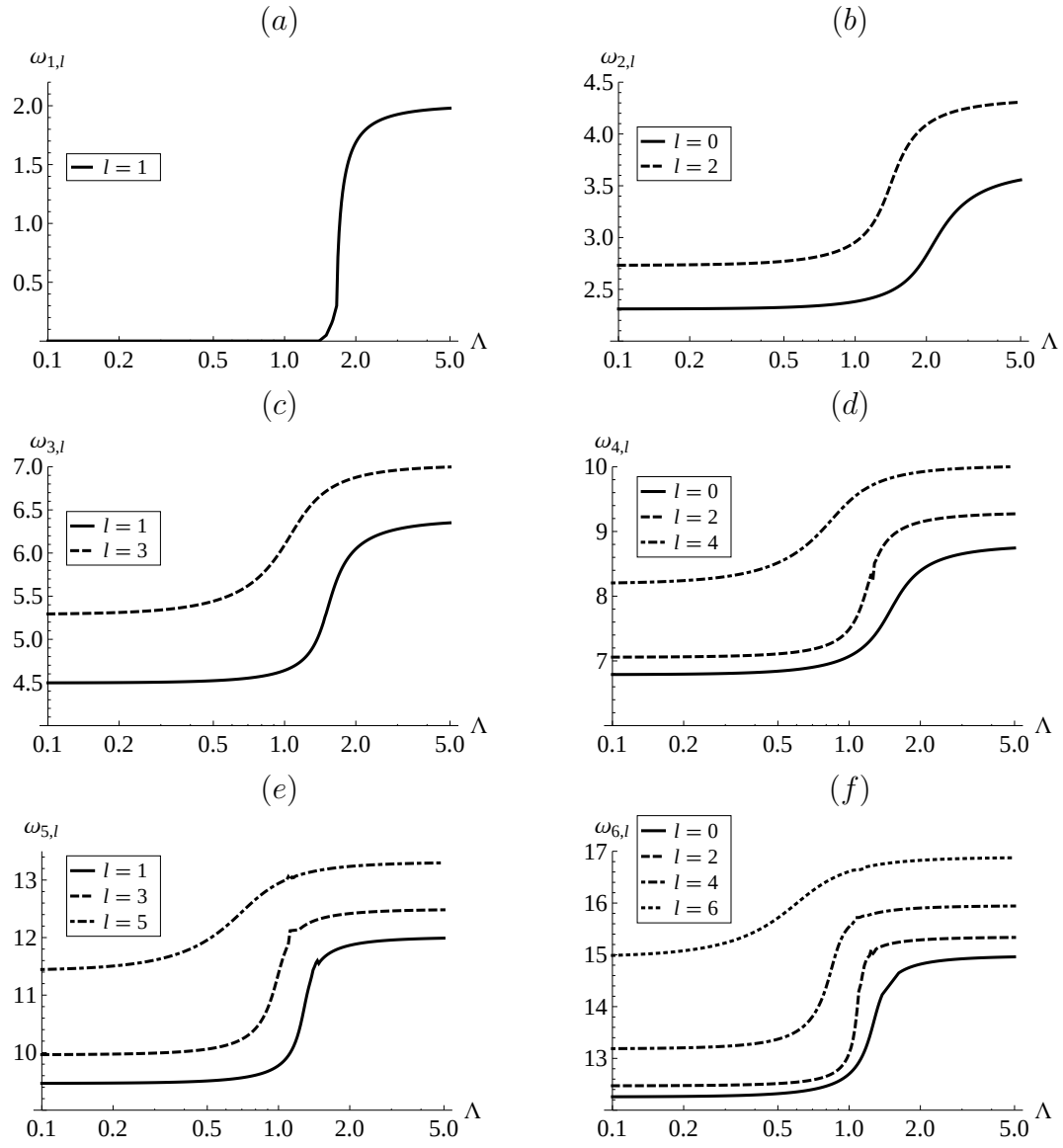

Figure 5.27: Oscillation frequency $\omega_{k,l}$, as it depends upon azimuthal wave-number l, against spreading parameter Λ for a typical super-hemispherical ($\alpha = 105°$) base-state with polar wave-number (a) $k = 1$, (b) $k = 2$, (c) $k = 3$, (d) $k = 4$, (e) $k = 5$, and (f) $k = 6$.

number. As shown in figure 5.26, the maximum relative frequency difference is approximately 10% for the sectoral mode shapes (i.e. modes with $k = l$).

The degeneracy of the hemispherical sessile drop can be lifted by breaking

the configurational symmetry of the base-state, as can be seen in figures 5.18 & 5.19. One can study the effect of simultaneously applying the two degeneracy lifting mechanisms by considering the contact-line speed condition to either a sub-hemispherical or super-hemispherical base-state. These oscillation frequencies have been plotted against the spreading parameter Λ in figure 5.27 for the super-hemispherical base-state, $\alpha = 105°$. One can directly compare figures 5.26 & 5.27 to show that deviations in volume away from the hemispherical base-state, controlled by the static contact-angle, lead to a larger magnitude in frequency shift amongst mode shapes of identical polar wave-number. Also, the degree of frequency splitting is much larger and more pronounced for the natural limit $\Lambda \to 0$ than it is for the pinned contact-line limit $\Lambda \to \infty$. For example, the frequency difference between the $k, l = 6, 0$ and $k, l = 6, 6$ modes approaches 25% for the natural disturbance, while this difference is only 14% when the contact-line is fixed. In addition, the transition from natural to pinned disturbance occurs at different values of the spreading parameter. Moreover, for fixed polar wave-number k there is the possibility that mode shapes of varying azimuthal wave-number l will oscillate with either a free-like or pinned-like contact-line at some particular value of the spreading parameter. Consider figure 5.27(f), the $[6, 0]$ and $[6, 6]$ modes are in the natural and pinned regime at $\Lambda = 0.8$, respectively.

Mode crossings

One can imagine that as the static contact-angle is increased there is the possibility of mode crossings, whereby two mode shapes might share the same characteristic frequency (i.e. the classic ordering of the mode shapes could be distorted). Classically, the number of 'nodes' or zeroes of a given eigenfunction and the spectral ordering of the corresponding eigenvalue are coincident. For example, the eigen-

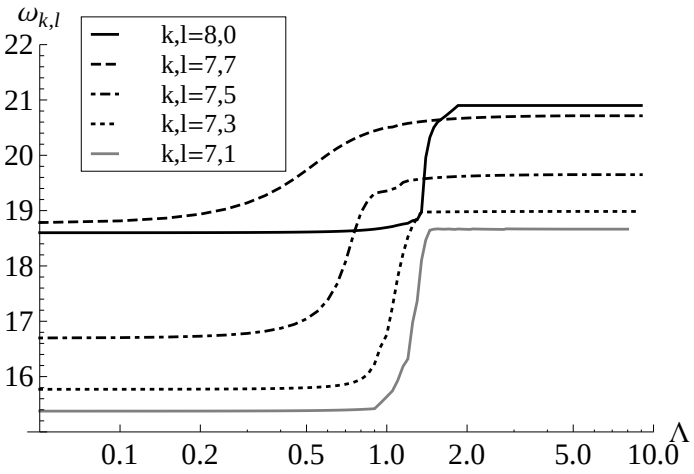

Figure 5.28: Modal crossings from the dynamic contact-line condition: oscillation frequency $\omega_{k,l}$ as measured by the spreading parameter Λ for $\alpha = 105°$.

function which corresponds to the third numerical eigenvalue has three nodes. To examine the possibility of these mode crossings, one can independently vary either one or both of the degeneracy lifting mechanisms; the static contact-angle α or the spreading parameter Λ. The latter is most applicable to systems with a dynamic contact-line and the contact-line dynamics are of interest, whereas the former is useful when the motion of the three-phase contact-line is well-known.

Figure 5.28 plots the oscillation frequency against the spreading parameter Λ for the super-hemispherical base-state with $\alpha = 105°$. Here the axisymmetric $k, l = 8, 0$ mode shape is degenerate with respect to mode shapes with polar wave-number $k = 7$ and azimuthal wave-numbers $l = 3, 5, 7$ at some finite value of the spreading parameter. The most interesting comparison from figure 5.28 is between the axisymmetric $k, l = 8, 0$ and sectoral $k, l = 7, 7$ mode shapes. Here the two mode shapes have nearly identical frequencies in the pinned limit $\Lambda \to \infty$, but the transition to the natural regime $\Lambda \to 0$ occurs at different values of the spreading

parameter. Moreover, the contact lines of the $k, l = 7, 7$ mode shape stay essentially pinned for a larger range of Λ. This specific type of mode crossing behavior can be used to explain one of the instabilities observed in drop-atomization experiments (Vukasinovic *et al.*, 2007). In these experiments, a sessile drop with pinned contact-lines is placed on a vertically-driven vibrating plate and the driving frequency is varied until resonance is observed. The frequency is then fixed and the resulting shape is axisymmetric with pinned contact lines. Next, the forcing amplitude is increased until the contact-line becomes de-pinned, which results in an azimuthal disturbance generated along the contact-line. As the forcing amplitude is increased further, the azimuthal instability propagates to the entire drop surface and finally drop-atomization occurs. One can use figure 5.28 to relate the mode crossing phenomenon to the generation of the azimuthal instability in the drop-atomization experiments. Recall that the horizontal asymptotes of the curves from figure 5.28 are regions where the interface disturbance essentially satisfies either the natural or pinned contact-line conditions. As the forcing amplitude increases, the mobility of the contact-line increases or Λ decreases and the drop de-pins, albeit for an instant. In relation to figure 5.28, the $k, l = 8, 0$ curve is traversed in the direction of decreasing Λ for increasing forcing amplitude until this mode shape de-pins and collapses onto the $k, l = 7, 7$ mode shape, which has a similar resonant frequency and pinned contact-lines. Equivalently, as the contact-line de-pins an azimuthal instability is necessarily generated to preserve the sessile drop's preference for a pinned contact-line. Although a quantitative comparison with these experiments is not performed here, this type of mode crossing behavior is characteristic of the de-pinning azimuthal instability.

Alternatively, mode crossings may be analyzed by fixing the disturbance class and varying the volume via the static contact-angle. This has been done in fig-

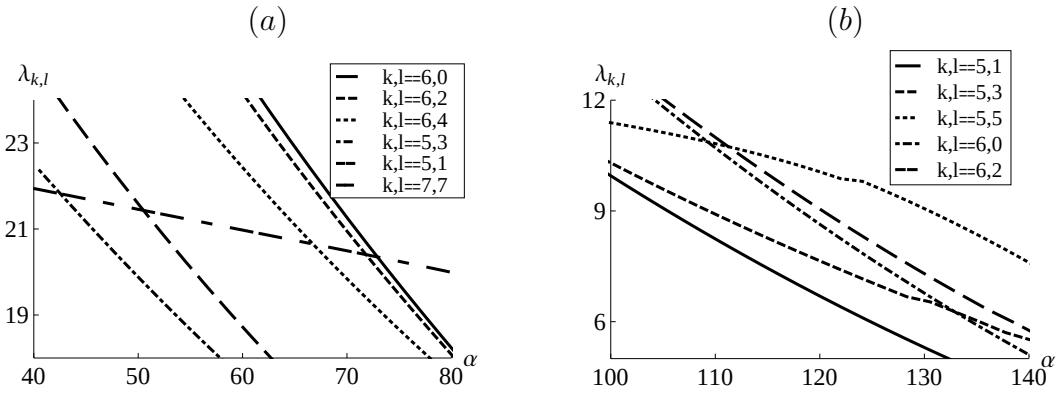

Figure 5.29: Modal crossings controlled by base-state volume: frequency $\lambda_{k,l}$ as a function of static contact-angle α for (a) natural and (b) pinned disturbances.

ure 5.29, which plots frequency $\lambda_{k,l}$ against contact-angle α for a range of wave-number pairs. Here the direction of mode crossings is controlled by category of base-state, either sub-hemispherical or super-hemispherical. As the contact-angle increases from 90°, high polar wave-number modes cross the low-polar wave-number modes, as in figure 5.29(b). Likewise, figure 5.29(a) shows that decreasing the contact-angle from 90° results in low wave-number modes crossing high wave-number modes. In general, the number of possible mode crossings is controlled by the magnitude of deviation from the hemispherical base-state.

Periodic table of mode shapes

As shown in figure 5.29, the ordering of mode shapes by their frequency can be distorted for a range of contact angles. Detailed knowledge regarding the 'filling' of the frequency space is of fundamental interest and is of practical importance in applications like the drop-atomization experiment, among others. A direct analogy can be made between the filling of frequency space for the sessile drop and the

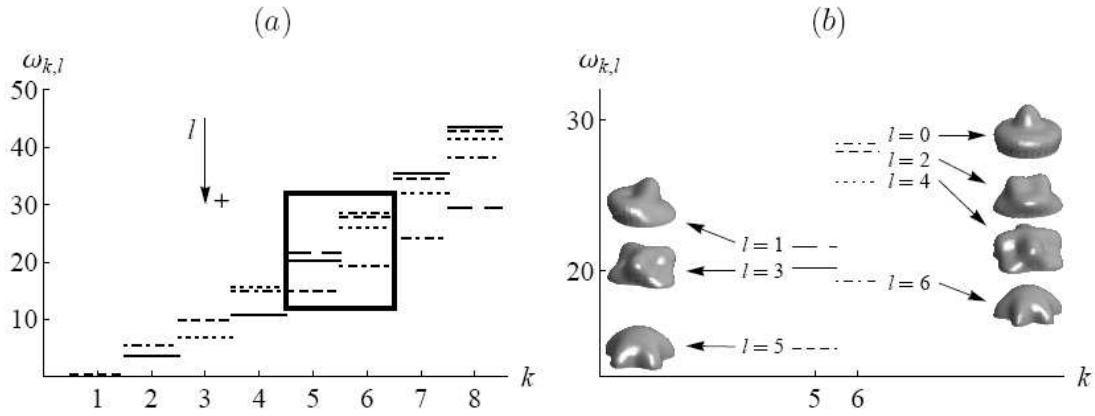

Figure 5.30: Spectral lines: (a) frequencies $\omega_{k,l}$, as they depend upon azimuthal wave-number l, against polar wave-number k and (b) blow-up of polar wave-numbers $k = 5, 6$ with natural mode shapes for $\alpha = 60°$.

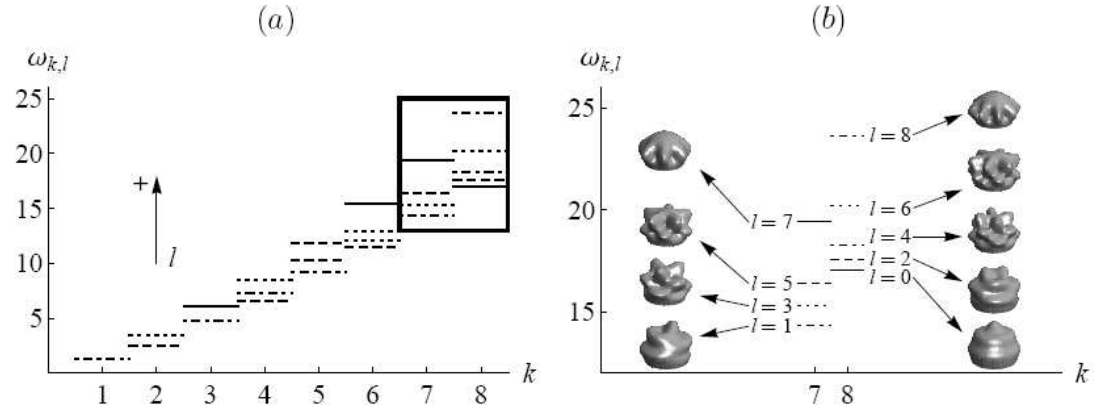

Figure 5.31: Spectral lines: (a) frequencies $\omega_{k,l}$, as they depend upon azimuthal wave-number l, against polar wave-number k and (b) blow-up of polar wave-numbers $k = 7, 8$ with pinned mode shapes for $\alpha = 120°$.

filling of the periodic table by energy level. Consider the energy spectrum of the hydrogen atom model in quantum mechanics, which consists of an electron orbiting a nucleus under a spherically-symmetric potential. Here the energy levels are degenerate with respect to angular momentum quantum number, much like the sessile drop with hemispherical base-state is degenerate with respect to azimuthal wave-number under a natural disturbance. Both problems can be formulated using a variational approach and both degeneracies are attributed to the symmetry of their respective systems. Similar to the degeneracy lifting of the sessile drop, a number of symmetry-breaking mechanisms exist for the hydrogen atom model, such as spin-orbit coupling, hyperfine splitting, etc. These mechanisms help to explain the unique manner in which the periodic table is filled by energy level. For example, the $4s$ orbital is filled before the $3d$ orbital, because the former state has a lower energy than the latter. This peculiar filling order would not be possible if the respective degeneracy were not broken. As shown in figures 5.30 & 5.31, the frequency space of the sessile drop fills in a manner parallel to the filling of atomic orbitals by energy level. Here the order in which resonant mode shapes were to appear in a frequency sweep is identified by traversing the graph in the direction of increasing frequency. Once again, the direction of splitting is independent of the class of kinematic disturbance and controlled by the type of base-state, either sub-hemispherical or super-hemispherical. The direction of frequency splitting is indicated in figure 5.30 for a sub-hemispherical base-state $\alpha = 60^\circ$ subject to a natural disturbance and figure 5.31 for a super-hemispherical base-state $\alpha = 120^\circ$ given a pinned disturbance. The magnitude of frequency splitting is controlled by the static contact-angle α and contact-line conditions through the spreading parameter Λ. Therefore, in making the analogy to the 'periodic table of mode shapes', one must recognize that there exists a family of periodic tables that are

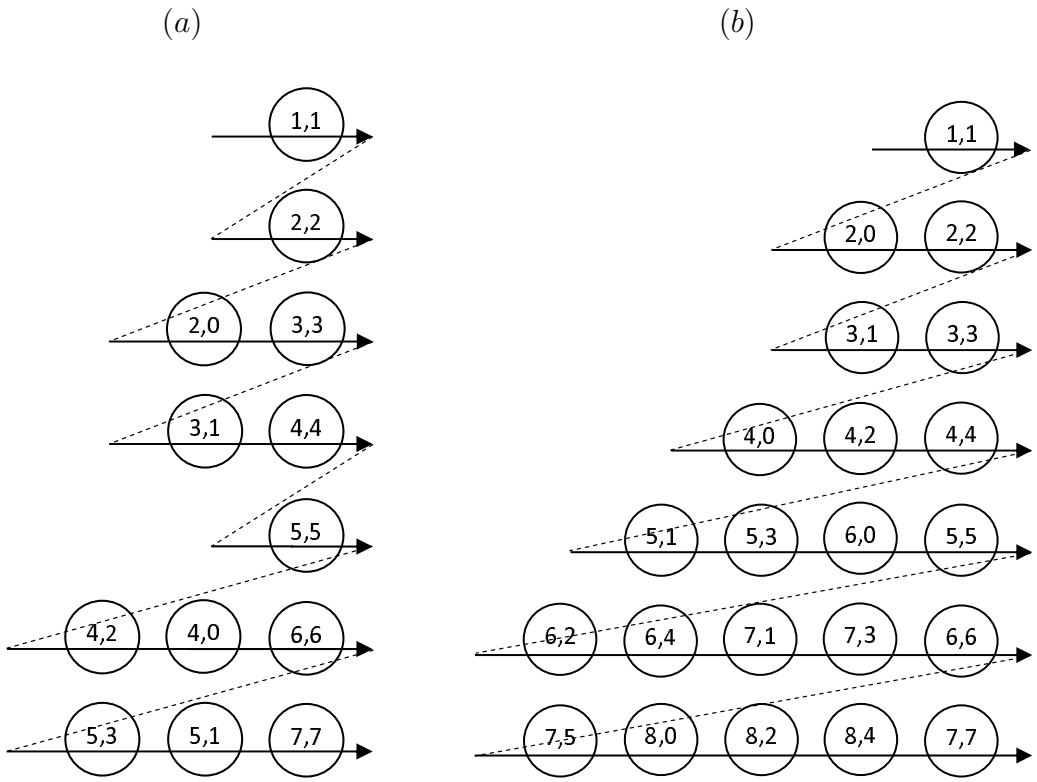

Figure 5.32: Periodic table of mode shapes: filling order for (a) sub-hemispherical drop ($\alpha = 60°$) subject to a natural disturbance and (b) super-hemispherical drop ($\alpha = 120°$) with pinned contact-lines.

distinguished by α and Λ, but related by an *Aufbau* principle, which states that the mode shapes are 'filled' in order of increasing frequency. For example, two such periodic tables are shown in figure 5.32, which display the filling order for the set of parameters used to generate the spectral plots of figures 5.30,5.31, respectively.

5.6 Concluding remarks

The dynamic stability of an inviscid sessile drop has been studied here. To that end, the linearized hydrodynamic equations governing the motion of the drop interface are formulated as a functional eigenvalue equation on linear operators. Here the drop interface is subject to two distinct classes of disturbance, either i) kinematic or ii) dynamic. A kinematic disturbance depends solely upon the geometry of the three-phase contact-line, whereas a dynamic disturbance is related to dynamic 'field' quantities there. Two such kinematic disturbances are considered here; the i) fixed contact-angle (natural) and ii) fixed contact-line (pinned). The dynamic disturbance class uses a constitutive law that relates the 'dynamic' contact-angle to the contact-line speed via a spreading parameter. Once the disturbance class is established, the frequency spectrum for the sessile drop may be computed using one of two equivalent formulations, deemed the forward and inverse problem. Both problems are reduced to a set of algebraic equations using the variational procedure of Rayleigh-Ritz. The kinematic disturbance class is handled most expediently by solving the inverse problem, whereas an ad hoc solution method is used for the contact-line speed condition. Here select results from the 'natural' disturbance class are utilized and the structure of the second variation of surface energy is exploited to show that contact-angle variation associated with the contact-line speed condition is a purely dissipative process.

The computational results presented here are in excellent agreement with existing literature. To the extent that comparisons can be made, a few of the most relevant points-of-contact will be summarized next. The vast majority involve the hemispherical base-state ($\alpha = 90^\circ$), because of the additional symmetry that greatly reduces the complexity of the computations required. For example, the nat-

ural frequencies computed here, which are degenerate with respect to azimuthal wave-number l, can be identified with (2.1) as the Rayleigh frequencies (Rayleigh, 1879). Likewise, Lyubimov *et al.* (2006) implement a linearized Hocking condition, which is related to the contact-line speed condition used here, to compute the axisymmetric frequencies ($l = 0$), shown in figure 5.20 (d, e, f), as a function of a parameter inversely related to the spreading parameter Λ. A similar study has been performed by Lyubimov *et al.* (2004) for non-trivial azimuthal wave-numbers $l \neq 0$ (c.f. figure 5.26). In contrast to the results mentioned above for the hemispherical base-state, Basaran & DePaoli (1994) use a computational-based approach to study the effect of base-state volume on the first axisymmetric mode shape ($[k, l] = [2, 0]$). They assume pinned contact-lines and are able to handle large-amplitude disturbances. Their computed frequencies, which do not vary significantly with the size of disturbance, are in excellent agreement with figure 5.6 (b), especially in the small-amplitude limit.

This problem is parameterized by azimuthal wave-number l, volume via the static contact-angle α and the boundary conditions on the three-phase contact-line, which can be controlled by the spreading parameter Λ. The spreading parameter is a measure of the mobility of the contact-line and its asymptotic limits $\Lambda \to 0$ and $\Lambda \to \infty$ correspond to the natural and pinned disturbances classes, respectively. Equivalently, one can vary the spreading parameter and smoothly change between the two kinematic boundary conditions. At finite values of the spreading parameter, energy is dissipated according to dynamic contact-angle variation and gives rise to damped oscillation amplitudes. As could be expected, the computed decay rates are greatest for the higher wave-number mode shapes. However, it is the low polar wave-number mode shapes that dissipate the most energy over a complete oscillation cycle, counterintuitive to bulk viscous effects, where higher

wave-number modes dissipate more energy. This peculiarity is attributed to the viscous dissipation mechanism of dynamic contact-angle variation controlled by the contact-line mobility. It has been shown that the contact-line displacement is largest for the lowest order modes, thus, these shapes dissipate the most energy according to this constitutive law. To further validate this interpretation, it has been shown that perturbations to sub-hemispherical $\alpha < 90^\circ$ base-states dissipate more energy than super-hemispherical $\alpha > 90^\circ$ base-states, because of the greater contact-line mobility of the former. Moreover, in the limit of the drop touching a support plane on a generating line $\alpha \to 180^\circ$, the contact-line is essentially immobile, no energy is dissipated and one cannot distinguish between the two kinematic disturbances.

Although the majority of the motions of the sessile drop are oscillatory, there does exist an unstable mode shape. Here a sessile drop subject to a natural disturbance exhibits instability for a range of contact angles $90^\circ < \alpha < 180^\circ$. This instability is characterized by an advancing contact-line, which is accelerating relative to the corresponding receding contact-line, thereby displacing mass from one side of the drop to the other. Under this disturbance class there is no such mechanism to resist this motion, therefore the drop is able to 'walk' along the support surface. To suppress this 'walking' instability, one can force the contact lines to be pinned, which precludes the translating motion. Alternatively, the contact-line speed condition generates effective dissipation and can potentially suppress this instability. That is, if the positive dissipation exactly balances the negative energy difference between the perturbed state and the base-state, then the base-state is neutrally stable (c.f. figure 5.24). A thorough understanding of this instability potentially has many useful industrial applications, whereby translational motion of droplets is desirable, such as the cleansing of microprocessor chips via fluid

droplets.

The special case of the hemispherical $\alpha = 90^\circ$ sessile drop exhibits a frequency degeneracy with respect to azimuthal wave-number l, when subjected to a natural disturbance. This degeneracy is attributed to the additional configurational symmetry of the hemispherical base-state. Recall that the governing equations have been derived from a variational principle and that Noether's theorem states that continuous symmetries imply degeneracies for Hamiltonian systems. Implicit in Noether's theorem is the assumption that the boundary conditions for the variational problem are the 'natural' ones. With regards to the sessile drop, the 'natural' boundary conditions are those that generate disturbances, which preserve the static contact-angle or belong to the natural disturbance class. Thus, the azimuthal degeneracy of the hemispherical base-state could have been anticipated. This degeneracy is lifted in two ways, either i) varying the boundary conditions on the three-phase contact-line via the spreading parameter Λ or ii) adjusting the volume of the base-state via the static contact-angle α. As shown in figure 5.19, pinning the contact lines of the drop breaks this degeneracy. Here for a fixed polar wave-number k, the frequencies with the highest azimuthal wave-number l can be up to 10% greater than the mode shape with the lowest azimuthal wave-number (c.f. figure 5.26). Likewise, volume effects break the degeneracy as in figure 5.18 for the natural disturbance class. This behavior persists for non-zero values of the spreading parameter Λ. Furthermore, one can superimpose the two degeneracy lifting mechanisms to create large frequency ranges for fixed polar wave-number, much like the behavior shown in figure 5.27.

By controlling the volume of the base-state via the static contact-angle, it has been shown that there exists the possibility for mode crossings (or the ordering of

mode shapes can be altered). Two types of mode crossing are observed. The first is controlled by the spreading parameter Λ and is relevant to problems where the contact-line dynamics are of interest. Typical mode crossing behavior of this type is a potential explanation for a contact-line instability present in drop-atomization experiments (Vukasinovic *et al.*, 2007). Namely, a vertically-driven sessile drop with pinned contact lines exhibits an instability, whereby its contact-line de-pins for an instant and an azimuthal instability is generated. Although a quantitative comparison is precluded, figure 5.28 illustrates this type of characteristic behavior. The second type of mode crossing behavior is related to the drop volume through the static contact-angle and is shown in figure 5.29. For a fixed polar wave-number k, the super-hemispherical base-states have oscillation frequencies that increase as the azimuthal wave-number l increases. In contrast, frequencies for sub-hemispherical base-states decrease with increasing azimuthal wave-number. In both cases the relative difference in frequencies between the mode shapes with smallest and largest azimuthal wave-number is controlled by the magnitude of deviation from the hemispherical base-state. Accordingly, as this deviation grows the possibility of mode crossings greatly increases. Here if one were to perform a frequency sweep, the order in which resonant mode shapes are excited is altered in comparison to the classical modal ordering. The 'filling' of frequency space by these broken-states is analogous to the filling of the periodic table by energy levels, where the distinct ordering is a result of a number of symmetry-breaking mechanisms, such as spin-orbit coupling, etc. With regards to the sessile drop, the symmetry breaking mechanisms are the wetting conditions on the three-phase contact-line and the base-state volume, which are controlled by the spreading parameter Λ and static contact-angle α, respectively. For a prescribed set of parameter values (Λ, α), one can construct the corresponding 'periodic table of mode shapes' from

the spectral data using an *Aufbau* principle, whereby the mode shapes are filled in order of increasing frequency (c.f. figure 5.32).

CHAPTER 6

CAPILLARY INSTABILITIES OF THE STATIC RIVULET: VARICOSE AND SINUOUS MODES

6.1 Introduction

A rivulet is a narrow stream of liquid flowing down a solid surface that shares an interface, held by surface tension, with the surrounding gas. The most commonly referred to example is the stream of water seen on automobile windshields. The rivulet has the distinguishing feature of two distinct contact lines. The contact-line is defined as the geometric curve that intersects the interface between two immiscible fluids and a solid support. The equilibrium positions or the motion of these contact-lines generates a number of geometric configurations. For example, the straight rivulet has parallel contact lines, steady, fully-developed flow and a cylindrical meniscus (Towell & Rothfeld, 1966). This base-state exhibits a number of instabilities, such as drop formation from capillary break-up, rivulet meandering and the development of surface waves (e.g. Schmuki & Laso, 1990).

A static rivulet is characterized by a constant mean curvature and the absence of a velocity field. In the absence of a base-flow, the sole instability mechanism is Plateau-Rayleigh break-up (capillary instability), whereby the interface evolves into a series of individual droplets in an attempt to maximize its surface area. In a series of experiments, Plateau (1863) showed that the liquid cylinder is unstable to lengths longer than its base-state circumference. Plateau attempted to interpret the final drop size from this limit, which was ultimately proved incorrect. Lord Rayleigh (1879) corrected Plateau's misinterpretation by computing the dispersion relation from the governing hydrodynamic equations. Rayleigh was able to show

that the maximal growth rate and corresponding wave-number gave a characteristic time and size for drop formation, respectively. Davis (1980) computes static stability bounds for the static rivulet under a number of contact-line conditions but, unlike Plateau, derives his results from the hydrodynamic equations and corresponding disturbance energy-balance equation. One can directly compare Davis' results to Brown & Scriven (1980), who use a variational approach to study the cylindrical fillet protruding from an infinite slot for both constant pressure and constant volume disturbances, because static stability is unaffected by the support geometry. The agreement is perfect in the common limit of the constant volume disturbance. A number of authors have studied cylindrical interfaces under other wetting geometries. For example, Langbein (1990) studies the interior or exterior wetting of a V-groove, Roy & Schwartz (1999) analyze a number of cross-sectional containers; such as planar, V-groove, circular and elliptical, and Bostwick & Steen (2010) consider the cylindrical-cup support.

A rivulet with an axial base flow is susceptible to kinematic-wave instabilities characteristic of thin film flows–particularly so if the rivulet is relatively flat–in addition to capillary instability. In a series of papers, Davis *et al.* study the long wave-length instabilities on a rivulet corresponding to gravity-driven flow down a vertical plane (Weiland & Davis, 1981; Young & Davis, 1987). They report kinematic-wave instabilities for wide rivulets with immobile contact lines and capillary instability of narrow rivulets. Although their analysis is able to handle a wide range of effects and predict the varicose instability, *they do not capture rivulet meandering or the sinuous instability.* For reference, the varicose and sinuous modes are defined according to their symmetry or anti-symmetry about the vertical mid-plane of a cross-section, respectively. Among other results, Benilov (2009) uses the lubrication approximation to show that a shallow rivulet

with pinned contact lines that wets the under-side of a plate (pendant) is unstable to a range of axial wave-numbers. In addition, an induced shear flow is seen to stabilize this instability, which is a somewhat surprising result considering that inertial effects tend to de-stabilize.

With respect to rivulet meandering, Culkin & Davis (1983) derive a stability index to measure the stabilizing effects of surface tension and de-stabilizing effects of inertia under dynamic wetting conditions. Unable to account for contact-angle hysteresis, the stability index was only marginally effective at capturing the meandering instability mechanism observed in their experiments. Kim *et al.* (2004) use a perturbation analysis to try to capture the meandering instability for a rivulet base-state corresponding to plug flow. By balancing pressures at the contact-line, they are able to derive a dispersion relation that depends upon the base-state geometry, a Weber number and wetting conditions on the contact-line. The response of the fluid to a disturbed interface shape is not included in their analysis. Similarly, Grand-Piteira *et al.* (2006) derive a rivulet meandering criteria from a force balance on the contact-line that incorporates contact-angle hysteresis, capillary effects and inertia from a gravity-driven base flow. They find, among other observations, that the base-flow is also hysteretic and thus the shape of the meandering rivulet varies only with increasing flow rate.

In this chapter, the linear stability of the static rivulet under a number of contact-line conditions is considered. The first type of disturbance preserves the static contact-angle (natural), while the second has a fixed contact-line (pinned). The governing hydrodynamic equations for this inviscid, incompressible flow are derived and then reduced to an eigenvalue problem by a normal mode analysis. The problem is parameterized by axial wave-number k and static contact-angle

α (base-state volume). The integro-differential equation, governing the motion of the interface, is formulated as a functional eigenvalue problem on linear operators, which is then solved using a spectral method to deliver the dispersion relations. Static stability is greatly influenced by the type of interface disturbance and can be recovered from the hydrodynamic formulation by setting the growth rate to zero.

Once the contact-line disturbance class is set, allowable solutions to the governing equations are decomposed further into the *varicose* and *sinuous mode* types. That is, there are two mode types for both the natural and pinned disturbance classes to yield four types of interface disturbance in total. With regards to stability, the *varicose mode* is the more *unstable* mode type and the *pinned disturbance* is seen to be relatively *stabilizing* in comparison to the natural disturbance. Static stability of the varicose mode is shown to agree with the results of Davis (1980). The dispersion relations for the varicose mode exhibit behavior typical of capillary instability. Specifically, there exists a fastest growing shape that is distinguished by a non-trivial axial wave-number k_m. The sinuous mode with pinned contact lines is stable to all static contact angles or base-state volumes. However, the *sinuous mode* does exhibit *instability* to the *natural disturbance* for the super-circular ($90^\circ < \alpha < 180^\circ$) base-state. Unlike the varicose instability, this instability does not exhibit the typical character of Plateau-Rayleigh break-up. For a range of contact angles, the fastest growing or critical disturbance is characterized by $k_m = 0$ or the disturbance is independent of the axial coordinate. This is a 'long-wave' instability. Typical capillary instability persists outside this interval.

This chapter begins by defining the hydrodynamic equations that govern the motion of the rivulet, whose interface has been given a small disturbance. A nor-

mal mode expansion reduces the governing equations to a functional eigenvalue problem on linear operators. To compute the dispersion relations, a Rayleigh-Ritz procedure is used to reduce the operator equation to a standard algebraic eigenvalue problem. The type of disturbance and volume of the base-state, controlled by the static contact-angle α, are the relevant parameters in this problem and can greatly influence the dispersion relations. The types of disturbance considered here are defined both on the contact-line and according to their symmetry about the vertical-mid plane. To conclude, the computational results are discussed and concluding remarks are given.

6.2 Mathematical formulation

A cylindrical-cap interface (rivulet) held by uniform surface tension σ, on a planar support, is a static equilibrium configuration. When gravitational effects are neglected, the static base-state is a circular arc in the $x-y$ plane extended to infinity in the axial (z) direction. A parametric representation of this equilibrium shape Γ is given by

$$X(s,z;\alpha) = -\frac{1}{\sin(\alpha)}\sin(s), \tag{6.1a}$$

$$Y(s,z;\alpha) = \frac{1}{\sin(\alpha)}\left(\cos(s)-\cos(\alpha)\right), \tag{6.1b}$$

$$Z(s,z;\alpha) = z, \tag{6.1c}$$

where $s \in [-\alpha,\alpha]$ and $z \in [-\infty,\infty]$ are the arc-length and axial coordinates, respectively. Here lengths have been scaled with respect to the base radius r. The interface is given a small disturbance $\eta(s,z,t)$ (c.f. figure 6.1) which generates pressure gradients on the surface according to the Young-Laplace equation

$$p/\sigma = \kappa_1 + \kappa_2 \equiv 2H, \tag{6.2}$$

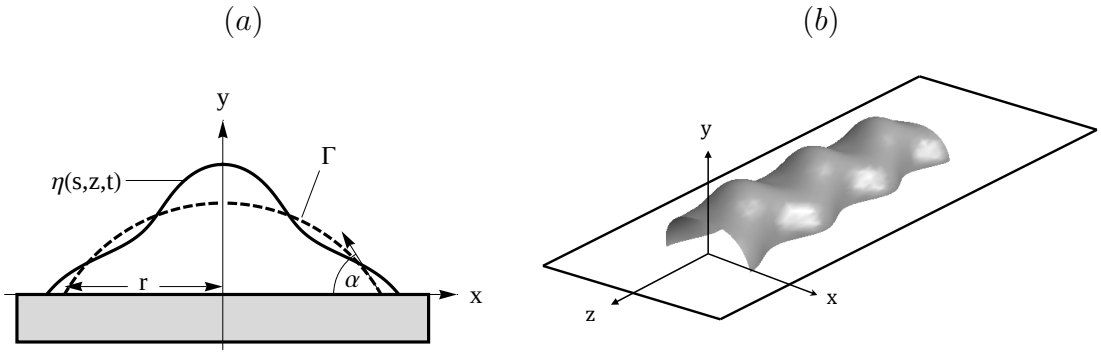

Figure 6.1: Definition sketch of the rivulet in (a) polar and (b) three-dimensional perspective views.

and equivalently a capillary-driven flow. Accordingly, the circular arc base-state has principal curvatures $\kappa_1 = \sin\alpha$ and $\kappa_2 = 0$, a constant mean curvature $2H = \sin\alpha$, and is therefore in static equilibrium.

6.2.1 Field equations

The governing equations for this incompressible, irrotational flow are written via a velocity potential $\boldsymbol{v} = \boldsymbol{\nabla}\Psi$ and pressure p;

$$\nabla^2\Psi = 0 \quad [D] \tag{6.3a}$$

$$p = \rho\frac{\partial\Psi}{\partial t} \quad [D], \tag{6.3b}$$

$$p/\sigma = -\Delta_\Gamma\eta - \left(\kappa_1^2 + \kappa_2^2\right)\eta \;\; [\partial D^f]. \tag{6.3c}$$

$$\frac{\partial\Psi}{\partial n} = -\frac{\partial\eta}{\partial t} \quad [\partial D^f] \tag{6.3d}$$

$$\boldsymbol{\nabla}\Psi\cdot\hat{\boldsymbol{y}} = 0 \quad [\partial D^s] \tag{6.3e}$$

Here a fluid of density ρ occupies a domain

$$D \equiv \{(x,y,z)|\ 0 \le x \le X(s,\varphi;\alpha),\ 0 \le y \le Y(s,\varphi;\alpha),\ -\infty \le z \le \infty\} \tag{6.4}$$

that is bound by a free surface ∂D^f and a planar surface-of-support ∂D^s;

$$\partial D^f \equiv \{(x,y,z)\,|\,x = X(s,z;\alpha),\ y = Y(s,z;\alpha),\ z = z\}, \tag{6.5a}$$

$$\partial D^s \equiv \{(x,y,z)\,|\,y = 0\}. \tag{6.5b}$$

As required by incompressibility, the velocity potential satisfies Laplace's equation (6.3a) on the fluid domain and a no-penetration condition (6.3e) on the planar surface-of-support. The pressure in the drop domain is expressed by the linearized Bernoulli equation (6.3b). Similarly, the pressure evaluated on the free surface is given by the linearized Young-Laplace equation (6.3c) with Δ_Γ defined as the Laplace-Beltrami operator or surface Laplacian (e.g. Myshkis *et al.*, 1987). Lastly, a kinematic condition (6.3d) relates the normal velocity of the fluid to the velocity of the interface disturbance on the free surface.

6.2.2 Normal-mode reduction

Normal modes,

$$\Psi(\boldsymbol{x},t) = \phi(\boldsymbol{x})\mathrm{e}^{\gamma t},\ \ \eta(s,z,t) = y(s,z)\mathrm{e}^{\gamma t} \tag{6.6}$$

are used to reduce the hydrodynamic field equations (6.3) to

$$\nabla^2\phi = 0\ \ [D], \tag{6.7a}$$

$$\frac{\partial\phi}{\partial n} = 0\ \ [\partial D^s], \tag{6.7b}$$

$$-\Delta_\Gamma\frac{\partial\phi}{\partial n} - \left(\kappa_1^2 + \kappa_2^2\right)\frac{\partial\phi}{\partial n} = \lambda^2\phi\ \ [\partial D^f], \tag{6.7c}$$

$$\int_\Gamma \frac{\partial\phi}{\partial n} = 0, \tag{6.7d}$$

$$\lambda^2 \equiv \frac{\rho\gamma^2 r^3}{\sigma}. \tag{6.7e}$$

Here (6.7) is recognized as an eigenvalue problem in the scaled growth rate (6.7e) with (6.7a-6.7c) following directly from (6.3). In addition, the auxiliary condi-

tion (6.7d) is required to ensure the linear perturbations are volume preserving (incompressibility).

6.2.3 Operator formalism

Equation (6.7c) represents the balance of momentum on the interface and can be simplified using the properties of the equilibrium surface,

$$\left(\frac{\partial\phi}{\partial n}\right)_{zz} + \sin^2\alpha\left[\left(\frac{\partial\phi}{\partial n}\right)_{ss} + \left(\frac{\partial\phi}{\partial n}\right)\right] = \lambda^2\phi. \tag{6.8}$$

As the planar support is independent of the axial coordinate z, one may define $\phi = \phi\,\mathrm{e}^{ikz}$ (with purposeful redundant notation) and Fourier transform (6.8) to generate

$$\left(\frac{\partial\phi}{\partial n}\right)'' + \left(1-k^2\right)\left(\frac{\partial\phi}{\partial n}\right) = \frac{\lambda^2}{\sin^2\alpha}\phi. \tag{6.9}$$

The solution of this inhomogeneous differential equation is parameterized by axial wave-number k and given by

$$\frac{\partial\phi}{\partial n}(s) = \hat{\lambda}^2\int_{-\alpha}^{\alpha} G(s,\tau;k)\phi(\tau)\,\mathrm{d}\tau, \tag{6.10}$$

where $\hat{\lambda} \equiv \lambda/\sin\alpha$ and $G(s,\tau;k)$ is the Green's function or fundamental solution of the differential equation. Alternatively, one may view (6.10) as a functional eigenvalue problem on linear operators,

$$M^{-1}[\phi] = \hat{\lambda}^2 K^{-1}[\phi], \tag{6.11}$$

with

$$M^{-1}[\phi] \equiv \frac{\partial\phi}{\partial n}, \tag{6.12a}$$

$$K^{-1}[\phi](s) \equiv \int_{-\alpha}^{\alpha} G(s,\tau;k)\phi(\tau)\,\mathrm{d}\tau. \tag{6.12b}$$

To compute the eigenvalue spectrum of (6.10) using the operator formalism, one must construct the Green's function or integral operator (6.12b).

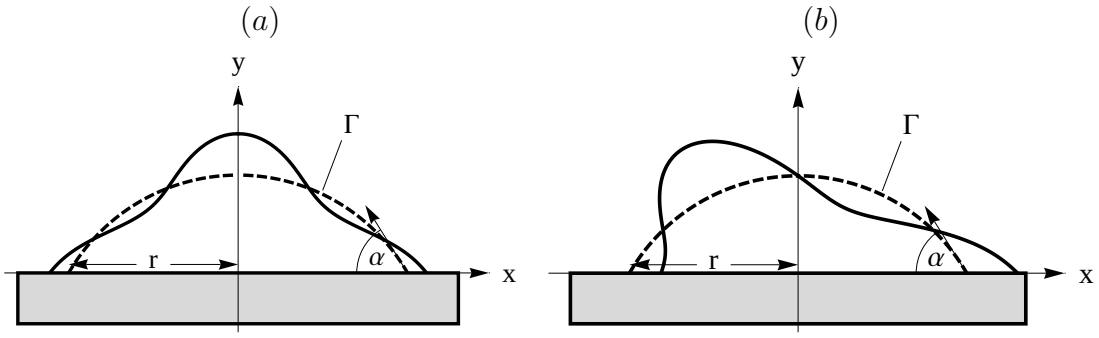

Figure 6.2: Natural disturbances: polar view of the (a) varicose and (b) sinuous modes.

6.2.4 Contact-line conditions

Before one can construct the Green's function, the boundary conditions on the three-phase contact-line must be specified.

Natural

The first type preserves the static contact-angle α,

$$\left(\frac{\partial}{\partial s}\left(\frac{\partial \phi}{\partial n}\right) + \cos(\alpha)\frac{\partial \phi}{\partial n}\right)\Bigg|_{s=\pm\alpha} = 0, \tag{6.13}$$

represents the linearization of the Young-Dupré equation (1.4), which is derived in Appendix A, and is termed the natural disturbance (c.f. figure 6.2).

Pinned

The second class is shown in figure 6.3 and has immobile or 'pinned' contact-lines,

$$\left(\frac{\partial \phi}{\partial n}\right)\Bigg|_{s=\pm\alpha} = 0. \tag{6.14}$$

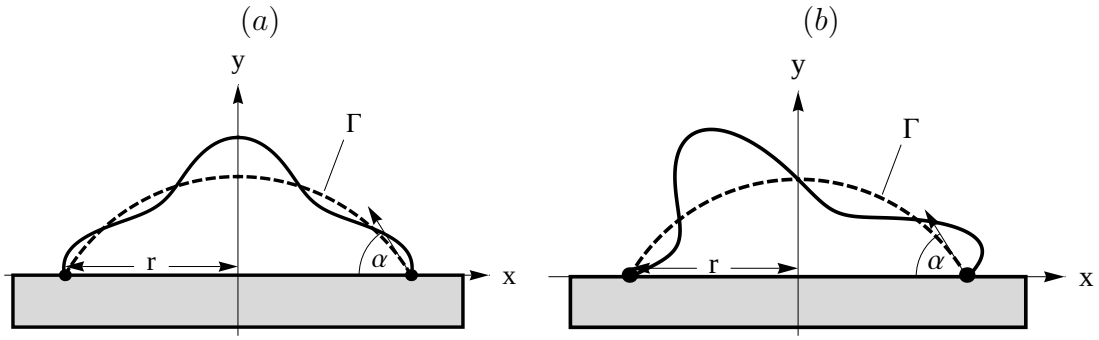

Figure 6.3: Pinned contact-line disturbances: polar view of the (a) varicose and (b) sinuous modes.

Symmetry decomposition into varicose and sinuous modes

Here it has been assumed that the wetting conditions on both contact-lines $s = \pm\alpha$ are identical, which allows one to decompose the solutions of (6.7) according to their symmetry about the vertical mid-plane. The varicose modes or even solutions are symmetric and satisfy

$$\left(\frac{\partial\phi}{\partial n}\right)'\Big|_{s=0} = 0, \tag{6.15}$$

while the anti-symmetric or odd solutions satisfy the following condition

$$\left(\frac{\partial\phi}{\partial n}\right)\Big|_{s=0} = 0, \tag{6.16}$$

and are deemed the sinuous modes. For reference, typical mode types are shown in figure 6.4.

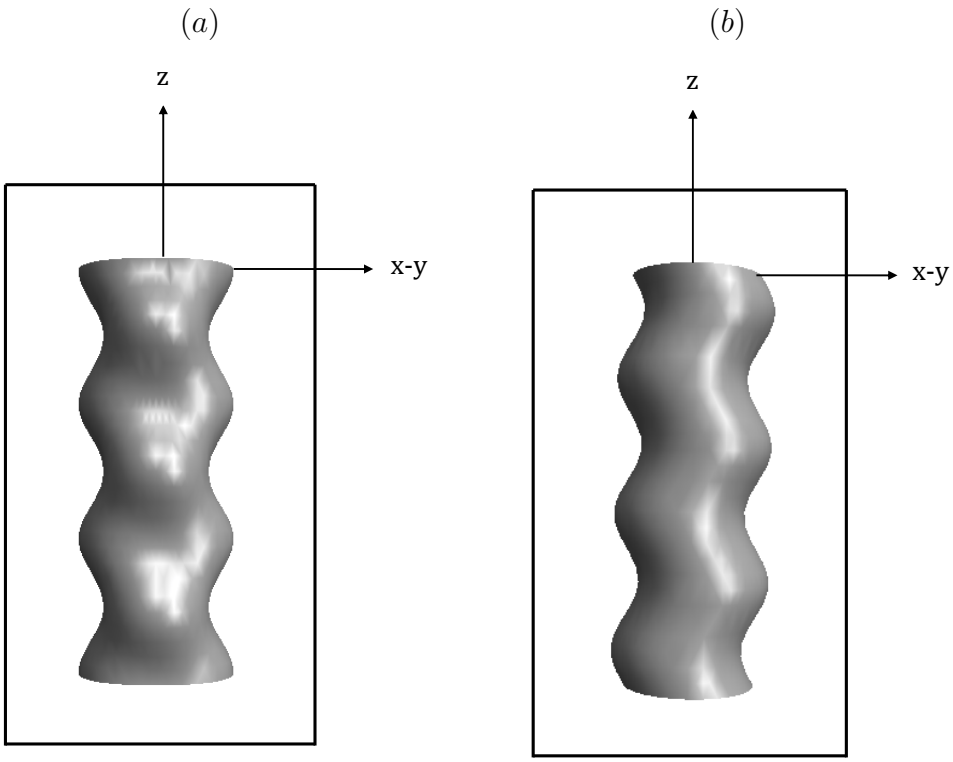

Figure 6.4: Top view of typical three-dimensional (a) varicose and (b) sinuous mode shapes.

6.2.5 Green's function construction

The following representation of the Green's function is particularly suited to the symmetric decomposition,

$$G(s,\tau;k) = \begin{cases} \frac{U(\tau;k)V(s;k)}{W(s;k)} & 0 < s < \tau < \alpha \\ \frac{U(s;k)V(\tau;k)}{W(s;k)} & 0 < \tau < s < \alpha. \end{cases} \tag{6.17}$$

Here U(left-hand) and V(right-hand) are the homogeneous solutions of (6.9) that satisfy the boundary conditions on the vertical mid-plane $s = 0$ and the contact-line $s = \alpha$, respectively. Likewise, W is the Wronskian of the two solutions.

Right-hand solution

The right-hand solution V is independent of the symmetry about the mid-plane, but does depend upon the wetting conditions on the three-phase contact-line. With respect to the natural boundary conditions (6.13), the right hand solution is given by

$$V^n(s) = \cos(\beta s) + A \sin(\beta s) \tag{6.18}$$

with

$$A = \frac{\beta \sin \beta\alpha - \cos\alpha \cos \beta\alpha}{\beta \cos \beta\alpha + \cos\alpha \sin \beta\alpha}, \tag{6.19}$$

and

$$\beta \equiv \sqrt{1 - k^2}. \tag{6.20}$$

Similarly, application of the pinned contact-line condition (6.14) generates the following right hand solution,

$$V^p(s) = \sin\beta(s - \alpha). \tag{6.21}$$

To distinguish between disturbance classes, a *superscript n will denote the natural solution*, while a *superscript p will refer to the pinned contact-line solutions.* Similarly, a subscript v or s will distinguish the varicose and sinuous modes, respectively.

Left-hand solution

With regards to the decomposition of solutions by symmetry, the left-hand solutions U are independent of the contact-line conditions. The varicose modes satisfy (6.15) and have the left-hand solution

$$U_v(s) = \cos(\beta s), \tag{6.22}$$

while the Wronskian for the natural W_v^n and pinned W_v^p disturbances are given by

$$W_v^n(s) = A\beta, \tag{6.23a}$$

$$W_v^p(s) = \beta\cos(\beta\alpha), \tag{6.23b}$$

respectively.

Similarly, the anti-symmetric sinuous modes satisfy (6.16) and have the following left-hand solution

$$U_s(s) = \frac{\sin(\beta s)}{\beta}, \tag{6.24}$$

with the Wronskians defined as follows

$$W_s^n(s) = -1, \tag{6.25a}$$

$$W_s^p(s) = \sin(\beta\alpha), \tag{6.25b}$$

for the natural and pinned disturbances, respectively.

6.2.6 Solution of operator equation

To compute the spectrum of (6.11), the operator equation is reduced to a truncated set of linear algebraic equations using the variational procedure of Rayleigh-Ritz. The method is sketched here, while a more thorough illustration is given in Segel (1987). To begin, the eigenvalues λ of the operator equation

$$B\,[y] = \lambda A\,[y] \tag{6.26}$$

are the stationary values of the functional

$$\lambda = \min\frac{(B[y], y)}{(A[y], y)}, \quad y \in S, \tag{6.27}$$

where S is a predetermined function space. A solution series,

$$y = \sum_{i=1} c_i y_i, \tag{6.28}$$

constructed from functions $y_i \in S$ are applied to the functional (6.27) and minimized with respect to the coefficients c_i to generate a set of algebraic equations

$$\sum_{j=1} \left(b_{ij} - \lambda a_{ij}\right) c_j = 0, \tag{6.29a}$$

$$b_{ij} \equiv \int B[y_i]\, y_j, \tag{6.29b}$$

$$a_{ij} \equiv \int A[y_i]\, y_j, \tag{6.29c}$$

from which the eigenvalues may be computed.

With regards to the problem considered here, a solution series

$$\phi = \sum_{j=1}^{N} a_j \phi_j, \tag{6.30}$$

constructed from properly chosen basis functions ϕ_j is applied to the operator equation (6.11) and inner products are taken to generate the following algebraic eigenvalue problem,

$$\sum_{j=1}^{N} \left(m_{ij} - \hat{\lambda}^2 \kappa_{ij}\right) a_j, \tag{6.31a}$$

$$m_{ij} \equiv \int_0^\alpha \frac{\partial \phi_i}{\partial n} \phi_j \,\mathrm{d}s, \tag{6.31b}$$

$$\kappa_{ij} \equiv \int_0^\alpha \int_0^\alpha K^{-1}\left[\phi_i\right] \phi_j \,\mathrm{d}\tau \mathrm{d}s, \tag{6.31c}$$

with

$$\begin{aligned}\kappa_{ij} = &\left(\int_0^\alpha \frac{U(s)}{W(s)} \phi_j(s)\,\mathrm{d}s\right)\left(\int_0^\alpha V(\tau)\phi_i(\tau)\,\mathrm{d}\tau\right) \\ &+ \int_0^\alpha \frac{V(s)}{W(s)}\phi_j(s) \int_0^s U(\tau)\phi_i(\tau)\,\mathrm{d}\tau\mathrm{d}s - \int_0^\alpha \frac{U(s)}{W(s)}\phi_j(s)\int_0^s V(\tau)\phi_i(\tau)\,\mathrm{d}\tau\mathrm{d}s.\end{aligned} \tag{6.32}$$

Allowable solutions of (6.11) must satisfy the hydrodynamic equations and more specifically, Laplace's equation (6.7a) on the fluid domain and the no-penetration condition (6.7b) on the surface-of-support. To satisfy these conditions, the following basis functions are used for the varicose modes,

$$\phi_j^{(v)} = I_{2(j-1)}(kr)\cos(2(j-1)\theta), \tag{6.33}$$

and the sinuous modes,

$$\phi_j^{(s)} = I_{2j-1}(kr)\sin((2j-1)\theta), \tag{6.34}$$

where I_l are modified Bessel functions (Arfken & Weber, 2001). Here the basis functions (6.33) & (6.34) are defined on the equilibrium surface through the coordinate transformations,

$$r = \sqrt{x^2(s;\alpha) + y^2(s;\alpha)}, \tag{6.35a}$$

$$\cos\theta = \frac{x(s;\alpha)}{\sqrt{x^2(s;\alpha) + y^2(s;\alpha)}}, \tag{6.35b}$$

$$\sin\theta = \frac{y(s;\alpha)}{\sqrt{x^2(s;\alpha) + y^2(s;\alpha)}}, \tag{6.35c}$$

with $x(s;\alpha)$ and $y(s;\alpha)$ defined in (6.1). Similarly, the normal derivatives of the basis functions are needed to compute the matrix elements of (6.31b),

$$\begin{aligned}
&\frac{\partial}{\partial n}\left(I_{2j}(kr)\cos(2j\theta)\right) = \\
&\qquad \frac{k}{2}\left[I_{2j+1}(kr) + I_{2j-1}(kr)\right]\cos(2j\theta)\left(-\sin(s)\cos(\theta) + \cos(s)\sin(\theta)\right) \\
&\qquad -\frac{k}{2}\left[I_{2j-1}(kr) - I_{2j+}(kr)\right]\sin(2j\theta)\left(\sin(s)\sin(\theta) + \cos(s)\cos(\theta)\right),
\end{aligned} \tag{6.36}$$

$$\begin{aligned}
&\frac{\partial}{\partial n}\left(I_{2j}(kr)\sin(2j\theta)\right) = \\
&\qquad \frac{k}{2}\left[I_{2j+1}(kr) + I_{2j-1}(kr)\right]\sin(2j\theta)\left(-\sin(s)\cos(\theta) + \cos(s)\sin(\theta)\right) \\
&\qquad +\frac{k}{2}\left[I_{2j-1}(kr) - I_{2j+}(kr)\right]\cos(2j\theta)\left(\sin(s)\sin(\theta) + \cos(s)\cos(\theta)\right).
\end{aligned} \tag{6.37}$$

Here the normal derivatives of the potential functions are given in mixed coordinates for efficiency in presentation and may be simplified further using the coordinate transformation (6.35).

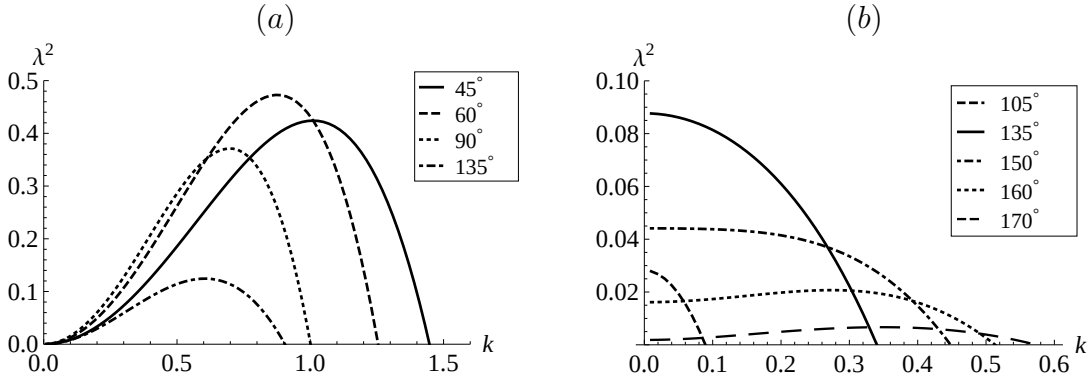

Figure 6.5: Dispersion relations: growth rate λ^2 vs. axial wave-number k for (a) varicose and (b) sinuous modes, subject to a natural disturbance.

6.3 Results

The eigenvalues of the matrix equation (6.31a), as they depend upon the axial wave-number k, are computed using standard numerical techniques for both the varicose and sinuous modes under either the natural (6.13) or pinned (6.14) disturbance class. For a given eigenvalue $\hat{\lambda}^{2(l)}$ with associated eigenvector $a_j^{(l)}$, the corresponding eigenfunction is the velocity potential

$$\phi = \sum_{j=1}^{N} a_j^{(l)} \phi_j, \tag{6.38}$$

which is related to the shape of the interface disturbance

$$y = \sum_{j=1}^{N} a_j^{(l)} \frac{\partial \phi_j}{\partial n}. \tag{6.39}$$

The unstable growth rates ($\lambda^2 > 0$) and stable oscillation frequencies ($\lambda^2 < 0$) are computed using a truncation of $N = 8$ terms in the solution series (6.30). Here recall that $\lambda = (\sin\alpha)\hat{\lambda}$. Typical dispersion relations for the varicose and sinuous modes are given in figure 6.5.

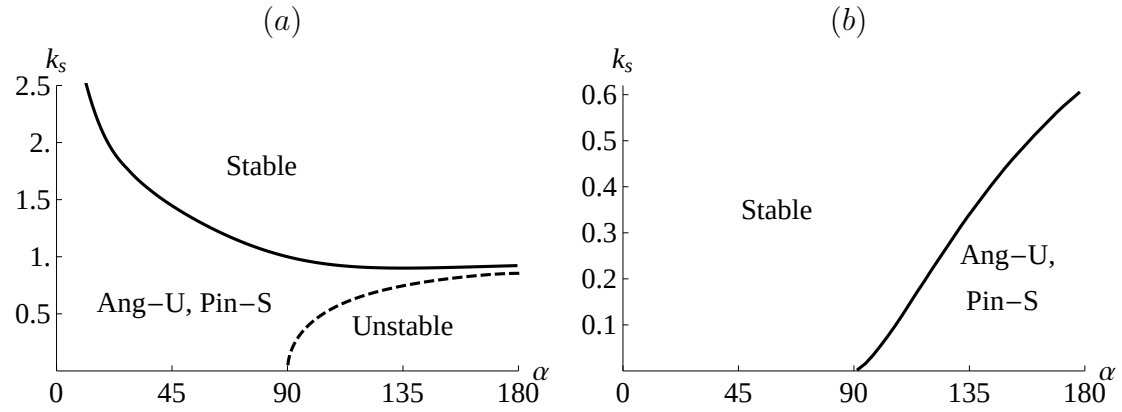

Figure 6.6: Static stability boundary k_s against contact-angle α for (a) varicose and (b) sinuous modes for the natural (Ang) and pinned (Pin) disturbances. Here stable (S) and unstable (U) regions are noted.

6.3.1 Static stability

With regards to static stability k_s, the varicose modes are more unstable than the sinuous modes. That is, the varicose mode is unstable to a greater range of axial wave-numbers, as shown in figure 6.6. In addition, for a fixed mode type a pinned contact-line disturbance is always stabilizing when compared to the natural disturbance. Static stability results for the varicose mode are summarized in figure 6.6(a) and can be directly compared to those computed by Davis (1980). The agreement is excellent. Despite the fact that the varicose mode is the dominant instability, the sinuous mode does exhibit instability to natural disturbances when the cylindrical base-state is super-circular $\alpha > 90°$. However, pinning the contact lines stabilizes the sinuous mode for all contact angles (and, equivalently, volumes) (c.f. figure 6.6(b)).

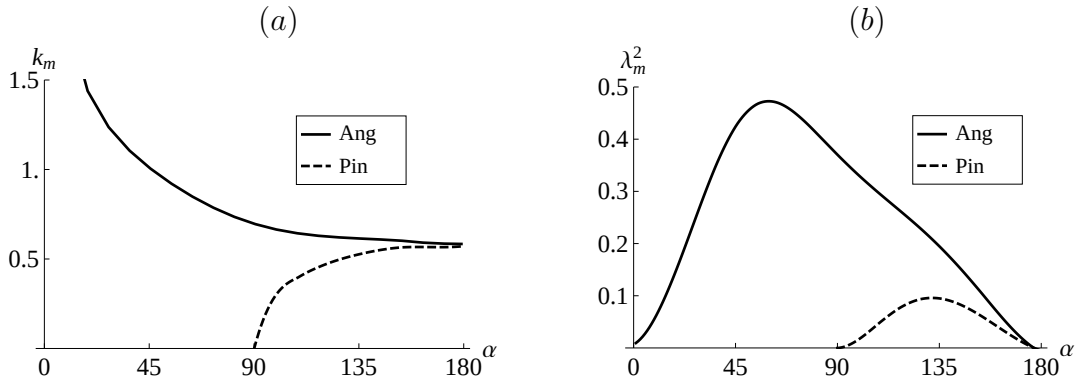

Figure 6.7: Fastest growing varicose mode: (a) wave-number k_m and (b) growth rate λ_m^2 against contact-angle α for natural (Ang) and pinned (Pin) disturbances.

6.3.2 Critical disturbance

A characteristic feature of the Plateau-Rayleigh instability is the existence of a fastest growing mode-shape distinguished by its axial wave-number k_m and growth rate λ_m^2. For example, the critical disturbance to the unconstrained Rayleigh jet (liquid cylinder) has a maximum growth rate $\lambda_m^2 = 0.343$ and wave-number $k_m = 0.69$. As shown in figure 6.7, the critical wave-number and maximum growth rate are modified according to the disturbance class and static contact-angle, but the behavior characteristic of Plateau-Rayleigh break-up persists for all of the varicose modes. Figure 6.8(a, b) displays typical varicose instability mode shapes for both disturbance classes. In the limit of a cylinder touching a planar support along a generating line ($\alpha \to 180°$), the stability results for the natural and pinned contact-line disturbance are indistinguishable (c.f. figures 6.6(a),6.7). More specifically, the contact-line is essentially immobile for the natural disturbance in this limit.

The sinuous mode exhibits behavior unlike that of the varicose mode and uncharacteristic of the Plateau-Rayleigh instability. For example, figure 6.9 shows

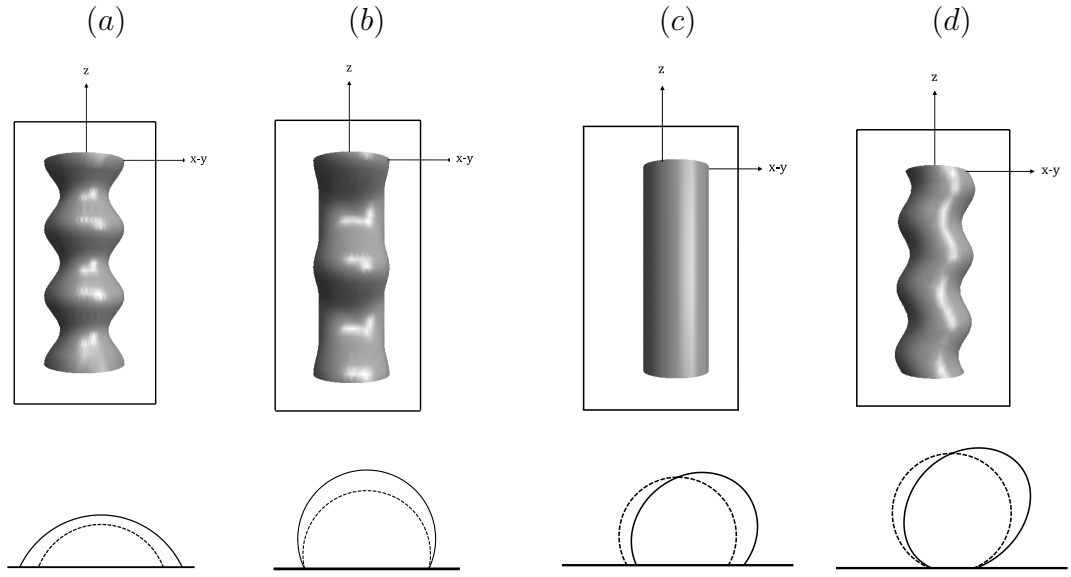

Figure 6.8: Typical instability mode shapes. The varicose mode for the (a) natural and (b) pinned contact-line disturbance. The natural sinuous mode with a (c) polar ($k = 0$) and (d) typical axial ($k \neq 0$) disturbance.

that for a range of contact-angle $90° < \alpha < 150°$ the wave-number of maximum growth is $k_m = 0$; that is, the critical disturbance is a polar one. Figure 6.8(c) plots a typical instability mode shape from this regime. Physically, this instability is characterized by an advancing contact-line, which is accelerating relative to the receding contact-line, thereby causing the cylindrical interface to 'walk' horizontally along the surface-of-support in the direction normal to the cylindrical axis. Outside this interval, typical capillary instability or Plateau-Rayleigh break-up occurs, as in figure 6.8(d).

Lastly, one can compare the effects of the type of support-surface. For example, figure 6.10 plots the maximum instability growth rate for the varicose modes of a cylindrical interface with pinned contact lines and in contact with either a planar or cylindrical-cup support (Bostwick & Steen, 2010) against contact-angle. Since

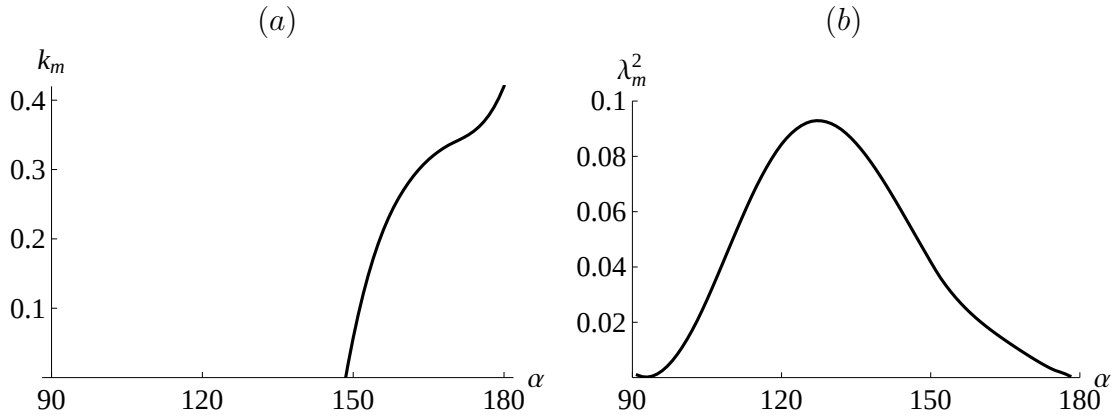

Figure 6.9: Fastest growing sinuous mode: (a) wave-number k_m and (b) growth rate λ_m^2 against contact-angle α for the natural disturbance.

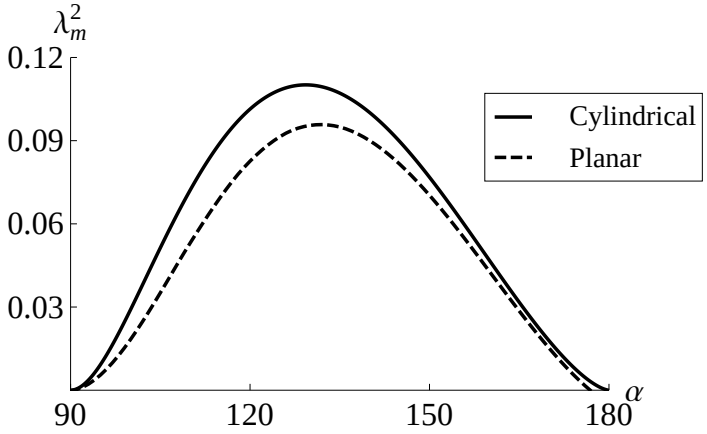

Figure 6.10: Comparison between the varicose mode with pinned contact-lines contacting either a cylindrical or planar support: maximum growth rate λ_m^2 against contact-angle α.

it depends solely upon the free surface shape, *static stability* is unaffected by the support geometry and is therefore identical for these two configurations. However, the *maximal growth rate* for the interface constrained by a cylindrical-cup support (see figure 4.1), reported by Bostwick & Steen (2010), is always larger than that for the corresponding interface in contact with a planar support.

6.4 Concluding Remarks

A number of authors have investigated the series of instabilities exhibited by fluid rivulets. It is common practice to use the lubrication approximation for film flow and asymptotics in the long wave-length limit to study the dynamics of the rivulet. Young & Davis (1987) use these approximations to study the varicose modes of the rivulet with a unidirectional gravity-driven base flow down a vertical plane. In the absence of a base flow, the rivulet is susceptible to capillary instability or Plateau-Rayleigh break-up, which can be greatly affected by the wetting conditions on the three-phase contact-line. For example, Davis (1980) computes the static stability bounds for the static rivulet under a number of contact-line conditions. In this chapter, the hydrodynamic equations are derived and then solved to give the dispersion relations for the static rivulet subject to the contact-line conditions used by Davis (1980). Thus, this work is intended to extend the work of Davis (1980) in a manner similar to how Lord Rayleigh (1879) extended the work of Plateau (1863) on the stability of liquid cylinders.

The dispersion relations for the static rivulet are computed from a functional eigenvalue equation using a Rayleigh-Ritz variational procedure. One major benefit associated with formulating the problem in a functional analysis setting is that interchanging boundary conditions on the contact-line and/or mode types is straightforward. Static stability of the varicose modes agrees well with Davis (1980), who does not need to distinguish between varicose and sinuous modes, because the varicose modes are the more unstable of the two mode types. This is confirmed by the computations performed here.

The sinuous mode exhibits instability to the super-circular base-state that is subject to a fixed contact-angle (natural) disturbance. This instability does not

share the typical characteristics of Plateau-Rayleigh break-up. More specifically, for a range of contact angles, the critical or fastest growing disturbance is distinguished by an axial wave-number $k_m = 0$ which, unlike Plateau-Rayleigh break-up, are 'long-wave instabilities'. The instability mode shape is characterized by an advancing contact-line, which is accelerating relative to its receding contact-line. Thus, fluid is displaced from one side of the rivulet to the other in what amounts to translational center-of-mass motion in the horizontal direction normal to the cylindrical axis (c.f. figure 6.8(c)). Outside this interval, typical capillary instability occurs, as shown in figure 6.8(d). Cataloging the sinuous instability may be important in understanding the phenomenon of rivulet meandering. From this analysis, rivulet meandering can only occur when the contact-lines are mobile.

With respect to the varicose modes, the rivulet is unconditionally unstable to natural disturbances and unstable to the super-circular base-states when the contact-lines are pinned. Accordingly, the growth rates of the critical disturbance are always larger for the natural disturbances, because they are less restrictive than a disturbance with pinned contact-lines. Finally, to compare the effects of the constraint geometry, the maximum growth rates for the cylindrical interface in contact with a planar support (rivulet) and a cylindrical-cup support (Bostwick & Steen, 2010) are compared. Here, static stability of the two configurations is coincident, but a larger critical growth rate occurs for the cylindrical-cup support.

CHAPTER 7

STABILITY BOUNDS FOR THE CATENOID

7.1 Introduction

One of the classic problems in the calculus of variations involves constructing surfaces of minimal area for a given set of boundary conditions. The catenoid is an example of one of these minimal surfaces, which are characterized by their mean curvature being zero. The connection between the mathematical description of these equilibrium surfaces and the theory of capillarity is well established and originated with the works of Young (1805) and Laplace (1806), who formulated the basic principles of surface tension. Namely, by assuming a fluid interface held by constant surface tension has a configurational energy proportional to its surface area, one can show a capillary surface is in static equilibrium if it has a constant mean curvature, and equivalently a constant pressure. Accordingly, static capillary surfaces are governed by the nonlinear Young-Laplace equation (an Euler-Lagrange equation). The resulting family of capillary surfaces is parameterized by mean curvature. Given a particular equilibrium surface, one would like to know under what conditions this configuration might be realized physically. To address this issue, one must introduce the notion of stability.

'Static stability' generally refers to the potential energy associated with a specific configuration, whereby one can infer relative stability by comparing the energies of two adjacent configurations. The state with lower energy is stable relative to the one with higher energy. Additionally, one can say that the equilibrium configuration in question is a local minima of energy, or is locally stable, if the comparison of adjacent configurations is exhaustive. For example, Plateau (1863,

1873) has used this notion of stability to derive the well-known Plateau limit: a cylindrical interface is unstable if its axial length is longer than the base-state circumference. One should note that the aforementioned notion of stability has implicitly assumed that the equilibrium configurations in question have been subject to the same 'class' of disturbance. In the theory of capillary surfaces, two disturbance classes are of particular interest; those which preserve either i) volume or ii) pressure of the equilibrium configuration.

In general, two calculations are involved when determining the static stability of a given equilibrium; determining the i) equilibrium surface and then its corresponding ii) stability. The latter is normally more complicated than the former. According to the calculus of variations, to deduce stability one must show the second variation is positive. One way is to prove i) Legendre's condition and ii) the absence of a conjugate point or negative eigenvalue of Jacobi's equation (Bolza, 1904). The stability calculation can be complicated further through the introduction of a conservation of volume constraint, an auxiliary condition needed for incompressible fluids. Using a conjugate point criteria, Howe (1887) has worked directly with the second variation to generate stability results for the zero-gravity, axisymmetric capillary surface under the constant-volume constraint. These results for the axisymmetric liquid bridge have been summarized by Gillette & Dyson (1971) in the zero-gravity limit.

To partially circumvent the calculation of the second variation, one may utilize the tools of bifurcation theory and constrained variational principles. The methodology is sketched here and expanded upon further in Appendix D. To begin, one may introduce a Lagrange multiplier in order to embed the volume in the surface-area functional and calculate families of equilibria from the augmented functional.

This is an iso-perimetric problem. As shown by Maddocks (1987) for an arbitrary Hilbert space, stability limits are always located at the 'turning points' of a preferred bifurcation diagram derived from the augmented functional. This method projects the second variation onto a constrained function space and uses an index theory to deliver the desired result. To use the theory, some information regarding the unconstrained second variation is needed. Hence, the stability calculation may be greatly simplified, but not eliminated. This theory has been applied to the axisymmetric liquid bridge by Lowry & Steen (1995).

Alternatively, one may work indirectly with the second variation by exploiting its structure and using elementary results from the calculus of variations to obtain static stability bounds for the family of catenoids, as well as the axisymmetric liquid bridge. A similar method has been used by Davis (1980) for the static rivulet under a variety of contact-line conditions. The technique developed in this chapter is termed the 'bounding' method. To validate the use of the bounding method, the static stability limit for the catenoid with fixed contact-lines (pinned) is computed and compared with known results, Erle *et al.* (1970). Next, static stability bounds are derived for the class of disturbances that preserves the static contact-angle. There are apparently no existing results regarding the stability of the catenoid subject to the fixed contact-angle (natural) disturbance. Lastly, the linearized hydrodynamic problem is solved and dispersion relations are computed in order to compare with the stability limit obtained by the bounding method.

The stability computed from the hydrodynamic approach is referred to as 'dynamic' stability. Equilibrium configurations are dynamically stable if starting from a bounded set of initial disturbances, the evolution of the disturbance stays within the 'neighborhood' of the equilibrium for all time. Static stability can be recov-

ered from the linearized hydrodynamic equations by setting the growth rate to zero. Thus, one can directly compare the stability limits from the hydrodynamic approach and the bounding method, which will serve as another validation of the proposed method. In addition, the computed linear growth rates give physical insight into the development of this instability.

The stability of the catenoid, subject to a variety of disturbances, is considered in this Chapter. First, a method is proposed to compute the static stability limit of the family of catenoids without explicitly calculating the second variation. Here the extreme-value theorem and some elementary results from the calculus of variations allow one to derive the result, which agrees well with the previous literature in the appropriate limit. To validate the static results computed from this method, the linearized hydrodynamic equations are formulated and growth rates are computed, from which one can compare directly with the static stability limit. The agreement is excellent. Finally, the bounding method is applied to the general axisymmetric liquid bridge to derive the corresponding static stability bound. Here information with regards to the equilibrium surface is the only information required to be input to the stability criteria.

7.2 Static stability

The catenoid is a surface-of-revolution, a solution of the Young-Laplace equation, can be defined parametrically as

$$X(s,\varphi;c) = c\cosh\left(\frac{s}{c}\right)\cos\varphi, \tag{7.1a}$$

$$Y(s,\varphi;c) = c\cosh\left(\frac{s}{c}\right)\sin\varphi, \tag{7.1b}$$

$$Z(s;c) = s, \tag{7.1c}$$

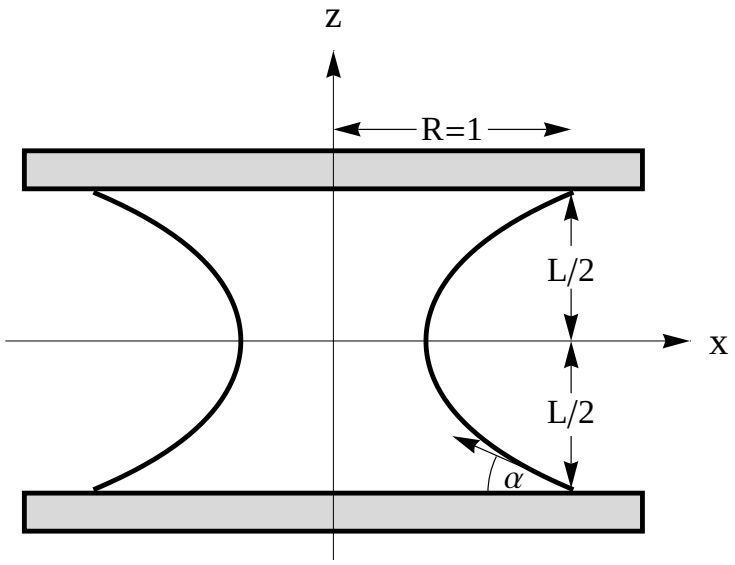

Figure 7.1: Definition sketch for the catenoid.

using arc-length $s \in [-\mathcal{S}, \mathcal{S}]$ and azimuthal angle $\varphi \in [0, 2\pi]$ as generalized surface coordinates (c.f. figure 7.1). This family of surfaces, as they depend upon the parameter c, have principal curvatures

$$\kappa_1 = -\kappa_2 = \frac{1}{c}\text{sech}^2\left(\frac{s}{c}\right) \tag{7.2}$$

and may be characterized by their mean curvature $H \equiv \kappa_1 + \kappa_2 = 0$.

As the catenoid is a solution of the Euler-Lagrange equations, stability is determined by giving the equilibrium surface a perturbation $y(s)$ and solving the eigenvalue problem associated with the second variation

$$-\Delta_\Gamma y(s) - \left(\kappa_1^2 + \kappa_2^2\right) y(s) = \lambda y(s). \tag{7.3}$$

The sign of the eigenvalue λ determines the stability of the equilibrium surface. Here the Laplace-Beltrami operator or surface Laplacian,

$$\Delta_\Gamma y = \frac{1}{\sqrt{g}}\frac{\partial}{\partial u^\alpha}\left(\sqrt{g}g^{\alpha\beta}\frac{\partial y}{\partial u^\beta}\right), \tag{7.4}$$

is defined on the equilibrium surface through the surface metric

$$g_{\alpha\beta} \equiv \boldsymbol{x}_\alpha \cdot \boldsymbol{x}_\beta = \begin{pmatrix} \cosh^2(s/c) & 0 \\ 0 & c^2 \cosh^2(s/c) \end{pmatrix}, \quad g = c^2 \cosh^4(s/c). \tag{7.5}$$

Finally, the eigenvalue problem (7.3) is augmented with a boundary condition at the three-phase contact-line and may or may not satisfy the volume conservation constraint

$$\int_\Gamma y(s)\mathrm{d}s = 0. \tag{7.6}$$

That is, the disturbance class to which the interface is subject may consist of either constant volume or constant pressure disturbances.

As an alternative to constructing an explicit solution to the boundary value problem (7.3), one can work directly with the second variation. By using the definition of the surface metric (7.5), the integral form of the second variation (7.3) can be written as a functional equation

$$I = \lambda \int_{-\mathcal{S}}^{\mathcal{S}} \cosh^2\left(\frac{s}{c}\right) y^2 \mathrm{d}s \tag{7.7}$$

with

$$I \equiv -\int_{-\mathcal{S}}^{\mathcal{S}} \left(y'' + \frac{2}{c^2}\mathrm{sech}^2\left(\frac{s}{c}\right) y \right) y \,\mathrm{d}s. \tag{7.8}$$

Using this formulation proves advantageous, because the structure of (7.7) allows one to pose a sufficient condition for stability.

Theorem 2 *The catenoid is stable to infinitesimal disturbances when the functional (7.8) is positive.*

To prove this theorem, note that the right hand side of (7.7) is positive for all functions y. The value of the functional I is dependent upon the boundary conditions at the three-phase contact-line and will be analyzed separately.

7.2.1 Pinned contact-line disturbance

In this section the contact-line is assumed to be immobile or pinned,

$$y(-1/2) = y(1/2) = 0, \tag{7.9}$$

and solutions to (7.7) are sought in both the constant pressure and constant volume disturbance classes. Here lengths have been scaled such that $\mathcal{S} = 1/2$ and the family of catenoids is parameterized by c.

To derive a stability criteria, begin by integrating functional (7.8) by parts and using contact-line conditions (7.9) to give

$$I = \int_{-1/2}^{1/2} \left(y'^2 - \frac{2}{c^2} \mathrm{sech}^2 \left(\frac{s}{c} \right) y^2 \right) \mathrm{d}s, \tag{7.10}$$

which is a quadratic form that can be bounded on the interval $s \in [-1/2, 1/2]$,

$$\int_{-1/2}^{1/2} \left(y'^2 - \frac{2}{c^2} \mathrm{sech}^2 \left(\frac{1}{2c} \right) y^2 \right) \mathrm{d}s \geq I \geq \int_{-1/2}^{1/2} \left(y'^2 - \frac{2}{c^2} y^2 \right) \mathrm{d}s, \tag{7.11}$$

using the extreme-value theorem. It follows from (7.11) that if

$$I_{min} \equiv \int_{-1/2}^{1/2} \left(y'^2 - \frac{2}{c^2} y^2 \right) \mathrm{d}s > 0, \tag{7.12}$$

the stability criteria of Theorem 2 is satisfied.

To compute the value of I_{min}, as it depends upon c, the following elementary result from the calculus-of-variations, often called the 'Poincare inequality', is used

$$\int_{-1/2}^{1/2} y'^2 \, \mathrm{d}s \geq \xi^2 \int_{-1/2}^{1/2} y^2 \, \mathrm{d}s. \tag{7.13}$$

This result is applied to the functional (7.12) to give

$$I_{min} = \left(\xi^2 - \frac{2}{c^2} \right) \int_{-1/2}^{1/2} y^2 \, \mathrm{d}s, \tag{7.14}$$

and equivalently the following stability criteria

$$c^2 > \frac{2}{\xi^2}. \tag{7.15}$$

Here the positive number ξ^2, defined in (7.13), is the smallest eigenvalue calculated from the boundary value problem

$$y'' + \xi^2 y = 0, \quad y(-1/2) = y(1/2) = 0. \tag{7.16}$$

As mentioned earlier, two classes of solution to (7.16) are considered. The first class has a constant-pressure and the solution is given by

$$y_p(s) = \cos(\pi s), \quad \xi_p^2 = \pi^2, \tag{7.17}$$

while the second class has constant-volume,

$$y_v(s) = \sin(2\pi s), \quad \xi_v^2 = (2\pi)^2. \tag{7.18}$$

Note that (7.18) satisfies (7.6) and therefore preserves volume. The smallest eigenvalue ξ^2 is the necessary input to the stability criteria (7.15) and is used to compute the critical parameter values

$$c_p = \frac{\sqrt{2}}{\pi}, \quad c_v = \frac{1}{\sqrt{2}\pi}, \tag{7.19}$$

for constant pressure and constant volume disturbances, respectively.

Results

The family of catenoids can be represented in the length-volume space by defining the slenderness

$$\Lambda \equiv \frac{L}{2R} = \frac{1}{c\cosh(1/2c)} \tag{7.20}$$

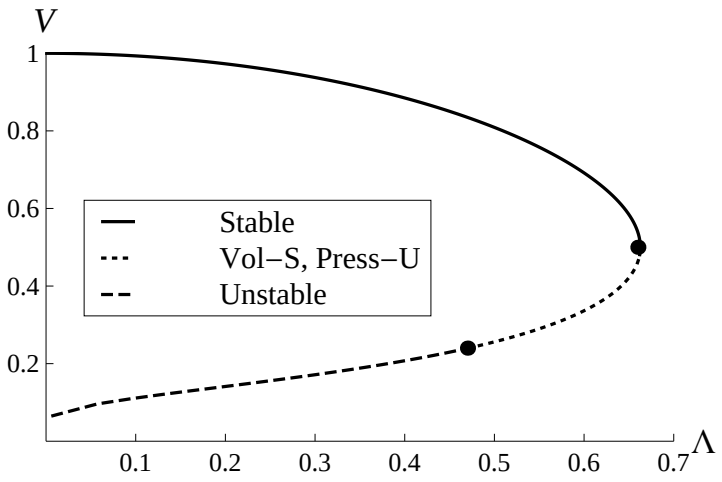

Figure 7.2: Stability diagram for the pinned contact-line disturbance class showing stable (solid line), unstable (dashed line) and conditionally stable (dotted) catenoids. Here the conditionally stable catenoid is stable (S) to constant-volume (Vol) and unstable (U) to constant-pressure (Press) disturbances.

and relative volume

$$V \equiv \frac{\int_{-1/2}^{1/2} \cosh^2(s/c)\,\mathrm{d}s}{\cosh^2(1/2c)}. \tag{7.21}$$

The computed critical slenderness for constant pressure $\Lambda_p = 0.66$ and constant volume $\Lambda_v = 0.47$ disturbances are summarized in the stability diagram of figure 7.2 (pinned catenoids). The stability of the catenoid with pinned contact lines has been reported by Erle *et al.* (1970), among others. However, the bounding method is new and has been shown to be quite satisfactory, as witnessed by the 0.01% error in the critical slenderness. In addition, one may infer that the instability is local in nature, because the extreme value theorem is inherently local in that it isolates the location of the maximal sum of squares of the principal curvatures.

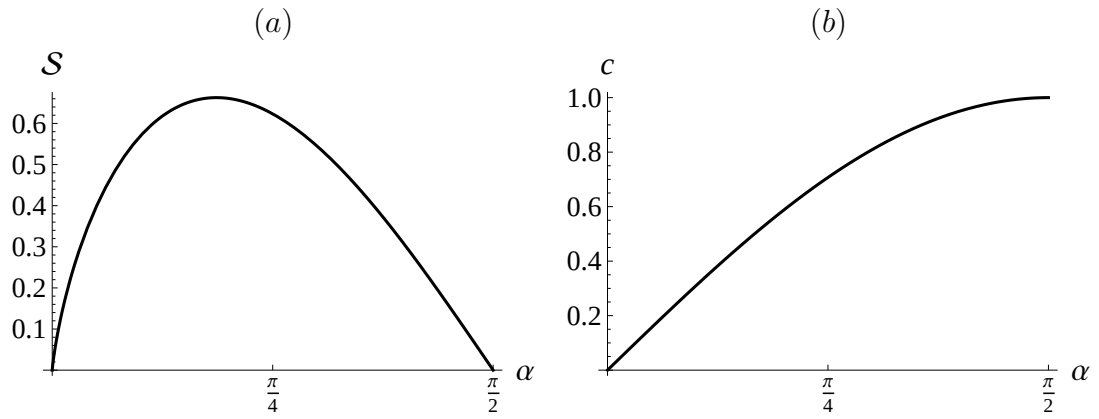

Figure 7.3: Scaling of catenoid by contact-angle: parameters (a) $\mathcal{S}$ and (b) c against contact-angle α.

7.2.2 Natural disturbance

The second class of disturbances preserves the static contact-angle α, in accordance with the Young-Dupré equation (1.4), and is termed the natural disturbance. Here lengths are scaled by the base radius R and the arc-length coordinate is defined as $s \in [-\mathcal{S}, \mathcal{S}]$, such that

$$\mathcal{S} \equiv \frac{2\sinh^{-1}(\cot\alpha)}{\cosh\left(\sinh^{-1}(\cot\alpha)\right)} \tag{7.22}$$

and

$$c = \frac{1}{\cosh\left(\sinh^{-1}(\cot\alpha)\right)} \tag{7.23}$$

are parameterized by the contact-angle α (c.f. figure 7.3). Equivalently, the family of catenoids can be represented in the length-volume space by defining the slenderness

$$\Lambda \equiv \frac{L}{2R} = \frac{\sinh^{-1}(\cot\alpha)}{\cosh\left(\sinh^{-1}(\cot\alpha)\right)} \tag{7.24}$$

and volume

$$V \equiv \frac{1}{2\cosh^2\left(\sinh^{-1}(\cot\alpha)\right)}\left[1 + \frac{\sinh\left(2\sinh^{-1}(\cot\alpha)\right)}{\sinh^{-1}(\cot\alpha)}\right], \tag{7.25}$$

which is scaled with the volume of a cylinder. To preserve the static contact-angle, allowable disturbances must satisfy the following kinematic conditions on the three-phase contact-line,

$$(-y' + k(\alpha)y)\,|_{s=-\mathcal{S}} = 0, \quad (y' + k(\alpha)y)\,|_{s=\mathcal{S}} = 0 \tag{7.26}$$

with

$$k(\alpha) \equiv \frac{\cot\alpha}{c(\alpha)}\operatorname{sech}^2\left(\frac{\mathcal{S}}{2c(\alpha)}\right). \tag{7.27}$$

To formulate the stability criteria for the natural disturbance, transform the functional (7.8) into a quadratic form

$$I = \int_{-\mathcal{S}}^{\mathcal{S}} \left(y'^2 - \frac{2}{c^2(\alpha)}\operatorname{sech}^2\left(\frac{s}{c(\alpha)}\right)y^2\right)\mathrm{d}s - k(\alpha)\left[y^2(\mathcal{S}) + y^2(-\mathcal{S})\right] \tag{7.28}$$

using boundary conditions (7.26) and integration by parts. Similar to what was done previously, the quadratic form (7.28) is bounded from below

$$I \geq I_{min} = \int_{-\mathcal{S}}^{\mathcal{S}} \left(y'^2 - \frac{2}{c^2(\alpha)}y^2\right)\mathrm{d}s - k(\alpha)\left[y^2(\mathcal{S}) + y^2(-\mathcal{S})\right] \tag{7.29}$$

using the extreme value theorem and stability again follows from Theorem 2. An inequality from the calculus of variations,

$$\int_{-\mathcal{S}}^{\mathcal{S}} y'^2\,\mathrm{d}s - k(\alpha)\left[y^2(\mathcal{S}) + y^2(-\mathcal{S})\right] \geq \zeta\int_{-\mathcal{S}}^{\mathcal{S}} y^2\,\mathrm{d}s, \tag{7.30}$$

is used to recast the critical functional (7.29) as

$$I_{min} = \left(\zeta(\alpha) - \frac{2}{c^2(\alpha)}\right)\int_{-\mathcal{S}}^{\mathcal{S}} y^2\,\mathrm{d}s \tag{7.31}$$

with stability assured if

$$\zeta(\alpha) - \frac{2}{c^2(\alpha)} > 0. \tag{7.32}$$

The Euler-Lagrange equations associated with the functional (7.29) give rise to the boundary value problem,

$$y'' + \zeta y = 0, \quad (-y' + k(\alpha)y)\,|_{-\mathcal{S}} = 0, \;\; (y' + k(\alpha)y)\,|_{\mathcal{S}} = 0, \tag{7.33}$$

whose smallest eigenvalue $\zeta(\alpha)$ is required in the stability criteria (7.32). As before, the constant pressure solution of (7.33) is expressed as

$$y_p(s) = \cos(\sqrt{\zeta_p}s), \quad \sqrt{\zeta_p}\tan\frac{\sqrt{\zeta_p}}{2} = k(\alpha) \tag{7.34}$$

while the constant volume solution satisfies (7.6) and is given by

$$y_v(s) = \sin(\sqrt{\zeta_v}s), \quad \sqrt{\zeta_v}\cot\frac{\sqrt{\zeta_v}}{2} = -k(\alpha). \tag{7.35}$$

Finally, to compute the critical contact-angle α from (7.32), the smallest eigenvalue $\zeta(\alpha)$ from (7.34) and (7.35) is needed.

Results

Computations show the constant pressure disturbance is unstable for all contact angles and the constant volume disturbance is stable for contact angles $\alpha > 21.6°$, or a critical slenderness $\Lambda = 0.61$. These results are summarized in the natural disturbance stability diagram of figure 7.4. The constant pressure stability result is not surprising, considering the contact-line is free to move along the surface of support with prescribed contact-angle. For example, as the contact-line moves, volume is allowed to leave the domain, resulting in the collapse of the catenoid, because energy decreases with decreasing surface area. This phenomenon is not present when volume is conserved as when the contact-line is pinned. Similar to the pinned disturbance, the conservation of volume constraint acts like a restoring force to the contact-line motion, much like the spring force resists the inertial motion in a simple harmonic oscillator.

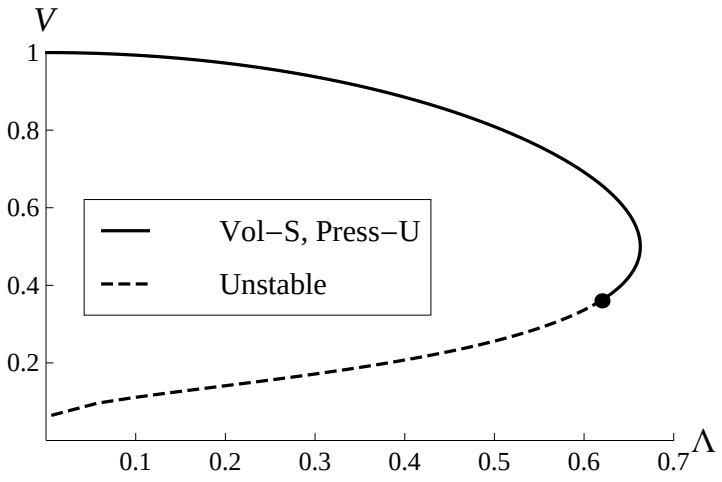

Figure 7.4: Stability diagram for the catenoid subject to the natural disturbance class showing unstable (dashed line) and conditionally stable (solid line) regions. The conditionally stable catenoid is stable (S) to constant-volume (Vol) and unstable (U) to constant-pressure (Press) disturbances.

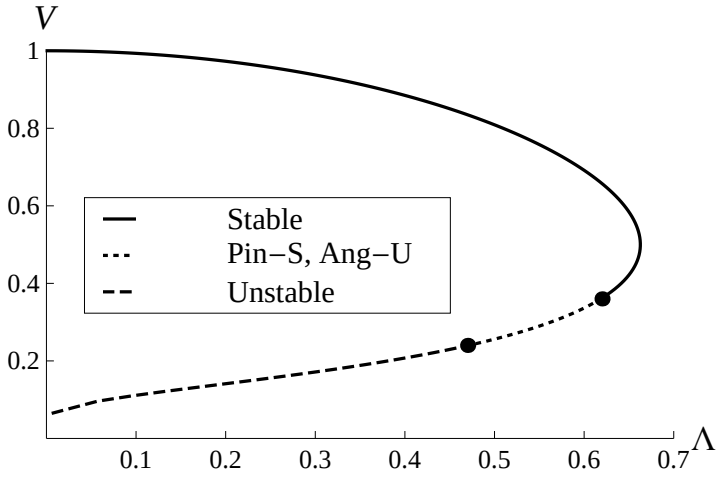

Figure 7.5: Constant-volume stability diagram showing stable (solid line), unstable (dashed line) and conditionally stable (dotted line) catenoids. The conditionally stable catenoid is unstable (U) to natural (Ang) and stable (S) to pinned (Pin) disturbances.

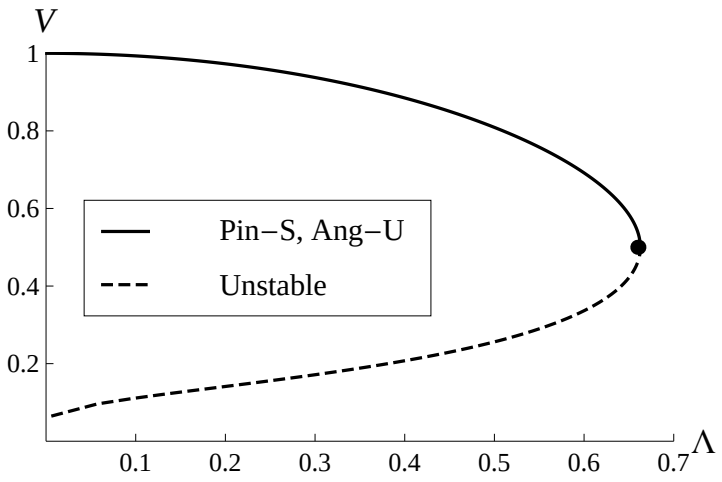

Figure 7.6: Constant-pressure stability diagram showing unstable (dashed line) and conditionally stable (solid line) catenoids. The conditionally stable catenoid is unstable (U) to natural (Ang) and stable (S) to pinned (Pin) disturbances.

7.2.3 Remarks

One may compare the effect of the disturbance class to which the catenoid is subject, either natural or pinned. As evident from figures 7.5 & 7.6, pinning the contact-line is shown to be stabilizing with respect to both constant-volume and constant-pressure disturbances, respectively. To clarify, when viewed as a variational problem constraints tend to stabilize by restricting the class of allowable solutions, as is the case with the pinned contact-line.

As stated earlier, the bounding technique localizes the variational problem by isolating the location of the maximal sum of squares of principal curvatures, which occurs at $s = 0$ for the catenoid. This implies that the instability is local, which is somewhat surprising considering that the disturbance classes are distinguished by their contact-line conditions, a large distance from $s = 0$. Nevertheless, the stability limit for the pinned disturbance is reconciled with the previous literature

to a more than acceptable degree of accuracy for this type of local approximation. To further validate this method, the stability limit for the natural disturbance will be calculated using the hydrodynamic approach. This approach is used, because the computed growth rates are physically significant and the static results are recovered by setting growth rate to zero.

7.3 Dynamic stability

The linearized hydrodynamic equations, governing the motion of the catenoidal interface, are formulated in this section. To compare with the static stability results obtained by the bounding method, solutions are sought in the space of functions which preserve static contact-angle α and conserve volume. To analyze this class of disturbance, the contact-angle parametrization of the catenoid (7.22) and (7.23) is used. Likewise, lengths are scaled with the base radius R, as shown in figure 7.1.

7.3.1 Hydrodynamic formulation

The domain (c.f. figure 7.1)

$$D \equiv \{(x,z)|\ 0 \le x \le X(s;\alpha),\ \ -\mathcal{S} \le z \le \mathcal{S}\} \tag{7.36}$$

of this inviscid fluid is bounded by a free surface ∂D^f and two parallel end-plates ∂D^s,

$$\partial D^f \equiv \{(x,z)\,|\ x = X(s;\alpha),\ z = Z(s;\alpha)\}, \tag{7.37a}$$

$$\partial D^s \equiv \{(x,z)\,|\ z = \pm\mathcal{S}\}. \tag{7.37b}$$

Recall that the total arc-length $\mathcal{S}$ implicitly defines the axial length $L = 2\mathcal{S}$, as in (7.22). The irrotational velocity field of this incompressible fluid is described by a velocity potential, $\boldsymbol{v} = \boldsymbol{\nabla}\Psi$, which satisfies Laplace's equation

$$\nabla^2\Psi = 0 \quad [D] \tag{7.38}$$

on the fluid domain and a no-penetration condition on the end-plates,

$$\boldsymbol{\nabla}\Psi \cdot \hat{\boldsymbol{z}} = 0 \quad [\partial D^s]. \tag{7.39}$$

The catenoidal interface is displaced by a small axisymmetric perturbation $\eta(s,t)$, whose velocity must be kinematically compatible with the normal velocity on the interface,

$$\frac{\partial\Psi}{\partial n} = -\frac{\partial\eta}{\partial t} \quad [\partial D^f]. \tag{7.40}$$

An interface given such a perturbation generates pressure gradients

$$p/\sigma = -\Delta_\Gamma\eta - \left(\kappa_1^2 + \kappa_2^2\right)\eta \quad [\partial D^f] \tag{7.41}$$

balanced by the Bernoulli pressure

$$p = \rho\frac{\partial\Psi}{\partial t} \quad [D], \tag{7.42}$$

evaluated at the fluid interface, as required by continuity. Equations (7.38)-(7.42) are the time-dependent field equations governing the motion of an incompressible, inviscid fluid, whose catenoidal interface is subject to a small axisymmetric disturbance. These equations are reduced to an eigenvalue problem by a normal mode analysis.

7.3.2 Normal-mode reduction

Normal modes

$$\eta(s,t) = y(s)\mathrm{e}^{i\omega t}, \quad \Psi(\boldsymbol{x},t) = \phi(\boldsymbol{x})\mathrm{e}^{i\omega t}, \tag{7.43}$$

are used to reduce the hydrodynamic equations (7.38)-(7.42) to an eigenvalue problem

$$\nabla^2\phi = 0 \;\; [D], \tag{7.44a}$$

$$\frac{\partial\phi}{\partial n} = 0 \;\; [\partial D^s], \tag{7.44b}$$

$$-\Delta_\Gamma \frac{\partial\phi}{\partial n} - \left(\kappa_1^2 + \kappa_2^2\right)\frac{\partial\phi}{\partial n} = \lambda^2\phi \;\; [\partial D^f], \tag{7.44c}$$

$$\int_\Gamma \frac{\partial\phi}{\partial n} = 0, \tag{7.44d}$$

$$\lambda^2 \equiv \frac{\rho\omega^2 R^3}{\sigma}. \tag{7.44e}$$

Equations (7.44a)-(7.44c) follow directly, whereas (7.44d) is necessary to enforce incompressibility or volume conservation. One should note that (7.44c) represents the balance of inertial and capillary pressures at the interface and is equivalent to the eigenvalue problem associated with the second variation (7.3). In contrast, the eigenvalue λ^2, which measures either the unstable growth rate or frequency of oscillation, may be interpreted physically. This follows from the fact that (7.44 $a-d$) were derived from the hydrodynamic equations. Moreover, static stability is obtained by setting the eigenvalue to zero.

Operator formalism

Equation (7.44c) is an operator equation that can be formulated using one of two equivalent approaches. The first uses the normal interface velocity as the basis function and is referred to as the forward problem,

$$K\left[\frac{\partial\phi}{\partial n}\right] = \lambda^2 M\left[\frac{\partial\phi}{\partial n}\right], \tag{7.45}$$

while the second has the velocity potential as the relevant basis function and is known as the inverse problem,

$$M^{-1}[\phi] = \lambda^2 K^{-1}[\phi]. \tag{7.46}$$

Stationary values of both functionals necessarily satisfy Laplace's equation (7.44a) and conserve volume according to (7.44d), but the forward problem requires a sufficiently general solution to the following Neumann type boundary value problem,

$$\nabla^2\psi = 0, \quad \left.\frac{\partial\psi}{\partial n}\right|_\Gamma = y_k(s), \tag{7.47}$$

which is not analytically tractable for this geometry. One approach would be to use a more computationally intensive approach. Alternatively, one may treat

$$M^{-1}[\phi] \equiv \cosh^2\left(\frac{s}{c}\right)\frac{\partial\phi}{\partial n} \tag{7.48}$$

as the differential operator and compute the integral operator, inverse to K. This formulation is called the inverse problem and will be used to compute the spectrum of (7.44).

7.3.3 Solution of operator equation

The eigenvalue spectrum of (7.44) is computed by a Rayleigh-Ritz procedure. This procedure reduces the inverse operator formulation (7.46) of the governing equation to a set of algebraic equations or a standard eigenvalue problem. To begin, one must construct the inverse operator K^{-1}.

Inverse-operator construction

The differential operator

$$K\,[y] \equiv y'' + \frac{2}{c^2(\alpha)}\mathrm{sech}^2\left(\frac{s}{c(\alpha)}\right)y \tag{7.49}$$

is defined on the equilibrium surface and subject to the following boundary conditions on the contact-line,

$$\begin{gathered}(-y' + \chi y)\big|_{s=-\mathcal{S}} = 0, \quad (y' + \chi y)\big|_{s=\mathcal{S}} = 0, \\ \chi(s) = \cot(\alpha)\frac{1}{c(\alpha)}\operatorname{sech}^2\left(\frac{s}{c(\alpha)}\right),\end{gathered} \tag{7.50}$$

a necessary condition to ensure interface disturbances preserve the static contact-angle. The inverse operator

$$K^{-1}[y] \equiv \int_{-\mathcal{S}}^{\mathcal{S}} G(s,q)y(q)\,\mathrm{d}q \tag{7.51}$$

is related to the fundamental solution of the corresponding differential operator, or Green's function,

$$G(s,q) = \begin{cases} v_1(q)v_2(s) + \frac{1}{2}w(s,q) & -\mathcal{S} < q < s < \mathcal{S} \\ v_1(s)v_2(q) + \frac{1}{2}w(s,q) & -\mathcal{S} < s < q < \mathcal{S}. \end{cases} \tag{7.52}$$

The functions v_1 and v_2 satisfy

$$v_k'' + \frac{2}{c^2(\alpha)}\operatorname{sech}^2\left(\frac{s}{c(\alpha)}\right)v_k = 0,\ v_1(0) = 0, v_1'(0) = 1,\ v_2(0) = 1, v_2'(0) = 0 \tag{7.53}$$

and belong to the kernel of K, while

$$\begin{aligned}w(s,q) = \left(\frac{\tau_1}{\tau_2}\right)v_2(s)v_2(q) - \left(\frac{\tau_2}{\tau_1}\right)v_1(s)v_1(q) - v_1(s)v_2(q) - v_1(q)v_2(s) \\ + \frac{1}{\tau_3}F(s)F(q)\end{aligned} \tag{7.54}$$

with

$$\tau_1 = v_1'(\mathcal{S}) + \chi(\mathcal{S})v_1(\mathcal{S}), \quad \tau_2 = v_2'(\mathcal{S}) + \chi(\mathcal{S})v_2(\mathcal{S}), \tag{7.55a}$$

$$F(s) = [v_2(s)\psi_1(s) - v_1(s)\psi_2(s)] + \left[\left(\frac{\tau_2}{\tau_1}\right)\psi_2(\mathcal{S}) - \psi_1(\mathcal{S})\right]v_2(s), \tag{7.55b}$$

$$\psi_k(s) = \int_0^s v_k(q)\,\mathrm{d}q, \tag{7.55c}$$

$$\tau_3 = -\int_0^{\mathcal{S}} F(s)\,\mathrm{d}s. \tag{7.55d}$$

Rayleigh-Ritz reduction

The eigenvalue spectrum may be computed by reducing the operator equation (7.46) to a set of linear algebraic equations using a Rayleigh-Ritz procedure with the following basis functions,

$$\phi_k(r,z) = c_k \left[\Phi_k(r,z) - d_k\right], \quad d_k \equiv \frac{1}{\mathcal{S}} \int_0^{\mathcal{S}} \Phi_k|_\Gamma \, \mathrm{d}s, \tag{7.56}$$

which are chosen to satisfy the no-penetration condition (7.44b) identically. The basis functions are scaled such that their average value on the equilibrium line is zero, a sufficient condition to ensure volume is conserved, as required by the assumption of incompressibility. Owing to the symmetry of the boundary conditions (7.50) on the three-phase contact-line, the eigenvalue problem may be decomposed into its odd/even extension using the pertinent basis functions,

$$\Phi_k^{(o)}(r,z) = I_0\left((k-1/2)\,\frac{\pi r}{L}\right) \sin\left((k-1/2)\,\frac{\pi z}{L}\right), \tag{7.57a}$$

$$\Phi_k^{(e)}(r,z) = I_0\left(k\frac{\pi r}{L}\right) \cos\left(k\frac{\pi z}{L}\right). \tag{7.57b}$$

Here I_0 is the modified Bessel function of the first kind and $L = 2\mathcal{S}$ with $\mathcal{S}$ given by (7.22). A superscript "o, e" will be used to distinguish the odd and even solutions, respectively.

The necessary input to the Rayleigh-Ritz procedure is a solution series

$$\phi = \sum_{k=1}^{N} a_k \phi_k, \tag{7.58}$$

constructed from the basis functions (7.56), which are used to reduce the functional eigenvalue problem (7.46) to the following set of linear algebraic equations,

$$\sum_{k=1} \left(m_{ik} - \lambda^2 \kappa_{ik}\right) a_k = 0, \tag{7.59a}$$

$$m_{ik} \equiv \int M^{-1}[\phi_i]\phi_k \, \mathrm{d}s, \quad \kappa_{ik} \equiv \int K^{-1}[\phi_i]\phi_k \, \mathrm{d}s. \tag{7.59b}$$

The corresponding matrix elements in the odd/even extensions are expressed as

$$m_{ik}^{(o)} = m_{ki}^{(o)} = 2c_i c_k \int_0^{\mathcal{S}} \cosh^2\left(s/c(\alpha)\right) \frac{\partial \phi_i}{\partial n}(s)\phi_k(s)\,\mathrm{d}s, \tag{7.60a}$$

$$\kappa_{ik}^{(o)} = \kappa_{ki}^{(o)} = -2c_i c_k \left[\left(\frac{\tau_2}{\tau_1}\right)\zeta_i\zeta_k - \zeta_i\eta_k - \zeta_k\eta_i + \epsilon_{ik} + \epsilon_{ki}\right], \tag{7.60b}$$

and

$$m_{ik}^{(e)} = m_{ki}^{(e)} = 2c_i c_k \int_0^{\mathcal{S}} \cosh^2\left(s/c(\alpha)\right) \frac{\partial \phi_i}{\partial n}(s)\phi_k(s)\mathrm{d}s, \tag{7.61a}$$

$$\kappa_{ik}^{(e)} = \kappa_{ki}^{(e)} = 2c_i c_k \left[\left(\frac{\tau_1}{\tau_2}\right)\eta_i\eta_k + \left(\frac{1}{\tau_3}\right)\xi_i\xi_k - \epsilon_{ik} - \epsilon_{ki}\right], \tag{7.61b}$$

respectively. Here the following definitions have been used

$$\zeta_k \equiv \int_0^{\mathcal{S}} v_1(s)\phi_k(s)\mathrm{d}s, \tag{7.62a}$$

$$\eta_k \equiv \int_0^{\mathcal{S}} v_2(s)\phi_k(s)\mathrm{d}s, \tag{7.62b}$$

$$\epsilon_{ik} \equiv \int_0^{\mathcal{S}} v_1(s)\phi_i(s) \int_0^s v_2(q)\phi_k(q)\mathrm{d}q\,\mathrm{d}s, \tag{7.62c}$$

$$\xi_k \equiv -\int_0^{\mathcal{S}} F(s)\phi_k(s)\mathrm{d}s. \tag{7.62d}$$

Finally, the scale factor c_k, from (7.60) and (7.61), is chosen such that the coordinate functions are of order one on the equilibrium surface,

$$c_k = \frac{1}{\sqrt{2}}\left(\int_0^{\mathcal{S}} \cosh^2\left(s/c(\alpha)\right) \frac{\partial \phi_k}{\partial n}(s)\phi_k(s)\mathrm{d}s\right)^{-1/2}. \tag{7.63}$$

7.3.4 Results

The eigenvalues, as they depend on the contact-angle α, are computed from (7.59) using $N = 8$ terms in the solution series (7.58). Computations exhibit relative error for the first three eigenvalues of 0.1% for this truncation. Given an eigenvalue λ_j^2 and eigenvector $a_k^{(j)}$, the instability or oscillatory mode shape is given by

$$y^{(j)}(s) = \sum_{k=1}^{N} a_k^{(j)} c_k \left(\frac{\partial \phi_k}{\partial n}\right)(s). \tag{7.64}$$

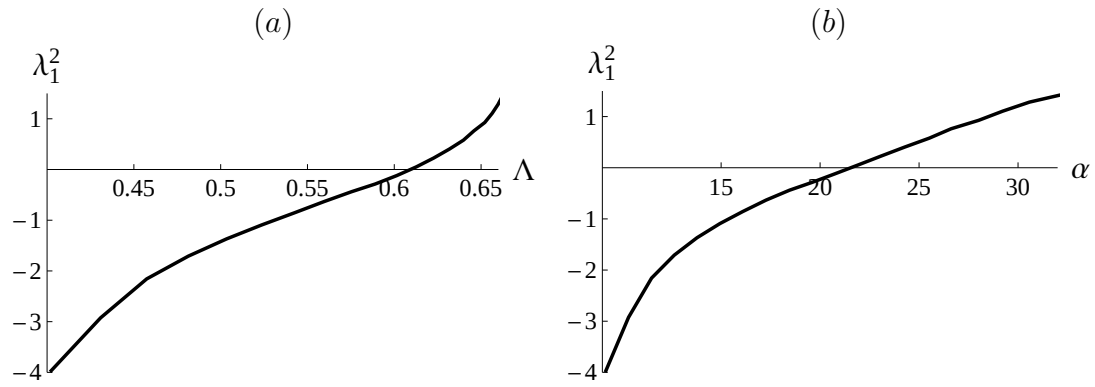

Figure 7.7: Unstable growth rate $\lambda_1^2 < 0$ vs. (a) slenderness Λ and (b) contact-angle α for the catenoid given a natural disturbance.

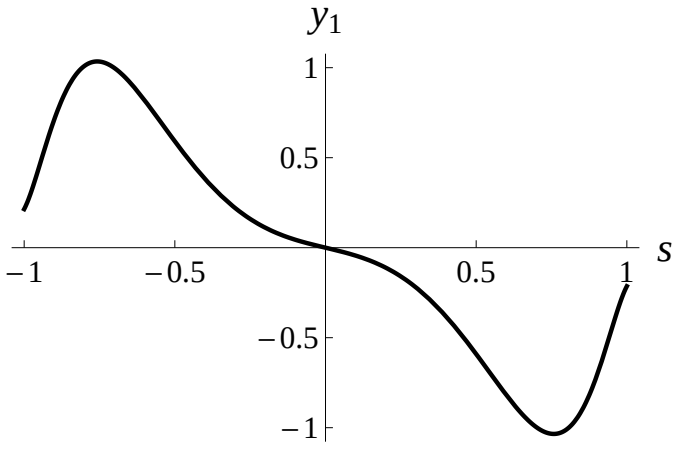

Figure 7.8: Typical instability mode shape for the natural disturbance ($\alpha = 20°$).

The primary goal in formulating the hydrodynamic equations was to compare with the static stability results from the bounding method. Computations reveal the $j = 1$ mode shape is unstable $\lambda^2 < 0$ for a range of contact angles $\alpha < 21.6°$, as shown in figure 7.7(b). Likewise, the critical slenderness $\Lambda = 0.61$, seen in figure 7.7(a), is in excellent agreement with the static stability results of the previous section, obtained by the bounding method. For reference, a typical unstable mode shape is shown in figure 7.8 using a scaled arc-length coordinate. Additionally,

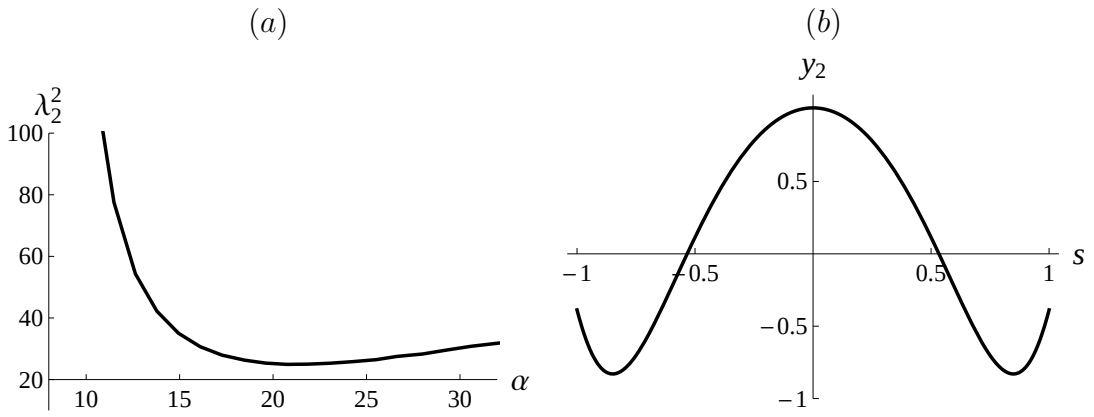

Figure 7.9: Oscillation mode ($n = 2$): (a) Frequency $\lambda_2^2 > 0$ vs. contact-angle α and (b) sample mode shape for $\alpha = 25°$.

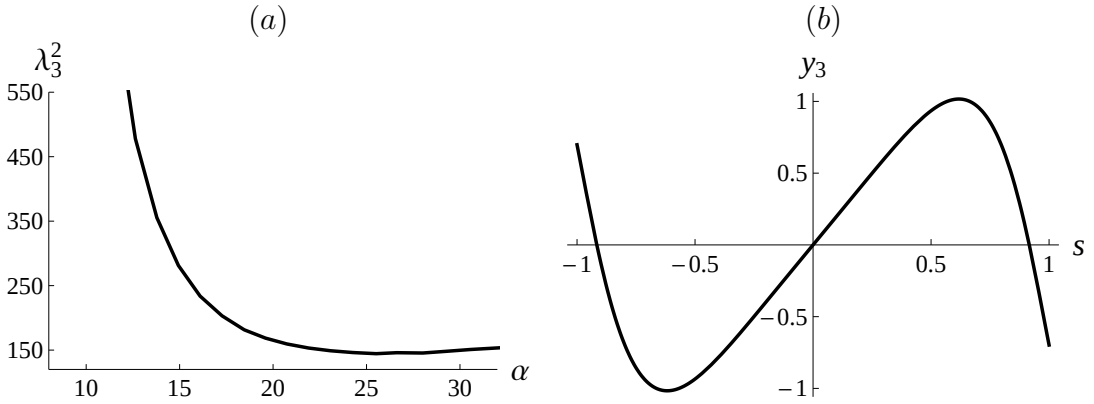

Figure 7.10: Oscillation mode ($n = 3$): (a) Frequency $\lambda_3^2 > 0$ vs. contact-angle α and (b) sample mode shape for $\alpha = 20°$.

the first mode shape, important in applications as it is the first to be excited, will exhibit oscillations with characteristic frequency for contact angles greater than the critical value.

The higher order mode shapes are readily computed and may be of interest. Here, oscillatory motion $\lambda^2 > 0$ persists for mode numbers $j \geq 2$. These results are summarized in figures 7.9 & 7.10, which plot frequency as a function of contact-angle, as well as typical $j = 2$ and $j = 3$ mode shapes, respectively.

7.4 Static stability of the axisymmetric liquid bridge

In view of the satisfactory results of the bounding technique, as it applies to the catenoid, one could ask if such a stability criteria could be formed for any liquid bridge or surface-of-revolution. To begin, a parametric description of an axisymmetric surface-of-revolution is given by

$$x(s,\varphi) = \varrho(s)\cos\varphi, \quad y(s,\varphi) = \varrho(s)\sin\varphi, \quad z(s,\theta) = \psi(s), \tag{7.65}$$

using arc-length $s \in [-\mathcal{S}, \mathcal{S}]$ and azimuthal angle $\varphi \in [0, 2\pi]$ as surface coordinates. The surface metric associated with this surface of revolution is expressed as

$$g_{\alpha\beta} = \left[g^{\alpha\beta}\right]^{-1} \equiv \boldsymbol{x}_\alpha \cdot \boldsymbol{x}_\beta = \begin{pmatrix} \varrho'^2 + \psi'^2 & 0 \\ 0 & \varrho^2 \end{pmatrix}; \quad g = \varrho^2\left(\varrho'^2 + \psi'^2\right), \tag{7.66}$$

and can be used in conjunction with the definition of the Laplace-Beltrami operator (7.4) to generate the second variation

$$\int_{-\mathcal{S}}^{\mathcal{S}} \left(-y''y - \frac{\left(\sqrt{g_{\theta\theta}/g_{ss}}\right)'}{\left(\sqrt{g_{\theta\theta}/g_{ss}}\right)} y'y - g_{ss}\left(\kappa_1^2 + \kappa_2^2\right) y^2 \right) \mathrm{d}s = \lambda \int_{-\mathcal{S}}^{\mathcal{S}} g_{ss}\, y^2 \,\mathrm{d}s, \tag{7.67}$$

associated with this solution of the Euler-Lagrange equations. Here, the following definitions have been used

$$g_{ss} = \varrho'^2 + \psi'^2, \quad g_{\theta\theta} = \varrho^2. \tag{7.68}$$

If one assumes that the surface has pinned contact lines,

$$y(-\mathcal{S}) = y(\mathcal{S}) = 0, \tag{7.69}$$

the second variation (7.67) can be recast as

$$I = \lambda \int_{-\mathcal{S}}^{\mathcal{S}} g_{ss}\, y^2 \,\mathrm{d}s, \tag{7.70}$$

where I is a quadratic form given by

$$I \equiv \int_{-\mathcal{S}}^{\mathcal{S}} \left[(y')^2 - \left[g_{ss} \left(\kappa_1^2 + \kappa_2^2 \right) - \frac{1}{2} \left(\left(\sqrt{g_{\theta\theta}/g_{ss}} \right)' / \left(\sqrt{g_{\theta\theta}/g_{ss}} \right) \right)' \right] y^2 \right] \mathrm{d}s. \tag{7.71}$$

As done previously, this functional can be bounded

$$I \geq I_{min} \equiv \int_{-\mathcal{S}}^{\mathcal{S}} \left[(y')^2 - K y^2 \right] \mathrm{d}s \tag{7.72}$$

using the extreme value theorem, where the constant K,

$$K \equiv \max \left[g_{ss} \left(\kappa_1^2 + \kappa_2^2 \right) + \frac{1}{2} \kappa_1 \kappa_2 + \frac{1}{2} \left(\frac{\varrho'}{\varrho} \right)^2 \right], \tag{7.73}$$

is simply the maximum value of the functional on the domain $s \in [-\mathcal{S}, \mathcal{S}]$. As before, one may use a result from the calculus of variations (7.13) to recast (7.72) as

$$I_{min} = \left(\xi^2 - K \right) \int_{-\mathcal{S}}^{\mathcal{S}} y^2 \mathrm{d}s. \tag{7.74}$$

The stability criteria can now be stated for the constant pressure,

$$K < \left(\frac{\pi}{2S} \right)^2, \tag{7.75}$$

and constant volume disturbance

$$K < \left(\frac{\pi}{S} \right)^2, \tag{7.76}$$

respectively.

7.4.1 Plateau-Rayleigh instability

To illustrate the effectiveness of the bounding technique, consider the classic Plateau-Rayleigh instability of a cylindrical liquid bridge. The cylindrical interface has principal curvatures $\kappa_1 = 1, \kappa_2 = 0$ and the following parametric representation

$$\varrho = 1, \quad \psi = s, \quad g_{ss} = 1. \tag{7.77}$$

Here, lengths have been scaled by the radius of the cylinder and the family of cylinders is uniquely described by its axial length $L = 2\mathcal{S}$. The functional (7.73) has constant value $K = 1$ for the cylindrical interface and is required to compute the stability limit. According to the stability criteria (7.75) and (7.76), the cylinder is stable to constant pressure disturbances if

$$1 < \left(\frac{\pi}{L}\right)^2, \tag{7.78}$$

and constant volume disturbances provided

$$1 < \left(\frac{2\pi}{L}\right)^2, \tag{7.79}$$

or for lengths smaller than the base-state circumference. Hence, the stability window from the bounding technique and the classic Plateau limit are coincident, further validating this approach.

7.4.2 Remarks

In general, stability calculations involve solving a boundary value problem associated with the second variation or computing conjugate points, which prove to be cumbersome in all but the simplest geometries. This difficulty, as it pertains to the boundary value problem, is circumvented by utilizing the bounding method proposed here. Specifically, the stability criteria, (7.75) and (7.76), are uniquely determined by the geometric properties of the equilibrium shape through the constant K (7.73) and total arc-length $2\mathcal{S}$.

7.5 Concluding remarks

The linear stability of the catenoidal interface has been analyzed using both a static and dynamic approach. Static stability is determined by the sign of the second variation of surface energy, while dynamic stability can be inferred from the computed growth rates, or solutions of the governing hydrodynamic equations. Recall, the static limit can be recovered from the dynamics by setting the growth rate to zero. In both approaches, 'allowable' solutions are sought in one of two disturbance classes, distinguished by their respective boundary conditions on the three-phase contact-line. The first is termed 'natural' and preserves the static contact-angle, in accordance with the Young-Dupré equation, while the second has a fixed/immobile contact-line and is referred to as 'pinned'. The disturbance class is enlarged further in the static approach to include both constant-pressure and constant-volume disturbances. As could be expected, stability can be greatly influenced by the disturbance class considered.

Using the static approach, a sufficient condition for stability of the catenoid is derived by a bounding method. This method exploits the structure of the second variation, which can be manipulated into a quadratic form and bounded using the extreme value theorem. The lower bound of the quadratic form is a critical functional from which stability may be deduced. Finally, by exploiting elementary results from the calculus of variations, a criteria for static stability is stated for the natural and pinned disturbances. The static stability limit for the catenoid with pinned contact lines is a well-known result and can be used to validate the bounding method, which is in excellent agreement with previous literature (Erle *et al.*, 1970). Using the same approach, it has been shown that natural disturbances are destabilizing when compared to the pinned contact-line disturbance class. Specif-

ically, a catenoid subject to a natural disturbance is shown to be unstable for all contact angles when pressure is held constant. Alternatively, one may stabilize the catenoid to this disturbance class by fixing the volume. Here the family of catenoids with contact-angle $\alpha > 21.6^\circ$ are stabilized. Lastly, one may infer that the instability of the catenoid is a local instability, because the bounding method relies on the inherently local extreme value theorem.

It has been shown, by application of the bounding method, that one need not construct a general solution to the boundary value problem associated with the second variation to generate a sufficient condition for stability. To reconcile the stability limit obtained by the bounding method, the hydrodynamic equations are derived and linear growth rates are computed. The dynamic approach gives rise to an integro-differential equation, governing the interface deflection, which is shown to be structurally equivalent to the second variation of the static approach. Growth rates are then computed by formulating the governing boundary value problem as a functional eigenvalue equation on linear operators. Computations show the static and dynamic stability limits are coincident, further validating the bounding method. That is, a catenoid subject to a natural disturbance exhibits oscillatory motion provided $\alpha > 21.6^\circ$. Unlike the static approach, the dynamic approach gives rise to instability growth rates and oscillation frequencies that may be interpreted physically.

Finally, to illustrate the utility of the bounding method, a sufficient condition for static stability of the axisymmetric liquid bridge with pinned contact lines is derived. As with the catenoid, one only needs information regarding the geometric properties of the equilibrium surface to generate the relevant stability criteria. A limiting case of the liquid bridge is the cylindrical interface, whose stability is ex-

pressed by the well-known Plateau limit and recovered using the bounding method. Although the bounding method is clearly an approximation, it has produced quite satisfactory results and requires very little analysis or computation, as is the case for most stability calculations.

CHAPTER 8

FUTURE WORK

To conclude this thesis, a number of final remarks will be given with regards to open questions that stem from this work.

8.1 'Walking' instability

One of the more interesting and perhaps unexpected results presented here is the 'walking' instability of the $[1,1]$ mode shape, which has been related to the drop's horizontal center-of-mass motion. There remains a number of questions to be answered regarding this instability, most of which are related to the small amplitude assumption, linearization of the governing equations and more specifically the constitutive law that relates the contact-angle to contact-line speed $\alpha = f(u_{CL})$ there. As shown in figure 5.24, the super-hemispherical base-state is unstable for a range of values of the spreading parameter Λ–the spreading parameter is an artifact from the linearization of the constitutive law. Interpretation of the analysis presented here depends upon how appropriate a model for experiment that constitutive law is. In addition, how relevant is its linearization, shown in figure 5.5, to the dynamics at the contact-line of any particular experimental system? As stated earlier, contact-angle hysteresis is observed in experiment but not allowed in the analysis presented here, because of the small-amplitude assumption. One extension of this analysis would be to include moderate-amplitude disturbances, which would allow one to study the effect of the weakly-nonlinear terms and also contact-angle hysteresis on the walking instability.

Another related issue is the possible coupling of oscillatory modes to the walking

instability. For example, Noblin *et al.* (2009) report ratchet-like motion of vibrated drops, whereby the translational motion or the walking instability is enhanced by a 'pumping' motion, which appears to be related to the drop's vertical center-of-mass motion. An obvious question is why does this motion enhance the $[1, 1]$ instability, if indeed, it does so? Finally, can any mode shape be coupled with the $[1, 1]$ mode to enhance droplet motion and which one generates the greatest enhancement?

8.2 Forced oscillations

One would like to compare the theoretical predictions given in this thesis against experimental results. To compare, one must answer the following question: to what extent can the assumptions made in this analysis be realized experimentally? In general, drop motion is induced by some type of external forcing, which may or may not have a large influence on the dynamics. For example, consider the two following experimental set-ups used to generate drop motion. How might they relate to the harmonic oscillator structure of the governing equations derived here? The first uses acoustic excitation to induce drop motion. The harmonic oscillator analogue to this experimental set-up is pure mechanical forcing, whereby the drop response is most pronounced at the natural frequencies. Alternatively, one might excite the drop by a mechanically-vibrated plate, which generates pressure gradients on the drop surface and is more characteristic of parametric excitation, as occurs in Faraday waves (Faraday, 1831). Although this experimental set-up differs greatly from the theoretical analysis, one might use some of the characteristic features of the parametrically-excited oscillator to relate the theory to experiment. More specifically, the defining feature of parametric resonance is the period-doubling phenomenon, whereby droplet motion is induced when the forcing frequency is

equal to twice the natural frequency. As before, the natural frequency data is available from the current analysis and may serve as a guide in determining if parametric resonance occurs. Finally, it is possible to simultaneously excite two distinct modes if the natural frequencies for the two mode shapes satisfy $\omega_A/2 = \omega_B = \omega_F$. Here a forcing frequency ω_F can generate a state of parametric resonance in mode A and pure resonance in mode B.

It has been suggested that results from this thesis may be used to interpret one of the instabilities seen in the experiments by Vukasinovic *et al.* (2007), where a de-pinning event at the contact-line triggers an azimuthal instability there. As shown in figure 5.28, a modal crossing occurs at some finite value of the spreading parameter Λ, which is implicitly related to the forcing amplitude via the contact-angle variation. In their experiments, Vukasinovic *et al.* (2007) show that this transition always takes an axisymmetric into a non-axisymmetric shape. However, it seems plausible that such a modal crossing may occur between two distinct non-axisymmetric shapes.

8.3 Contact-line speed condition

Computations show that implementation of the contact-line speed condition (5.30) generates effective dissipation controlled by the spreading parameter Λ (c.f. figures 5.20-5.23). The effective dissipation results from the particular form of the contact-line constitutive law and scales differently than bulk viscous effects. It would be interesting to conduct experiments to verify this scaling. If successful, the experiments would characterize the spreading parameter and also validate the assumption of this particular contact-line constitutive law.

APPENDIX A

LINEARIZATION OF YOUNG-DUPRÉ EQUATION

The Young-Dupré equation represents the balance of forces at the three-phase contact-line of a fluid interface and relates the vectors normal to the free surface ($\boldsymbol{n}$) and surface-of-support ($\boldsymbol{n_1}$) to the contact-angle α. Similarly, the variation (linearization) of the Young-Dupré equation generates the relevant boundary condition on the three-phase contact-line that preserves the static contact-angle α. To derive this condition, consider the perturbed equilibrium surface shown in figure 1.2 and decompose the variation $\delta\boldsymbol{x}$ to the equilibrium surface into its perpendicular $\delta_\perp\boldsymbol{x}$ and parallel $\delta_\parallel\boldsymbol{x}$ components,

$$\delta\boldsymbol{x} = \delta_\perp\boldsymbol{x} + \delta_\parallel\boldsymbol{x} = y\,\boldsymbol{n} + \delta_\parallel\boldsymbol{x}. \tag{A.1}$$

Here the linear surface perturbation y has been defined as

$$\delta_\perp\boldsymbol{x} \equiv y\,\boldsymbol{n}, \tag{A.2}$$

or with respect to the variation of the equilibrium surface in the direction of the surface normal $\boldsymbol{n}$. The variation of the Young-Dupré equation gives

$$\delta\left(\boldsymbol{n}\cdot\boldsymbol{n_1}\right) = -\left(\sin\alpha\right)\hat{\alpha} \tag{A.3}$$

or a balance equation which relates the geometry of the disturbed interface to the deviation in static contact-angle $\hat{\alpha}$. One can use the decomposition (A.1) to write the geometric (kinematic) variation of (A.3) as

$$\delta\left(\boldsymbol{n}\cdot\boldsymbol{n_1}\right) = \left(\delta_\perp\boldsymbol{n} + \delta_\parallel\boldsymbol{n}\right)\cdot\boldsymbol{n_1} + \boldsymbol{n}\cdot\left(\delta_\perp\boldsymbol{n_1} + \delta_\parallel\boldsymbol{n_1}\right), \tag{A.4}$$

which can be further simplified with following identities;

$$\delta_{\perp}\boldsymbol{n} = -\frac{\partial y}{\partial s}\boldsymbol{e}, \tag{A.5a}$$

$$\delta_{\parallel}\boldsymbol{n} = \frac{\partial \boldsymbol{n}}{\partial s}\left(\boldsymbol{e}\cdot\delta\boldsymbol{x}\right), \tag{A.5b}$$

$$\delta_{\perp}\boldsymbol{n_1} = 0, \tag{A.5c}$$

$$\delta_{\parallel}\boldsymbol{n_1} = \frac{\partial \boldsymbol{n_1}}{\partial s_1}\left(\boldsymbol{e_1}\cdot\delta\boldsymbol{x}\right). \tag{A.5d}$$

Here (A.5a) follows directly from the definition of the surface perturbation (A.2), (A.5b) & (A.5d) are standard differentials and (A.5c) represents the variation normal to the support surface, which is trivial because the motion of fluid interface there is strictly in the direction $\boldsymbol{e_1}$ tangent to the support. In addition, s and s_1 are arc-length coordinates defined on the equilibrium surface and surface-of-support, respectively.

The Frenet-Serret equations in the plane,

$$\frac{\partial \boldsymbol{n}}{\partial s} = -k\boldsymbol{e}, \tag{A.6}$$

relates the directional change in the vector normal $\boldsymbol{n}$ with respect to its arc-length coordinate s to the normal curvature k of that curve in the tangential direction $\boldsymbol{e}$ (see Kreyszig, 1991). This equation applies to both the free surface $(s, \boldsymbol{n}, \boldsymbol{e})$ and surface-of-support $(s_1, \boldsymbol{n_1}, \boldsymbol{e_1})$ and allows one to reduce (A.5b) & (A.5d) to

$$\frac{\partial \boldsymbol{n}}{\partial s}\left(\boldsymbol{e}\cdot\delta\boldsymbol{x}\right)\cdot\boldsymbol{n_1} = -k\left(\boldsymbol{e}\cdot\boldsymbol{n_1}\right)\left(\boldsymbol{e}\cdot\delta\boldsymbol{x}\right), \tag{A.7a}$$

$$\frac{\partial \boldsymbol{n_1}}{\partial s_1}\left(\boldsymbol{e_1}\cdot\delta\boldsymbol{x}\right)\cdot\boldsymbol{n} = -\bar{k}\left(\boldsymbol{e_1}\cdot\boldsymbol{n}\right)\left(\boldsymbol{e_1}\cdot\delta\boldsymbol{x}\right), \tag{A.7b}$$

where the normal curvatures of the free and support surfaces have been defined as k and $\bar{k}$, respectively. The vectors $\boldsymbol{n}, \boldsymbol{n_1}, \boldsymbol{e}, \boldsymbol{e_1}$ are coplanar and are related by the

following vector identities;

$$\boldsymbol{e} \cdot \delta\boldsymbol{x} = (\boldsymbol{n} \cdot \boldsymbol{n_1})\, \boldsymbol{e_1} \cdot \delta\boldsymbol{x} = (\cos\alpha)\ \boldsymbol{e_1} \cdot \delta\boldsymbol{x}, \tag{A.8a}$$

$$\boldsymbol{n} \cdot \delta\boldsymbol{x} = (\boldsymbol{n} \cdot \boldsymbol{e_1})\, \boldsymbol{e_1} \cdot \delta\boldsymbol{x} + (\boldsymbol{n} \cdot \boldsymbol{n_1})\, \boldsymbol{n_1} \cdot \delta\boldsymbol{x}, \tag{A.8b}$$

$$\boldsymbol{e_1} \cdot \boldsymbol{n} = -\boldsymbol{e} \cdot \boldsymbol{n_1} = \sin\alpha. \tag{A.8c}$$

Finally, one uses (A.7) and the vector identities (A.8) on (A.4) to generate the linearized Young-Dupré equation

$$\frac{\partial y}{\partial s} + \left(k\cot\alpha - \frac{\bar{k}}{\sin\alpha} \right) y = -\hat{\alpha}. \tag{A.9}$$

If the variation in contact-angle $\hat{\alpha} = 0$, then (A.9) boundary condition on the three-phase contact-line that ensures the linear surface disturbance y preserves the static contact-angle.

APPENDIX B

MODIFIED BOUNDARY CONDITION CALCULATIONS FOR THE IMMISCIBLE VISCOUS DROP

B.1 Modified boundary conditions

Here the details required to determine T_n^i and T_n^e from the modified boundary conditions (3.66) are given. For efficiency in presentation, define

$$\widetilde{\mathcal{J}}_n \equiv \mathcal{J}_{n+3/2}\left[(\gamma^*/\epsilon_i)^{1/2}\right];\ \widetilde{\mathcal{H}}_n \equiv \mathcal{H}^{(1)}_{n-1/2}\left[(\mu\gamma^*/\epsilon_i)^{1/2}\right]. \tag{B.1}$$

To begin, use the definition of the velocity field (3.21) on (3.66a) to give

$$T_n^i\left[\frac{1}{\widetilde{\mathcal{J}}_n}\right] + T_n^e\left[\frac{1}{\widetilde{\mathcal{H}}_n}\right] = -\gamma d_n\left[\frac{2n+1}{n(n+1)}\right]. \tag{B.2}$$

Similarly, equations (3.17a),(3.21) & (3.57) used on (3.66b) give

$$\begin{aligned}\left[\mu_e\left\{T_n^e\left(1+\frac{2}{\widetilde{\mathcal{H}}_n}\right)+\gamma d_n\frac{2\,(n+2)}{n+1}\right\}-\mu_i\left\{T_n^i\left(1-\frac{2}{\widetilde{\mathcal{J}}_n}\right)+\gamma d_n\frac{2\,(n-1)}{n}\right\}\right]\\ \times\left[1-\Gamma(x)\right]P_n^{(1)}(x)=\mu_i\left[-T_n^i\frac{2}{\widetilde{\mathcal{J}}_n}-\gamma d_n\frac{1}{n}\right]\Gamma(x)P_n^{(1)}(x)\end{aligned} \tag{B.3}$$

To isolate T_n^i and T_n^e, recognize that the sum on n is implicit and both sides of (B.3) may be expanded as a series in $P_n^{(1)}(x)$ to give:

$$\begin{aligned}T_n^i\left[\mu_i\frac{L_n}{\widetilde{\mathcal{J}}_n}-\mu_i\left(1-\frac{2}{\widetilde{\mathcal{J}}_n}\right)(1-L_n)\right]+T_n^e\left[\mu_e\left(1+\frac{2}{\widetilde{\mathcal{H}}_n}\right)(1-L_n)\right]\\ =\gamma d_n\left[2\left(\mu_i\frac{n-1}{n}-\mu_e\frac{n+2}{n+1}\right)(1-L_n)-\mu_i\frac{L_n}{n}\right].\end{aligned} \tag{B.4}$$

Equations (B.2) and (B.4) are solved to give T_n^i and T_n^e as functions of d_n, or the interface perturbation y.

B.2 Immiscible drop operator equation

To derive the operator equation for an immiscible drop, begin by using the scalings (3.69) to recast (3.68) in the form

$$\sum_{n=1}\Bigg\{\left[\left(\rho\frac{1}{n+1}+\frac{1}{n}\right)\gamma^{*^2}+2\left(n-1\right)\left(n+2\right)\left(\mu-1\right)\gamma^{*}\epsilon_i\right]d_n+n\left(n+2\right)\mu\gamma^{*}\epsilon_i T_n^e \\ -\left(n-1\right)\left(n+1\right)\gamma^{*}\epsilon_i T_n^i\Bigg\}=-\left[\left(1-x^2\right)y_{xx}-2xy_x+2y\right], \tag{B.5}$$

where T_n^i and T_n^e are determined by solving equations (B.2,B.4) to give

$$T_n^i=\frac{\mu\left(1+\frac{2}{\widetilde{\mathcal{H}}_n}\right)\left(1-L_n\right)\frac{2n+1}{n(n+1)}+2\left[\left(1-L_n\right)\left(\frac{n-1}{n}-\mu\frac{n+2}{n+1}\right)-\epsilon_i\frac{L_n}{n}\right]\frac{1}{\widetilde{\mathcal{H}}_n}}{\frac{1}{\widetilde{\mathcal{H}}_n}\left[\epsilon_i\frac{L_n}{\widetilde{\mathcal{J}}_n}-\left(1-\frac{2}{\widetilde{\mathcal{J}}_n}\right)\left(1-L_n\right)\right]-\frac{1}{\widetilde{\mathcal{J}}_n}\left[\mu\left(1+\frac{2}{\widetilde{\mathcal{H}}_n}\right)\left(1-L_n\right)\right]}d_n \tag{B.6}$$

and

$$T_n^e=\frac{\left[\left(1-\frac{2}{\widetilde{\mathcal{J}}_n}\right)\left(1-L_n\right)-\epsilon_i\frac{L_n}{\widetilde{\mathcal{J}}_n}\right]\frac{2n+1}{n(n+1)}-\left[2\left(\frac{n-1}{n}-\mu\frac{n+2}{n+1}\right)\left(1-L_n\right)-\epsilon_i\frac{L_n}{n}\right]\frac{1}{\widetilde{\mathcal{J}}_n}}{\frac{1}{\widetilde{\mathcal{H}}_n}\left[\epsilon_i\frac{L_n}{\widetilde{\mathcal{J}}_n}-\left(1-\frac{2}{\widetilde{\mathcal{J}}_n}\right)\left(1-L_n\right)\right]-\frac{1}{\widetilde{\mathcal{J}}_n}\left[\mu\left(1+\frac{2}{\widetilde{\mathcal{H}}_n}\right)\left(1-L_n\right)\right]}d_n. \tag{B.7}$$

Equations (B.6) & (B.7) may be substituted into (B.5) to produce an integro-differential operator equation for an immiscible drop with material parameters ρ, μ and ϵ_i.

APPENDIX C

ROTATIONAL WAVE SOLUTION OF THE VISCOUS DROP UNDER SPHERICAL-BELT CONSTRAINT

Previously, the assumption was made that the vorticity could be written in the form (3.18) using a properly chosen vector potential $\boldsymbol{B}$. This assumption gave rise to solutions with non-trivial radial velocities at the interface or the shape oscillations. To derive the rotational wave solutions, one introduces a vector potential $\boldsymbol{A}$ that generates a radial component of vorticity,

$$\boldsymbol{\omega} = \boldsymbol{\nabla} \times \boldsymbol{\nabla} \times \boldsymbol{A}, \quad \boldsymbol{A} = A(r,\theta)\boldsymbol{e_r}. \tag{C.1}$$

This class of solution does not have a radial component to its velocity field, but rather tangential velocities. As with the other field quantities, $A(r,\theta)$ can be expanded as

$$A(r,\theta) = \sum_{n=1} S_n(r) P_n(\cos\theta). \tag{C.2}$$

Substitution of the vector potential (C.1) into the vorticity equation (3.11c) gives

$$\frac{\mu}{\rho}\frac{d^2 S_n}{dr^2} + \gamma S_n - \frac{\mu}{\rho}\frac{n\,(n+1)}{r^2} S_n = 0, \tag{C.3}$$

whose general solution is written as

$$S_n^i(r) = \left(\frac{r}{R}\right)^{1/2} S_n^i(R) \frac{J_{n+1/2}\,(z^i)}{J_{n+1/2}\,(Z^i)}, \quad S_n^e(r) = \left(\frac{r}{R}\right)^{1/2} S_n^e(R) \frac{H^{(1)}_{n+1/2}\,(z^e)}{H^{(1)}_{n+1/2}\,(Z^e)} \tag{C.4}$$

with

$$z^{i,e} \equiv r\left(\gamma\frac{\rho_{i,e}}{\mu_{i,e}}\right)^{1/2}, \; Z^{i,e} \equiv R\left(\gamma\frac{\rho_{i,e}}{\mu_{i,e}}\right)^{1/2}. \tag{C.5}$$

The remaining unknowns $S_n^i(R), S_n^e(R)$ are determined from the shear boundary conditions

$$v_\varphi^i = v_\varphi^e \quad \left[\partial D_1^f, \partial D_2^f\right], \tag{C.6a}$$

$$\tau_{r\varphi}^i = \tau_{r\varphi}^e \quad \left[\partial D_1^f, \partial D_2^f\right], \tag{C.6b}$$

$$v_\varphi^i = v_\varphi^e = 0 \quad \left[\partial D^s\right]. \tag{C.6c}$$

As before, using the indicator function these conditions may be transformed into a uniform set of boundary conditions,

$$v_{\varphi}^{i}|_{r=R} = v_{\varphi}^{e}|_{r=R}, \tag{C.7a}$$

$$\left(\tau_{r\varphi}^{i} - \tau_{r\varphi}^{e}\right)|_{r=R}\left[1 - \Gamma\left(x, \zeta_1, \zeta_2\right)\right] = C\Gamma\left(x, \zeta_1, \zeta_2\right) v_{\varphi}^{i}|_{r=R}, \tag{C.7b}$$

valid on the entire interface. The following relations,

$$v_{\varphi} = -\frac{1}{r}\frac{dP_n}{d\theta}S_n(r), \quad \tau_{r\varphi} = \mu\left[\frac{2}{r^2}S_n(r) - \frac{1}{r}\frac{dS_n}{dr}\right]\frac{dP_n}{d\theta}, \tag{C.8}$$

are applied to the modified boundary conditions (C.7) to generate the characteristic equation,

$$\mu\mathcal{H}_{n+1/2}\left(X^e\right) - \mathcal{J}_{n+1/2}\left(X^i\right) = (n+2)(\mu - 1) + (1-\mu)\frac{L_n}{1 - L_n}, \tag{C.9}$$

that determines the growth rate of the rotational waves. Here the following definitions have been used,

$$X^i \equiv \left(\gamma^*/\epsilon_i\right)^{1/2}, \tag{C.10a}$$

$$X^e \equiv \left(\mu\gamma^*/\epsilon_i\right)^{1/2}, \tag{C.10b}$$

$$L_n \equiv \left(\int_{-1}^{1}\left(P_n^{(1)}(x)\right)^2\Gamma(x, \zeta_1, \zeta_2)\,\mathrm{d}x\right)\left(\frac{2n+1}{2}\frac{(n-1)!}{(n+1)!}\right). \tag{C.10c}$$

APPENDIX D

CONSTRAINED VARIATIONAL PRINCIPLE

Consider the variational problem of minimizing a given functional $H(z)$, but subject to a finite number of subsidiary conditions

$$C_i(z) = k_i, \quad i = 1, \cdots, p. \tag{D.1}$$

Here z can be a vector in $\mathbb{R}^n$ or a function in a Hilbert space $\mathcal{H}$. In either representation, one generally introduces Lagrange multipliers μ_i and defines the augmented Lagrangian

$$F(z; \mu_i) = H(z) - \sum_{i=1}^{p} \mu_i C_i(z) \tag{D.2}$$

to enforce the auxiliary conditions (D.1). An equilibrium or critical point z^* of the Lagrangian F necessarily has a vanishing first variation,

$$\boldsymbol{\nabla} F(z^*; \mu_i) = \boldsymbol{\nabla} H(z^*) - \sum_{i=1}^{p} \mu_i \boldsymbol{\nabla} C_i(z^*) = 0. \tag{D.3}$$

Here $\boldsymbol{\nabla}$ denotes the appropriate derivative, gradient in $\mathbb{R}^n$ or the variational derivative in a function space. The structure of the constraints (D.1) reduces the first order conditions to

$$\boldsymbol{\nabla} F(z^*; \mu_i) = \boldsymbol{\nabla} H(z^*) = 0 \tag{D.4}$$

and one recognizes that the Euler-Lagrange equations for the functionals H, F are identical, but a 'constrained' extremal necessarily lies in the constraint manifold,

$$\mathcal{M} = \{z \mid C_i(z) = k_i, \;\; i = 1, \cdots, p\}. \tag{D.5}$$

With regards to stability, one can ask under what conditions is an extremal of H a constrained minimum (Maddocks, 1985) or can the functionals C_i and data k_i be chosen to make the extremal a constrained minima (Hestenes, 1951). When

referring to the stability of a constrained extremal, the weaker characterization is a conditional stability, which treats perturbations to the extremal that lie in the constraint manifold (D.5). A sharper definition of stability would involve perturbations to the data k_i, which define the constraint manifold itself. Both notions of stability involve analyzing the quadratic form of the second variation on a restricted sub-space or the constrained space.

The stronger definition of stability involves the augmented Lagrangian (D.2):

Lemma 1 *An extremal z^* of H is a constrained minimum if the following second order conditions are met,*

$$\big(h, \boldsymbol{\nabla}^2 F(z^*)h\big) > 0 \quad \{\forall\ h\ \neq 0 \quad s.t.\ \ \boldsymbol{\nabla} C_i(z^*) \cdot h = 0, \quad i = 1, \cdots, p\}. \tag{D.6}$$

As opposed to restricting to perturbations h that lie in the tangent space of the constraint manifold, an equivalent definition of stability involves the use of projection operators P,

$$\big(h, P^t \boldsymbol{\nabla}^2 F(z^*) P h\big) > 0, \ \ \forall\ h \neq 0. \tag{D.7}$$

Unlike the stability criteria (D.6) there is no restriction on the perturbations h to the extremal, but direct analysis of (D.7) or more specifically the construction of the projection operator P is difficult, except when the range of the tangent space $(\mathcal{R}\left(\boldsymbol{\nabla} C_i\right))$ is simply related to the eigenspaces of the second variation of F. If possible, one would like to avoid such computations. Here an index theory is used as an apparatus to derive a stability criteria that does precisely that. Before deriving the stability result, a few remarks regarding index theory are offered. An index theory is intimately related to catastrophe theory (Gilmore, 1981) and is generally used to define the local character of a non-degenerate extremal. For example, one can show that in $\mathbb{R}^2$ a local coordinate transformation always exists

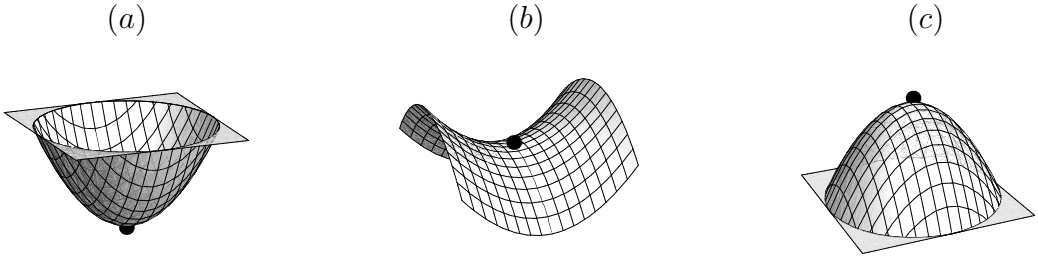

Figure D.1: Local energy landscape for (a) $E(0,2) = x_1^2 + x_2^2$ (Minimum), (b) $E(1,1) = x_1^2 - x_2^2$ (Saddle), and (c) $E(2,0) = -x_1^2 - x_2^2$ (Maximum)

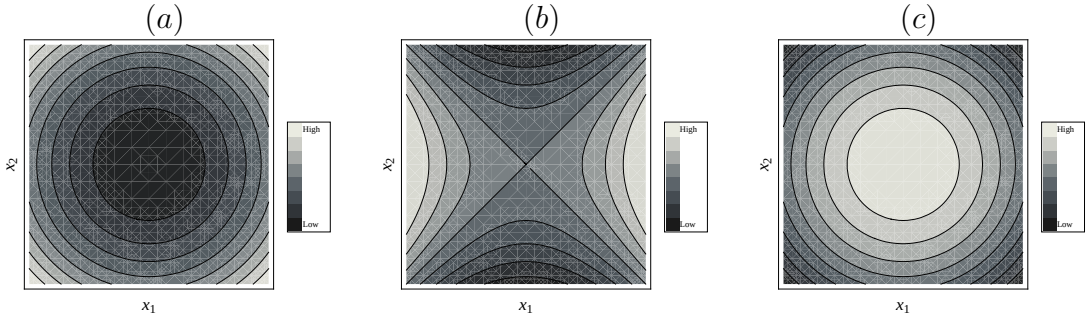

Figure D.2: Contour plot of the energy landscape for (a) $E(0,2) = x_1^2 + x_2^2$, (b) $E(1,1) = x_1^2 - x_2^2$, and (c) $E(2,0) = -x_1^2 - x_2^2$

which transforms the local 'energy' landscape of a non-degenerate extremal into one of three unique configurations(c.f. figure D.1),

$$E(0,2) = x_1^2 + x_2^2, \tag{D.8a}$$

$$E(1,1) = x_1^2 - x_2^2, \tag{D.8b}$$

$$E(2,0) = -x_1^2 - x_2^2. \tag{D.8c}$$

These landscapes are exhaustive for non-degenerate extremals and are distinguished by the number of negative eigenvalues of their respective second variation or their index. Geometrically, $E(0,2)$ has no negative eigenvalue, an index of zero and is a local minimum, $E(1,1)$ is saddle point with and index of one

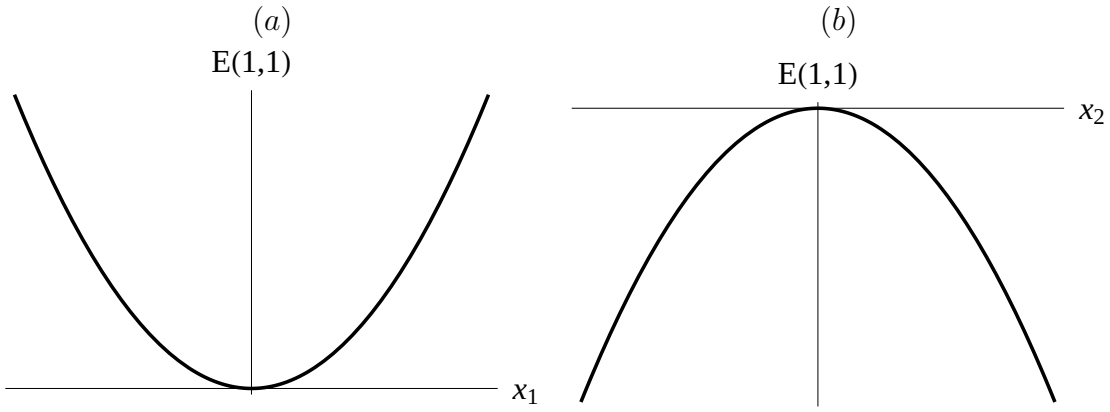

Figure D.3: Projection of the energy landscape for a saddle point showing slices of (a) constant x_2 (constrained minimum) and (b) constant x_1 (constrained maximum)

and $E(2,0)$ is a local maximum with an index of two(c.f. figures D.1,D.2). In either the constrained or unconstrained problem, $E(0,2)$ and $E(2,0)$ are always a local minimum and maximum, respectively (i.e. orientation does not change the local character). However, the saddle point $E(1,1)$ can be either a constrained minimum or maximum. For example, if one holds x_2 fixed the projected energy landscape is a local minimum(stable). Alternatively, holding x_1 fixed generates a constrained maximum(unstable). These projections are shown in figure D.3. In both such projections, one could have defined a 'constrained' index to describe the local character. Here the imposed constraint fixes the 'slice' of the energy landscape or the orientation from which an observer views the extremal. These particular projections are straight lines in the two-dimensional energy landscapes of figure D.2, but the idea of projections easily generalizes to non-linear constraints, which are simply curves in the energy space. The geometrical interpretation of a constrained index theory can be extended to the arbitrary Hilbert space, provided some assumptions are made about the functional in question.

With regards to the constrained variational problem considered here, the number of negative eigenvalues of $\boldsymbol{\nabla}^2 F(z^*)$ gives an 'unconstrained' index of the extremal of (D.2) when the null space of the second variation of F is trivial,

$$\mathcal{N}\left(\boldsymbol{\nabla}^2 F(z^*)\right) = \{0\}. \tag{D.9}$$

Similarly, if the null space of the projected second variation is orthogonal to the tangent space of the constraint manifold,

$$\mathcal{N}\left(P^t \boldsymbol{\nabla}^2 F(z^*) P\right) = \mathcal{N}\left(\boldsymbol{\nabla} C_i\right), \quad i = 1, \cdots, p, \tag{D.10}$$

the number of negative eigenvalues of $P^t \boldsymbol{\nabla}^2 F(z^*) P$ gives a 'constrained' index of H when restricted to the constraint manifold (D.5). Although a function space is infinite dimensional, the geometric interpretation of the constrained index from the last paragraph still holds true. One can use the definition of the constrained index and Lemma 1 to show that a constrained minimum necessarily has a constrained index of zero. As before, the constrained index is not trivial to compute and to simplify this computation, some select results from Maddocks (1985) on restricted quadratic forms will be given.

The quadratic form associated with the linear operator L is defined as

$$Q(u) = (u, Lu), \quad u \in \mathcal{S} \subset \mathcal{H}, \tag{D.11}$$

where $\mathcal{H}$ is a real Hilbert space endowed with the inner product $(\cdot, \cdot)$ and $\mathcal{S}$ is a dense sub-space of $\mathcal{H}$. Additionally, the operator L has the following properties: i) L is self-adjoint and Fredholm, ii) L has a finite number of negative eigenvalues σ^- with corresponding orthonormal eigenvectors ζ_i^-, and iii) L is positive on the orthogonal complement of $\text{span}\{\zeta_i^-\} \oplus \mathcal{N}(L)$. The orthogonal complement of the sub-space $\mathcal{S}$ is defined as

$$\mathcal{S}^\perp = \{\, u \in \mathcal{H} \mid (u, v) = 0 \ \ \forall\, v \in \mathcal{S}\}. \tag{D.12}$$

Finally, the following decomposition of the Hilbert space $\mathcal{H}$ and any sub-space thereof is needed.

Theorem 3 *Let $Q(u)$ be a quadratic form on a Hilbert space $\mathcal{H}$. Then there exists three subspaces $\mathcal{H}^-, \mathcal{H}^0, \mathcal{H}^+$ such that $\mathcal{H} = \mathcal{H}^- \oplus \mathcal{H}^0 \oplus \mathcal{H}^+$. The three sub-spaces are mutually orthogonal and orthogonal under the action of the operator L. Lastly, $Q(u)$ is negative on $\mathcal{H}^-$, zero on $\mathcal{H}^0$ and positive on $\mathcal{H}^+$.*

The stability criteria for the constrained variational problem in question is now derived. Consider the quadratic form induced by the second variation of the augmented Lagrangian $\left(h, \boldsymbol{\nabla}^2 F(z^*)h\right)$ and let the sub-space $\mathcal{S}$ be defined as

$$\mathcal{S} = \{\ \boldsymbol{\nabla} C_i(z^*)\ \ , i = 1, 2, \cdots, p\}, \tag{D.13}$$

or the tangent space to the constraint manifold. The second variation is Fredholm, therefore the orthogonal complement to $\mathcal{S}$ is uniquely determined by the span of the functions η_i defined by

$$\mathcal{S}^\perp = \{\ \eta_i,\ i = 1, 2, \cdots, p \mid \boldsymbol{\nabla}^2 F(z^*)\eta_i = \boldsymbol{\nabla} C_i(z^*)\}. \tag{D.14}$$

The Hilbert space is decomposed as follows

$$\mathcal{H} = \mathcal{S} \oplus \mathcal{S}^\perp, \tag{D.15}$$

with each sub-space decomposed as

$$\mathcal{S} = \mathcal{S}^- \oplus \mathcal{S}^0 \oplus \mathcal{S}^+, \tag{D.16a}$$

$$\mathcal{S}^\perp = \left(\mathcal{S}^\perp\right)^- \oplus \left(\mathcal{S}^\perp\right)^0 \oplus \left(\mathcal{S}^\perp\right)^+. \tag{D.16b}$$

Each subspace has its own index.

Lemma 2 *The following relationship exists between the Morse indices of the quadratic form* $\left(h, \boldsymbol{\nabla}^2 F(z^*)\, h\right)$ *on the two complementary sub-spaces,* $\mathcal{S}, \mathcal{S}^\perp$.

$$[\mathcal{H}] = [\mathcal{S}] + \left[\mathcal{S}^\perp\right] \tag{D.17}$$

That is, if the index on any two of the three spaces are known then the index on the remaining space is also known. By construction, $[\mathcal{H}]$ is the 'unconstrained' index and $[\mathcal{S}]$ is the 'constrained' index. As stated earlier, computation of the constrained index is difficult when compared to the computation of the unconstrained index. The goal will be to show that computing the unconstrained index and the index on the orthogonal complement is easier than directly computing the constrained index.

To begin, one would like to shown that the index on the orthogonal complement can be written as

$$\left(\eta_i, \boldsymbol{\nabla}^2 F(z^*)\eta_j\right) = \left(\eta_i, \boldsymbol{\nabla} C_j(z^*)\right) = \left(\boldsymbol{\nabla} C_i(z^*), \left(\boldsymbol{\nabla}^2 F(z^*)\right)^{-1} \boldsymbol{\nabla} C_j(z^*)\right). \tag{D.18}$$

This is proved by observing that any non-degenerate critical point can be embedded in the following way: $z^* = z^*(\mu)$, which can then be applied to the first order conditions

$$\boldsymbol{\nabla} H\left(z^*(\mu)\right) = \sum_{i=1}^{p} \mu_i \boldsymbol{\nabla} C_i\left(z^*(\mu)\right). \tag{D.19}$$

Next, differentiating (D.19) with respect to μ_j gives

$$\boldsymbol{\nabla}^2 H \frac{\partial z^*}{\partial \mu_j} = \sum_{i=1}^{p} \mu_i \boldsymbol{\nabla}^2 C_i \frac{\partial z^*}{\partial \mu_j} + \delta_{ij} \boldsymbol{\nabla} C_i \tag{D.20}$$

or re-arranging

$$\left(\boldsymbol{\nabla}^2 H - \sum_{i=1}^{p} \mu_i \boldsymbol{\nabla}^2 C_i\right) \frac{\partial z^*}{\partial \mu_j} = \sum_{i=1}^{p} \delta_{ij} \boldsymbol{\nabla} C_i. \tag{D.21}$$

Next, using the definition of the augmented Lagrangian gives

$$\boldsymbol{\nabla}^2 F\left(z^*(\mu)\right) \frac{\partial z^*}{\partial \mu_j} = \boldsymbol{\nabla} C_j\left(z^*(\mu)\right), \tag{D.22}$$

which allows one to explicitly construct the functions

$$\eta_j(\mu) = \frac{\partial z^*}{\partial \mu_j} = \left(\boldsymbol{\nabla}^2 F\left(z^*(\mu)\right)\right)^{-1} \boldsymbol{\nabla} C_j\left(z^*(\mu)\right) \tag{D.23}$$

that span the orthogonal complement, which are simply the derivatives of the equilibria with respect to the Lagrange multipliers μ_j.

Finally, the previous result can be used to relate the index on the orthogonal complement to the Hessian of the solution surface $F(z(\mu), \mu)$:

Lemma 3

$$\frac{\partial^2 F}{\partial \mu_i \partial \mu_j} = -\left(\eta_i, \boldsymbol{\nabla} C_j(z^*)\right) = \left(\boldsymbol{\nabla} C_i(z^*), \left(\boldsymbol{\nabla}^2 F(z^*)\right)^{-1} \boldsymbol{\nabla} C_j(z^*)\right). \tag{D.24}$$

To prove this result, differentiate the solution surface $F(z(\mu), \mu)$ with respect to μ_i

$$\frac{\partial F}{\partial \mu_i} = \boldsymbol{\nabla} H \frac{\partial z}{\partial \mu_i} - \sum_{k=1}^{p} \left(\delta_{ik} C_k + \mu_k \boldsymbol{\nabla} C_k \frac{\partial z}{\partial \mu_i}\right) \tag{D.25}$$

and then μ_j

$$\begin{aligned} \frac{\partial^2 F}{\partial \mu_i \partial \mu_j} = \boldsymbol{\nabla}^2 H \frac{\partial z}{\partial \mu_i}\frac{\partial z}{\partial \mu_j} + \left(\boldsymbol{\nabla} H - \sum_{k=1}^{p} \mu_k \boldsymbol{\nabla} C_k\right) \frac{\partial^2 z}{\partial \mu_i \partial \mu_j} \\ - \sum_{k=1}^{p} \left(\delta_{ik} \boldsymbol{\nabla} C_k \frac{\partial z}{\partial \mu_j} + \delta_{jk} \boldsymbol{\nabla} C_k \frac{\partial z}{\partial \mu_i} + \mu_k \boldsymbol{\nabla}^2 C_k \frac{\partial z}{\partial \mu_i}\frac{\partial z}{\partial \mu_j}\right). \end{aligned} \tag{D.26}$$

Applying the first order conditions and simplifying yields

$$\frac{\partial^2 F}{\partial \mu_i \partial \mu_j} = \boldsymbol{\nabla}^2 F \frac{\partial z}{\partial \mu_i}\frac{\partial z}{\partial \mu_j} - \sum_{k=1}^{p} \left(\delta_{ik} \boldsymbol{\nabla} C_k \frac{\partial z}{\partial \mu_j} + \delta_{jk} \boldsymbol{\nabla} C_k \frac{\partial z}{\partial \mu_i}\right) \tag{D.27}$$

and finally

$$\frac{\partial^2 F}{\partial \mu_i \partial \mu_j} = -\left(\boldsymbol{\nabla} C_i, \left(\boldsymbol{\nabla}^2 F\right)^{-1} \boldsymbol{\nabla} C_j\right). \tag{D.28}$$

That is, the index of the orthogonal complement is simply the number of positive eigenvalues of the Hessian of the solution surface. One can now state the stability result:

Theorem 4 *Given a non-degenerate extremal of F, the constrained index is the unconstrained index minus the number of positive eigenvalues of the Hessian matrix $\partial^2 F/\partial\mu_i\partial\mu_j$.*

A number of immediate results are available from Theorem 2.

Lemma 4 *Suppose a non-degenerate extremal $(z^*(\hat{\mu}), \hat{\mu})$ is smoothly embedded in a family of extremals $z^*(\mu)$. Then, $z^*(\hat{\mu})$ is a constrained local minimum if and only if the number of positive principal curvatures of $F(\mu)$ equals the number of negative eigenvalues of $\boldsymbol{\nabla}^2 F(z^*(\hat{\mu}))$.*

Lemma 5 *Given p constraints and an extremal with unconstrained index l, the extremal z^* is never a constrained minimum when $l > p$.*

Finally, the class of constrained variational problem considered here is particularly suited to branch continuation. As stated earlier, computations regarding the second variation cannot be eliminated but may be simplified. The second variation enters Theorem 2 only through the unconstrained index, which is a much simpler computation that the constrained index. The second requirement of Theorem 2 is the number of positive principal curvatures of the equilibrium solution, which may be computed solely from the first order conditions using finite differences.

D.1 Coupled non-linear springs

An example problem is used as an apparatus to illustrate the results of this subsection. Consider the static stability of the coupled non-linear spring system shown

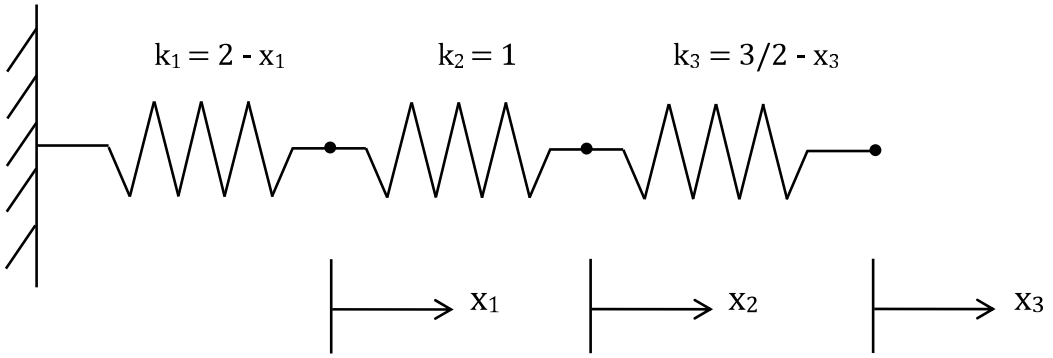

Figure D.4: Schematic of the system of coupled non-linear springs

in figure D.4. The system has a configurational energy given by

$$U(\boldsymbol{x}) = x_1^2 - \frac{x_1^3}{3} + \frac{x_2^2}{2} + 3\frac{x_3^2}{4} - \frac{x_3^3}{3}, \tag{D.29}$$

and is subject to the following set of constraints

$$x_1 + x_2 + x_3 = l_1, \tag{D.30a}$$

$$x_3 - x_1 = l_2, \tag{D.30b}$$

which fixes the total length l_1 and the relative difference l_2 between the first and last springs. To compute the equilibria and their stability one introduces the Lagrange multipliers μ_1, μ_2 and defines the augmented Lagrangian

$$F(\boldsymbol{x}, \mu_1, \mu_2) = x_1^2 - \frac{x_1^3}{3} + \frac{x_2^2}{2} + 3\frac{x_3^2}{4} - \frac{x_3^3}{3} - \mu_1(x_1 + x_2 + x_3) - \mu_2(x_3 - x_1). \tag{D.31}$$

As before, the first variation

$$\boldsymbol{\nabla} F = \left(2x_1 - x_1^2 - \mu_1 + \mu_2, x_2 - \mu_1, 3x_3/2 - x_3^2 - \mu_1 - \mu_2\right) \tag{D.32}$$

generates the necessary conditions for equilibrium,

$$x_1^* = 1 \pm \sqrt{1 + (\mu_2 - \mu_1)} \tag{D.33a}$$

$$x_2^* = \mu_1 \tag{D.33b}$$

$$x_3^* = 3/4 \pm \sqrt{(3/4)^2 - (\mu_1 + \mu_2)}. \tag{D.33c}$$

The four equilibria are parameterized by μ_1, μ_2;

$$\boldsymbol{x_1^*} = \left(1 + \sqrt{1 + \mu_2 - \mu_1},\ \mu_1\ ,\ 3/4 - \sqrt{(3/4)^2 - (\mu_1 + \mu_2)}\right), \tag{D.34a}$$

$$\boldsymbol{x_2^*} = \left(1 - \sqrt{1 + \mu_2 - \mu_1},\ \mu_1\ ,\ 3/4 - \sqrt{(3/4)^2 - (\mu_1 + \mu_2)}\right), \tag{D.34b}$$

$$\boldsymbol{x_3^*} = \left(1 + \sqrt{1 + \mu_2 - \mu_1},\ \mu_1\ ,\ 3/4 + \sqrt{(3/4)^2 - (\mu_1 + \mu_2)}\right), \tag{D.34c}$$

$$\boldsymbol{x_4^*} = \left(1 - \sqrt{1 + \mu_2 - \mu_1},\ \mu_1\ ,\ 3/4 + \sqrt{(3/4)^2 - (\mu_1 + \mu_2)}\right). \tag{D.34d}$$

To use Theorem 2, one needs to compute the unconstrained index for the respective equilibria, which one can compute from the second variation

$$\boldsymbol{\nabla}^2 F = \begin{pmatrix} 2\,(x_1 - 1) & 0 & 0 \\ 0 & 1 & 0 \\ 0 & 0 & 2x_3 - (3/2) \end{pmatrix}, \tag{D.35}$$

to show that the unconstrained index of the respective equilibria are

$$\left[\boldsymbol{x_1^*}\right] = 1, \tag{D.36a}$$

$$\left[\boldsymbol{x_2^*}\right] = 0, \tag{D.36b}$$

$$\left[\boldsymbol{x_3^*}\right] = 2, \tag{D.36c}$$

$$\left[\boldsymbol{x_4^*}\right] = 1. \tag{D.36d}$$

Here $\boldsymbol{x_2^*}$ is an unconstrained minimum and therefore necessarily a constrained minimum. According to Lemma 5, the remaining equilibria have an unconstrained

index of $l = 1, 2$, and are candidates to be a constrained minima because there are $p = 2$ constraints. Lastly, one computes the number of positive eigenvalues of the Hessian matrix $\partial^2 F/\partial\mu_i\partial\mu_j$ and then applies Theorem 2 to determine the constrained index. Figure D.5 plots the solution surface for each equilibria against the Lagrange multipliers with gray shading indicating the extremal is a constrained minima. Projecting the solution surface onto the parameter space $\mu_1 - \mu_2$ generates the stability diagram shown in figure D.6. In the stability diagram, all equilibria with a non-trivial unconstrained index are a constrained minima in certain regions of parameter space. Somewhat surprisingly, the equilibria with unconstrained index of two can be a constrained minima.

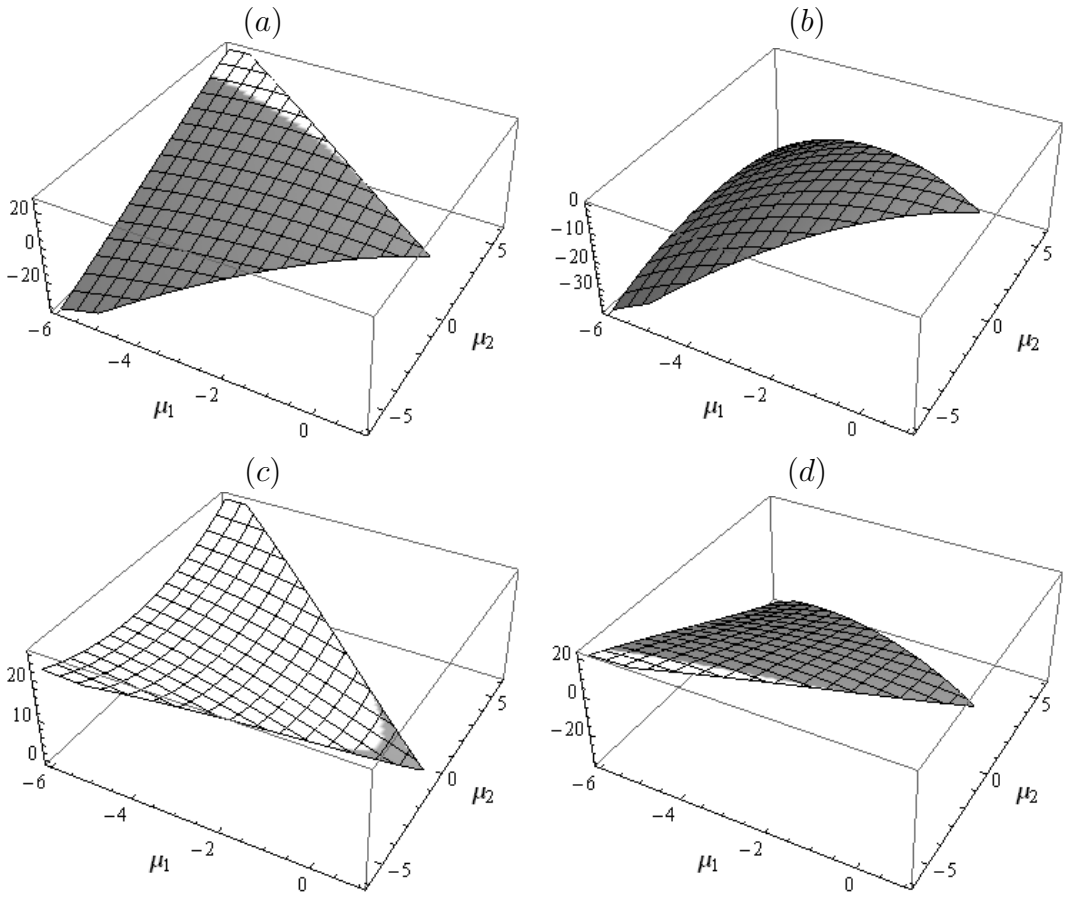

Figure D.5: Solution surface (a) $F(\boldsymbol{x}_1^*)$, (b) $F(\boldsymbol{x}_2^*)$, (c) $F(\boldsymbol{x}_3^*)$ and (d) $F(\boldsymbol{x}_4^*)$ against Lagrange multipliers μ_1, μ_2, where gray shading indicates a constrained minimum.

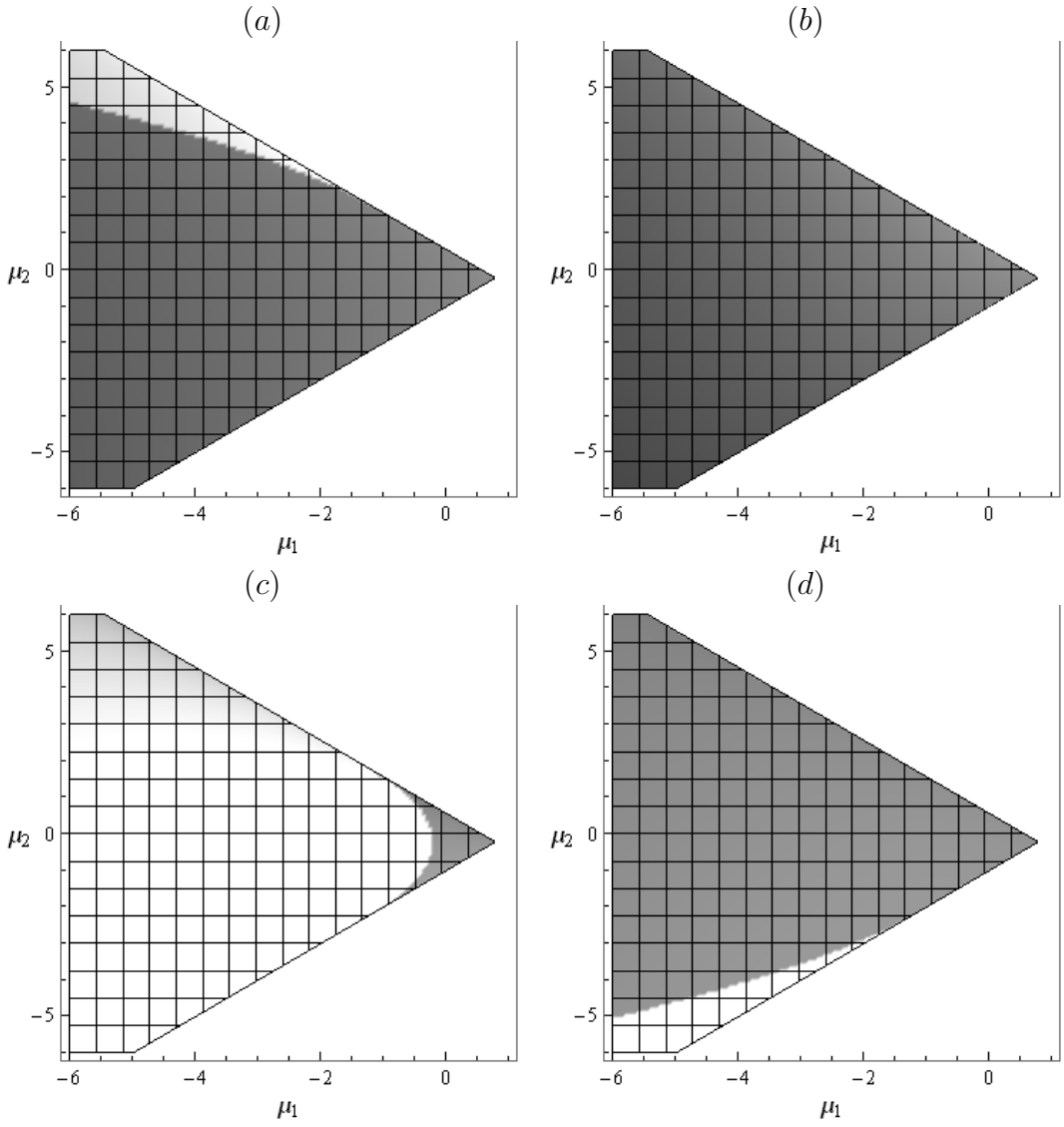

Figure D.6: Stability diagram for extremal (*a*) $\boldsymbol{x}_1^*$, (*b*) $\boldsymbol{x}_2^*$, (*c*) $\boldsymbol{x}_3^*$ and (*d*) $\boldsymbol{x}_4^*$ against Lagrange multipliers μ_1, μ_2. Gray shading indicates the extremal is a constrained local minimum.

BIBLIOGRAPHY

Arfken, G.B. & Weber, H.J. 2001 *Mathematical Methods for Physicists*. San Diego, CA: Harcourt Academic Press.

Basaran, O. 1992 Nonlinear oscillations of viscous liquid drops. *J. Fluid Mech.* **241**, 169–198.

Basaran, O. & DePaoli, D. 1994 Nonlinear oscillations of pendant drops. *Phys. Fluids* **6**, 2923–2943.

Bauer, H.F. & Chiba, M. 2004 Oscillations of captured spherical drop of frictionless liquid. *Journal of Sound and Vibration* **274**, 725–746.

Bauer, H.F. & Chiba, M. 2005 Oscillations of captured spherical drop of viscous liquid. *Journal of Sound and Vibration* **285**, 51–71.

Benilov, E.S. 2009 On the stability of shallow rivulets. *J. Fluid Mech.* **636**, 455474.

Bian, X., Perlin, M., Schultz, W. & Agarwal, M. 2003 Axisymmetric slosh frequencies of a liquid mass in a circular cylinder. *Phys. Fluid* **15**, 3659–3664.

Bolza, O. 1904 *Lectures on the calculus of variations*. Chicago: University of Chicago Press.

Bostwick, J.B. & Steen, P.H. 2009 Capillary oscillations of a constrained liquid drop. *Phys. Fluids* **21**, 032108.

Bostwick, J.B. & Steen, P.H. 2010 Stability of constrained cylindrical interfaces and the torus lift of plateau-rayleigh. *J. Fluid Mech.* **647**, 201–219.

Brown, R.A. & Scriven, L.E. 1980 On the multiple equilibrium shapes and stability of an interface pinned on a slot. *J. Colloid and Interface Science* **78**, 528–542.

Brunet, P., Eggers, J. & Deegan, R.D. 2009 Motion of a drop driven by substrate vibrations. *Eur. Phys. J. Special Topics* **166**, 11–14.

Byrne, C.J., Theisen, E.A., Reed, B.L. & Steen, P.H. 2006 Capillary puddle vibrations linked to casting-defect formation in planar-flow melt spinning. *Metallurgical and Materials Transactions B* **37B**, 445–456.

Chandrasekhar, S. 1961 *Hydrodynamic and Hydromagnetic Stability*. Oxford: Oxford University Press.

Courant, R. & Hilbert, D. 1953 *Methods of Mathematical Physics, Vol. II*. New York, NY: Wiley-Interscience Publications.

Courty, S., Lagubeau, G. & Tixier, T. 2006 Oscillating droplets by decomposition on the spherical harmonic basis. *Physical Review E* **73**, 045301.

Culkin, J.B. & Davis, S.H. 1983 Meandering of water rivulets. *AIChE Journal* **30**, 263–267.

Daniel, S., Sircar, S., Gliem, J. & Chaudhury, M.K. 2004 Racheting motion of liquid drops on gradient surfaces. *Langmuir* **20**, 4085–4092.

Davis, S.H. 1980 Moving contact lines and rivulet instabilities. part 1. the static rivulet. *J. Fluid Mechanics* **98**, 225–242.

Deegan, R.D., Brunet, P. & Eggers, J. 2008 Complexities of splashing. *Nonlinearity* **21**, C1–C11.

DePaoli, W.D., Feng, J.Q., Basaran, O.A. & Scott, T.C. 1995 Hysteresis in forced oscillations of pendant drops. *Phys. Fluids* **7**, 1181–1183.

Drazin, P.G. 1981 *Introduction to Hydrodynamic Stability*. Cambridge, UK: Cambridge University Press.

Dussan, E.B. V. 1979 On the spreading of liquid on solid surfaces: static and dynamic contact lines. *Ann. Rev. Fluid Mech.* **11**, 371–400.

Erle, M.A., Gillette, R.D. & Dyson, D.C. 1970 Stability of interfaces of revolution with constant surface tension-the case of the catenoid. *Chemical Engineering Journal* **1**, 97–109.

Faraday, M. 1831 On a peculiar class of acoustical figures, and on certain forms assumed by groups of particles upon vibrating elastic surfaces. *Phil. Trans. R. Soc. Lond.* **121**, 299340.

Fayzrakhmanova, I.S. & Straube, A.V. 2009 Stick-slip dynamics of an oscillated sessile drop. *Phys. Fluids* **21**, 072104.

Field, M., Golubitsky, M. & Stewart, I. 1991 Bifurcations on hemispheres. *Journal of Nonlinear Science* **1**, 201–223.

Ganan, A. & Barerro, A. 1990 Free oscillations of liquid captive drops. *Microgravity Science and Technology* **3**, 70–86.

Gillette, R.D. & Dyson, D.C. 1971 Stability of fluid interfaces of revolution between equal solid circular plates. *Chemical Engineering Journal* **2**, 44–54.

Gillette, R.D. & Dyson, D.C. 1972 Stability of axisymmetric liquid-fluid interfaces towards general disturbances. *Chemical Engineering Journal* **3**, 196–199.

Gilmore, R. 1981 *Catastrophe theory for scientists and engineers*. New York, NY: Dover.

Grand-Piteira, N. Le, Daerr, A. & Limat, L. 2006 Meandering rivulets on a plane : a simple balance between inertia and capillarity. *Phys. Rev. Letters* **96**, 254503.

Griffel, D.H. 1985 *Applied Functional Analysis*. Mineola, NY: Dover Publications.

Hestenes, M.R. 1951 Applications of the theory of quadratic forms in hilbert space to the calculus of variations. *Pac. J. Math.* **41**, 525–581.

Hocking, L.M. 1987*a* The damping of capillary-gravity waves at a rigid boundary. *J. Fluid Mech.* **179**, 253–266.

Hocking, L.M. 1987*b* Waves produced by a vertically oscillating plate. *J. Fluid Mech.* **179**, 267–281.

Howe, W. 1887 PhD thesis, Friedrich-Wilhelms Universität zu Berlin, Berlin.

James, A., Smith, M.K. & Glezer, A. 2003*a* Vibration-induced drop atomization and the numerical simulation of low-frequency single-droplet ejection. *J. Fluid Mech.* **476**, 29–62.

James, A., Vukasinovic, B., Smith, M.K. & Glezer, A. 2003*b* Vibration-induced drop atomization and bursting. *J. Fluid Mech.* **476**, 1–28.

Joseph, D.D. 2006 Helmholtz decomposition coupling rotational to irrotational flow of a viscous fluid. *PNAS* **103**, 1427214277.

Kim, H.Y., Kim, J.H. & Kang, B.H. 2004 Meandering instability of a rivulet. *J. Fluid Mech.* **498**, 245256.

Kreyszig, E. 1991 *Differential Geometry*. New York, NY: Dover Publications.

Kuiper, S. & Hendriks, B 2004 Variable-focus liquid lens for miniature cameras. *Appl. Phys. Lett.* **85**, 1128.

Lamb, H. 1932 *Hydrodynamics*. Cambridge, UK: Cambridge University Press.

Lanczos, C. 1986 *The Variational Principles of Mechanics*. New York, NY: Dover Publications.

Langbein, D. 1990 The shape and stability of liquid menisci at solid edges. *J. Fluid Mechanics* **213**, 251–265.

Laplace, R.S. 1806 *An essay on the cohesion of fluids*. Paris: Coureier.

Lopez, C.A. & Hirsa, A.H. 2008 Fast focusing using a pinned-contact liquid lens. *Nature Photonics 2* **9**, 610–613.

Lopez, C.A., Lee, C.C. & Hirsa, A.H. 2005 Electrochemically activated adaptive liquid lens. *Appl. Phys. Lett.* **87**, 134102.

Lowry, B.J. & Steen, P.H. 1995 Capillary surfaces: Stability from families of equilibria with application to the liquid bridge. *Proc. R. Soc. London* **449**, 411–439.

Lundgren, T.S. & Mansour, N.N. 1988 Oscillations of drops in zero gravity with weak viscous effects. *J. Fluid Mech.* **194**, 479–510.

Lyubimov, D.V., Lyubimova, T.P. & Shklyaev, S.V. 2004 Non-axisymmetric oscillations of a hemispheric drop. *Fluid Dyn.* **39**, 851.

Lyubimov, D.V., Lyubimova, T.P. & Shklyaev, S.V. 2006 Behavior of a drop on an oscillating solid plate. *Phys. Fluids* **18**, 012101.

MacRobert, T.M. 1967 *Spherical Harmonics*. New York, NY: Pergamon.

Maddocks, J.H. 1985 Restricted quadratic forms and their application to bifurcation and stability in constrained variational principles. *SIAM J. Math. Anal.* **16**, 47–68.

Maddocks, J.H. 1987 Stability and folds. *ARMA* **99**, 301–328.

Majumbar, S.R. & Michael, D.H. 1976 The equilibrium and stability of two-dimensional pendent drop. *Proc. R. Soc. Lond. A* **351**, 89–115.

May, H.J. & Lowry, B.J. 2008 Microgravity/microscale double-helical fluid containment. *Proc. R. Soc. A* **464**, 855–875.

Michael, D.H. 1981 Meniscus stability. *Annual Review of Fluid Mechanics* **13**, 189–215.

Miles, J. & Henderson, D. 1990 Parametrically forced surface waves. *Annual Review of Fluid Mechanics* **22**, 143165.

Miller, C.A. & Scriven, L.E. 1968 The oscillations of a fluid droplet immersed in another fluid. *J. Fluid Mech.* **32**, 417–435.

Myshkis, A.D., Babskii, V.G., Slobozhanin, N.D. & Tyuptsov, A.D. 1987 *Low-Gravity Fluid Mechanics*. Oxford: Springer.

Noblin, X., Buguin, A. & Brochard-Wyart, F. 2004 Vibrated sessile drops: transition between pinned and mobile contact lines. *Eur. Phys. Journal E* **14**, 395–404.

Noblin, X., Buguin, A. & Brochard-Wyart, F. 2005 Triplon modes of puddles. *Phys. Rev. Letters* **94**, 166102.

Noblin, X., Kofman, R. & Celestini, F. 2009 Ratchet-like motion of a shaken drop. *Phys. Rev. Letters* **19**, 194504.

Padrino, J.C., Funada, T. & Joseph, D.D. 2007 Purely irrotational theories for the viscous effects on the oscillations of drops and bubbles. *International Journal of Multiphase Flow* **34**, 61–75.

Patzek, T.W., Benner, R.E., Basaran, O.A. & Scriven, L.E. 1991 Nonlinear oscillations of lnviscid free drops. *Journal of Computational Physics* **97**, 489–515.

Plateau, J.A.F. 1863 Experimental and theoretical researches on the figures on equilibrium of a liquid mass withdrawn from the action of gravity. *A. Rep. Board Reg. Smithson. Inst.* pp. 207–285.

Plateau, J.A.F. 1873 *Statique Expérimentale et Théorique des Liquides Soumis aux Seules Forces Moléculaires*. Paris, France: Paris, Gauthier-Villars.

Prosperetti, A. 1980*a* Free oscillations of drops and bubbles: the initial-value problem. *J. Fluid Mech.* **100**, 333–347.

Prosperetti, A. 1980*b* Normal-mode analysis for the oscillations of a viscous liquid drop in an immiscible liquid. *J. Mecanique* **19**, 149–182.

Prosperetti, A. 1980*c* Viscous effects on perturbed spherical flows. *Quart. Appl. Math.* **34**, 339–352.

Rayleigh, Lord 1879 On the capillary phenomenon of jets. *Proc. R. Soc. Lond.* **29**, 71–97.

Reid, W.H. 1960 The oscillations of a viscous liquid drop. *Q. Appl. Math.* **18**, 86–89.

Renardy, Y., Popinet, S., Duchemin, L., Renardy, M., Zaleski, S., Josserand, C., Drumright-Clarke, M.A., Richard, D., Clanet, C. & Quèrè, D. 2003 Pyramidal and toroidal water drops after impact on a solid surface. *J. Fluid Mech.* **484**, 69–83.

Richard, D., Clanet, C. & Quere, D. 2002 Contact time of a bouncing drop. *Nature(London)* **417**, 811.

Rodot, H., Bisch, C. & Lasek, A. 1979 Zero-gravity simulation of liquids in contact with a solid surface. *Acta. Astronautica* **6**, 1083–1092.

Roy, R.V. & Schwartz, L.W. 1999 On the stability of liquid ridges. *J. Fluid Mech.* **391**, 293–318.

Russo, M.J. & Steen, P.H. 1986 Instability of rotund capillary bridges to general disturbances: Experiment and theory. *J. Colloid and Interface Science* **113**, 154–163.

Schmuki, P. & Laso, M. 1990 On the stability of rivulet flow. *J. Fluid Mech.* **215**, 125–143.

Segel, L.A. 1987 *Mathematics Applied to Continuum Mechanics*. New York, NY: Dover Publications.

Slobozhanin, L., Alexander, J. I. D. & Resnick, A. 1997 Bifurcation of the equilibrium states of a weightless liquid bridge. *Phys. Fluids* **9**, 1893–1905.

Steen, P.H. & Karcher, C. 1997 Fluid mechanics of spin casting. *Ann. Rev. Fluid Mechanics* **29**, 373–397.

Steiner, J. 1882 *Gesammelte Werke*. Berlin, Germany: Reimer.

Strani, M. & Sabetta, F. 1984 Free vibrations of a drop in partial contact with a solid support. *J. Fluid Mech.* **141**, 233.

Strani, M. & Sabetta, F. 1988 Viscous oscillations of a supported drop in an immiscible fluid. *J. Fluid Mech.* **189**, 397.

Theisen, E.A., Vogel, M.J., Hirsa, C.A., Lopez, A.H. & Steen, P.H. 2007 Capillary dynamics of coupled spherical-cap droplets. *J. Fluid Mech.* **580**, 495.

Towell, G.D. & Rothfeld, L.B. 1966 Hydrodynamics of rivulet flow. *AIChE Journal* **12**, 972–980.

Trinh, E. & Wang, T.G. 1982 Large-amplitude free and driven drop-shape oscillation: experimental results. *J. Fluid Mech.* **122**, 315–338.

Tsamopoulos, J.A. & Brown, R.A. 1983 Nonlinear oscillations of inviscid drops and bubbles. *J. Fluid Mech.* **127**, 519–537.

Vogel, M., Ehrhard, P. & Steen, P. 2005 The electroosmotic droplet switch: Countering capillarity with electrokinetics. *PNAS* **102**, 11974–11979.

Vukasinovic, B., Smith, M.K. & Glezer, A. 2007 Dynamics of a sessile drop in forced vibration. *J. Fluid Mech.* **587**, 395–423.

Walter, J. 1973 Regular eigenvalue problems with eigenvalue parameter in the boundary condition. *Mathematische Zeitschrift* **133**, 301–312.

Wang, T.G., Anilkumar, A.V. & Lee, C.P. 1996 Oscillations of liquid drops : results from usml-1 experiments in space. *J. Fluid Mech.* **308**, 1–14.

Weiland, R.H. & Davis, S.H. 1981 Moving contact lines and rivulet instabilities. part 2. long waves on flat rivulets. *J. Fluid Mechanics* **107**, 261–280.

Wilkes, E. & Basaran, O. 1999 Hysteretic response of supported drops during forced oscillations. *J. Fluid Mech.* **393**, 333–356.

Wilkes, E. & Basaran, O. 2001 Drop ejection from an oscillating rod. *J. Colloid Interface Sci.* **242**, 180–201.

Young, G.W. & Davis, S.H. 1987 Rivulet instabilities. *J. Fluid Mech.* **176**, 1–31.

Young, T. 1805 An essay on the cohesion of fluids. *Phil. Trans. R. Soc. London* **95**, 65–87.

Zhang, D.Y., Justis, N. & Lo, Y.H. 2004 Fluidic adaptive lens of transformable lens type. *Appl. Phys. Lett.* **84**, 4194.

Zhang, D.Y., Lien, V., Berdichevsky, Y., Choi, J. & Lo, Y.H. 2003 Fluidic adaptive lens with high focal length tunability. *Appl. Phys. Lett.* **82**, 3171.